Design, Fabrication and Characterization of Terahertz System-on-Chip Filters

by

Seyedali Dehghanian

B.Sc., Shiraz University, 2012
M.Sc., Amirkabir University of Technology (AUT), 2017

A Dissertation Submitted in Partial Fulfillment of the
Requirements for the Degree of

DOCTOR OF PHILOSOPHY

in the Department of Electrical and Computer Engineering

© Seyedali Dehghanian, 2025
University of Victoria

All rights reserved. This dissertation may not be reproduced in whole or in part,
by photocopying or other means, without the permission of the author.

We acknowledge and respect the Lək'ʷəŋən (Songhees and X'ʷsepsəm/Esquimalt)
Peoples on whose territory the university stands, and the Lək'ʷəŋən and WS̱ÁNEĆ
Peoples whose historical relationships with the land continue to this day.

Design, Fabrication and Characterization of Terahertz System-on-Chip Filters

by

Seyedali Dehghanian

B.Sc., Shiraz University, 2012
M.Sc., Amirkabir University of Technology (AUT), 2017

Supervisory Committee

Dr. R. Levi Smith, Co-supervisor
(Department of Electrical and Computer Engineering)

Dr. Thomas Darcie, Co-supervisor
(Department of Electrical and Computer Engineering)

Dr. Peter Wild, Outside Member
(Department of Mechanical Engineering)

ABSTRACT

Terahertz System-on-Chip (TSoC) technology has emerged as a compact and integrated alternative to conventional free-space Terahertz (THz) systems, addressing critical challenges such as signal propagation losses, pulse distortion, high implementation costs, and system integration complexities. Despite these advancements, a gap remains in fully exploiting the potential of TSoC platforms for the design and optimization of integrated THz filters.

This work presents the design, simulation, and experimental validation of multiple integrated THz filters within the TSoC framework. Leveraging impedance-engineered Coplanar Strip (CPS) transmission lines, these filters achieve precise frequency selectivity, enabling controlled signal transmission and rejection at THz frequencies. Specifically, the investigated designs include: (i) a band-stop THz Apodized Bragg Grating (TABG), (ii) a planar multimodal periodic filter at THz frequencies, and (iii) low-pass planar all-pole network filters based on stepped-impedance Bessel designs of orders 3, 4, and 5. The fabricated filters were experimentally validated using Terahertz Time-Domain Spectroscopy (THz-TDS), demonstrating strong agreement between simulated results obtained using commercial software (ANSYS HFSS) and measured data, thereby confirming the effectiveness of the proposed designs.

To further automate the design process of THz filters—particularly in scenarios where conventional methods are impractical or insufficient—this study introduces an inverse-design methodology based on a natural selection optimization technique. Leveraging the Genetic Algorithm (GA), the proposed approach systematically and efficiently explores the design space to achieve optimal filter characteristics. The flexibility of this framework enables accommodation of diverse design objectives, including varying center frequencies, rejection depths, and impedance matching requirements, making it a promising tool for next-generation TSoC components. This approach not only streamlines the filter design process but also establishes a foundation for the automated synthesis of other THz components, such as couplers, multiplexers, and power dividers.

The experimental results presented in this work confirm the practical feasibility of planar filters for real-world applications. By offering valuable insights into the rapidly advancing TSoC framework, this dissertation establishes a solid foundation for the continued exploration of compact planar filters using both classical and modern design methodologies. Future research can build upon these contributions by bridging the gap between academic developments and industrial applications, and by extending the methodologies to a broader class of components, with the aim of further enhancing the performance and versatility of integrated THz technologies.

Contents

List of Tables

List of Figures

Acronyms

AlAs Aluminium Arsenide

ADC Analog-to-Digital Converter

Au Gold

CPS Coplanar Strip

CPW Coplanar Waveguide

CW Continuous-Wave

DC Direct Current

DI Deionized

DFG Difference Frequency Generation

DFT Discrete Fourier Transform

FDTD Finite-Difference Time-Domain

FEM Finite Element Method

FBG Fiber Bragg Grating

FFT Fast Fourier Transform

FWHM Full Width at Half Maximum

GA Genetic Algorithm

GaAs Gallium Arsenide

GHz Gigahertz

GVD Group Velocity Dispersion

HF Hydrofluoric

LPF Low-Pass Filter

LOR Lift-off Resist

LT-GaAs Low-Temperature Gallium Arsenide

MBE Molecular Beam Epitaxy

PCS Photoconductive Switch

PEC Perfect Electric Conductor

PR Photo Resist

PVD Physical Vapor Deposition

QCL Quantum Cascade Laser

QS Quasi-Static

RD-SOS Radiation-Damaged Silicon-on-Sapphire

RMSE Root Mean Squared Error

RTD Resonant Tunneling Diode

SI-GaAs Semi-Insulating Gallium Arsenide

SRR split-ring resonator

SSPP spoof surface plasmon polariton

TABG THz Apodized Bragg Grating

TEM Transverse Electro-Magnetic

THz Terahertz

THz-TDS Terahertz Time-Domain Spectroscopy

TSoC Terahertz System-on-Chip

UV Ultra Violet

VDW Van der Waals

VNA Vector Network Analyzer

ACKNOWLEDGEMENTS

I extend my sincere gratitude to my supervisor, Dr. R. Levi Smith, whose consistent support, thoughtful guidance, and leadership have been instrumental throughout my research journey. I am also deeply grateful to Prof. Thomas Darcie, whose expert advice and steady encouragement significantly contributed to the refinement and progress of this work. I would like to thank my supervisory committee, including Prof. Peter Wild, for their valuable input and guidance in shaping the direction of my dissertation.

Finally, I would like to express my appreciation to my lab mates, Dr. Mohsen Haghighat, Mani Asadi and Ghazal Mansoori for their camaraderie and support throughout this endeavor.

DEDICATION

Dedicated to my beloved parents, sister and brother, and to my beautiful girlfriend, Gazelle Raha, for their unwavering support, their endless love, and their boundless patience.

Chapter 1

Introduction

This dissertation presents the design, simulation, and experimental validation of terahertz (THz) filters integrated into a THz system-on-chip (TSoC) platform. The proposed filters utilize impedance engineered Coplanar Striplines (CPSs) to achieve frequency selectivity. The investigated designs include a band-stop THz apodized Bragg grating (TABG), a multimodal periodic band-stop filter, and low-pass planar network filters based on stepped-impedance Bessel designs. The experimental results were obtained using a modified THz time-domain spectrometer (THz-TDS) which was found to exhibit alignment with the simulation data, supporting the viability of these structures for on-chip THz spectral control.

To advance beyond the constraints of traditional design methodologies, this dissertation introduces an inverse-design framework that incorporates computational optimization techniques to enhance THz filter performance. This methodology enables automated refinement of structural geometries and impedance profiles to meet specific frequency-dependent S-parameter requirements. By integrating these strategies, the design process becomes more adaptable to compact, high-performance filter implementations. The ongoing and future work will aim to generalize this framework for a wider class of THz components and further its integration within next-generation TSoC systems.

This chapter outlines the motivation behind this research, emphasizing the need for compact, low-loss, and high-performance THz filters within the TSoC platform. In addition, it presents the major and minor contributions of this work and clarifies the role of each collaborator in achieving the reported results.

1.1 Motivation

The growing demand for compact, efficient, and high-performance THz systems has driven significant advances in recent years. However, conventional THz waveguides and free space systems exhibit detriments such as high radiation losses, pulse distortion, and complex fabrication requirements that continue to hinder their adoption in practical applications. Among the key components of the THz systems, filters play an essential role in defining the performance of the system by selectively transmitting desired frequency bands while suppressing unwanted signals. However, the design of low-loss, low-dispersion on-chip THz filters remains a challenging problem.

Recently, an innovation in TSoC technology has demonstrated the potential of low-loss and low-dispersion THz integrated circuits utilizing a thin silicon nitride membrane platform [7]. This approach integrates thin-film photoconductive devices directly with CPS transmission lines, enabling efficient generation and detection of THz pulses with minimal distortion and reduced radiation losses, achieving performance beyond 2 THz.

Despite recent advances, the design and characterization of high-performance filters tailored for the TSoC platform remain a critical yet largely unexplored research challenge. Accurate engineering of these filters is essential for optimizing signal integrity, minimizing insertion loss, and improving overall system performance in the THz regime. As a result, this area offers significant opportunities for scientific discovery and technological innovation, paving the way for next-generation THz integrated circuits with enhanced efficiency and functionality.

This dissertation is dedicated to the design, fabrication, and characterization of THz filters, leveraging the capabilities of the thin silicon nitride membrane-based TSoC platform. By applying principles of electromagnetics, wave propagation, and circuit theory, this research addresses key challenges in achieving frequency selectivity, low insertion loss, and compact, scalable THz filter designs.

Four distinct planar filter designs are presented, each optimized for compactness and high performance within the 0–2 THz range. The first two are band-stop configurations that are constructed from periodic unit cells to achieve sharp and tunable spectral rejection at targeted frequencies. The third design explores planar Low-Pass Filter (LPF)s based on Bessel responses of varying orders, selected for their maximally flat group delay and minimal phase distortion. Lastly, an inverse design approach is employed to systematically investigate a wide range of potential configurations, resulting in compact and performance-optimized filter structures. These design refinements are carefully tailored to meet the stringent performance requirements of TSoC applications, contributing to innovative and practical advances in this rapidly evolving field.

The findings of this research lay the foundation for the development of advanced THz planar filters, enabling a wide range of applications such as THz spectroscopy, high-resolution imaging, precision inspection, and next-generation communication systems.

1.2 Organization of the Dissertation

This dissertation follows a paper-based format and comprises six research articles. Four of these papers reflect the primary contributions of the author and collaborators, while the remaining two are included as minor contributions. Subsequent sections summarize each contribution and specify the author's role in each project.

To provide context for these contributions, the dissertation is organized into a series of chapters that frame the research within its technical, methodological, and conceptual foundations. Chapter 2 reviews the technical background essential for understanding the TSoC platform and the principles of THz filter design. Chapter 3 details the methodologies employed in this work, including the measurement setup and fabrication process. Chapter 4 presents the primary research contributions in a condensed format and discusses their significance. Chapter 5 summarizes the key findings, compares their outcomes, reflects on their implications, and proposes directions for future research. The appendix contains copies of all published or submitted manuscripts in their original publisher formats. This structure is intended to guide the reader through a coherent and insightful exploration of the research.

1.3 Major Contributions

The following subsections provide a brief overview of the author's contributions, with a more detailed discussion presented in Chapter 4.

1.3.1 Demonstration of an Integrated Terahertz Band-Stop Filter Using an Apodized Bragg Grating [1]

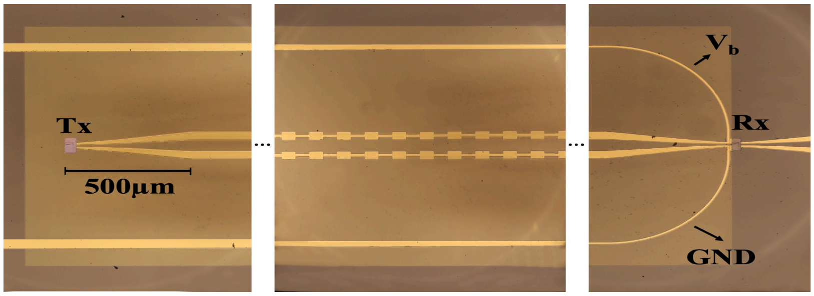

Figure 1.1: Microscopic image of the TABG filter

This paper presents the implementation and experimental validation of an on-chip integrated TABG designed as a band-stop filter. The proposed TABG exhibits a center frequency of 0.8 THz with a stop-band width of 200 GHz. To evaluate its performance, the TABG is integrated into a TSoC platform, facilitating wideband characterization across the DC–1.5 THz frequency range. Experimental measurements of signal transmission through the TABG demonstrate strong agreement with theoretical predictions and simulation results, achieving a rejection of approximately 20 dB within the stop-band (Fig. 1.1).

Contributions: I was responsible for the simulation, fabrication, and testing of the TABG, as well as the preparation of the manuscript. W. Gomaa designed the initial structure. M. Haghighat assisted with the fabrication of the PCS. T. Darcie contributed to the manuscript and provided valuable guidance throughout the project. L. Smith supervised all aspects of the work, including PCS fabrication, structural design, device testing, and manuscript writing.

1.3.2 Demonstration of a Planar Multimodal Periodic Filter at THz Frequencies [2]

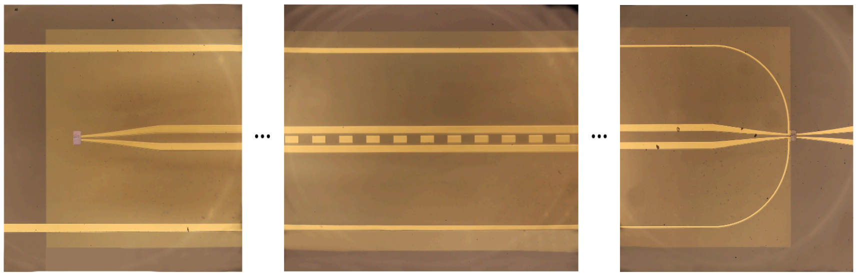

Figure 1.2: Microscopic image of the THz band-stop periodic filter

This paper presents a proof-of-concept THz band-stop periodic filter composed of alternating sections of CPS and the odd mode of a finite-ground-plane Coplanar Waveguide (CPW). The theoretical framework and design methodology for developing the filter are outlined. The fabricated filter exhibits a center frequency of $f_c = 0.8$ THz with a bandwidth of $\Delta f = 0.07$ THz. Experimental results demonstrate strong agreement with theoretical predictions and simulations, validating the proposed design approach (Fig. 1.2).

Contributions: I designed the structure, performed the simulations, and conducted the testing of the THz band-stop filter. M. Haghighat assisted with the fabrication of the PCS, while T. Darcie contributed to manuscript preparation. L. Smith guided the project, including idea development, PCS fabrication, filter design, experimental validation, and manuscript writing.

1.3.3 Demonstration of a Terahertz Integrated Planar Network Synthesis Filter [3]

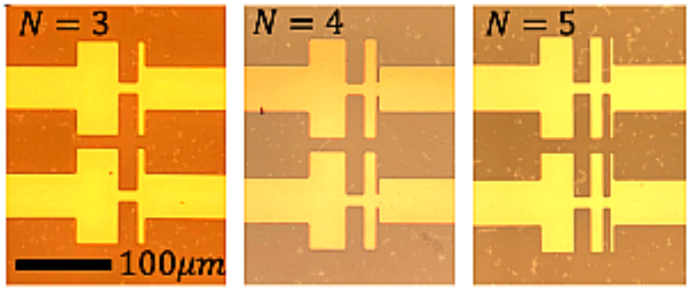

Figure 1.3: Microscopic image of the Bessel filters ($N = 3, 4, 5$)

At THz frequencies, few experimental studies demonstrate the use of all-pole network synthesis filters in planar waveguides. In this work, we fabricate three integrated planar LPFs for THz applications, all designed with the same cut-off frequency ($f_c = 0.8$ THz) but with different filter orders ($N = 3, 4, 5$). Experimental results show increasing roll-off rates with higher filter orders and minimal pulse distortion, consistent with theoretical expectations (Fig. 1.3).

Contributions: I was responsible for the design, simulation, and testing of the integrated THz planar network synthesis filters. M. Haghighat contributed to the fabrication of the PCS, while T. Darcie assisted with manuscript preparation. L. Smith supervised the project, including PCS fabrication, filter design, experimental validation, and manuscript writing.

1.3.4 Genetic Algorithm-Based Inverse Design of Guided Wave Planar Terahertz Filters [4]

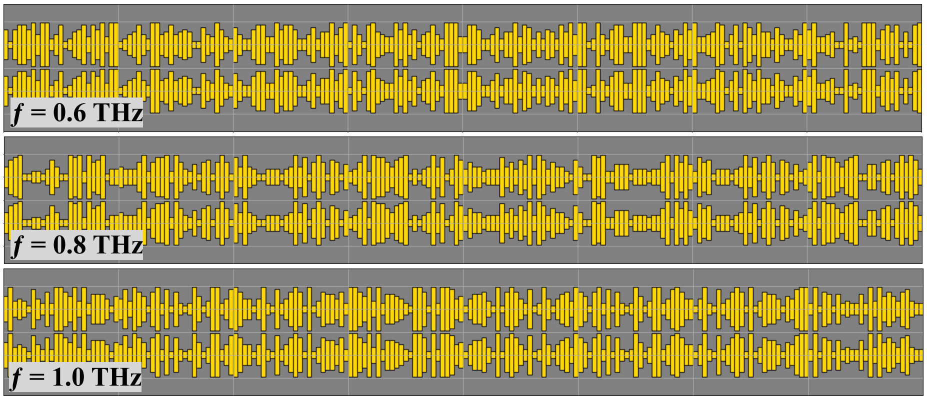

Figure 1.4: Illustration of THz non-intuitive filter structures generated through the GA-based optimization approach.

This manuscript presents a genetic algorithm (GA)-based inverse design framework for synthesizing high-performance planar THz filters integrated with CPS transmission lines. The method efficiently explores high-dimensional design spaces to generate filter geometries that match user-defined S-parameter magnitude and phase responses, while enforcing structural connectivity for compatibility with TSoC platforms. To accelerate the optimization process, filter performance is evaluated using the ABCD matrix method, offering a significant computational advantage over full-wave simulations. Final validation is performed through Finite Element Method (FEM) simulations. As a proof of concept, band-stop filters are designed with center frequencies of 0.6, 0.8, and 1.0 THz, each targeting a 150 GHz bandwidth, demonstrating tunable rejection depths within a fixed physical footprint. Optimization is guided by minimizing the root-mean-square error (RMSE) between the simulated and target S-parameters.

Contributions: I developed the main idea, implemented the GA, and performed the coding and simulations. T. Darcie assisted with manuscript preparation. L. Smith supervised the project, provided feedback, and contributed to the writing.

1.4 Minor Contributions

1.4.1 Demonstration of Terahertz Spoof Surface Plasmon Polariton Waveguides Using Coplanar Striplines with Internal Corrugations [5]

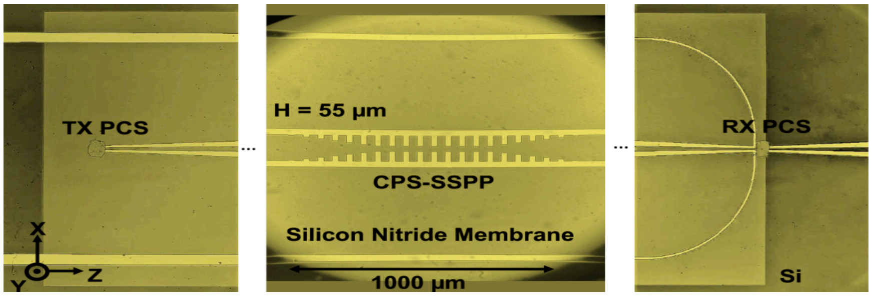

Figure 1.5: Microscopic image of the THz spoof surface plasmon polariton waveguide

This paper presents the design and experimental verification of a THz spoof surface plasmon polariton (SSPP) waveguide based on a CPS with internal corrugations (Fig. 1.5), compared to an external corrugation configuration. Internal corrugations are chosen to enhance mode conversion efficiency and reduce insertion loss. Simulations predict this effect, which is experimentally validated by exciting the SSPP mode for two corrugation depths (55 μm and 65 μm). The observed SSPP band-edge frequency shift from 0.89 THz to 0.72 THz aligns with simulation results.

Contributions: I contributed to the fabrication of the PCS and assisted with the testing and measurement processes.

1.4.2 Terahertz band-stop Filter Using Varying Radii Split-Ring Resonators [6]

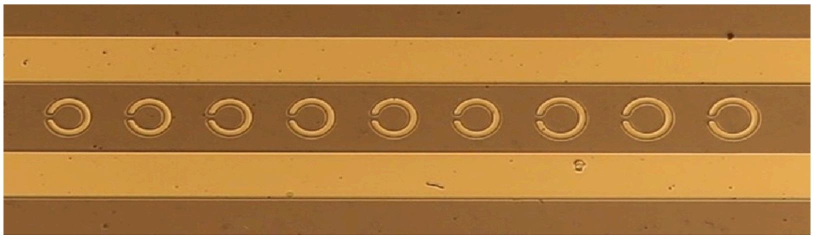

Figure 1.6: Microscopic image of the THz band-stop filter based on split-ring resonator

This paper presents a proof-of-concept THz band-stop filter based on split-ring resonator (SRR). The design consists of nine SRRs arranged into three groups with radii of 13 $\mu m, 14$ μm, and 15 μm, positioned between the conductors of a CPS (Fig. 1.6). Each SRR group produces a notch filter at a distinct center frequency, collectively forming a band-stop filter with a center frequency of 1.09 THz and a 3 dB bandwidth of 0.36 THz. The transmission response is experimentally measured using a modified THz time-domain spectrometer, showing strong agreement with theoretical and simulation results. This study highlights the potential of varying-radius SRRs as sub-wavelength filter elements for THz applications.

Contributions: My role involved the fabrication of PCS and participating in the testing and measurement of the filter's performance.

Chapter 2

Review and Theoretical Background

2.1 Terahertz Gap

The THz gap, spanning frequencies from 100 GHz to 10 THz, represents a unique region in the electromagnetic spectrum, bridging electronics and photonics (Fig. 2.1). During the past few decades, significant research efforts have been directed toward harnessing the unique properties of electromagnetic waves at THz frequencies for various applications where their unique characteristics, such as their ability to penetrate optically opaque materials, sensitivity to molecular interactions, and large bandwidths, make them highly valuable in multiple scientific and technological disciplines. However, despite their promising advantages, the widespread adoption of THz technology remains limited due to fundamental challenges in efficient generation, detection, and system integration [8].

One of the most promising applications of THz waves is in high-speed wireless communication. The availability of a broad frequency spectrum in the THz range enables ultrafast data transmission rates, exceeding those achievable with conventional microwave frequencies. As a result, THz waves are considered a key enabler for next-generation wireless communication systems, including 6G networks, high capacity backhaul links, and short-range ultra wideband communication. Several studies have investigated the feasibility of THz-based communication networks, with Kleine et al. [10] providing a comprehensive review of THz communication technologies, Chen et al. [11] exploring the prospects of THz-based wireless systems, and Tekbiyik

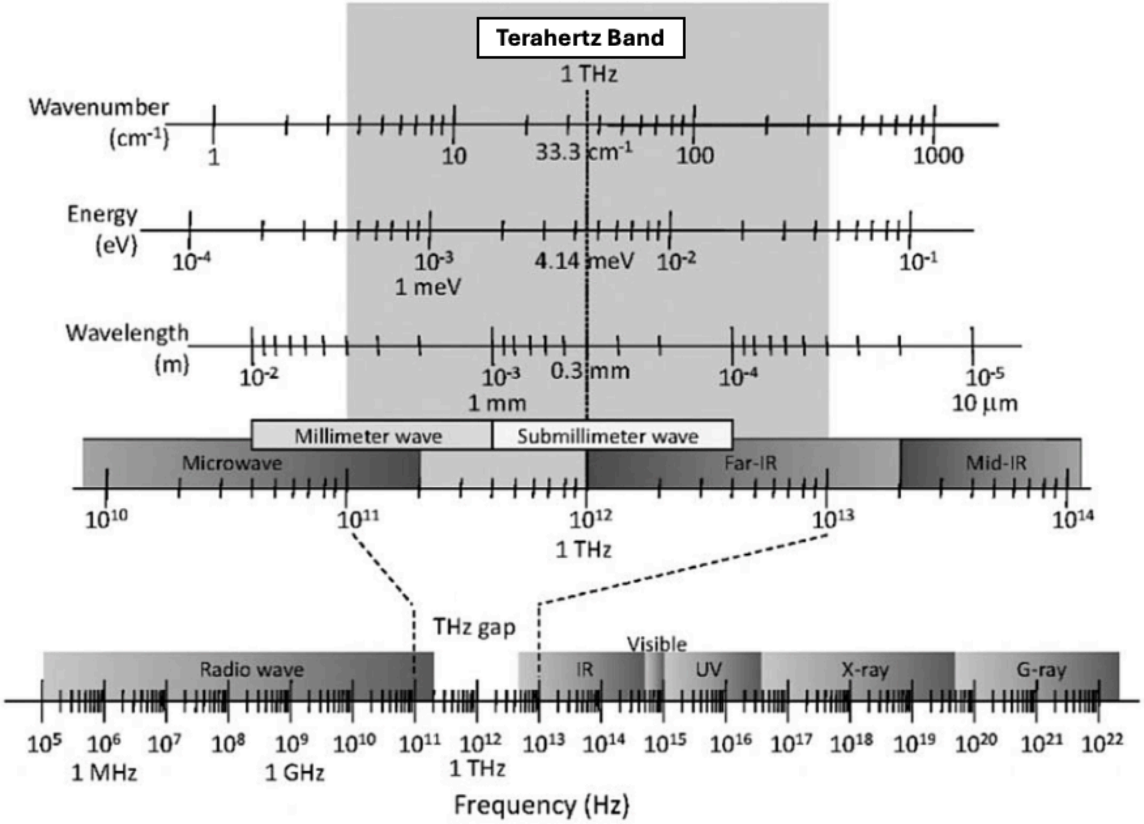

Figure 2.1: Electromagnetic wave spectrum and THz band (reprinted with permission from [9]) © 2009 Yun-Shik Lee.

et al. [12] analyzing the potential of THz frequencies in achieving terabit-per-second data transmission.

Beyond telecommunications, low-energy THz waves (4.14 meV at 1 THz) possess unique penetration properties, making them valuable for noninvasive imaging and security screening. Unlike X-rays, THz radiation is non-ionizing, offering a safer alternative for biomedical diagnostics, material inspection, and personnel screening. Its ability to penetrate nonmetallic materials, such as clothing, plastics, ceramics, and dry biological tissues, has been widely explored for imaging applications. Several studies have investigated these capabilities. Jepsen et al. [13] examined the use of THz radiation for noninvasive imaging, while Peiponen et al. [14] discussed its role in material characterization. Yang et al. [15] highlighted its potential in biomedical applications. In addition, Afsah et al. [16] provided a comprehensive review of THz-based screening methods, and Lee et al. [9] outlined the principles of THz imaging for personnel security. The short wavelengths of THz radiation also enable high-resolution imaging, making it particularly suitable for biological imaging and fine structural analysis [17].

Additionally, THz waves play a critical role in spectroscopy and material characterization. Many materials exhibit distinct absorption features in the THz frequency range, enabling precise identification of chemical compounds, pharmaceuticals, and hazardous substances. This property has made THz spectroscopy an essential tool in advanced sensing applications, particularly in pharmaceutical quality control, gas detection, and non-destructive material testing. Research in this area has demonstrated the effectiveness of THz spectroscopy across various domains: Danciu et al. [18] and Tewari et al. [19] explored its applications in chemical analysis, while Guo et al. [20] investigated its potential for detecting molecular structures. Additionally, Smye et al. [21] analyzed the interaction of THz radiation with molecular vibrations, further emphasizing its importance for material characterization.

2.2 THz Generation and Detection

The generation and detection of THz waves are critical to unlocking their full potential in the previously mentioned applications. THz wave generation requires the efficient conversion of energy into the desired frequency range, while detection involves the capture and analysis of signals with high sensitivity. However, both processes are hindered by material constraints, efficiency limitations, and the need for precise electronic or photonic circuit control to minimize losses and optimize performance.

The development of femtosecond lasers has played a crucial role in advancing THz wave generation and detection, enabling compact, high-power, and broadband THz sources. Research in this area has shown promising results, particularly in semiconductor-based THz emitters driven by ultra-fast laser pulses. Lee et al. [22, 23] showcased efficient THz generation using photoconductive and nonlinear optical mechanisms, while Ducournau et al. [24] explored silicon-based THz sources leveraging femtosecond laser excitation for integrated photonic systems. Tonouchi et al. [25] pioneered laser-driven THz generation techniques, laying the foundation for modern ultrafast THz photonics. Furthermore, Mathanker et al. [26] enhanced femtosecond laser-based THz detection, improving system sensitivity and spectral resolution.

To provide a comprehensive overview of widely adopted techniques, Table 2.1 summarizes key THz generation and detection methods along with their operating principles, advantages, limitations, and frequency ranges. These methods represent the foundation of current THz system design and serve as a comparative basis for selecting application-specific platforms.

Table 2.1: Summary of common THz generation and detection techniques with key advantages and limitations

Technique	**Principle**	**Key Advantages**	**Limitations**	**Frequency Range (THz)**	**Ref.**
THz Generation					
Optical Rectification	Nonlinear polarization induced by femtosecond laser pulses in electro-optic crystals.	Broadband, ultrafast, coherent	Low conversion efficiency; requires intense laser sources	0.1–3	[27]
Difference Frequency Generation (DFG)	Mixing of two optical waves in a nonlinear crystal produces radiation at their frequency difference.	Tunable, narrow-band, coherent	Requires precise phase matching and dual lasers	0.5–6	[28]
Photoconductive Switching	Transient photocurrent in a biased semiconductor excited by femtosecond pulses emits THz.	Broadband, compact, scalable	Limited power output; substrate heating at high repetition rates	0.1–4	[29, 30]
Quantum Cascade Lasers (QCLs)	Emission via engineered intersubband transitions in semiconductor heterostructures.	Coherent, tunable, compact	Typically requires cryogenic cooling; narrow-band operation	1.2–5	[31, 32]
THz Detection					
Photoconductive Detection	Conductivity modulation of a photoconductive antenna by incident THz pulses enables time-domain sampling.	Fast, sensitive, time-resolved	Requires optical gating; low responsivity at higher frequencies	0.1–5	[33]
Bolometers	Absorption of THz energy induces a measurable thermal change in a temperature-sensitive element.	High sensitivity, broadband	Slow response time; often requires cryogenic cooling	0.1–30	[34]
Heterodyne Detection	Mixing of the THz signal with a local oscillator in a nonlinear element generates an RF beat signal.	High spectral resolution, coherent	Requires stable LO source; narrow detection bandwidth	0.1–10	[35]
Field-Effect Transistors (FETs)	Incident THz field modulates transport characteristics of high-mobility transistors.	CMOS-compatible, scalable	Limited sensitivity; typically narrow-band	0.1–3	[36]

Among available methods, Photoconductive Switching offers distinct advantages for both THz wave generation and detection. Its sub-picosecond response time enables precise time-domain measurements, making it well-suited for ultrafast spectroscopy and high-speed imaging. PCS devices also support broadband operation across approximately 0.1–4 THz, facilitating applications in molecular spectroscopy, material characterization, and high-data-rate communication.

In addition to their broadband capabilities, PCS devices exhibit high optical-to-THz conversion efficiency, enabling robust signal generation with minimal losses—critical for accurate measurements and enhanced sensitivity. Their compact, integrable form factor further supports seamless integration with other THz components, promoting the development of portable and scalable systems. Due to their performance, cost-effectiveness, and reliability, PCS devices were selected as the primary platform for THz generation and detection in this study. All simulations, measurements, and system evaluations presented herein are based on this method and operating frequency range.

2.2.1 Photoconductive Switch

Figure 2.2 illustrates the structure of a PCS, which consists of a photoconductive substrate integrated with a patterned metal dipole antenna. A laser beam is focused onto the gap between the dipole arms, where the substrate absorbs the optical energy and generates electron-hole pairs. A DC bias voltage applied across the dipole creates an electric field that accelerates the photogenerated carriers, resulting in a transient photocurrent. This current couples to the antenna structure and induces the emission of THz radiation [9, 37, 38]. Depending on the operational mode, a PCS can function either in continuous-wave mode via photomixing or in pulsed mode through photoconductive switching.

In photoconductive switching, a biased photoconductive substrate is excited by an ultrashort femtosecond laser pulse, resulting in the generation of THz radiation. Unlike photomixing, which relies on the optical beating of two Continuous-Wave (CW) lasers, photoconductive switching employs high-peak-power optical pulses to induce carrier excitation. When a bias voltage is applied, the photoexcited carriers accelerate within the photoconductive substrate, producing an impulse current that subsequently decays due to the finite carrier lifetime of the material. Compared to photomixing, photoconductive switching provides higher conductance and greater THz output power, due to intense peak excitation, which enhances overall generation efficiency.

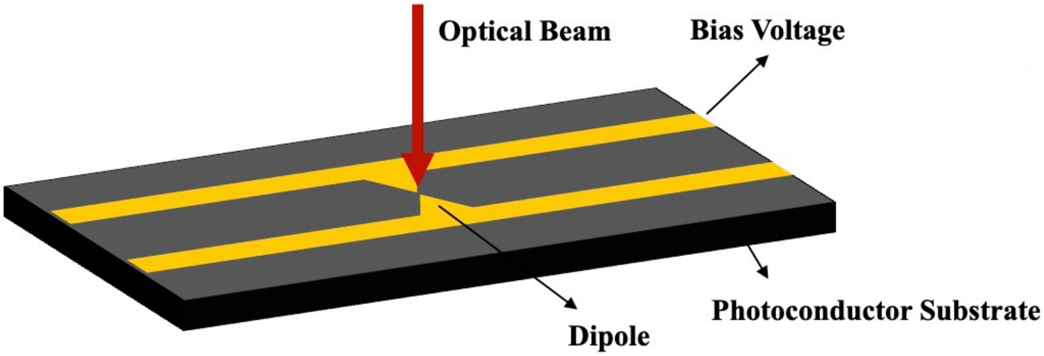

Figure 2.2: Schematic diagram of a PCS consisting of a semiconductor substrate integrated with a dipole antenna.

Figure 2.3 illustrates the electric dipole radiation emitted from a PCS. The dipole approximation is valid since the characteristic size of the source, which is comparable to the optical beam spot size, w_0 (10 μm in this work), is significantly smaller than the wavelength of the emitted THz radiation, λ_{THz} (300 μm at 1 THz).

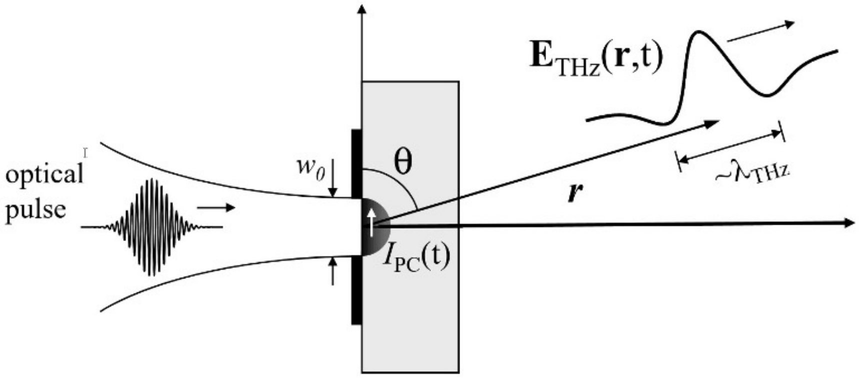

Figure 2.3: Radiation of an electric dipole from a PCS (reprinted with permission from [9]). © 2009 Yun-Shik Lee.

The electric field of the THz dipole radiation in free space can be expressed as

$$\mathbf{E}_{THz}(t) = \frac{\mu_0}{4\pi}\frac{\sin\theta}{r}\frac{d^2}{dt_r^2}\left[p(t_r)\right]\hat{\theta}, \tag{2.1}$$

where $p(t_r)$ represents the dipole moment of the source at the retarded time t_r, and μ_0 is the permeability of free space. The equation characterizes the THz radiation field generated via photoconductive switching, incorporating the spatial distribution of the emitted wave, the angular dependence of the radiation pattern, and the temporal evolution of the THz signal.

Efficient emission and detection of THz radiation using PCSs require ultrafast switching behavior, particularly in the sub-picosecond regime. The activation (turn-on) time is primarily dictated by the duration of the incident laser pulse [39], whereas the deactivation (turn-off) time is governed by the carrier lifetime of the photogenerated electrons and holes in the semiconductor substrate. Therefore, achieving high-speed operation depends not only on using femtosecond laser pulses but also on selecting materials with extremely short carrier lifetimes. In addition, high carrier mobility and high breakdown voltage are desirable characteristics to improve overall performance and reliability of the PCS [9].

Among the available materials, Low Temperature Gallium Arsenide (LT-GaAs) is widely used for PCS fabrication due to its subpicosecond carrier lifetime. LT-GaAs is typically made via molecular beam epitaxy (MBE) at substrate temperatures ranging from 180–240°C, followed by rapid thermal annealing [40, 41]. Growth at such low temperatures introduces a high density of point defects, including arsenic antisites, arsenic interstitials, and gallium vacancies. These defect states facilitate rapid carrier trapping, effectively shortening the carrier lifetime. Substrate growth temperatures around 200°C have been shown to yield the shortest lifetimes (approximately 0.2 ps), making LT-GaAs highly suitable for ultrafast THz switching applications [40].

2.3 THz Field Sampling

An LT-GaAs PCS can function as both a transmitter and a receiver. As a transmitter, an electrical bias is applied to the active region via contact pads. As a receiver, the contact pads are connected to a lock-in amplifier, enabling the detection of low-amplitude photocurrents in the 100 pA to 10 nA range, generated by the incident THz field.

Currently, commercially available measurement systems, such as Vector Network Analyzer (VNA)s, unable to achieve a sampling rate of 20×10^{12} samples per second ($F_s \geq 2 \cdot F_{\max}$, as per the Nyquist-Shannon sampling theorem). Even the most advanced and expensive VNAs—such as millimeter-wave systems with frequency extenders—are limited to approximately 1.5 THz. Consequently, time-domain optical sampling methods are necessary for reconstructing the temporal profile of ultrafast THz pulses.

In the receiver, when the optical pulse interacts with the semiconductor, photocarriers are generated and exist for the duration of the carrier lifetime (τ_c). These photocarriers get accelerated by the incoming THz field, resulting in a photocurrent

$$J(t) = \int_{-\infty}^{t} \sigma_s(t - t_0) E_{\mathrm{THz}}(t_0) dt_0, \tag{2.2}$$

where $\sigma_s(t)$ is the receiver surface conductivity. The detailed calculation for this current can be found in [9].

In the frequency domain, Eq. (2.2) can be expressed as the pointwise product of the individual Fourier transforms using the convolution theorem:

$$F\{J\} = F\{\sigma_s\} \cdot F\{E_{\mathrm{THz}}\} \tag{2.3}$$

The equation can be understood by considering the ideal scenario, where the received photocurrent is directly proportional to E_{THz}. This condition is satisfied when the Fourier transform of the material's time-dependent conductivity, $\mathcal{F}\{\sigma_s(t)\}$, is flat across the spectral bandwidth of interest. This response is achieved when $\sigma_s(t)$ closely approximates an impulse function, which means that the duration of the carrier response must be significantly shorter than 1 ps.

Among candidate materials, LT-GaAs and Radiation-Damaged Silicon-on-Sapphire (RD-SOS) offer short carrier lifetimes of approximately 0.2 ps and 0.6 ps, respectively [42], whereas Semi-Insulating Gallium Arsenide (SI-GaAs) typically exhibits much longer lifetimes, on the order of hundreds of picoseconds [43].

Figure 2.4 illustrates the temporal surface conductivity $\sigma_s(t)$ for SI-GaAs, LT-GaAs, and RD-SOS. Among these, the response of LT-GaAs is distinguished by a sharp onset and rapid decay, closely approximating an ideal impulse function. This behavior makes LT-GaAs especially well-suited for time-domain THz applications requiring both high temporal resolution and broad spectral bandwidth. Accordingly, LT-GaAs is employed in this work as the photoconductive material for both THz emission and detection.

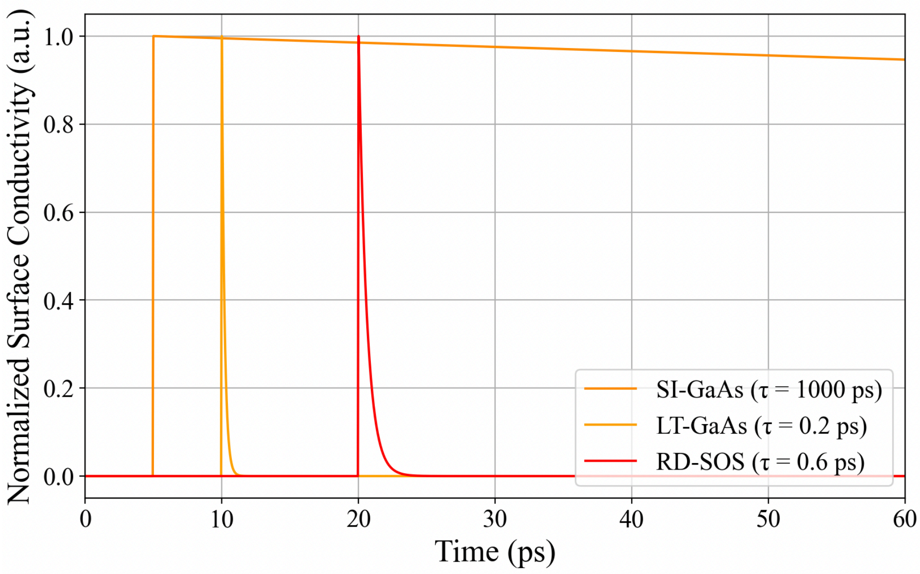

Figure 2.4: SI-GaAs, LT-GaAs and RD-SOS surface conductivity.

2.4 Terahertz System-on-Chip

Following the selection of LT-GaAs for efficient THz emission and detection, the next critical step involves integrating these components into a unified, scalable architecture. Achieving practical THz functionality requires more than optimizing individual device performance; it requires the seamless cointegration of generation, transmission, filtering, and detection within a compact and low-loss system. To meet these requirements while maintaining compatibility with large-scale fabrication, this work adopts a terahertz system-on-chip (TSoC) approach.

A TSoC is an integrated platform designed for operation in the THz frequency range, embedding multiple functionalities on a single chip. These include THz generation via PCS devices, signal transmission through low-loss waveguides, frequency-selective filtering, and coherent detection [7]. This high degree of integration minimizes interconnect losses and physical footprint while enhancing overall system performance. As a result, TSoC architectures represent a promising pathway for advanced applications such as high-speed wireless communication, non-invasive sensing, and real-time imaging [7].

In all experiments performed on the TSoC platform, the signal path followed the configuration illustrated in Fig. 2.5. To enable a meaningful comparison of filter performance, the system architecture—including the photoconductive source and detector, DC block, tapering section, and CPS transmission line—was held constant across all measurements. Only the planar filter section was varied. This controlled setup ensured uniform excitation and detection conditions, thereby enabling direct assessment of the spectral response and transmission characteristics attributable solely to each filter design.

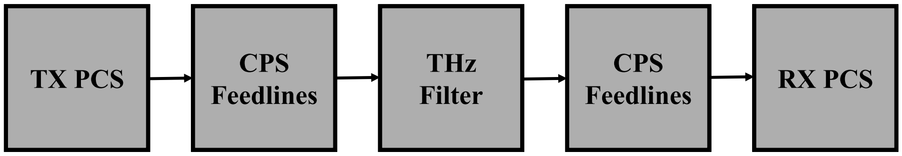

Figure 2.5: Schematic diagram of the signal path on the TSoC platform.

Figure 2.6 illustrates the TSoC platform and its key components, highlighting the design features that enable efficient operation at THz frequencies. Figure 2.6(a) shows the TSoC structure mounted on an ultra-thin silicon nitride membrane, visible as the white plane, which serves both as mechanical support and as a low-loss, THz-transparent substrate. This material choice minimizes signal attenuation and distortion. Further discussion of the silicon nitride membrane's role and properties is provided in Section 2.5.2.

Figure 2.6(b) indicates the location of the LT-GaAs PCS used as the transmitter, which acts as the THz radiation source in the system. Figures 2.6(c) and 2.6(d) highlight the placement of the LT-GaAs receiver and its connection to the gold pads beyond the DC block gap, demonstrating precise alignment for efficient THz signal detection. Figure 2.6(e) presents a cross-sectional schematic of the CPS transmission line positioned on the membrane. The waveguiding behavior, including the attenuation and dispersion characteristics, is analyzed in detail in Section 2.5.

Fabrication involved the preparation of multiple small LT-GaAs PCS devices, each measuring 40 μm $\times 70$ μm $\times 1.8$ μm, as described in Chapter 3. These devices were bonded onto the CPS transmission lines on the silicon nitride membrane, ensuring mechanical stability along with optimal optical and electrical alignment.

The primary focus of this research is on planar THz filters integrated within the TSoC platform. However, before addressing the specifics of filter design, it is important to understand the key components that make up the TSoC system. Consequently, the following sections provide a detailed analysis of the system architecture, including the role of tapering structures and waveguiding technology, along with

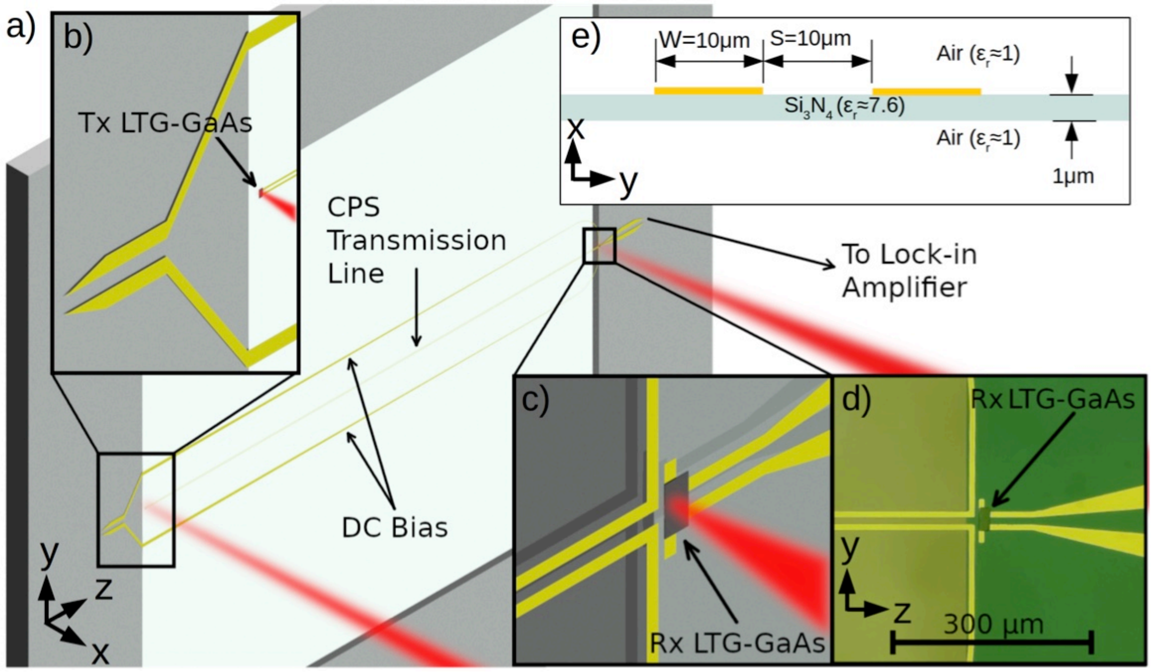

Figure 2.6: Illustration of the TSoC platform highlighting its main components. (a) TSoC structure on a silicon nitride membrane. (b) Location of the LT-GaAs transmitter. (c) Image showing the LT-GaAs receiver connection. (d) Microscopic image of the LT-GaAs receiver. (e) Cross-sectional view of the CPS transmission line at the transmitter and receiver PCS interfaces, demonstrating integrated component design for efficient signal transmission. Reprinted with permission from [7] © 2019 Optica Publishing Group.

their associated attenuation and dispersion characteristics. With a comprehensive description of the structural and functional elements of the system, the discussion then transitions to the design and integration of planar THz filters within this architecture.

2.4.1 Tapering Structure

The development of low-loss ultra-wideband interconnections between building block components with varying dimensions is necessary to allow efficient signal propagation. Tapered transmission lines provide an effective means of gradually transforming both physical dimensions and characteristic impedance, thereby facilitating seamless transitions between distinct transmission line geometries. The primary objective of such tapers is to deliver an ultra-wideband transition region between two cross-sectional profiles within the spatial constraints of the wafer. Although longer tapers may be explored, they are often impractical; shorter tapers are preferred because they optimize wafer area and improve fabrication feasibility.

In [44], the efficacy of transmission line tapers for interfacing two distinct CPS transmission line configurations was evaluated through both experimental measurements and simulations, spanning frequencies up to 2.0 THz with a spectral resolution of 25 GHz. The study demonstrated that tapering facilitates the transition from a compact device-constrained transmission line geometry ($W_1 = 10\ \mu$m, $S_1 = 10\ \mu$m) to a lower-loss configuration ($W_2 = 40\ \mu$m, $S_2 = 70\ \mu$m), thereby reducing overall attenuation. In addition, it established design constraints for the tapered sections to minimize dispersion and pulse distortion. Figure 2.7 illustrates the taper structure investigated in this work.

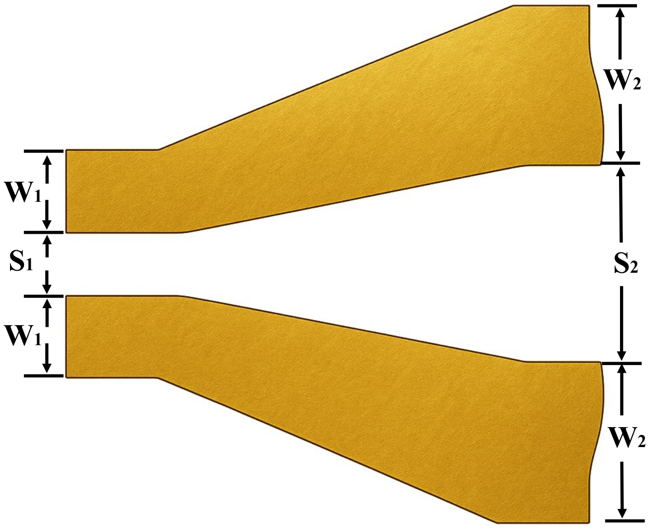

Figure 2.7: Taper structure adopted from prior work [44], illustrating the geometric parameters used to reduce mode mismatch and minimize insertion loss in the CPS transmission line.

2.5 THz Field Guiding Technologies

To ensure signal integrity and minimize propagation losses, the implementation of low-loss waveguides with minimal dispersion is necessary in the THz frequency regime. The choice of an appropriate waveguide is largely determined by the operating frequency range [45]. At lower frequencies (below 10 GHz), conventional guiding structures such as twisted pair conductors, coaxial cables, and metallic waveguides are commonly employed [46]. In contrast, at optical frequencies (above 100 THz), optical fibers and nanophotonic waveguides serve as the primary transmission medium [47].

As mentioned above, photoconductive switching is employed in this work for the generation and detection of THz signals. As a result, the resulting signal exhibits a broadband frequency spectrum, spanning from 0.1 THz to 2 THz. Consequently, the primary design considerations discussed in this dissertation are centered within this spectral range.

The active region of a PCS device functions similarly to a small current line (approximately 10–20 μm), implying that waveguides are excited by a localized source rather than by a plane wave. Therefore, only waveguides with small modal cross-sectional areas are suitable for efficient excitation. In larger waveguide structures, the fundamental mode profile often does not align with the localized current source, leading to the excitation of higher-order resonant modes and degraded performance. To mitigate this issue, smaller waveguide structures are preferred, as they minimize undesired resonances and improve coupling efficiency, although at the cost of increased attenuation.

Moreover, integration feasibility is a critical consideration when selecting waveguide structures for practical implementations. Planar waveguides offer notable advantages in this regard. Specifically, CPS and CPW structures are exceptionally suitable for integrated THz systems due to their planar configurations, compatibility with standard fabrication processes, and the ability to accurately match impedance to small current sources [48,49]. Therefore, these planar guiding wave structures represent an attractive solution for compact and efficient waveguide integration within TSoC applications.

2.5.1 Coplanar Strip Transmission Line and Coplanar Waveguide

A CPS consists of two parallel conductive strips placed on the same dielectric plane, without an underlying ground plane (Fig. 2.8(a)). It supports a quasi-Transverse Electro-Magnetic (TEM) mode of propagation, where the electric field is mainly confined between the two conductors. CPS exhibits lower dispersion and reduced conductor loss compared to conventional microstrip lines due to the absence of a dielectric substrate between the signal paths. However, CPS is more susceptible to radiation losses at higher frequencies due to its open structure [50].

In contrast, a CPW consists of a central signal conductor placed between two ground planes (Fig. 2.8(b)). This configuration offers enhanced electromagnetic shielding and compatibility with ground-referenced components. Depending on the application requirements, one of these transmission lines is typically preferred. For example, CPS offers advantages for differential signal transmission, impedance matching, and antenna feed networks, while CPW is generally chosen for applications that require improved electromagnetic shielding and straightforward integration with ground reference circuitry.

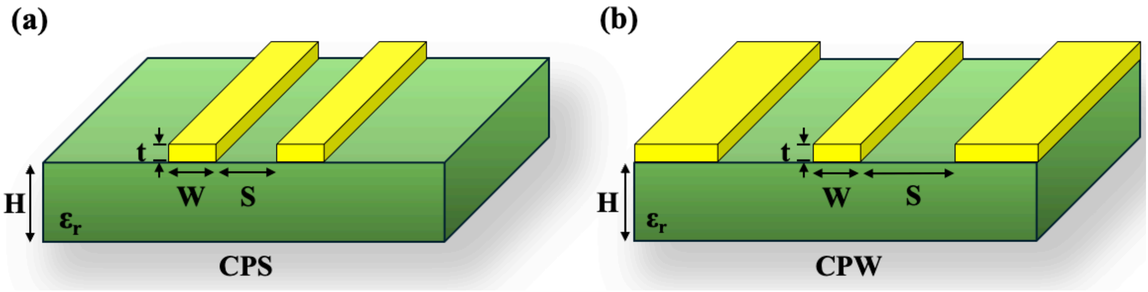

Figure 2.8: Cross-sectional illustration of CPS and CPW structures on a dielectric substrate with relative permittivity ε_r. These planar configurations are commonly used in integrated THz systems.

In this work, integrated systems primarily utilize CPS, except in scenarios requiring multimode operation [2]. The structural configurations of CPS and CPW transmission lines are illustrated in Fig. 2.8(a) and (b), respectively. A CPS transmission line consists of two narrow metal conductors, usually made of thin gold, with width W and separated by a gap S. These striplines are deposited on a dielectric substrate of thickness H. CPS supports the quasi-TEM mode, which closely resembles a true TEM mode, except for the presence of minor electric and magnetic field components aligned with the direction of propagation. These longitudinal components arise due to wave propagation across multiple dielectric media.

A CPW consists of a central conductor strip of width W, symmetrically flanked by two ground planes, each separated from the central conductor by a gap S. These conductors, typically made from high-conductivity metals such as gold, are deposited on a dielectric substrate of thickness H with relative permittivity ε_r. Similarly to CPS, CPW supports a quasi-TEM mode; however, it also enables multi-modal propagation. This multimodal characteristic allows for unique design possibilities that are not achievable with traditional two-conductor transmission lines [2].

The analysis of CPS transmission lines can be effectively performed using the quasi-static approximation, as outlined in [50, 51]. This approach assumes that electromagnetic field variations are sufficiently slow, allowing the effects of wave propagation to be neglected. Consequently, key transmission line parameters can be formulated in a simplified manner. In this framework, the capacitance (C), characteristic impedance (Z_{CPS}), and effective permittivity ($\varepsilon_{\mathrm{eff}}$) of the CPS structure can be estimated taking into account design variables such as metal thickness (t), substrate thickness (H), and relative permittivity (ε_r).

To determine the effective permittivity of the CPS, the total capacitance per unit length is given by

$$C = C_a + C_s, \tag{2.4}$$

where C_a denotes the capacitance per unit length due to the electric field in free space (i.e., in the absence of a dielectric substrate), and C_s represents the capacitance contribution from the dielectric substrate of thickness H and relative permittivity ε_r. In this formulation, it is assumed that all electric field lines are confined within the substrate, and the dielectric contribution is modeled as having a permittivity of $\varepsilon_r - 1$ relative to free space [50].

To calculate C_a and C_s, a series of conformal mappings specific to a CPS with a substrate of finite thickness is required. In this analysis, an imaginary plane positioned between the striplines is treated as an electric wall, while the interface between the substrate and air is regarded as a magnetic wall.

The capacitance C_a between the striplines in the CPS, resulting from the presence of air, can be viewed as two identical capacitors connected in series between the striplines and the electric wall [50] and is given by

$$C_a = \varepsilon_0 \frac{K(k_1')}{K(k_1)}, \tag{2.5}$$

where

$$k_1 = \frac{S}{S + 2W}, \tag{2.6}$$

which is the metal strips geometry and

$$k_1' = \sqrt{1 - k_1^2}. \tag{2.7}$$

The complete elliptic integral of the first kind is denoted as $K(k)$.

The capacitance per unit length due to the dielectric C_s, with a relative permittivity of $(\varepsilon_r - 1)$, is calculated assuming that the electric field is entirely confined within the substrate. The expression is as follows:

$$C_s = \varepsilon_0 \frac{\varepsilon_r - 1}{2} \frac{K(k_2')}{K(k_2)}, \tag{2.8}$$

where

$$k_2 = \frac{tanh(\frac{\pi S}{4H})}{tanh(\frac{\pi(S+W)}{4H})}, \tag{2.9}$$

and

$$k_2' = \sqrt{1 - k_2^2}. \tag{2.10}$$

By substituting into Eq. 2.4, we obtain:

$$\varepsilon_0 \varepsilon_{\text{eff}} \frac{K(k_1')}{K(k_1)} = \varepsilon_0 \frac{K(k_1')}{K(k_1)} + \varepsilon_0 \frac{(\varepsilon_r - 1)}{2} \frac{K(k_2')}{K(k_2)}. \tag{2.11}$$

Rearranging the expression, we derive the equation for ε_{eff}:

$$\varepsilon_{eff} = 1 + \frac{\varepsilon_r - 1}{2} \frac{K(k_1)}{K(k_1')} \frac{K(k_2')}{K(k_2)}. \tag{2.12}$$

The equation for the characteristic impedance of the transmission line is [50]:

$$Z_{CPS} = \frac{120\pi}{\sqrt{\varepsilon_{eff}}} \frac{K(k_1)}{K(k_1')}. \tag{2.13}$$

In the case of an ultra-thin substrate (e.g., $H \approx 1\,\mu\text{m}$), the majority of electric field lines reside in the air, causing the effective permittivity ε_{eff} to approach 1. In this regime, the substrate-related capacitance term in Eq. 2.8 becomes negligibly small compared to C_a and can therefore be ignored. As a result, the effective permittivity obtained from Eq. 2.12 can be approximated as unity, leading to a simplified expression for the characteristic impedance, derived from Eq. 2.13, given by:

$$Z_{\text{CPS}} \approx 120\pi \frac{K(k_1)}{K(k_1')}. \tag{2.14}$$

2.5.2 Attenuation

In the frequency domain, the propagation of the electric field can be expressed as follows:

$$\hat{E}_{\mathrm{out}}(\omega) = e^{-jk(\omega)z}\hat{E}_{\mathrm{in}}(\omega), \tag{2.15}$$

where $\hat{E}_{\mathrm{in}}(\omega)$ and $\hat{E}_{\mathrm{out}}(\omega)$ are the Fourier transforms of the input and output pulses, respectively, after propagating a distance z. The spectral wave number, $k(\omega)$, is defined as:

$$k(\omega) = \beta(\omega) - j\alpha(\omega), \tag{2.16}$$

where $\beta(\omega)$ represents the spectral phase constant, which governs phase delay, and $\alpha(\omega)$ denotes the spectral attenuation constant, which accounts for signal loss during propagation (Np/unit length).

The attenuation of a propagating wave arises because of various loss mechanisms, such as conductor loss, dielectric loss, and radiation loss. As referenced in Eq. 2.15, attenuation is associated with the imaginary component of the spectral wave number, denoted $k(\omega)$. The expression for a propagating wave can be written as:

$$\hat{E}_{\mathrm{out}}(\omega) = e^{-j\beta(\omega)z}e^{-\alpha(\omega)z}\hat{E}_{\mathrm{in}}(\omega). \tag{2.17}$$

This equation illustrates that, beyond the phase delay caused by dispersion, the magnitude of the electric field is reduced exponentially along the propagation direction due to the attenuation factor $\alpha(\omega)$. The reduction in field amplitude follows an exponential decay, where the amplitude decreases to $1/e$ of its initial value at a given distance.

Power Loss per Unit Length

The power loss per unit length, denoted P_l, is obtained by computing the derivative of the power flow along a lossy transmission medium. Suppose that at position $z = 0$, the input power is P_0, and in the absence of reflection, the received power at a distance z is given by:

$$P(z) = P_0 e^{-2\alpha z}. \tag{2.18}$$

The rate of power loss per unit length can then be determined by differentiating Eq. (2.18) with respect to z:

$$P_l(z) = -\frac{\partial P(z)}{\partial z} = 2\alpha P_0 e^{-2\alpha z} = 2\alpha P(z). \tag{2.19}$$

From this expression, the attenuation constant α can be derived by evaluating the power loss at $z = 0$:

$$\alpha = \frac{P_l(z=0)}{2P_0}. \tag{2.20}$$

The attenuation coefficient, α, is a key parameter that quantifies energy dissipation along a transmission line or waveguide. It directly influences signal integrity by causing amplitude reduction over distance, a critical consideration in high-frequency applications such as THz waveguides, where radiation and dielectric losses are especially pronounced.

Dielectric Loss

Dielectric loss occurs because of the interaction of an electromagnetic wave with a lossy dielectric material. It is characterized by the imaginary part of the complex permittivity:

$$\varepsilon(\omega) = \varepsilon'(\omega) - j\varepsilon''(\omega), \tag{2.21}$$

where $\varepsilon'(\omega)$ represents the real part of the permittivity (which influences wave propagation), and $\varepsilon''(\omega)$ denotes the imaginary part, which accounts for energy dissipation in the material.

A commonly used parameter to quantify dielectric loss is the dielectric loss tangent, defined as:

$$\tan\delta_e = \frac{\varepsilon''(\omega)}{\varepsilon'(\omega)}. \tag{2.22}$$

The dielectric loss tangent $\tan\delta_e$ characterizes the ratio of energy dissipated to energy stored in the dielectric material. For the silicon nitride (Si_3N_4) substrate used in this work, $\tan\delta_e = 0.00526$.

Using this, Eq. 2.21 can be rewritten as:

$$\varepsilon(\omega) = \varepsilon'(\omega)\left[1 - j\tan\delta_e(\omega)\right] = \varepsilon_0\varepsilon_r(\omega)\left[1 - j\tan\delta_e(\omega)\right]. \tag{2.23}$$

The dielectric attenuation coefficient α_d describes how much the wave amplitude decreases due to dielectric loss. To determine α_d, we first calculate the input power P_0 by integrating the Poynting vector on the surface [46]:

$$P_0 = \frac{1}{2}\,\mathrm{Re}\int_S \vec{E} \times \vec{H}^* \cdot d\vec{s}. \tag{2.24}$$

The power lost as a result of the dielectric medium is given by:

$$P_{ld} = \frac{\omega\varepsilon''(\omega)}{2}\int_V |\vec{E}|^2 ds. \tag{2.25}$$

The dielectric attenuation coefficient per unit length is then defined as:

$$\alpha_d = \frac{P_{ld}}{2P_0} = \frac{\frac{\omega\varepsilon''(\omega)}{2}\int_V |\vec{E}|^2\, dV}{\mathrm{Re}\int_S \vec{E} \times \vec{H}^* \cdot d\vec{s}}. \tag{2.26}$$

To gain further insight, we approximate the input power P_0 as inversely proportional to the characteristic impedance $Z_0(\omega)$, that is, $P_0 \propto \frac{1}{Z_0(\omega)}\int |\vec{E}|^2\, dS$ [46]. If we assume similar spatial distribution of fields in both integrals, the field-dependent terms approximately cancel, leading to the following proportionality:

$$\alpha_d \propto \omega\varepsilon''(\omega) Z_0(\omega). \tag{2.27}$$

This result implies that dielectric loss increases with frequency and is dependent on the permittivity of the material and the impedance of the transmission line.

Conductor Loss

Conductor loss attenuation arises due to the finite conductivity (σ) of the waveguide or conductor, which leads to resistive heating. The attenuation coefficient associated with conductor loss is:

$$\alpha_c = \frac{P_{lc}}{2P_0}, \tag{2.28}$$

where P_{lc} is the power dissipated due to the resistance of the conductor, given by [46]:

$$P_{lc} = \frac{R_s(\omega)}{2} \int_S |\vec{H}_t|^2 ds. \tag{2.29}$$

Surface resistance $R_s(\omega)$ plays a crucial role in conductor loss and is calculated as:

$$R_s(\omega) = \frac{1}{\sigma \delta_s(\omega)}, \tag{2.30}$$

where δ_s is the skin depth, which represents how deeply an electromagnetic wave penetrates the conductor before it is significantly attenuated. It is given by:

$$\delta_s = \sqrt{\frac{2}{\omega \mu(\omega) \sigma}}. \tag{2.31}$$

This skin depth effect causes high-frequency currents to be confined near the surface of the conductor, increasing the effective resistance. Using this, the surface resistance can also be expressed as:

$$R_s(\omega) = \sqrt{\frac{\pi f \mu(\omega)}{\sigma}}. \tag{2.32}$$

Thus, the surface resistance increases with the square root of frequency, meaning that higher frequencies experience greater conductor loss.

The conductor attenuation coefficient per unit length is then calculated as:

$$\alpha_c = \frac{P_{lc}}{2P_0} = \frac{R_s(\omega) \int_S |\vec{H}_t|^2 ds}{2 \operatorname{Re} \int_S \vec{E} \times \vec{H}^* \cdot d\vec{s}}. \tag{2.33}$$

Since the conductor loss depends on the wave impedance $Z_0(\omega)$, we obtain:

$$\alpha_c \propto \frac{R_s(\omega)}{Z_0(\omega)} \propto \frac{1}{Z_0(\omega)} \sqrt{\frac{\omega \mu(\omega)}{\sigma}}. \tag{2.34}$$

This relationship shows that conductor loss is proportional to the square root of frequency and is inversely proportional to conductivity. Therefore, the use of materials with higher conductivity reduces loss, while higher frequencies result in increased attenuation. For the gold conductors used in this work, a conductivity of $\sigma_{\mathrm{Au}} = 4.1 \times 10^7$ S/m was assumed in the simulations.

Radiation Loss

Leaky-wave radiation is a phenomenon that occurs when a propagating electromagnetic field interacts with a dielectric interface, causing part of the energy to radiate into the surrounding medium. The difference between the wavenumber of the propagating wave and the radiated wave in the substrate determines this radiation mechanism [52, 53].

The leaky-wave radiation loss in a CPS transmission line depends on factors such as waveguide geometry, dielectric properties, and operating frequency. It can be expressed as [52]:

$$\alpha_{\text{rad}}^{\text{CPS}} = \pi^5 \left(\frac{3-\sqrt{8}}{2}\right) \sqrt{\frac{\varepsilon_{\text{eff}}(f)}{\varepsilon_r}} \left(1 - \frac{\varepsilon_{\text{eff}}(f)}{\varepsilon_r}\right)^2 \frac{(S+2W)^2 \varepsilon_r^{3/2}}{c^3 K'(k) K(k)} f^3, \tag{2.35}$$

where $\varepsilon_{\text{eff}}(f)$ represents the effective relative permittivity that varies with frequency, ε_r is the substrate's relative permittivity, and the speed of light is denoted by c.

To minimize leaky-wave radiation losses, two primary approaches can be considered:

1. **Reducing the Stripline Geometry:** Decreasing the stripline dimensions (S and W) in a CPS transmission line can help mitigate radiation losses. However, this reduction comes at the cost of increased conductor losses, as narrower striplines lead to higher characteristic impedance (Z_0). While a higher Z_0 can reduce the attenuation constant α_c in Eq. 2.34, it also decreases the conduction area, thus increasing resistive losses. This trade-off makes the approach impractical for scalable designs, particularly in high-performance TSoC applications.

2. **Using a Thin Substrate Membrane:** An alternative and effective strategy involves fabricating the CPS transmission line on a thin substrate membrane [54]. Leaky-wave radiation losses in planar transmission lines primarily arise due to the permittivity contrast between the substrate and air. This mismatch introduces unwanted radiation loss and signal distortion. A low-permittivity thin membrane effectively minimizes this permittivity mismatch, thereby reducing leaky-wave radiation losses and suppressing pulse dispersion. The experimental results in [54] demonstrate that no significant frequency-dependent mismatch was observed up to 1 THz, confirming the effectiveness

of this approach.

Although reducing the substrate thickness effectively suppresses radiation loss, it may also lead to surface wave excitation because of resonance effects. The critical substrate thickness for silicon nitride ($n = 2.76$) at THz frequencies within the operational bandwidth of 0.1–2 THz is approximately $H = 27.1\mu$m (at 2 THz), as determined by the relation:

$$f = \frac{c}{2nH} \tag{2.36}$$

At this thickness, surface waves resonate within the operational range, leading to signal degradation. However, by reducing the substrate thickness to $H = 1\mu$m, the resonance frequency shifts to $f(1\mu m) = 54.3$ THz, which is well beyond the operational bandwidth. This effectively eliminates surface wave interference, ensuring optimal wave confinement and significantly improving overall device performance.

Thus, employing an ultra-thin substrate membrane not only mitigates leaky-wave radiation losses but also minimizes resonance effects, making it a highly suitable approach for high-frequency THz applications.

2.5.3 Dispersion

When an electromagnetic wave propagates through a medium, its components travel at different velocities, which can be characterized by two primary parameters: the phase velocity (v_p) and the group velocity (v_g). These velocities describe different aspects of wave propagation and play a crucial role in understanding wave behavior in various media.

Phase Velocity

The phase velocity, v_p, refers to the speed at which a single phase point (such as a peak or trough) of a wave moves through space. It is mathematically defined as:

$$v_p = \frac{\omega}{\beta}, \tag{2.37}$$

where ω is the angular frequency of the wave, and β is the phase constant, which is dependent on the properties of the medium. In a homogeneous dielectric medium, the phase constant is given by:

$$\beta = \omega\sqrt{\mu\epsilon}, \tag{2.38}$$

where μ is the permeability and ϵ is the permittivity of the material.

If the phase velocity varies with frequency, different frequency components of a wave pulse travel at different speeds. This phenomenon is known as frequency dispersion. As a result, the shape of a broadband signal can change over time as different frequency components experience varying propagation delays [46].

Group Velocity

In THz wave propagation, electromagnetic waves are commonly modeled as wave packets consisting of a range of frequency components. The speed at which the envelope of such a wave packet travels through a medium is referred to as the group velocity, v_g. It is defined as

$$v_g(\omega) = \frac{\partial\omega}{\partial\beta(\omega)}, \tag{2.39}$$

where $\beta(\omega)$ denotes the frequency-dependent propagation constant. The group velocity plays a crucial role in the transmission of narrow pulses by dictating the rate at which energy and information is transmitted. If v_g varies with frequency, the individual spectral components of the pulse propagate at different speeds, leading to temporal broadening of the pulse. This effect, known as group velocity dispersion (GVD), can adversely affect signal integrity in THz applications.

For nondispersive materials, as observed in ideal TEM mode propagation, the phase and group velocities are equal, $v_p = v_g$. This condition is satisfied when the relative permittivity of the medium, ε_r, remains constant and does not vary with frequency. However, in real-world materials, ε_r is often frequency-dependent, resulting in dispersion effects.

The dispersive properties of the CPS transmission line have been numerically and analytically analyzed by Hasnain et al. [55]. Their work derives an analytical approximation from numerical simulations, modeling the phase constant as:

$$\beta(f) = 2\pi\frac{f}{c}\sqrt{\epsilon_{\text{eff}}(f)}, \tag{2.40}$$

where $\epsilon_{\text{eff}}(f)$ is the effective frequency-dependent dielectric constant, given by:

$$\sqrt{\epsilon_{\text{eff}}(f)} = \sqrt{\epsilon_q} + \frac{\left(\sqrt{\epsilon_r} - \sqrt{\epsilon_q}\right)}{1 + a\left(\frac{f}{f_{\text{te}}}\right)^{-b}}. \tag{2.41}$$

Here, ϵ_q represents the quasi-static effective permittivity, defined as:

$$\epsilon_q = \frac{\epsilon_r + 1}{2}. \tag{2.42}$$

The term f_{te} corresponds to the cutoff frequency for the transverse electric surface wave (TE_1) mode, expressed as [52]:

$$f_{\text{te}} = \frac{c}{4H\sqrt{\epsilon_r - 1}}, \tag{2.43}$$

where c is the speed of light in a vacuum, and H denotes the substrate thickness. The exponent b is approximately 1.8 and is considered independent of the transmission line geometry. The parameter a, which influences the dispersion characteristics, is empirically related to the transmission line dimensions through:

$$\log(a) \approx u \log(S/W) + v, \tag{2.44}$$

where

$$u \approx 0.54 - 0.64q + 0.015q^2, \tag{2.45}$$

$$v \approx 0.43 - 0.86q + 0.54q^2, \tag{2.46}$$

$$q = \log(S/H). \tag{2.47}$$

In the case of an ultra-thin membrane substrate (e.g., ≈ 1 μm), the electromagnetic field is no longer strongly confined within the dielectric. Instead, a substantial portion of the electric field extends into the surrounding air, which has a relative permittivity close to unity. As a result, the quasi-static effective permittivity ϵ_q, as defined in Eq. 2.42, approaches 1 due to the diminishing influence of the substrate. This, in turn, causes the frequency-dependent effective permittivity $\epsilon_{\text{eff}}(f)$, described in Eq. 2.41, to also approach unity.

This phenomenon, often referred to as a reduction in dielectric loading, occurs because the thinner substrate reduces the interaction between the guided mode and the dielectric material. As the electromagnetic mode becomes increasingly delocalized into the surrounding air, the dependence of the phase velocity on frequency decreases. Since dispersion arises from the frequency variation of the phase constant $\beta(f)$, which is governed by $\epsilon_{\text{eff}}(f)$, this reduction in dielectric loading leads to a significant suppression of dispersion. Consequently, the transmission line exhibits a more stable phase velocity across a broad frequency range, which is highly desirable in THz systems.

2.6 THz Filters

Following the introduction of the key components comprising the TSoC, the focus now shifts to the design and functionality of the integrated THz filters. These filters act as important devices in electromagnetic systems, enabling precise control over the spectral content of transmitted signals. By allowing signal transmission within a defined passband and attenuating frequencies in adjacent stopband regions, they ensure efficient signal conditioning. Based on their frequency-selective characteristics, filters are commonly categorized as low-pass, high-pass, band-stop, or band-pass types.

The choice of filter type is primarily dictated by the spectral and functional requirements of the intended application. LPFs are commonly used in signal conditioning to suppress high-frequency noise and preserve the fidelity of low-frequency signals [56, 57]. High-pass filters are applied in tasks such as feature extraction, electromagnetic shielding, and impedance matching, where attenuation of low-frequency components is necessary [58]. Bandpass filters play a central role in communication systems by isolating specific frequency channels, allowing efficient multiplexing and minimizing interference [59]. Band-stop (or notch) filters, in contrast, are designed to attenuate undesired frequency bands while allowing nearby frequencies to pass with minimal loss [60]. These filters are particularly valuable in wireless communication, sensing, and spectroscopy applications, where the elimination of persistent interference or background noise at known frequencies is required to maintain signal integrity.

At THz frequencies, the design of efficient filters requires a thorough examination of the frequency response associated with different structural configurations. Numerous techniques originally developed for microwave frequencies have been extended to the THz regime. Among these, periodic filters, realized by embedding reactive elements into transmission lines, have remained foundational because of their sharp roll-off characteristics, low insertion loss, and strong out-of-band rejection. In parallel, alternative design strategies such as metamaterial-based filters [61], resonant cavity structures [6], and plasmonic filters [5] are actively pursued to address the unique physical constraints and fabrication challenges encountered in the THz domain.

Targeting the 0–2 THz range, Table 2.2 provides a comparative summary of recent experimental filter designs, highlighting key performance metrics such as filter type, center or cutoff frequency, bandwidth, insertion loss, physical length, and fabrication platform. Special attention is given to compactness and integration compatibility with the TSoC architecture. While many of these designs demonstrate favorable spectral responses, they often involve trade-offs in size, performance, or fabrication complexity. Except for [62], [56], and [63], none of the filters listed in the table are compatible with system-level integration. Motivated by these limitations, this work focuses on developing planar, compact, and low-loss filters specifically tailored for seamless integration into the TSoC platform.

Table 2.2: Comparison of THz filters operating in the range of 0.1–2 THz reported in the literature

Ref.	**Filter Type**	**Center/ Cutoff Frequency (GHz)**	**Bandwidth (GHz)**	**Insertion Loss (dB)**	**Filter Length (mm)**	**Material and Fabrication**
[64]	Band-pass: WR-3 rectangular waveguide filter	285	22	1.2	2.9	SU-8 photoresist micromachining and gold electroplating
[65]	Band-pass: E-plane rod-loaded WR-3 rectangular waveguide filter	237.5	15	2	5.84	Silicon micromachining, Gold thermocompression bonding
[59]	Band-pass: Cavity rectangular waveguide filter with quasi-Chebyshev response	340	80	0.61	6	Multilayer metal structure fabricated via micromachining and bonding
[65]	Band-pass: E-plane rod-loaded rectangular waveguide	237.5	15	2	2.34	Silicon micromachining, gold thermocompression bonding
[66]	Band-stop: Tunable notch filter using single slit in tapered parallel-plate waveguide (TPPWG)	1351–1519	11–12	–	9	Stainless steel slit in aluminum TPPWG, micromachined
[66]	Low-pass: Bragg-based filter using multiple slits in TPPWG	780	780	–	10	Stainless steel slit in aluminum TPPWG, micromachined

Ref.	Filter Type	Center/ Cutoff Frequency (GHz)	Bandwidth (GHz)	Insertion Loss (dB)	Filter Length (mm)	Material and Fabrication
[67]	Band-pass: Rectangular waveguide filter integrated in THz transceiver	340	60	2	5	CNC-milled metal waveguide filter
[68]	Band-pass: Dual-resonance bilayer complementary metamaterial filter	315 / 480	33 / 45	1.9 / 6	10	Aluminum on quartz substrate, fabricated via photolithography, electron beam evaporation, and plasma etching
[57]	Low-pass: Cascaded metamaterial filter (m-LPF) with staggered metal gratings	1080 (cutoff for m-LPF4)	110	<1.2	–	Gold on silicon substrate, fabricated via photolithography, and wet etching
[69]	Band-pass: Composite metamaterial with multiple resonances	115–173	500	≈ 3	–	Copper on PET, fabricated via UV-lithography and e-gun deposition on PET substrate
[70]	Band-pass: Electromagnetically Induced Transparency (EIT)-analog MEMS metamaterial filter	1832	≈ 300	64.5	–	Gold bar and wire pair, MEMS-actuated, fabricated on SOI wafer
[71]	Band-pass: Tunable metamaterial filter with copper-array and polymer multilayer	590 / 700 / 840	300, tunable up to 660–1050	–	0.280 (array)	Copper/Zeonor/PMI, fabricated using vacuum evaporation, lithography, and polymer spinning
[63]	Band-stop: On-chip SSPPs filter with CSRRs and SRRs	143	30	>10	3.4	Ti/Al/Ti/Au on 50 μm quartz substrate via photolithography and lift-off process
[62]	Band-stop: SRR-loaded planar filter using CPS	510 (first notch)	20	–	1	Gold CPS on 1 µm Si_3N_4 membrane, fabricated by photolithography
[72]	Band-pass/Band-stop: Whispering-Gallery Mode Resonator (WGMR)-based tunable on-chip filter	461	0.5	28 (BP), 17 (BS)	14	HRFZ-Si WGMR with Au micro-heater, fabricated by lithography and ICP etching
[56]	Low-pass: Elliptic-function planar filter using CPS bends	600	600	1.1	1.4	Gold CPS on 1 µm Si_3N_4 membrane, fabricated by photolithography
[73]	High-pass: THz plasmonic filter using 2D metallic wire lattice	700	500	–	2.1	Microstereolithography of polymer lattice, gold sputtering

Ref.	**Filter Type**	**Center/ Cutoff Frequency (GHz)**	**Bandwidth (GHz)**	**Insertion Loss (dB)**	**Filter Length (mm)**	**Material and Fabrication**
[60]	Band-stop: All-dielectric guided-mode resonance (GMR) filter	402 and 581 (TE)	≈ 20 and 10	≈1.2	30	Quartz grating micro-machined using etching, stacked configuration with 2 identical filters
[74]	Band-pass: Dual-mode rectangular waveguide filter (TE301/TE102)	1017	22	2.9	1	Micromachining on silicon, gold-plated and bonded with gold-to-gold thermo-compression

Based on recent advancements in CPS technology and the development of the low-loss ultra-thin membrane platform, planar CPS-based filters have become highly promising for TSoC integration. This dissertation presents four compact, high-performance filter designs operating across the 0–2 THz frequency range. These designs emphasize spectral selectivity, fabrication compatibility, and miniaturization to support scalable on-chip systems. Among these, the first two filters [1,2] adopt band-stop configurations, designed using a periodic synthesis approach to enable sharp and tunable spectral rejection at specific frequency bands.

The third filter design [3] explores planar low-pass structures based on Bessel responses of various orders, selected for their flat group delay and minimal phase distortion, characteristics critical for high-speed THz communication. These filters maintain strong frequency selectivity and low insertion loss while achieving highly compact footprints. Fabricated prototypes confirm this compactness, with total lengths among the shortest reported THz LPFs ($N = 3 \to 69$ μm, $N = 4 \to 70$ μm, $N = 5 \to 70$ μm). This level of miniaturization makes them especially suitable for integration into dense TSoC architectures.

2.6.1 Periodic Structures

This section provides a focused discussion on the design and analysis of periodic filters. A fundamental example is a transmission line or waveguide periodically loaded with reactive elements to form a spatially repeating structure. Reactive elements, typically alternating high- and low-impedance sections, are often modeled using equivalent lumped reactances in the shunt or series with the line, offering a versatile framework for the analysis and design of their electromagnetic behavior. This modeling approach enables precise control over filter response parameters, including bandwidth and stopband rejection.

2.6.2 Analysis of Infinite Periodic Structures

The ABCD matrix method is used to analyze the infinitely periodic transmission line structure illustrated in Fig. 2.9. The structure is divided into identical unit cells, each comprising a transmission line segment of length d with a shunt susceptance b placed at its midpoint. The susceptance is normalized with respect to the characteristic impedance Z_0, simplifying the analysis and allowing for generalized results across various platforms. The periodic repetition of these unit cells forms the foundation for the overall propagation behavior of the system, including the dispersion relation and the band structure.

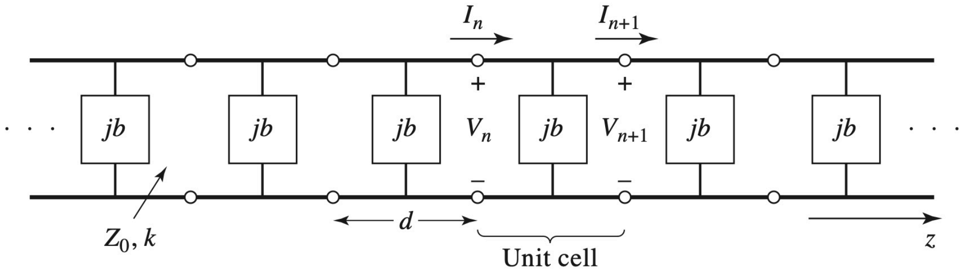

Figure 2.9: The equivalent circuit of a periodically loaded transmission line, which consists of an unloaded line with characteristic impedance Z_0 and propagation constant k (reprinted from [46]).

To analyze wave propagation through an infinite periodic transmission line, the structure is modeled as a cascade of identical unit cells, each represented by a two-port network. This approach enables the use of ABCD matrix formalism to relate the voltage and current at the input and output ports of each unit cell. Each unit cell consists of a transmission line section of length $d/2$, followed by a lumped shunt susceptance b, and another transmission line section of length $d/2$.

The voltages and currents at the nth and $(n+1)$th unit cells are related through the ABCD matrix as follows:

$$\begin{bmatrix} V_n \\ I_n \end{bmatrix} = \begin{bmatrix} A & B \\ C & D \end{bmatrix} \cdot \begin{bmatrix} V_{n+1} \\ I_{n+1} \end{bmatrix}, \tag{2.48}$$

where A, B, C, and D are the transmission matrix elements of the unit cell. These elements incorporate the distributed nature of the transmission line as well as the lumped reactive loading, and depend on the characteristic impedance, propagation constant, unit cell length d, and shunt element b. These parameters, in their normalized form as depicted in Fig. 2.10 for the ABCD matrix of two-port circuits, can be expressed as:

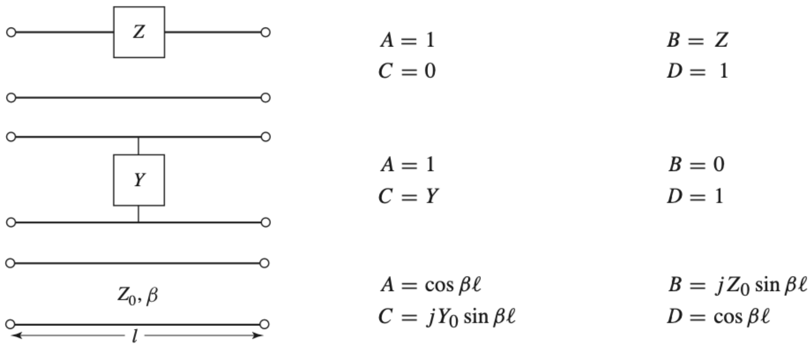

Figure 2.10: ABCD parameters of some useful two-port circuits

$$\begin{aligned}\begin{bmatrix} A & B \\ C & D \end{bmatrix} &= \begin{bmatrix} \cos\theta/2 & j\sin\theta/2 \\ j\sin\theta/2 & \cos\theta/2 \end{bmatrix} \cdot \begin{bmatrix} 1 & 0 \\ jb & 1 \end{bmatrix} \cdot \begin{bmatrix} \cos\theta/2 & j\sin\theta/2 \\ j\sin\theta/2 & \cos\theta/2 \end{bmatrix} \\ &= \begin{bmatrix} \cos\theta - b/2\sin\theta & j(\sin\theta + b/2\cos\theta - b/2) \\ j(\sin\theta + b/2\cos\theta + b/2) & \cos\theta - b/2\sin\theta \end{bmatrix}\end{aligned} \tag{2.49}$$

Let $\theta = kd$, where k is the propagation constant of the unloaded line. It can be verified that $AD - BC = 1$, which fulfills the reciprocity condition and implies that the network exhibits identical transmission and reflection properties in both propagation directions [46].

A critical parameter in the analysis of wave propagation through periodically loaded transmission lines is the characteristic impedance observed at the terminals of a unit cell. This impedance, commonly referred to as the Bloch impedance, quantifies the ratio of voltage to current for a wave propagating through an infinite periodic structure. It is defined as

$$Z_B = Z_0 \frac{V_{n+1}}{I_{n+1}}, \tag{2.50}$$

where V_{n+1} and I_{n+1} denote the normalized voltage and current at the $(n+1)$-th unit cell, respectively. For a wave propagating in the $+z$ direction, we must have

$V(z) = V(0)e^{-\gamma z}$ and $I(z) = I(0)e^{-\gamma z}$, for a phase reference at $z = 0$. Since the structure is infinitely long, the voltage and current at the nth terminals can differ from those at the $n+1$ terminals only by the propagation factor $e^{-\gamma d}$. Thus, $V_{n+1} = V_n e^{-\gamma d}$, and $I_{n+1} = I_n e^{-\gamma d}$.

Using Eq. 2.48, the voltages and currents at the n and $n+1$ terminals is given by

$$\begin{bmatrix} V_n \\ I_n \end{bmatrix} = \begin{bmatrix} A & B \\ C & D \end{bmatrix} \begin{bmatrix} V_{n+1} \\ I_{n+1} \end{bmatrix} = \begin{bmatrix} V_{n+1}e^{\gamma d} \\ I_{n+1}e^{\gamma d} \end{bmatrix}. \tag{2.51}$$

Rearranging this equation, we obtain:

$$\begin{bmatrix} A - e^{\gamma d} & B \\ C & D - e^{\gamma d} \end{bmatrix} \begin{bmatrix} V_{n+1} \\ I_{n+1} \end{bmatrix} = 0. \tag{2.52}$$

For a nontrivial solution to exist, the determinant of the coefficient matrix must vanish, leading to the characteristic equation:

$$AD + e^{2\gamma d} - (A + D)e^{\gamma d} - BC = 0. \tag{2.53}$$

Solving the above equation for $e^{\gamma d}$ yields the dispersion relation:

$$e^{\gamma d} = \frac{(A + D) \pm \sqrt{(A + D)^2 - 4}}{2}. \tag{2.54}$$

Using the matrix relation from Eq. (2.52), we can isolate the relationship between voltage and current as:

$$(A - e^{\gamma d})V_{n+1} + BI_{n+1} = 0. \tag{2.55}$$

Substituting this result into Eq. (2.50), we derive the general form of the Bloch impedance:

$$Z_B = \frac{-BZ_0}{A - e^{\gamma d}}. \tag{2.56}$$

Combining Eqs. (2.54) and (2.56), the Bloch impedance admits two distinct solutions, corresponding to the two possible signs of the square root in the dispersion relation:

$$Z_B^{\pm} = \frac{-2BZ_0}{A - D \mp \sqrt{(A + D)^2 - 4}}. \tag{2.57}$$

In the special case of a symmetric unit cell, where $A = D$, the expression for the

Bloch impedance simplifies considerably to:

$$Z_B^{\pm} = \frac{\pm B Z_0}{\sqrt{A^2 - 1}}. \tag{2.58}$$

The ± signs correspond to the Bloch impedances of forward- and backward-propagating waves, respectively. In symmetric networks, these impedances are equal in magnitude but opposite in sign, since the characteristic impedance of a backward-propagating wave is conventionally defined as negative [46].

2.6.3 Terminated Periodic Structures

This section analyzes a truncated periodic structure terminated with a load impedance Z_L, as illustrated in Fig. 2.11. Assuming operation within the passband, the incident and reflected voltages and currents in each unit cell are expressed using the real propagation term $j\beta nd$, rather than the general complex propagation constant γz. This formulation highlights the influence of terminal boundary conditions on wave propagation, facilitating the evaluation of impedance matching and reflection behavior.

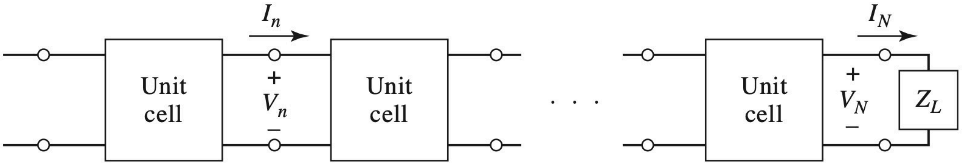

Figure 2.11: A periodic structure terminated with a normalized load impedance Z_L (reprinted from [46]).

By calculating the Bloch impedance from Eq. 2.50—a key step in determining the reflection coefficient between an infinite periodic filter and a load impedance, we can express the reflection coefficient at the termination (at $n = N$, corresponding to the last unit cell) as follows:

$$\Gamma = \frac{V_N^-}{V_N^+} = -\frac{Z_L/Z_B^+ - 1}{Z_L/Z_B^- - 1}. \tag{2.59}$$

In the scenario of a symmetric unit cell network, where $A = D$, we find that $Z_B^+ = -Z_B^- = Z_B$, leading to a simplified and familiar result [46]:

$$\Gamma = \frac{Z_L - Z_B}{Z_L + Z_B}. \tag{2.60}$$

To prevent reflections on the terminated periodic structure, it is essential to ensure that $Z_L = Z_B$, where Z_L and Z_B are both real for a lossless structure operating in a passband. If required, a quarter-wave transformer can be employed between the periodically loaded line and the load to achieve this matching.

The previously derived reflection coefficient enables precise evaluation of impedance mismatch in the terminated periodic structure. This assessment reveals the degree of matching between the load and the structure, aiding in the identification of signal reflections and guiding design optimizations to improve system performance.

2.7 Even and Odd Modes in Transmission Structures and Filter Design

Even and odd modes are fundamental to understanding electromagnetic wave propagation in waveguides and multi-conductor transmission lines, such as CPWs. These modes arise from structural symmetry and the boundary conditions governing electric field distributions. In the even mode, the electric field is symmetric with respect to the centerline, resulting in equal potential on the ground planes and a balanced field profile. This configuration minimizes radiation and supports stable, low-loss propagation, rendering the even mode the dominant configuration in most practical CPW-based systems.

In contrast, the odd mode exhibits an antisymmetric electric field distribution, characterized by opposing potentials on the ground planes. This configuration induces strong inter-conductor coupling, which may result in interference, radiation leakage, or mode conversion. While typically suppressed in conventional designs, odd modes are deliberately exploited in certain applications, including directional couplers, immittance inverters, and the creation of transmission zeros. The distinction between even and odd modes significantly influences the propagation constant, characteristic impedance, and interaction with adjacent structures. These effects are particularly pronounced in high-frequency circuits, where precise modal control is essential to maintaining signal integrity and minimizing unwanted coupling.

The strategic manipulation of even and odd modes is central to modern filter design. Even-mode propagation is commonly used in low-loss filters designed to isolate specific frequency bands. In contrast, odd modes offer unique opportunities in advanced synthesis techniques. For instance, periodic structures can alternate between even- and odd-mode sections to introduce stopbands or enhance rejection at specific out-of-band frequencies. This approach enables the development of compact, high-performance filters with engineered spectral profiles tailored to specific application requirements.

The ability to analyze and control even and odd modes is essential in the development of modern microwave, millimeter-wave, and emerging THz filters. A detailed discussion of their role in our second filter design—including key synthesis strategies and practical implementation benefits—is presented in Section 4.2.

2.8 Inverse Filter Design

Up to this point, we have discussed THz filter design methods rooted in classical microwave engineering principles. Although effective in many applications, these conventional methods face inherent limitations when applied to compact, high-performance THz systems. In particular, they are often inadequate for realizing nonintuitive geometries, and further miniaturization typically involves trade-offs, such as diminished stopband rejection. To address these challenges, inverse design presents a modern and computationally powerful alternative. Rather than relying on predefined topologies, it directly optimizes the device geometry to meet the specified electromagnetic performance criteria.

Inverse design methodologies, originally developed to optimize nanophotonic structures beyond the reach of traditional analytical techniques, have demonstrated remarkable success in nanophotonic systems [75]. Early implementations produced compact, high-performance devices with nonintuitive geometries tailored to specific optical transmission or field distribution requirements. In particular, their integration into photonic integrated circuits (PICs) has enabled densely integrated components with enhanced functionality, reduced footprints, and improved optical performance [75–80]. The maturity of inverse design in silicon photonics not only validates its effectiveness but also underscores its relevance for addressing similar challenges in emerging THz integrated systems, where compactness, spectral control, and nonintuitive geometries are equally critical.

Conventional design approaches typically rely on fixed geometries and manual parameter tuning. Inverse design, in contrast, formulates the desired electromagnetic response as an objective function and systematically searches for an optimal configuration subject to physical and fabrication constraints. This approach facilitates the realization of highly efficient and multifunctional THz components, including filters, waveguides, and antennas.

Recent studies have applied inverse design strategies to optimize THz components. Zhang et al. [81] proposed a GA-based inverse design framework to optimize dispersion profiles for broadband impedance matching. The resulting dual-metasurface absorber achieved 88% absorption across the 0.21–5 THz range, demonstrating both high performance and computational efficiency. In a subsequent study, the same group expanded this framework by incorporating multiple objective functions to enhance the robustness and automation of THz metasurface design [82].

Beyond GAs, machine learning-based approaches have been applied to accelerate and enhance the inverse design process. Li et al. [83] used artificial neural networks (ANNs) to accurately predict reflection spectra and optimize micro/nano THz metasurface structures with custom optical responses. Similarly, Mashayekhi et al. [84] developed an ANN-assisted inverse-designed graphene-based absorber, achieving 96.33% absorption across 0.5–10 THz and enabling rapid parameter selection for THz detection. Deep learning has also been extended to THz antenna design. Karahan et al. [85] introduced a deep neural network (DNN)-based inverse design approach for multiband graphene patch antennas operating between 2–5 THz. Their model achieved 13 frequency bands, up to 8.8 dB gain, full 360° beam steering, and 93% prediction accuracy, significantly accelerating the design cycle. Furthermore, Ding et al. [86] proposed a Finite-Difference Time-Domain (FDTD)-based inverse design framework for a 3D-printable diffractive optical element (DOE) capable of THz spectral splitting between 0.5–0.7 THz. Their simulation and experimental results demonstrated a compact, low-cost solution for portable THz spectroscopy and communication.

Figure 2.12 presents established inverse design demonstrations in nanophotonics (a–c) alongside recent advancements in THz applications (d–g). Although most THz inverse design efforts have concentrated on metasurfaces, inverse-designed THz filters remain largely unexplored, an area this work directly targets. In contrast, nanophotonics, particularly in the context of PICs, has produced several inversely designed filters that influence the design strategies adopted in this study. In particular, the genetically optimized on-chip wideband ultra-compact filter by Yu et al. [79] served as a conceptual foundation for our methodology.

In the inverse design of complex THz filters, one must determine the optimal geometric configuration that yields a desired spectral response. This typically involves searching through a large, high-dimensional, and discrete design space, where

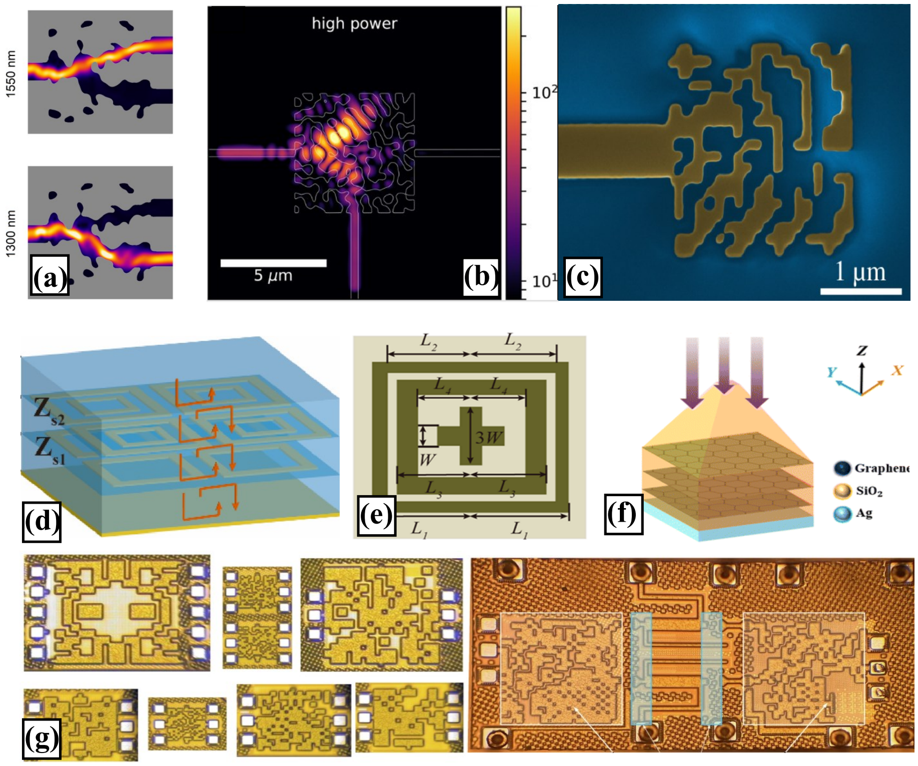

Figure 2.12: Selected examples of inverse design techniques in nanophotonic and THz applications. (a) Topology-optimized demultiplexer showing power flow at $\lambda = 1550$ nm and 1300 nm [77]. (b) Electric field amplitude in a nonlinear nanophotonic optical switch optimized using the adjoint method [78]. (c) Optical microscope image of a genetically optimized wideband ultracompact on-chip reflector [79]. (d) Broadband THz absorber designed using GA-optimized dual metasurfaces [81]. (e) High-efficiency, broadband THz metasurfaces synthesized via multi-objective GA [82]. (f) Deep-learning-based design of a metasurface for near-complete THz absorption [86]. (g) Deep-learning-enabled inverse design of multi-port RF and sub-THz passives and integrated circuits [85].

traditional analytical methods offer limited guidance. Although an exhaustive search could, in theory, yield the global optimum, the exponential growth in design permutations and associated computational cost typically renders this approach impractical. To address this, global optimization methods such as GAs provide an efficient alternative. By mimicking evolutionary processes, GAs iteratively refine candidate solutions without requiring gradient information, making them well-suited for large, discrete design spaces.

Given these advantages, we adopt GA for the THz inverse filter design problem, leveraging its ability to navigate high-dimensional search spaces and achieve target spectral responses with significantly reduced computational overhead. This approach offers several advantages that make it particularly suitable for the inverse design of complex structures. Unlike gradient-based optimization methods, GA does not require computation of gradients of the fitness (objective) function. This characteristic makes it more robust against local minima, which are common in non-convex high-dimensional design spaces [87].

In [4], we employed a GA to optimize the binary distribution of gold (Au) and air pixels within a planar THz filter structure. Each candidate solution was encoded as a chromosome that defined the spatial arrangement of pixels. These chromosomes evolved over successive generations through selection, crossover, and mutation. The GA parameters were carefully tuned to address the discrete, high-dimensional nature of the design space.

To enhance design diversity and convergence, key GA operators were employed. Mutation introduced variability by toggling individual bits, thereby altering the material assignment of specific pixels and enabling exploration of novel topologies that enhance the S-parameter response. Crossover combined advantageous traits from two parent solutions, while elitism preserved the best-performing individuals across generations. The population size was selected to balance exploration breadth with computational feasibility, given the cost associated with full-wave electromagnetic simulations [87].

Several strategies are employed to mitigate convergence to local minima in the nonconvex optimization landscapes defined by electromagnetic performance metrics. Increasing the mutation rate enhances diversity and enables broader exploration of the design space. Extending the number of generations allows additional opportunities for evolving high-performance filter geometries. If a locally optimal solution is suspected, its genome may be reintroduced in subsequent runs to promote refined exploration in its neighborhood. Running the GA multiple times with randomized initial populations supports statistical comparison across runs, providing insight into the robustness of the solutions and the sensitivity of the design space to initial conditions. Further details of this methodology are presented in Section 4.4.

2.9 Review Summary

This chapter provided a comprehensive overview of the fundamental concepts supporting the design and integration of THz filters in miniaturized platforms. It began by addressing the challenges associated with THz signal generation and detection, with particular emphasis on PCSs. The discussion then transitioned to the TSoC platform, including the function of tapering structures in facilitating impedance matching. Various field-guiding technologies were examined—particularly CPS and CPW transmission lines—alongside a detailed analysis of attenuation and dispersion phenomena critical to high-frequency signal integrity. Building on this foundation, the chapter explored THz filter design strategies, beginning with periodic structures. It further examined the role of even and odd modes in transmission lines. Finally, the chapter introduced inverse filter design as an advanced computational methodology for realizing compact, high-performance THz filters that surpass the limitations of traditional synthesis approaches.

Chapter 3

Methods

3.1 THz-Time Domain Spectroscopy

All measurements in this work were performed using a modified THz-TDS method. THz-TDS is a powerful technique for characterizing the electromagnetic properties of materials in the THz frequency range. It operates by transmitting short, broadband THz pulses through a sample and recording the transmitted signal as a function of time [88]. This time-resolved measurement enables the extraction of both amplitude and phase information.

To characterize short pulses, Fig. 3.1 illustrates the temporal and spectral behavior of Gaussian pulses with various Full Width at Half Maximum (FWHM). The FWHM defines pulse duration in the time domain and spectral bandwidth in the frequency domain, providing a standardized measure for pulse characterization. The figure demonstrates that to achieve a broad frequency response covering a range of 10 THz, extremely short pulses (FWHM $\ll$ 0.5 ps) are necessary. This follows from the Fourier time-frequency duality, where shorter pulses (i.e., narrower FWHM) result in broader spectral bandwidths, enabling efficient high-frequency THz generation and detection. As mentioned before, LT-GaAs, with a carrier lifetime of approximately 0.5 ps, is well-suited for broadband THz-TDS for operation in the 0.1 - 4 THz range.

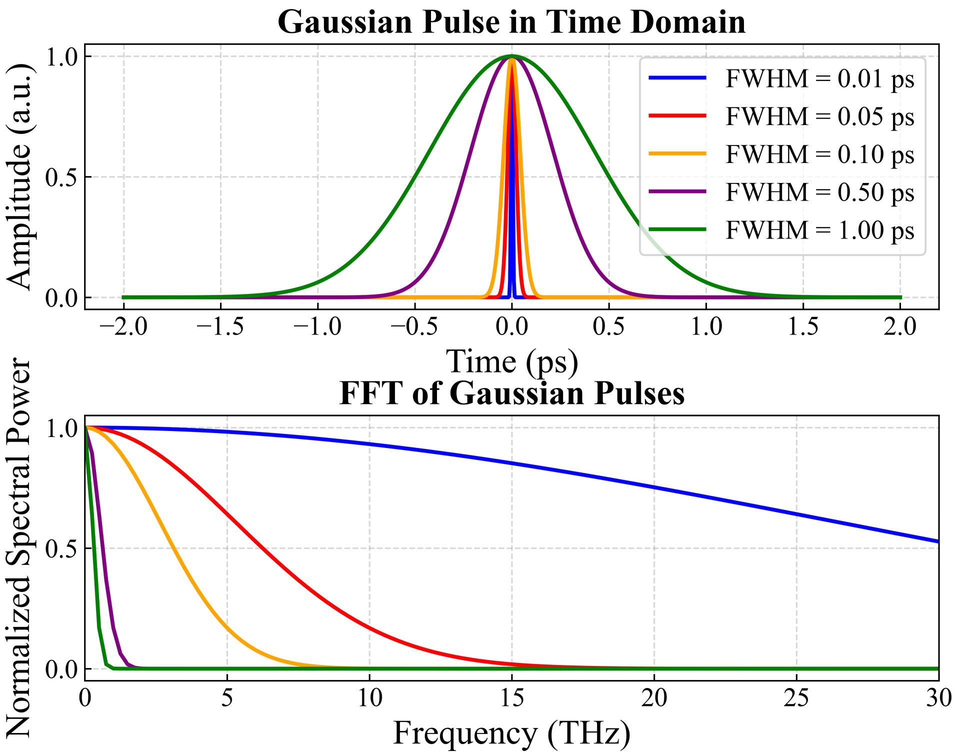

Figure 3.1: Comparative analysis of Gaussian time domain response and Fast Fourier Transform (FFT) for different FWHM values.

3.2 Measurement Setup

Figures 3.2 and 3.3 illustrate the modified THz-TDS experimental setup developed for this study. The system uses a femtosecond laser characterized by a pulse width of 80 fs, a wavelength of 780 nm, and a repetition rate of 80 MHz. The laser beam is split into two paths using a 50:50 beam splitter. In the transmitter path, the optical beam is modulated by an optical chopper before being focused onto the active region of the PCS. Conversely, in the receiver path, the optical beam traverses a mechanical delay line before being focused onto the active region of the PCS.

Both the mechanical delay line and the optical chopper can be positioned in either the transmitter or receiver path. The optical chopper serves as a modulator for the laser pulse, which is essential for generating a reference signal for the lock-in amplifier. This modulation facilitates the extraction of the desired information from the received signals with a better signal-to-noise ratio. The received pulse is sampled by varying the physical path-length difference between the transmitter and receiver. This ad-

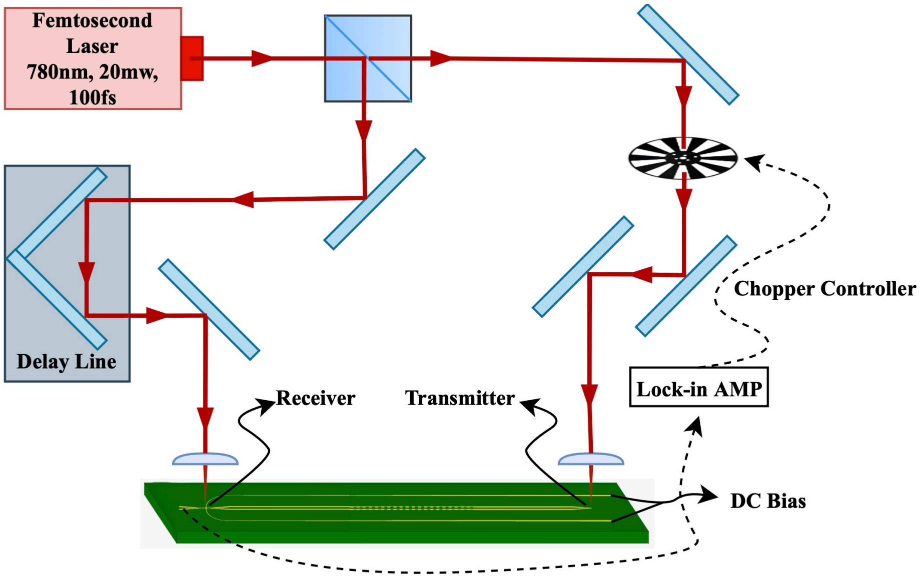

Figure 3.2: Schematic diagram of the experimental setup, showing the optical paths for the transmitter and receiver in the THz-TDS system.

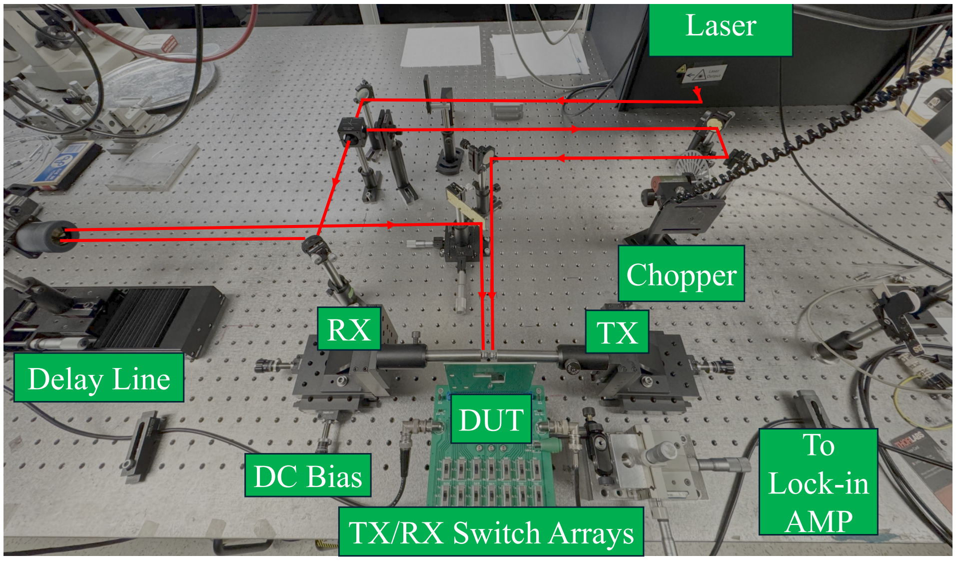

Figure 3.3: The modified THz-TDS measurement setup.

justment introduces a time delay in the optical path, enabling the system to capture different temporal points of the transmitted pulse. By systematically changing this path-length difference, a complete time-domain profile of the transmitted pulse can be recorded, enabling the analysis of the THz waveform.

For an active area with a 10 μm gap, the transmitter typically operates with an applied bias of approximately 24 V_{DC}. The receiver is connected to a lock-in amplifier, which is referenced to the optical chopper. This configuration facilitates the measurement of the induced photocurrent.

3.3 Fabrication of Terahertz System-on-Chip

This section provides a comprehensive overview of the fabrication process for the TSoC platform, which serves as the foundation for the works in [1–3, 5, 6]. The fabrication process involves the development of PCSs and silicon nitride membrane, which are essential for achieving the desired THz performance. The fabrication of PCSs was carried out in the University of Victoria cleanroom facility, where advanced lithographic and etching techniques were used to achieve high-precision patterning. For the fabrication of the silicon nitride membrane, we collaborated with 4D Labs, leveraging their 2 μm fabrication process to achieve high-quality thin-film deposition and mechanical stability at an affordable cost.

3.3.1 Fabrication of Photoconductive Switches

The fabrication process began with the development of the PCS, which functions as both the THz signal source and detector in all experimental configurations. Ensuring consistent, reliable, and high-performance operation was critical, necessitating the production of a sufficient number of high-quality devices. The primary goal was to fabricate an array of compact thin-film LT-GaAs-based PCSs with dimensions of 40 μm × 70 μm × 1.8 μm. Figure 3.4 presents an image of the target devices, highlighting their structural layout. This section provides a brief overview of the fabrication process; for a more detailed description, the readers are referred to [89].

LT-GaAs, selected as the active region material for its outstanding properties in the THz regime (as detailed in Section 2.3), offers unique advantages due to its electronic and structural characteristics. As previously discussed, this material is typically grown at low temperatures (200–300 °C), which leads to a high concentration of arsenic (As) antisite defects and gallium (Ga) vacancies. These defects result in high resistivity and semi-insulating behavior, making LT-GaAs well-suited for ultrafast photoconductive applications. However, the same defect-rich composition also increases its susceptibility to oxidation upon exposure to air [90, 91].

To mitigate this, a layer of Aluminium Arsenide (AlAs) is grown as a capping layer to protect the LT-GaAs surface from oxidation. Upon exposure to air, AlAs forms

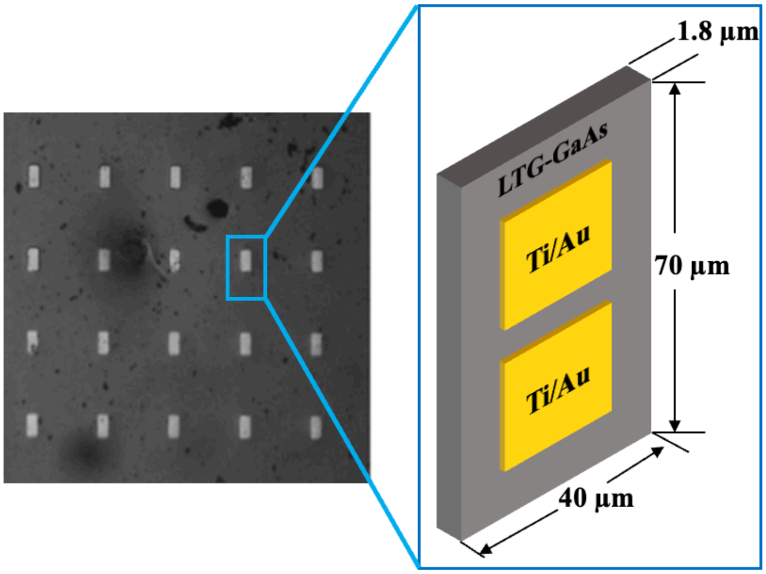

Figure 3.4: Array of thin-film LT-GaAs-based PCSs, including a detailed view of a single PCS with labeled dimensions.

a stable oxide layer (Al_2O_3), which serves as a protective barrier, preventing further oxidation of the underlying LT-GaAs [92]. In addition to its protective role, AlAs also functions as a sacrificial layer in the fabrication process. During the final step, when the sample is immersed in Hydrofluoric (HF) acid, the AlAs layer dissolves, leaving the LT-GaAs intact.

The AlAs layer was deposited using Molecular Beam Epitaxy (MBE), a highly controlled fabrication technique renowned for producing high-purity materials with precise thickness control and excellent structural integrity [93]. This layer was grown on a SI-GaAs substrate, which provides mechanical support and electrical isolation. Note that the thickness of the AlAs layer was selected to be 200 nm, while the LT-GaAs active region exceeded 2 µm (to ensure sufficient photoconductive volume), and the underlying SI-GaAs substrate was maintained at 600 µm.

With the multilayer wafer in hand, the first step was to cleave it into small square pieces (7 mm × 7 mm) to facilitate subsequent photolithography. Photolithography is a patterning technique used to selectively mask specific regions of the substrate surface. The process began with substrate cleaning, which was especially critical for GaAs substrates due to their susceptibility to organic contaminants, metal ions, and native oxide formation. To ensure a pristine and contaminant-free surface, the samples underwent a cleaning protocol, beginning with 10 minutes of sonication in acetone (to remove organic residues), followed by a thorough rinse in Deionized (DI) water to eliminate residual solvents.

Once the substrate surface was thoroughly cleaned and dried, the subsequent photolithography steps were executed on each sample, as illustrated in Fig. 3.5 and Fig. 3.6, and are summarized below.

1. The substrate was coated with a uniform layer of Lift-off Resist (LOR) 3A (thickness ≈ 1.5 μm) using a spin coater set at 2500 rpm for 30 seconds, with an acceleration rate of 10000 rpm per second. The spin coating process ensures a uniform and smooth LOR layer across the substrate, which is critical for defining the pattern during the photolithography process.

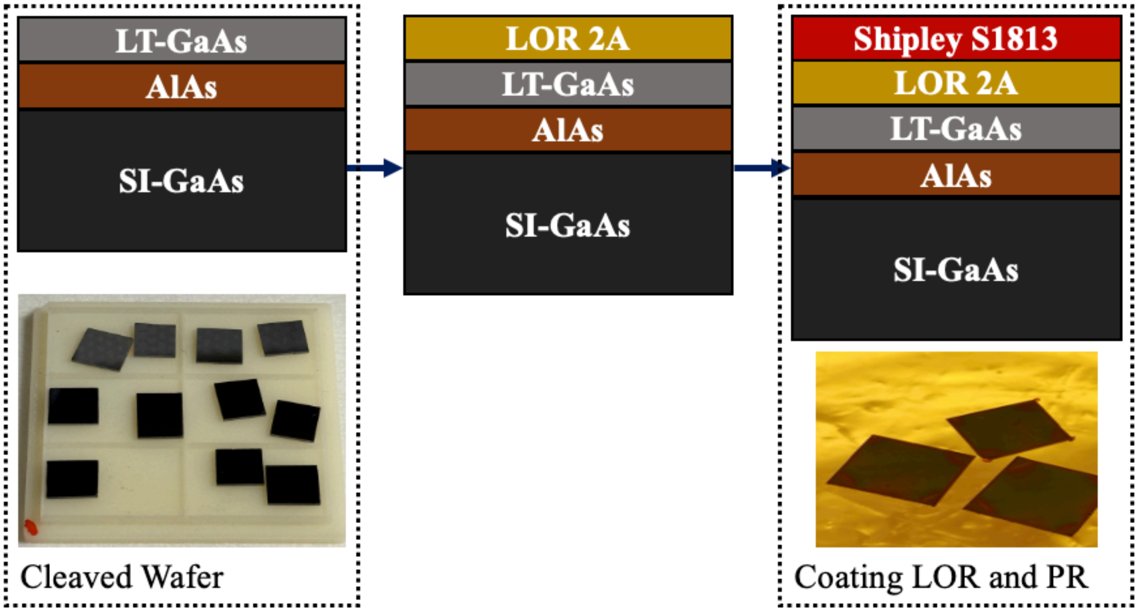

Figure 3.5: Coating on cleaved pieces of LT-GaAs wafer

2. The coated substrate was placed on a hotplate at 170 °C for 3 minutes to accelerate solvent evaporation from the LOR layer, thereby promoting solidification and ensuring a stable, adherent coating. After baking, the substrate was allowed to cool to room temperature to complete the solidification process and stabilize the layer prior to the next fabrication step.

3. Shipley S1813, a positive Photo Resist (PR), was applied to the substrate by spin coating at 5000 rpm for 30 seconds with an acceleration of 10000 rpm/s.

The positive PR layer was necessary for patterning the substrate under exposure to Ultra Violet (UV) light.

4. Similarly, the coated substrate was placed on a hotplate at 110°C for 1 minute. This baking step facilitates the removal of any residual solvent in the PR, making it more resistant to UV exposure. The substrate was then removed from the hotplate and allowed to cool to room temperature.

This procedure ensured a consistent and reliable coating of the substrate with both LOR and PR, providing a solid foundation for the subsequent fabrication steps. With the coating process completed, the next step involved mask alignment, which was performed according to the procedure illustrated in Fig. 3.6 and detailed in the following.

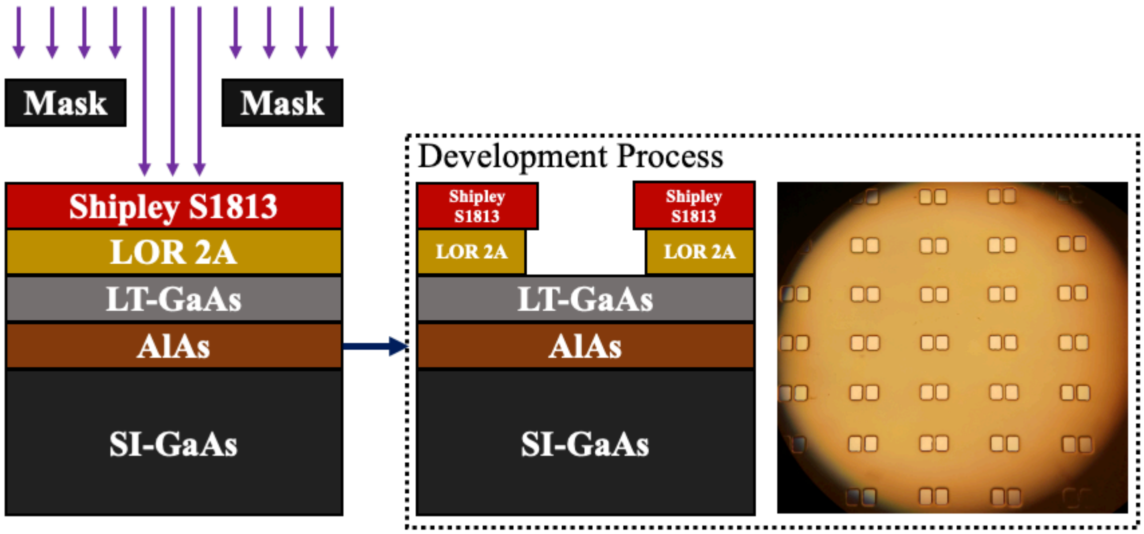

Figure 3.6: Schematic illustration of the mask alignment and development process.

1. A photomask, typically composed of a patterned chrome layer on a quartz substrate, was positioned between the UV light source and the PR-coated substrate. The mask selectively blocked UV radiation in predefined regions, thereby facilitating pattern transfer onto the underlying resist. A high-power, collimated UV light source with a programmable exposure timer was utilized in the mask aligner to ensure uniform exposure.

2. The photomask and the substrate were brought into close proximity to minimize diffraction effects and enhance the resolution of the transferred pattern.

3. The wafer was exposed to UV light with an intensity of $I_0 = 22$ mW/cm^2 for 4 seconds. This corresponds to an exposure dose of $E_0 = \Delta t \times I_0 = 88$ mJ/cm^2, which defines the total energy per unit area delivered to the PR, affecting its development behavior.

4. After UV exposure, the sample was developed to remove the exposed regions of the S1813 PR. To form the required undercut in the LOR layer, it was immersed in MF-319 developer for at least 60 seconds or until the pattern became clearly visible, followed by rinsing in DI water. This undercut was critical for ensuring a successful lift-off process.

The next stage involved metallization, in which metallic contacts were deposited using Physical Vapor Deposition (PVD), specifically through reactive sputtering. In this process, a controlled mixture of inert (argon) and reactive (nitrogen) gases is introduced into the sputtering chamber. The sputtered material reacts with the ambient gases to form a compound layer on the substrate surface.

To ensure strong adhesion and optimal electrical performance, a 10 nm titanium (Ti) layer was first deposited as an adhesion layer, followed by a 200 nm gold (Au) layer, selected for its superior electrical conductivity and environmental stability. The presence of the LOR layer was essential for a successful lift-off; without it, the Ti/Au film might form continuous sidewall coverage between the PR and the substrate, potentially leading to unintended electrical connections. The metal deposition and lift-off process are illustrated in Fig. 3.7.

Following gold deposition, the substrate was submerged in Remover PG—a proprietary solvent based on N-Methyl-2-Pyrrolidone (NMP)—for 1 hour to perform the lift-off process. To ensure complete metal removal, the sample was examined under a microscope every 15 minutes to verify that all unwanted metal had been removed from the surface. This soaking process effectively dissolved both the PR and LOR layers. Once the lift-off was complete, the substrate was thoroughly rinsed with DI water.

The same photolithography process was repeated on the sample, this time without the LOR layer, as gold contacts were already present. This step required precise mask alignment, where alignment markers on the mask were matched with previously defined lithographic features on the substrate. The second mask was complementary to the first, allowing UV light to pass through the active regions. Following alignment, the substrate underwent UV exposure and development.

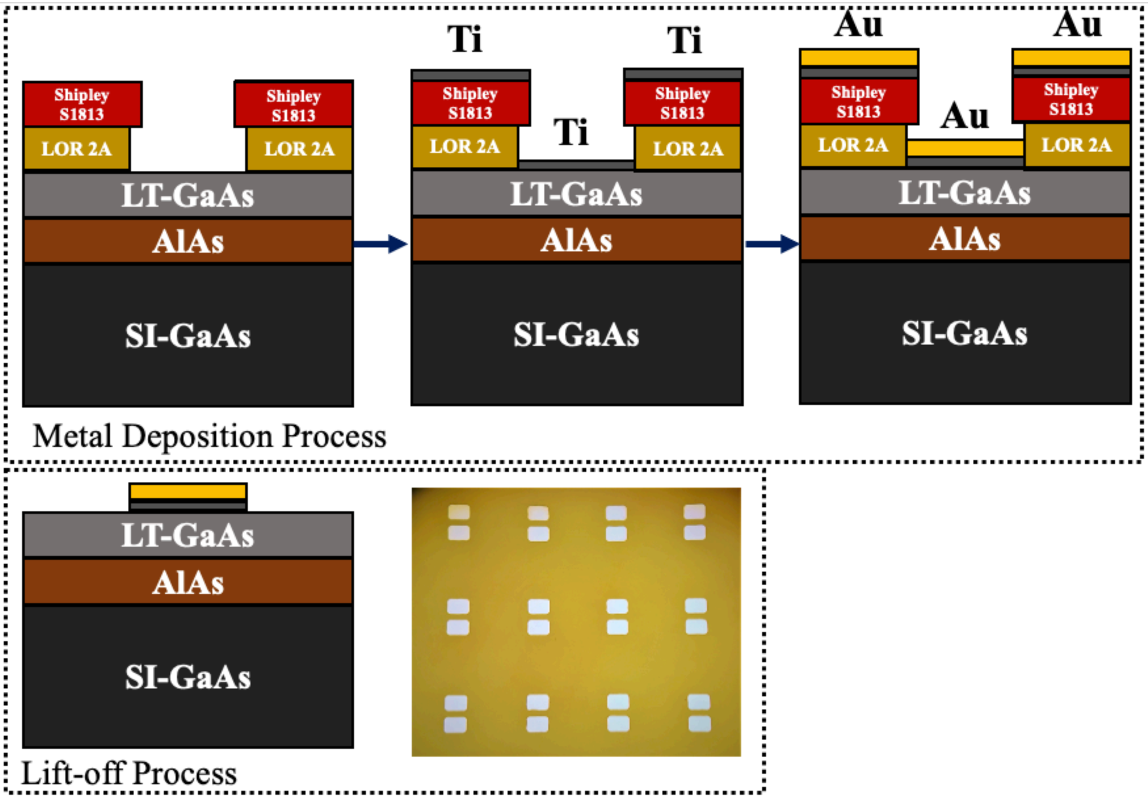

Figure 3.7: Metal deposition and lift-off procedure.

Subsequently, the entire substrate was submerged in a GaAs etchant—a mixture of citric acid and 30% hydrogen peroxide in a 5:1 ratio—for approximately 1 minute to initiate the etching process. The etching rate was then measured using a profilometer and was typically found to be around 200 nm/min. Based on this measurement, the substrate was reimmersed in the etchant until only 1 µm of the LT-GaAs layer remained.

It is important to note that during this step, several unexpected challenges were encountered. Specifically, during the mask design phase, different densities of PCSs were selected to serve as alignment masks in the lithography process. Through experimentation, it was observed that when the PCS density on a single chip was too high, the etching process did not proceed uniformly. This issue arose due to residual PR becoming trapped in the narrow gaps between adjacent structures, preventing complete removal during the development step. As a result, the remaining PR obstructed the etchant from fully accessing these confined regions, leading to incomplete etching and structural defects.

Figure 3.8(a) illustrates the optimal PCS density that enables successful fabrication. By maintaining adequate spacing between adjacent PCSs (approximately 20 µm), the etchant can effectively access all regions, resulting in well-defined and uniformly etched structures. In contrast, Fig. 3.8(b) shows high-density device layouts in which etching was unsuccessful due to insufficient spacing. In such cases, the etchant was unable to penetrate the narrow gaps between adjacent PCSs, leading to incomplete etching and structural defects. As a result, these poorly etched devices were rendered unusable for further processing, significantly impacting overall fabrication yield and device reliability.

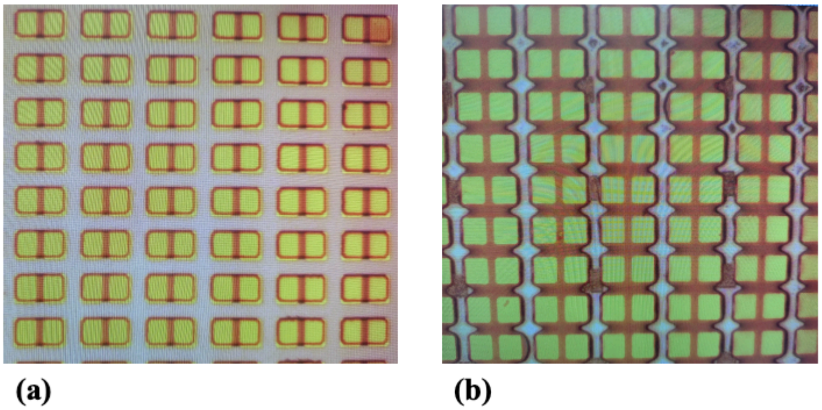

Figure 3.8: Impact of PCS density on the etching process. (a) A correctly optimized PCS density, ensuring proper etching and successful device fabrication. (b) A high-density PCS arrangement where incomplete etching has occurred, rendering the structures unusable for further processing.

As previously discussed, the LT-GaAs epilayer was grown on a sacrificial AlAs layer. Upon submerging the sample in HF acid, the AlAs layer underwent complete dissolution, while the LT-GaAs and underlying SI-GaAs layers remained structurally intact.

To protect the LT-GaAs epilayer during the process, an etch-resistant layer of Apiezon Wax W was applied by heating the sample to 130°C on a hotplate. A polystyrene rod was then carefully positioned and bonded to the wax to ensure a secure attachment. The rod, with the attached sample, was subsequently immersed in a 10% HF acid solution, such that the sample remained submerged while the rod itself was not fully immersed. After sufficient etching, the LT-GaAs epilayer detached from the substrate and was removed along with the polystyrene rod. To neutralize any residual HF, the sample was rinsed in a water–calcium carbonate solution, followed by a final rinse in DI water.

Figure 3.9 illustrates the step-by-step process of epitaxial layer lift-off, highlighting the role of wax bonding and selective HF etching in dissolving the sacrificial AlAs layer.

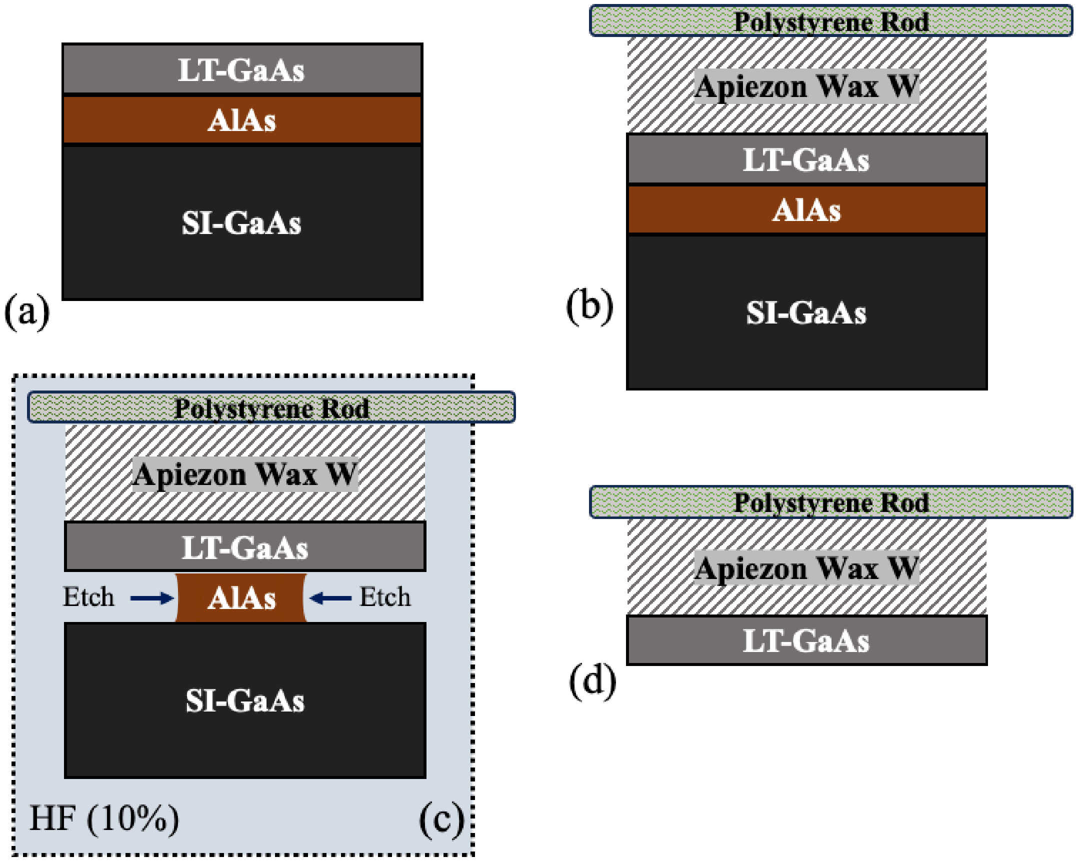

Figure 3.9: Schematic representation of the epitaxial layer lift-off process. (a) A clean substrate before processing. (b) Apiezon Wax W is melted onto the LT-GaAs surface, and a polystyrene rod is gently positioned to bond with the wax. (c) The polystyrene rod and bonded epilayer are immersed in HF acid to selectively dissolve the sacrificial AlAs layer. (d) After lift-off, the sample is removed, neutralized in a calcium carbonate solution, and rinsed with DI water.

Following the etching process, the sample was rinsed with DI water, and the polystyrene rod was carefully detached from the Apiezon Wax W. At this stage, the LT-GaAs epilayer was transferred to an alternative substrate (e.g., Mylar), provided the substrate was resistant to the solvent used for wax dissolution.

The final procedure involved extracting the LT-GaAs devices from the wax and transferring them onto another substrate for storage. This was accomplished by placing the samples, still bonded to the wax, onto a tilted Mylar membrane. Trichloroethylene (TCE) droplets were gently applied to the wax, causing it to liquefy. Once the wax was fully dissolved, a substantial portion of the thin-film LT-GaAs devices remained adhered to the Mylar membrane, with their front side now exposed on the surface.

Once the PCS devices were successfully bonded to the Mylar membrane, they were transferred onto a temporary substrate through a precise and controlled process. This procedure involved positioning the Mylar membrane with the device side facing the target substrate and carefully detaching the thin-film LT-GaAs regions using a sharp needle. Localized pressure was applied from the rear side of the membrane to facilitate detachment while minimizing mechanical stress on the fragile structure.

Figure 3.10 illustrates the step-by-step execution of this process. Several challenges were encountered during the accurate placement of PCS devices onto the membrane. First, transferring the device from one membrane (Fig. 3.10(b)) to another using a needle required extreme precision. Even minor external disturbances—such as airflow or mechanical vibrations—could cause the device to detach from the needle tip. Given the device's microscopic size, loss during this step often rendered recovery infeasible. Furthermore, after successful placement on the silicon surface (Fig. 3.10(c)), the PCS sometimes landed in an inverted orientation, necessitating additional repositioning. Based on experimental experience, a dual-needle technique was found to significantly improve control and placement accuracy during transfer.

Proper alignment of the conductive pads on top of the CPS transmission lines is critical, requiring precise lateral adjustments under a microscope. The LT-GaAs surface must be carefully inspected from a top-down perspective, and the device must be shifted meticulously using the needle to ensure exact placement. Figure 3.10(d) shows the correct placement of the device to act as the receiver.

A small water droplet is then applied to enhance adhesion between the device and CPS. During this step, both the needle and pipette must be handled delicately—placing the droplet close to the device to avoid displacement from fluid impact. Accidental contact between the needle and pipette must be strictly avoided to prevent damage to the fragile silicon nitride membrane, which could result in process failure.

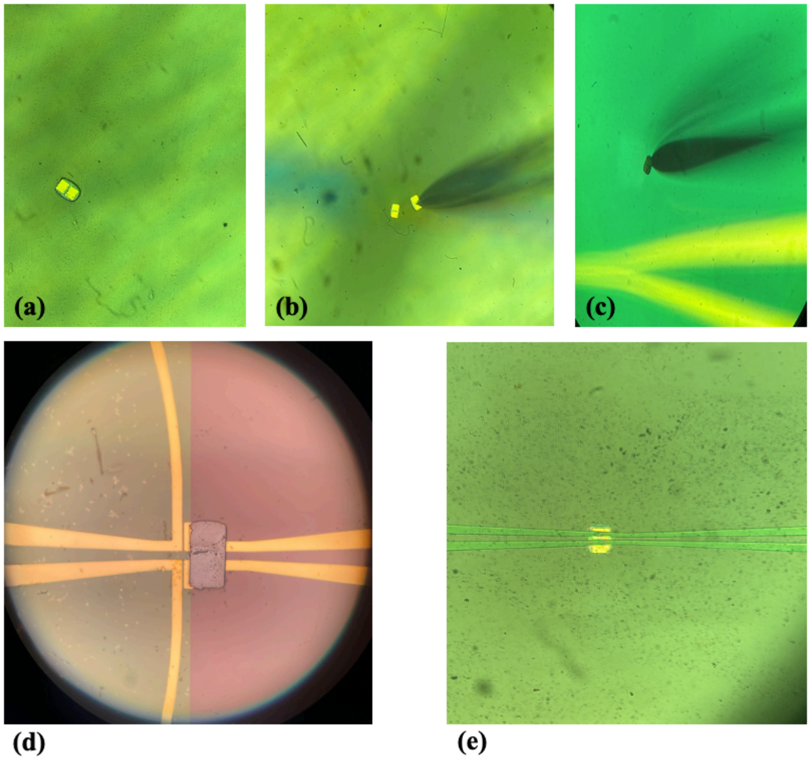

Figure 3.10: Step-by-step process for positioning the PCS on the transmission line for operation as a transmitter or receiver. (a) A PCS device after being released from the Mylar membrane onto a temporary substrate. (b) Attaching the device to the tip of a needle for manipulation. (c) Initial placement of the device on the silicon substrate, followed by precise adjustment to its predefined location, as shown in (d). (e) The circuit is flipped and viewed under a microscope to verify alignment between the gold contact pads and the CPS transmission line.

3.3.2 Fabrication of Silicon Nitride Membrane on Silicon Frame

In collaboration with 4D LABS, a robust and uniform 1 µm-thin silicon nitride membrane was fabricated on a 500 µm-thick double-side polished (DSP) silicon wafer to serve as a high-quality mechanical and dielectric support platform for integrating ultra-thin THz circuits. Figure 3.11 provides an overview of the fabrication process.

Although the fabrication was not directly conducted as part of this dissertation, a brief summary of the key steps is presented here for completeness. The formation of the silicon nitride membrane began with the deposition of a uniform silicon nitride layer on a DSP silicon wafer using Low-Pressure Chemical Vapor Deposition (LPCVD)—a technique renowned for delivering high-quality films with excellent thickness uniformity. The deposition process, lasting approximately 5 hours,

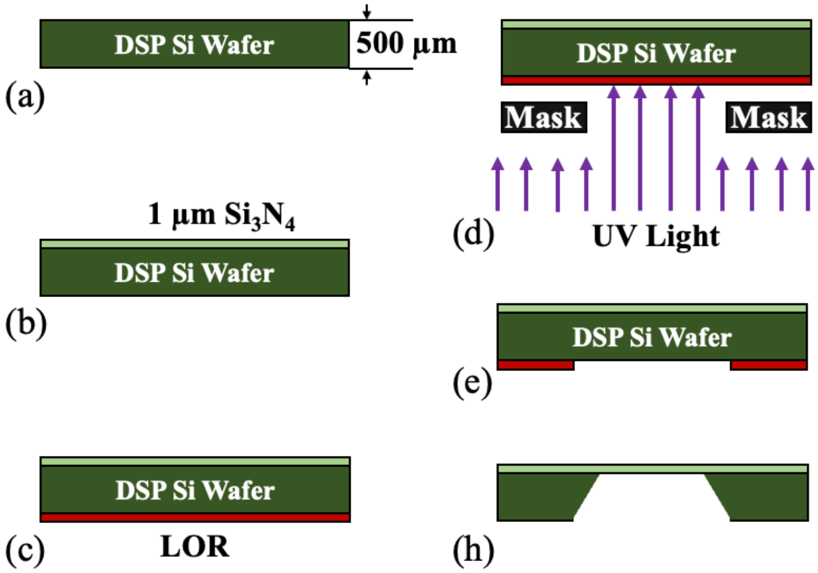

Figure 3.11: Fabrication of thin membrane on a DSP silicon wafer

produced a 1 µm-thick membrane, ensuring the mechanical stability and structural integrity necessary for subsequent fabrication steps.

Photolithography began with rigorous substrate preparation to ensure high-resolution patterning and robust resist adhesion. The silicon wafer was subjected to a standardized multi-step cleaning procedure, as previously outlined, followed by native oxide removal. This was achieved by immersing the wafer in a 1:1 solution of hydrochloric acid (HCl), effectively eliminating the 1–2 nm-thick oxide layer and exposing a pristine silicon surface essential for subsequent processing. A uniform LOR layer was then spin-coated onto the cleaned substrate, baked on a hotplate at 170 °C, and subsequently cooled under controlled conditions to stabilize the resist film for the next photolithographic steps.

Once the resist stack was properly formed, photolithographic patterning was carried out using a high-resolution chrome-on-quartz photomask. The aligned sample was subsequently exposed to a collimated UV light source to define the desired pattern. Following exposure, the substrate was immersed in MF-319 developer, which selectively dissolved the UV-exposed regions of the PR, thereby uncovering the underlying substrate surface. To conclude the process, the substrate was thoroughly rinsed with DI water to eliminate any residual developer and ensure surface cleanliness.

In this process, Potassium Hydroxide (KOH) etching is employed to selectively remove designated regions of the silicon substrate, thereby delineating the silicon nitride membrane structure. The etching parameters—including duration and solution composition—are precisely controlled to achieve a membrane thickness of 1 µm. KOH exhibits strong anisotropic etching characteristics, preferentially dissolving the silicon while preserving the integrity of the silicon nitride layer. This selective removal enables the formation of a uniform, well-defined membrane supported by the remaining silicon frame, ensuring both structural stability and dimensional accuracy.

Following the wet etching process, the same metallization and photolithography procedures were repeated. Figure 3.12(a) shows the CAD layout of the structure prior to fabrication. After fabrication, the DSP Si wafer was sectioned into four quadrants, each hosting distinct TSoC designs without integrated PCSs, as illustrated in Fig 3.12(b). Each circuit incorporates bias lines extending to peripheral contact pads to enable electrical interfacing. Finally, each quadrant was mounted on a PCB and integrated into the measurement setup for comprehensive characterization, as shown in Fig 3.12(c).

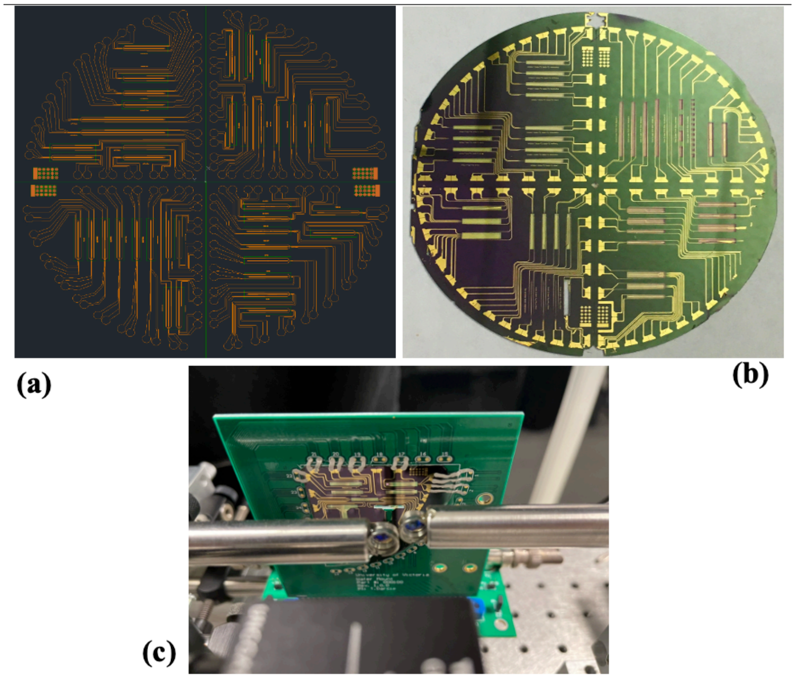

Figure 3.12: (a) CAD model of the designed wafer before fabrication. (b) Fabricated DSP Si wafer divided into four quadrants, each containing a TSoC design without PCSs. Bias lines connect each circuit to outer-edge connection pads. (c) Measurement setup where each quadrant is mounted onto a PCB for testing.

Chapter 4

Contribution

This chapter outlines the core contributions introduced in Chapter 1. The following sections provide a summary of the major achievements of this research. The selected figures and content are adapted from the authors' published or submitted manuscripts. For a detailed description of the methodologies and technical insights, the reader is referred to Appendices A through D, which follow the journal article format and include comprehensive design and performance assessments.

4.1 Demonstration of a Terahertz Band-Stop Filter Using an Apodized Bragg Grating (Appendix A)

This work presents the first experimental demonstration of a planar, on-chip THz band-stop filter based on a CPS transmission line. An Apodized Bragg Grating (TABG) structure is integrated into a TSoC platform to create a band-stop filter with a center frequency of 0.8 THz and a bandwidth of 200 GHz. The integrated TABG was characterized from DC to 1.5 THz. Experimental measurements demonstrate a stopband rejection of approximately 20 dB, showing strong agreement with both full-wave simulations and theoretical models.

This work introduces several key technical advances. First, it demonstrates a fully integrated apodized Bragg filter operating in the THz frequencies, incorporating the transmitter, feedlines, the TABG section, and the receiver. The TABG represents the first experimental demonstration of its performance, complementing previous simulation studies, and establishes a scalable, high-performance band-stop filter for THz applications. Second, it achieves the highest Bragg frequency reported in the THz gap using quasi-TEM CPS feedlines fabricated on a thin silicon nitride membrane. Third, it confirms that the theoretical principles governing periodic filters are applicable to THz Bragg structures. Finally, it reveals and analyzes radiative loss mechanisms at frequencies beyond the Bragg stopband in CPS grating configurations.

Inspired by Fiber Bragg Grating (FBG)s in optical communication systems, the TABG employs periodic modulation of the characteristic impedance along with an apodization profile to minimize side lobes in the reflection spectrum [94]. The filter comprises $N = 12$ unit cell sections and 4 apodization sections from each end, which facilitate a gradual transition in geometry and characteristic impedance between the feedlines and the grating unit cells. It features a stopband centered at 0.8 THz, with a calculated grating period of $\Lambda = 165$ μm, determined using:

$$\Lambda = \frac{c}{2 f_c \sqrt{\varepsilon_{re}}}, \tag{4.1}$$

where c is the speed of light, f_c is the center frequency, and ε_{re} is the effective relative permittivity of the propagating mode.

The fractional bandwidth of the filter is determined to be $\Delta f = 0.18$ THz, based on the impedance discontinuities between adjacent cells. Full-wave simulations performed using ANSYS HFSS ensure precise modeling of the characteristic impedance and effective permittivity ($\varepsilon_{\mathrm{re}} \approx 1.3$), ensuring design accuracy and performance reliability.

The fractional bandwidth, $\Delta f / f_c$, is influenced by the characteristic impedance contrast between adjacent cells and is given by [95]:

$$\frac{\Delta f}{f_c} = \frac{4}{\pi} \sin^{-1}\left(\frac{Z_{n+1} - Z_n}{Z_{n+1} + Z_n}\right), \tag{4.2}$$

where Z_n and Z_{n+1} represent the characteristic impedances of consecutive unit cells. Using Eq. (4.4) with Z_0 and Z_U from Table 4.1, the fractional bandwidth is calculated as $\Delta f = 0.18$ THz. Figure 4.1 illustrates an annotated portion of the TABG. The TABG response is defined by reflections caused by characteristic impedance discontinuities along the grating.

In microwave engineering, the Bragg filter is commonly referred to as a periodic filter, which can be described by a dispersion diagram and a Bloch impedance [46] (refer to Section 2.6.1 for further details). To calculate these quantities, we construct

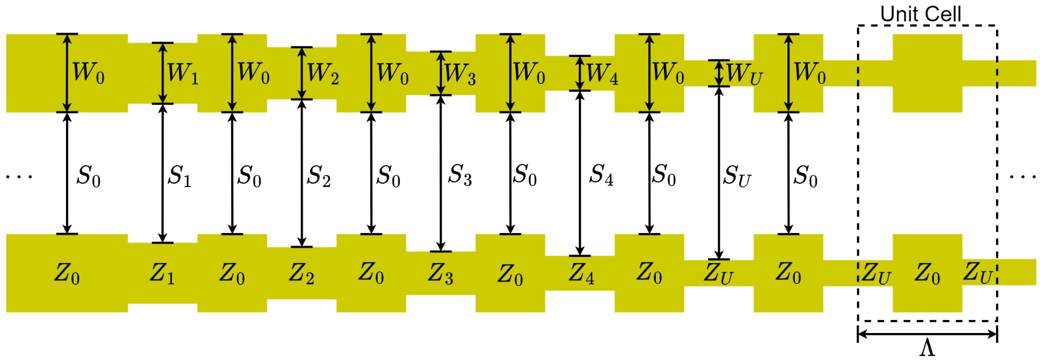

Figure 4.1: Apodization sections and grating unit cell where $\Lambda = 165\ \mu m$. Dimensions and characteristic impedances are found in Table 4.1.

Table 4.1: TABG dimensions and characteristic impedances for Fig. 4.1

n	0	1	2	3	4	U
W$_n$ [μm]	45	35	30	25	20	15
S$_n$ [μm]	70	80	85	90	95	100
Z$_n$ [Ω]	234	260	274	290	311	332

the ABCD matrix of the unit cell depicted in Fig. 4.1 as:

$$\begin{bmatrix} A & B \\ C & D \end{bmatrix} = \begin{bmatrix} \cos\left(\frac{\beta\Lambda}{4}\right) & jZ_U \sin\left(\frac{\beta\Lambda}{4}\right) \\ jY_U \sin\left(\frac{\beta\Lambda}{4}\right) & \cos\left(\frac{\beta\Lambda}{4}\right) \end{bmatrix} \cdot \begin{bmatrix} \cos\left(\frac{\beta\Lambda}{2}\right) & jZ_0 \sin\left(\frac{\beta\Lambda}{2}\right) \\ jY_0 \sin\left(\frac{\beta\Lambda}{2}\right) & \cos\left(\frac{\beta\Lambda}{2}\right) \end{bmatrix} \cdot \begin{bmatrix} \cos\left(\frac{\beta\Lambda}{4}\right) & jZ_U \sin\left(\frac{\beta\Lambda}{4}\right) \\ jY_U \sin\left(\frac{\beta\Lambda}{4}\right) & \cos\left(\frac{\beta\Lambda}{4}\right) \end{bmatrix}, \tag{4.3}$$

where $\beta = \frac{\omega\sqrt{\varepsilon_{re}}}{c}$ is the propagation constant.

After constructing the ABCD matrix, we obtain the dispersion diagram and Bloch impedance. The dispersion diagram is calculated using $\beta\Lambda = \text{Imag}\{\cosh^{-1}[(A + D)/2]\}$, and the result is plotted in Fig. 4.2 (a). This figure illustrates the stopband associated with the infinite periodic structure. Next, the Bloch impedance is calculated using Eq. (2.50), and the reflection coefficient between an infinite periodic filter and a load impedance is derived from Eq. (2.60). Using this equation, we illustrate the impact of apodization. If we negate the apodization sections, then $Z_L = Z_0$, resulting in a mismatch and a less desirable reflection spectrum. Alternatively, by adding an apodization section, we can significantly improve the matching and reduce reflections (Fig. 4.2 (b)).

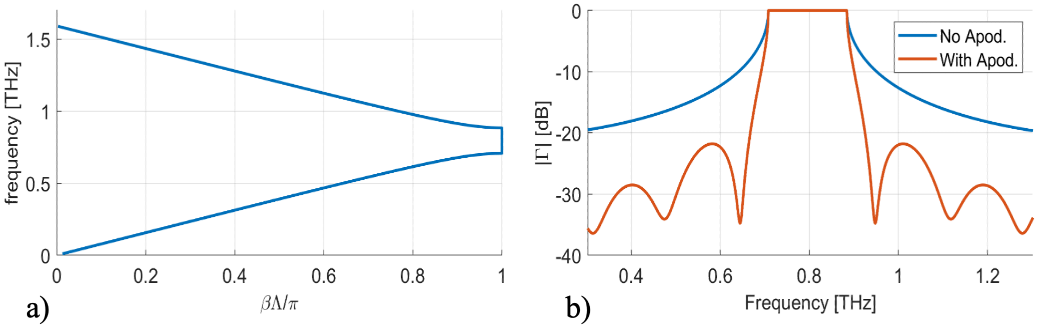

Figure 4.2: (a) Dispersion diagram for the TABG. (b) Reflection coefficient at the load of the TABG with and without an apodization section.

Experimental characterization is performed using a modified THz-TDS platform same as Fig. 3.2. This platform integrates the transmitter, receiver, and TABG onto a single wafer with planar circuitry defined on a 1 μm Si_3N_4 substrate, providing low loss and low dispersion at THz frequencies.

The thin silicon nitride substrate provides low-loss and low-dispersion transmission, which is critical for accurate device characterization at THz frequencies. Importantly, the use of this thin substrate is essential to mitigate radiation losses during wideband measurements, as discussed in Section 2.5.2. In contrast, the use of a thicker substrate would introduce substantial radiation loss and dispersion, degrading measurement accuracy, as reported in [7]. The effectiveness of this approach has been demonstrated in prior studies [44, 56, 62, 96].

In this study, the fabrication process closely follows the methodology described in Chapter 3. Figure 4.3(a) illustrates the Tx PCS placed atop a lithographically defined 200 nm gold CPS transmission line on the thin silicon nitride substrate. Following the transmitter PCS, the CPS transmission line transitions into a wider cross-section ($W = 45$ µm, $S = 70$ µm) to mitigate attenuation and optimize signal propagation [44]. Figure 4.3(b) presents a microscopic image of the TABG structure, while Fig. 4.3(c) portrays the receiver section, which consists of a DC block, DC bias lines for the Tx PCS, and bias lines to connect the Rx PCS to the lock-in amplifier.

Figure 4.4(a–b) presents the simulated and experimental temporal responses of the received THz-bandwidth pulse after transmission through the TABG structure. The corresponding spectral response, obtained by applying a Discrete Fourier Transform

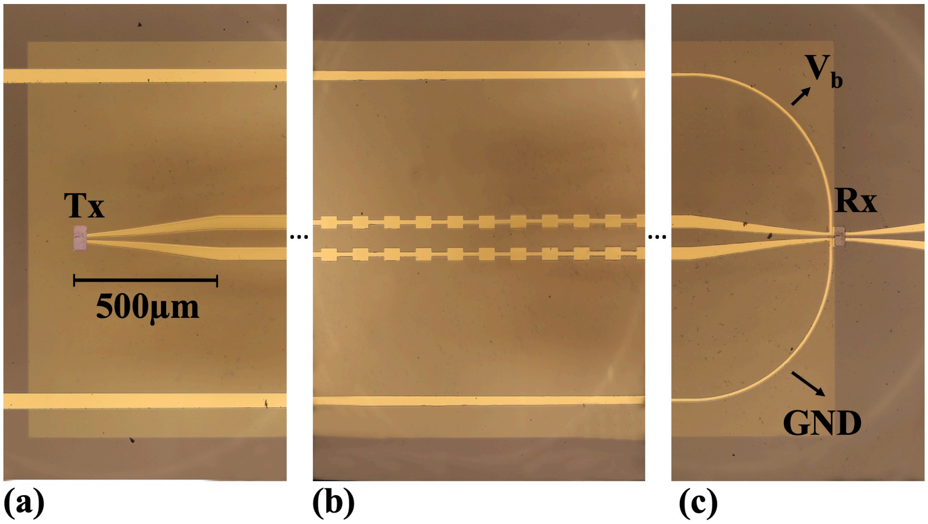

Figure 4.3: TSoC with TABG. (a) illustrates an LT-GaAs PCS (Tx) on a gold transmission line on a 1 µm-thin Si_3N_4 membrane. In (b), the TABG is displayed. (c) shows the LT-GaAs PCS receiver (Rx), coupling section, and the DC bias lines.

(DFT) to the time-domain signals, is shown in Fig. 4.4(c). For comparison, a reference trace representing a simulation without TABG is also included.

As expected, the spectral roll-off observed in both simulation and experiment results from the finite duration of the time-domain pulse. The maximum measurable frequency is defined by the point at which the spectral dynamic range (SDR) reaches zero [97]. Our measurement system exhibits a maximum SDR of approximately 60 dB, which gradually diminishes with increasing frequency. Referring to Fig. 4.4(c), the maximum measurement frequency corresponds to the point where the normalized power drops below −60 dB, occurring near 1.5 THz.

The experimental results exhibit strong agreement with the simulations in terms of stopband center frequency and bandwidth. However, a discrepancy is observed in the stopband rejection: the experimental rejection is approximately 30 dB, while the simulation predicts 45 dB. Several factors may explain this difference. First, limitations in the photolithographic process restrict the minimum feature size to approximately 2 µm, resulting in dimensional deviations between simulated and fabricated structures. Second, discrepancies may arise due to variations in material parameters between the simulation and the fabricated device, even if they are nominally similar. Additionally, the possibility of coupling to unintended modes with lower attenuation across the filter may contribute to the reduced experimental rejection.

In summary, this work demonstrated the first on-chip TABG filter integrated into

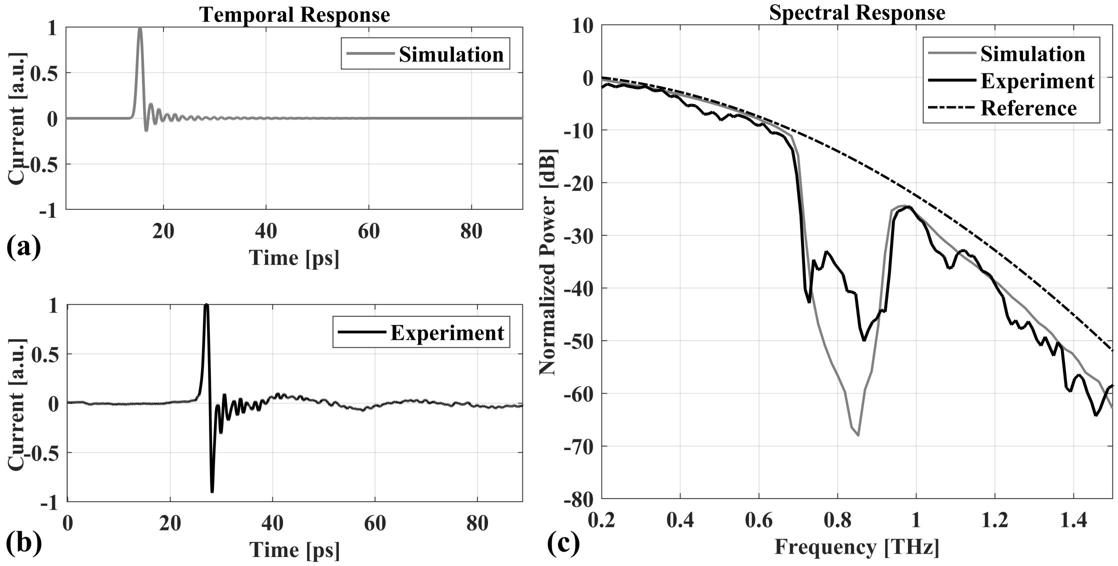

Figure 4.4: Experimental results of the received THz-bandwidth pulse after propagation through the TABG. (a) Simulated temporal response (ANSYS HFSS). (b) Experimental temporal response. (c) DFT of the experimental and simulated temporal responses.

a planar TSoC platform. The filter achieved a center frequency of 0.8 THz and a 0.2 THz bandwidth with strong agreement between simulation and experiment. The use of apodization improved spectral performance by reducing side lobes and enhancing roll-off. These results validate the potential of periodic structures for compact and scalable THz filtering and establish a foundation for future developments in integrated TSoC systems.

4.2 Demonstration of a Planar Multimodal Periodic Filter at THz Frequencies (Appendix B)

The previous work demonstrated that planar THz band-stop filters can be realized by modulating the impedance of CPS transmission line sections, effectively achieving strong filtering through impedance contrast within a uniform quasi-TEM mode structure. In the present work, we extend this concept by introducing a multimodal periodic architecture that takes advantage of additional design flexibility enabled by controlled mode conversion between CPS and the odd mode of a finite-ground CPW.

This CPS–CPW configuration creates a multimodal structure with unique spectral properties. The filter is designed for a center frequency of $f_c = 0.8$ THz and a bandwidth of $\Delta f = 0.07$ THz. Experimental characterization reveals excellent agreement with theoretical predictions and full-wave simulations, validating both the multimodal design framework and its potential for integrated THz applications. These filters are well suited for integration with other planar components such as phase shifters [98], hybrids [99], and reconfigurable diodes [100].

The designed filter consists of alternating sections of CPS and CPW (Fig. 4.5(a)), forming a structure similar to the Bragg grating previously demonstrated [1]. It features a grating period of $\Lambda = 173$ μm, corresponding to a center frequency of $f_c = 0.8$ THz. Figure 4.5(b) illustrates the transverse cross-section of the CPW section and Fig. 4.5(c) presents a section of the filter that clarifies the unit cells. The conductors have a width $W = 45$ μm, and the separation is $S = 80$ μm. The central conductor width W_m is set to 45 μm to achieve a stopband attenuation of approximately -20 dB for $N = 20$ filter periods. The substrate is a thin layer of silicon nitride ($H_s = 1$ μm) to reduce radiation loss, with gold (Au) conductors of 200 nm thickness for compatibility with transmitter/receiver bonding methods [101].

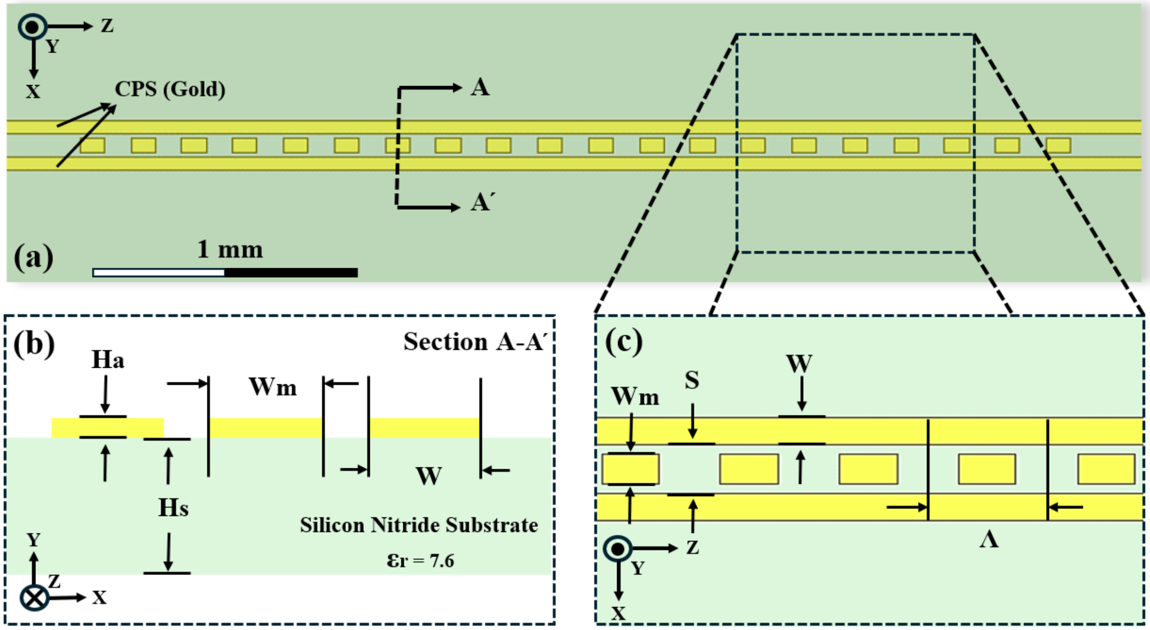

Figure 4.5: (a) Filter structure. (b) Cross-section of CPW sections. (c) Unit cell parameters.

Full-wave simulations using ANSYS HFSS software determine mode impedance, S-parameters, and field distributions. The conductors are modeled as gold (Au) with

$\sigma_{\mathrm{Au}}(0.8\ \mathrm{THz}) = 2.16 \times 10^7$ S/m, and the substrate is silicon nitride with $\varepsilon_{r,\mathrm{SiN}} = 7.6$ and $\tan \delta_{\varepsilon,\mathrm{SiN}} = 0.00526$ [102].

The CPW consists of three conductors, enabling it to support two distinct modes: the even mode and the odd mode. Superscripts are used to differentiate these modes, e.g., CPW^o for the odd mode and CPW^e for the even mode. Each mode has a distinct characteristic impedance: Z^o_{CPW} and Z^e_{CPW}. Typically, the CPW^e mode is the desired mode, while the CPW^o mode is often considered parasitic and suppressed by shortcircuiting the outer conductors.

However, in this work, the CPW^o mode is of primary importance, while the CPW^e mode plays a secondary role. On the other hand, the CPS, with its two conductors, supports only a single mode with a characteristic impedance of Z_{CPS}. The three modes are illustrated in the transverse plane in Fig. 4.6.

As shown in Fig. 4.6(a, b), the CPS mode closely resembles the CPW^o mode, suggesting significant modal coupling. Figure 4.7 illustrates the qualitative and quantitative effects of the CPW^o-CPS interface. Electric field vectors at 0.8 THz are presented for various widths of the central conductor (W_m) in Figs. 4.7(a–c), revealing minimal disruption at the CPW^o-CPS interface. To quantify transmission, $|S^o_{21}|^2$ (transmission between CPW^o and CPS) versus W_m is plotted in Fig. 4.7(d). Transmission between CPW^e and CPS, $|S^e_{21}|^2$, is not plotted because it is less than -60 dB, consistent with the expectation for symmetric CPWs [103].

The results in Fig. 4.7(d) demonstrate a strong coupling between the CPS and CPW^o modes, establishing the potential of this configuration as a building block for periodic filters. While the central conductor is not required to be rectangular or symmetric, such designs would introduce additional complexities, including the excitation of even modes and the presence of graded impedances, which are beyond the scope of this study. Additionally, the CPS-CPW transition could include a shunt admittance to model parasitic effects, but such contributions were found to have negligible impact on the periodic filter investigated here.

The center frequency of the periodic filter is determined by the period Λ, as given by Eq. 4.1. For $\varepsilon_{re} \approx 1.2$, the center frequency is $f_c = 0.8$ THz when $\Lambda = 173\ \mu$m. Additionally, the fractional bandwidth is governed by the characteristic impedances Z^o_{CPW} and Z_{CPS}, and is derived from Eq. 4.4. Subsequently, it is expressed as:

$$\frac{\Delta f}{f_c} = \frac{4}{\pi} \sin^{-1}\left(\frac{Z_{\mathrm{CPS}} - Z^o_{\mathrm{CPW}}}{Z_{\mathrm{CPS}} + Z^o_{\mathrm{CPW}}}\right). \tag{4.4}$$

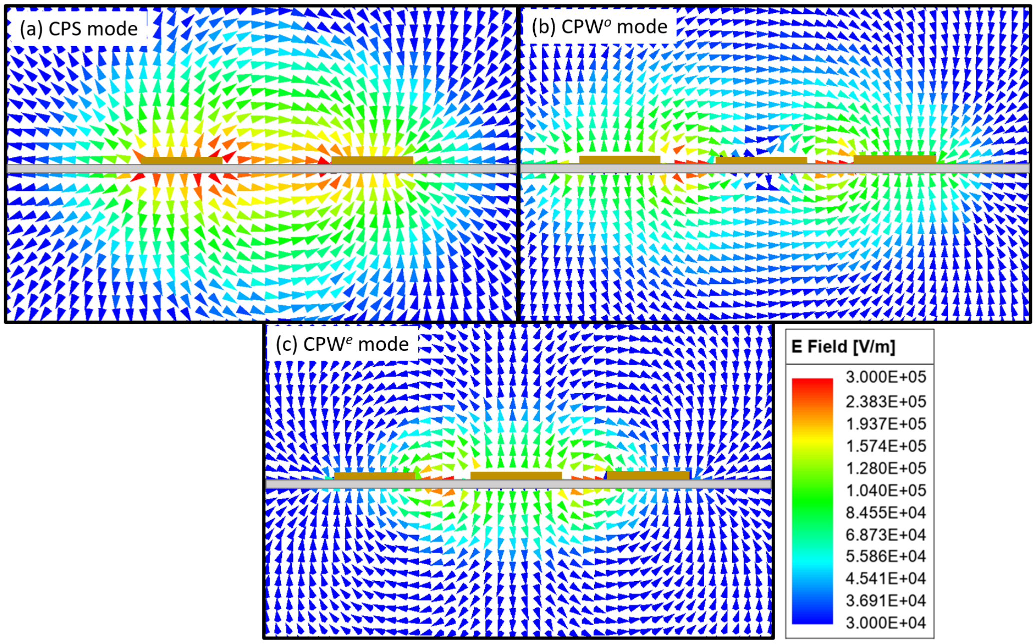

Figure 4.6: Illustrations of modes. (a) CPS mode. (b) CPW^o mode. (c) CPW^e mode. Conductors and substrates are overlaid for visibility, and their thicknesses are approximately 10× thinner than shown.

For initial design estimates, the quasi-static expressions for characteristic impedances are used. For the CPW odd-mode [104]:

$$Z^o_{\text{CPW}} = \frac{120\pi}{\sqrt{\varepsilon_{re}}} \frac{K(k_{\text{CPW}})}{K(k'_{\text{CPW}})}, \quad k_{\text{CPW}} = \frac{S}{S+2W}\sqrt{\frac{1-\left(\frac{W_m}{S}\right)^2}{1-\left(\frac{W_m}{S+2W}\right)^2}}, \tag{4.5}$$

where $k'_{\text{CPW}} = \sqrt{1-k^2_{\text{CPW}}}$ and $K(\cdot)$ is the complete elliptic integral of the first kind.

For the CPS mode [105]:

$$Z_{\text{CPS}} = \frac{120\pi}{\sqrt{\varepsilon_{re}}} \frac{K(k_{\text{CPS}})}{K(k'_{\text{CPS}})}, \quad k_{\text{CPS}} = \frac{S}{S+2W}, \tag{4.6}$$

where $k'_{\text{CPS}} = \sqrt{1-k^2_{\text{CPS}}}$.

From Eq. 4.5 and Eq. 4.6, as $W_m \to 0$, $k_{\text{CPW}} \to k_{\text{CPS}}$ and $Z^o_{\text{CPW}} \to Z_{\text{CPS}}$. Consequently, the fractional bandwidth reduces to zero, which is aligned with expectation of connecting two identical sections of transmission line (i.e., the CPW with $W_m = 0$ and a CPS). Figure 4.8(a) plots the characteristic impedance of the modes using the quasi-static expressions and at 0.8 THz which was obtained from full-wave sim-

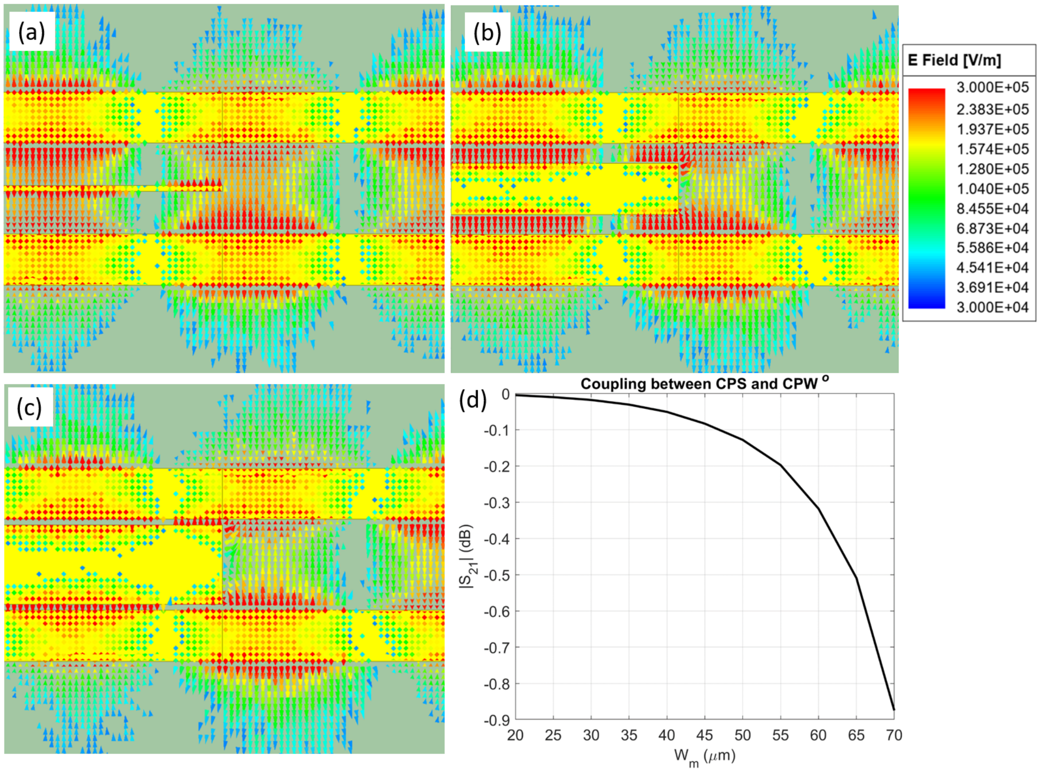

Figure 4.7: CPS-to-CPW^o mode coupling at 0.8 THz. (a) $W_m = 5$ µm. (b) $W_m = 45$ μm. (c) $W_m = 70$ μm. (d) $|S_{21}^o|^2$ for CPS-to-CPW^o as a function of W_m.

ulation. The quasi-static and 0.8 THz traces exhibit similar characteristics, but are shifted in value which is expected as the characteristic impedance of CPW and CPS are frequency dependent [106, 107]. The bandwidth is obtained using Eq. 4.4 and is plotted in Fig. 4.8(b) where a bandwidth of 0.07 THz is predicted for the experimental structure with $W_m = 45$ µm.

In summary, the design procedure begins by selecting the desired center frequency using Eq. 4.1. Next, the effective relative permittivity, ε_{re}, is obtained using full-wave simulation, but when using thin substrates (as in this work) then $\varepsilon_{re} \approx 1$. Next, the conductor width, W, should be selected to have desirable attenuation characteristics at THz frequencies such as $W = 30$ µm. The conductor separation, S, is then selected to obtain a desired characteristic impedance for the feedline, Z_{CPS} using Eq. 4.6 (or full-wave simulation). The central conductor width, W_m, is selected to obtain Z_{CPW}^o using Eq. 4.5 (or full-wave simulation) which produces the specified fractional bandwidth given by Eq. 4.4.

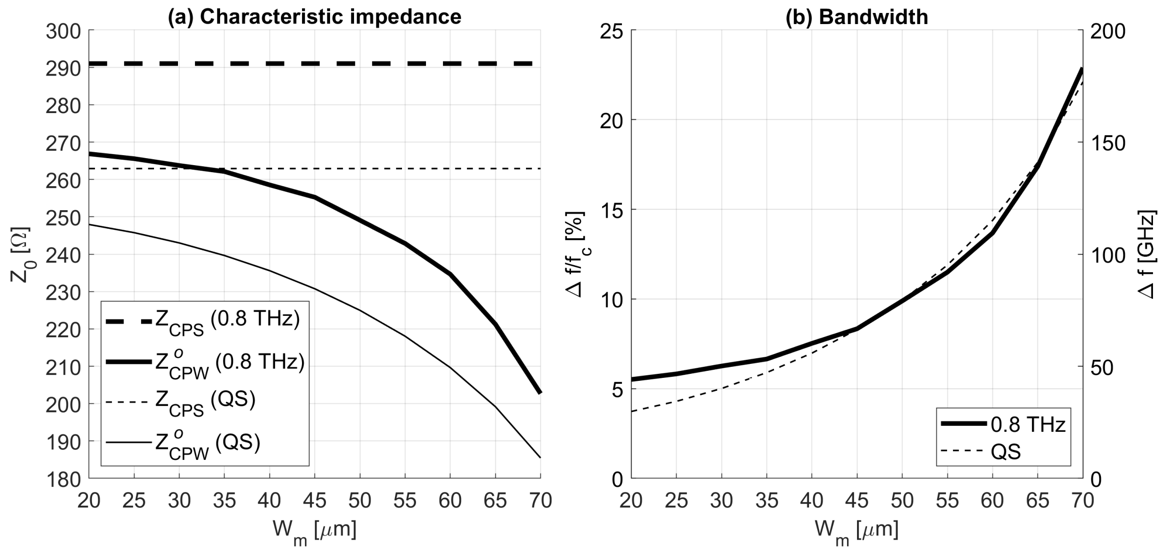

Figure 4.8: (a) Characteristic impedance using quasi-static expressions and full-wave simulation at 0.8 THz with S = 80 µm, W = 45 µm, H_s = 1 µm, H_a = 200 nm, and ε_r = 7.6. The impedance at 0.8 THz with W_m = 45 µm are $Z_{\text{CPS}} = 291\Omega$ and $Z^o_{\text{CPW}} = 254\Omega$. (b) The corresponding fractional bandwidth from Eq. 4.4 and bandwidth where f_c = 0.8 THz. At W_m = 45 µm, the bandwidth is 0.07 THz.

The periodic filter is constructed by cascading, N, units cells that consist of two quarter-wavelength ($\lambda/4$) sections of transmission lines with different characteristic impedances. Unit cells are modeled using ABCD matrices. To simplify the analysis, it is best to construct the unit cells ABCD matrix using a CPS of length $\Lambda/4$, a CPW^o of length $\Lambda/2$, and a CPS of length $\Lambda/4$. This enables a straightforward method to calculate the total ABCD matrix by raising the ABCD matrix of the unit cell to the power of N. The ABCD matrix for a unit cell (Fig. 4.5) is given by the following:

$$\begin{aligned}\begin{bmatrix} A_{cell} & B_{cell} \\ C_{cell} & D_{cell} \end{bmatrix} &= \begin{bmatrix} \cos(\beta_{\text{CPS}}\Lambda/4) & jZ_{\text{CPS}}\sin(\beta_{\text{CPS}}\Lambda/4) \\ j(1/Z_{\text{CPS}})\sin(\beta_{\text{CPS}}\Lambda/4) & \cos(\beta_{\text{CPS}}\Lambda/4) \end{bmatrix} \\ &\cdot \begin{bmatrix} \cos(\beta^o_{\text{CPW}}\Lambda/2) & jZ^o_{\text{CPW}}\sin(\beta^o_{\text{CPW}}\Lambda/2) \\ j(1/Z^o_{\text{CPW}})\sin(\beta^o_{\text{CPW}}\Lambda/2) & \cos(\beta^o_{\text{CPW}}\Lambda/2) \end{bmatrix} \\ &\cdot \begin{bmatrix} \cos(\beta_{\text{CPS}}\Lambda/4) & jZ_{\text{CPS}}\sin(\beta_{\text{CPS}}\Lambda/4) \\ j(1/Z_{\text{CPS}})\sin(\beta_{\text{CPS}}\Lambda/4) & \cos(\beta_{\text{CPS}}\Lambda/4) \end{bmatrix}.\end{aligned} \tag{4.7}$$

The ABCD matrix for N sections is given by:

$$\begin{bmatrix} A & B \\ C & D \end{bmatrix} = \begin{bmatrix} A_{cell} & B_{cell} \\ C_{cell} & D_{cell} \end{bmatrix}^N \tag{4.8}$$

The dispersion characteristics of the filter are obtained from Eq. 4.7 using the same methods presented in [1]. The result of this process is shown in Fig. 4.9 where a 0.07 THz stopband is observed.

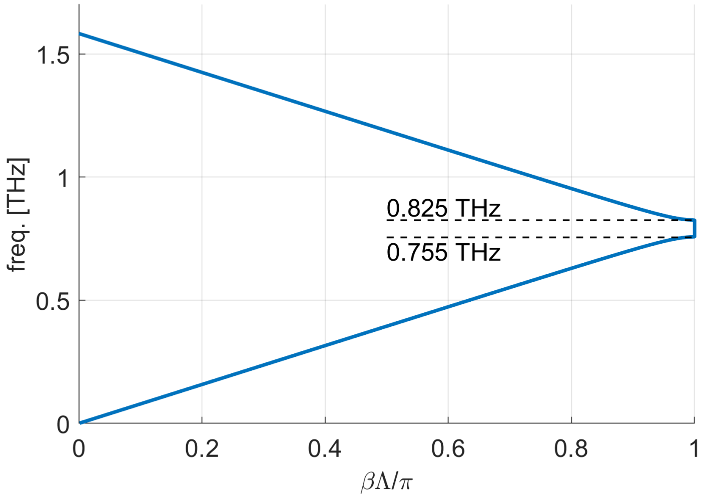

Figure 4.9: Dispersion diagram for the unit cell.

Lastly, the S-parameters are calculated from the ABCD matrix using standard methods [46]:

$$S_{11} = \frac{A + B/Z_{\mathrm{CPS}} - CZ_{\mathrm{CPS}} - D}{A + B/Z_{\mathrm{CPS}} + CZ_{\mathrm{CPS}} + D} \quad \text{and} \quad S_{21} = \frac{2}{A + B/Z_{\mathrm{CPS}} + CZ_{\mathrm{CPS}} + D} \tag{4.9}$$

The experimental setup follows the THz-TDS method described in Chapter 2 and fabrication adheres to the previously described process. The fabricated structure is shown in Fig. 4.10.

Figure 4.11 presents the experimental results for a reference structure and the periodic filter illustrated in Fig. 4.10(b-d). The temporal response is normalized and transformed into the spectral response via DFT. The spectral response in Fig. 4.11(c) reveals a stopband centered at 0.8 THz with a bandwidth of approximately 0.1 THz, aligned with theoretical predictions and full-wave simulations.

The observed spectral decay, characterized by an approximately linear slope of

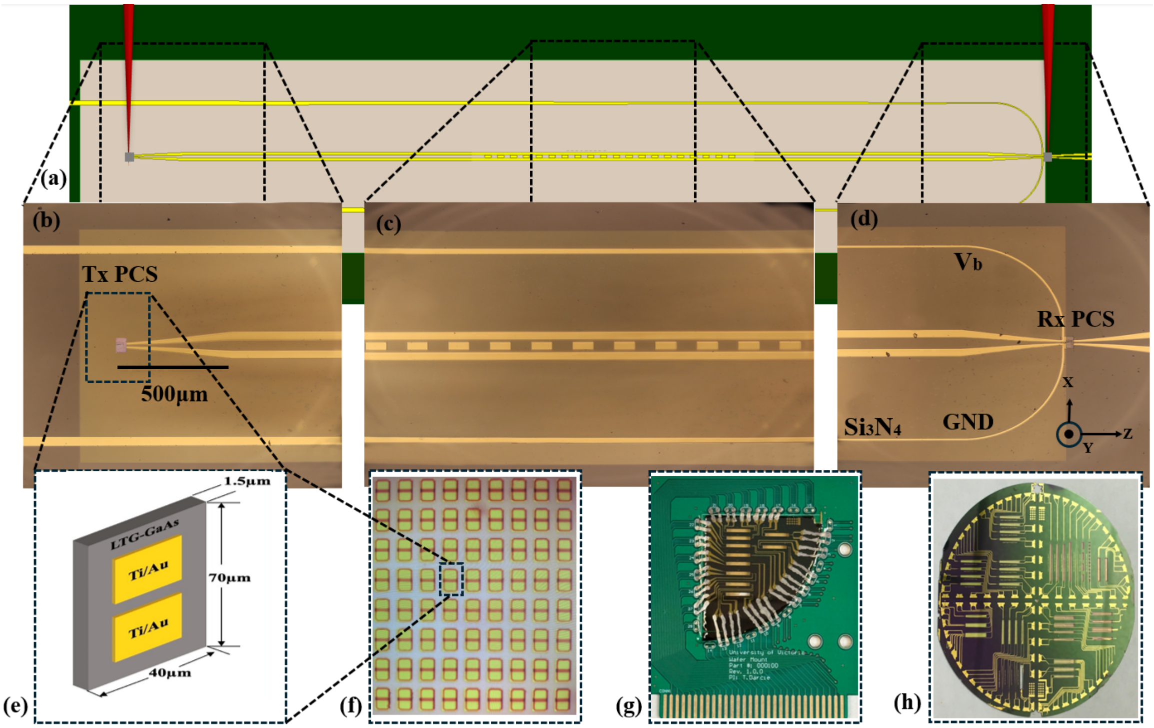

Figure 4.10: (a) The complete integrated system fabricated on a thin silicon nitride membrane. (b) The transmitter section, consisting of an LT-GaAs PCS, 200 nm thick gold CPS transmission line on a 1 µm silicon nitride layer. (c) A microscopic view of the periodic filter. (d) The receiver section, including the DC block and bias lines for the PCS and lock-in amplifier connection. (e) Thin films of LT-GaAs with dimensions of 40 µm × 70 µm × 1.8 µm, used in the PCS arrays. (f) The PCS arrays after fabrication, used in both transmitter and receiver sections. (g) A quarter wafer mounted on a PCB for alignment and connection to the measurement setup, ensuring precise signal transmission. (h) Fabricated circuits on the wafer before being diced into four quarters.

$-20\,\mathrm{dB/THz}$ on a semi-log scale, is attributed to the transient excitation and detection methods. This behavior is primarily influenced by the duration of the optical pulse duration and PCS carrier lifetime [108–110]. To aid in interpreting the results, we add the 20 dB/THz slope to the experimental data and plot it alongside the full-wave simulation results in Fig. 4.11(d). This slope is a characteristic of the transmitter and receiver; it does not mean that the filter exhibits a 20 dB/THz insertion loss. Applying the inverse slope correction to the spectral response flattens the spectrum to allow a better visual comparison against full-wave simulation ($|S_{21}|^2$). We find good relative agreement between the simulation and the experimental results, where the center frequency and bandwidth are in close agreement. We also observe the increased insertion loss above the stopband that is associated with diffractive grating radiation. The experimental bandwidth is also marginally wider than predicted, which probably originates from manufacturing differences.

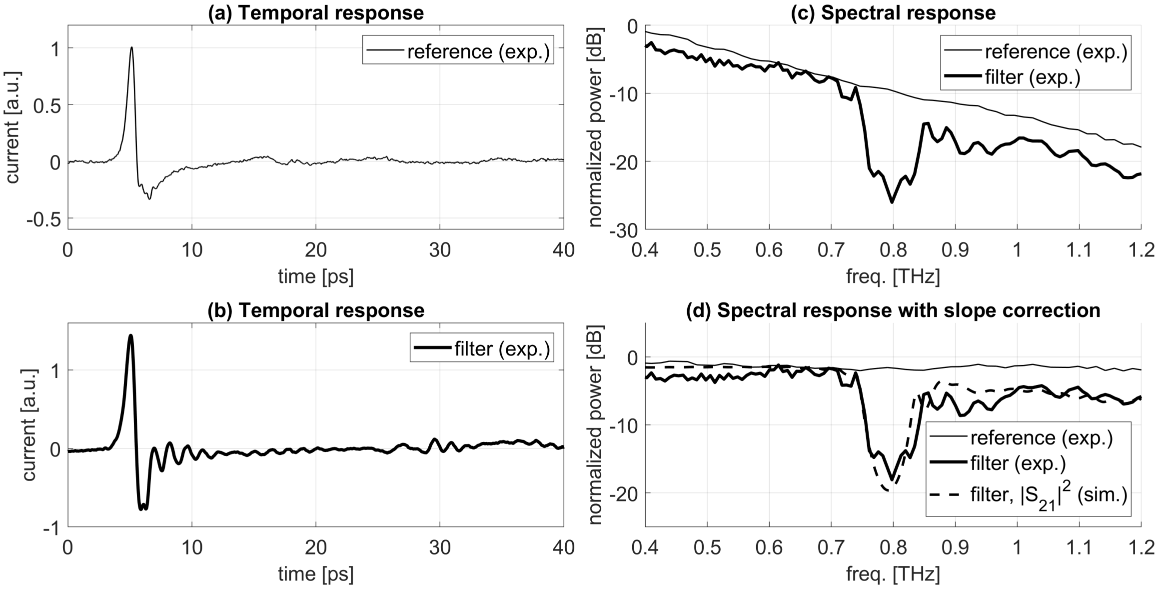

Figure 4.11: Experimental results. (a) Temporal response for a reference ($W_m = 0$ µm). (b) Temporal response for a periodic filter ($W_m = 45$ μm) spectrally normalized to the reference. (c) Spectral response for a reference and periodic filter obtained via DFT. (d) Spectral response with 20 dB/THz slope correction alongside a full-wave $|S_{21}|^2$ simulation results.

In summary, this work demonstrated a periodic band-stop filter based on alternating CPS and CPW sections. The filter exhibited a center frequency of $f_c = 0.8$ THz and bandwidth of $\Delta f \approx 0.1$ THz. The theory was based on cascading ABCD matrices that represented the CPS and the odd-mode of the CPW. The theory, simulation, and experiment are in agreement with each other.

4.3 Stepped-Impedance Low-pass Terahertz Filter (Appendix C)

Building on the success of previously demonstrated band stop filters, this study presents an investigation of the design, fabrication, and experimental validation of integrated planar LPFs operating at THz frequencies. Using established microwave filter synthesis methodologies, Bessel stepped-impedance LPFs with a cut-off frequency of 0.8 THz were systematically developed. The fabricated devices are experimentally characterized, confirming that planar filters operating at THz frequencies exhibit the anticipated filtering behavior with minimal pulse distortion. This work represents the first successful realization of an integrated planar all-pole network synthesis filter in the THz regime.

Here, we aim to demonstrate that microwave network synthesis methods for filter design remain valid at THz frequencies when applied to planar structures. Although many previous studies have successfully implemented filter synthesis at THz frequencies, they mainly focus on non-planar rectangular waveguide configurations [74,111,112]. These non-planar designs are more prevalent due to their compatibility with VNAs equipped with THz extension modules. However, such filters are typically restricted to band-pass operation because of the inherent mode propagation characteristics of rectangular waveguides.

Guided wave planar filters are made up of alternating transmission line sections, similar to those used in the previously discussed band stop filters [1,2]. The specific configuration, such as Butterworth, Bessel, or Chebyshev, determines the arrangement of these sections and the corresponding impedance profile required to achieve the desired frequency response. The design of a stepped-impedance filter relies on the appropriate selection of characteristic impedances for the high-impedance (Z_H) and low-impedance (Z_L) sections. The fundamental trade-off in impedance selection is between achieving a high impedance ratio (Z_H/Z_L), which improves filter roll-off, and maintaining practical fabrication constraints. The concept of a step-impedance filter is depicted in Fig. 4.12.

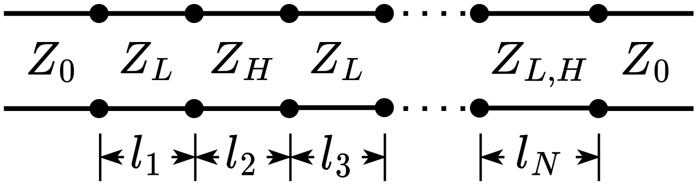

Figure 4.12: Stepped-impedance filter.

Bessel stepped-impedance LPFs have been selected for this proof of concept due to their advantageous properties, including a linear phase response and a compact physical footprint ($\approx 70\ \mu$m in length). The linear phase response results in minimal pulse distortion, which ensures that the transmitted pulse is not significantly broadened. Reducing pulse broadening enhances system performance by minimizing the impact of reflections and signal interference at the receiver, which ultimately improves spectral resolution.

The design specifications include a cutoff frequency of $f_c = 0.8$ THz, with filter orders of $N = 3, 4, 5$. Figure 4.13 illustrates the overall structure and the three different filters fabricated using the method discussed in Chapter 3. The feedline impedance, Z_0, was selected to correspond to a low-loss configuration ($\alpha \approx 0.8$ dB/mm [56]), which occurs when $S_0 = 70$ μm and $W_0 = 45$ μm.

For a stepped-impedance LPF, it is desirable to maximize the Z_H/Z_L ratio. However, the selection of Z_H and Z_L is constrained by fabrication limitations. To ensure consistency, the center-to-center spacing of the conductor $(S + W)$ is kept constant throughout the filter length. The minimum feature size is limited to 2 μm due to the resolution of the photolithography process. Given that $S_0 = 70$ μm and $W_0 = 45$ μm, the total spacing is $S + W = 115$ μm. Therefore, to meet the fabrication constraints, the following bounds must be satisfied: 2 μm $< S_{L,H} <$ 113 μm and 2 μm $< W_{L,H} <$ 113 μm.

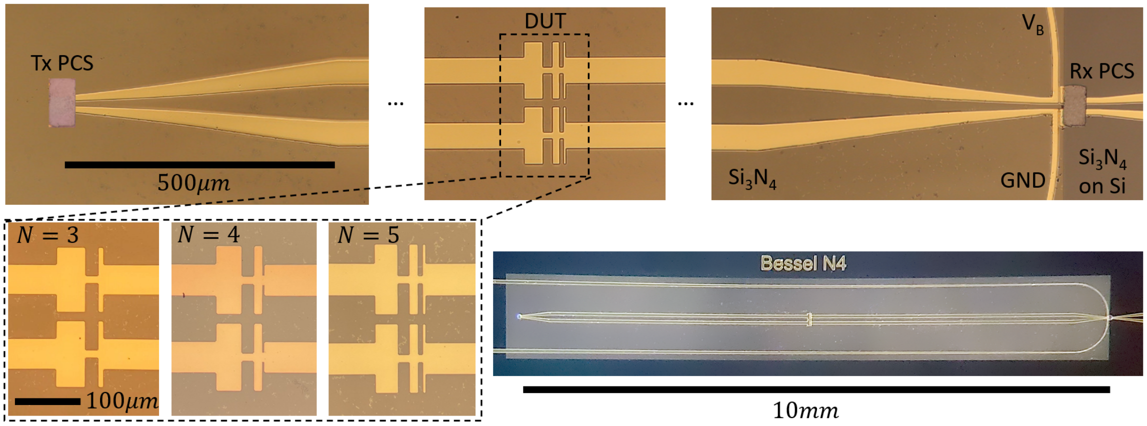

Figure 4.13: Microscope images of the TSoC structure with integrated filters.

Based on previous findings [7], where structures with a conductor width of $W = 10$ μm exhibited favorable performance with minimal resistive loss, we adopted this dimension for high-impedance sections in this design, setting $W_H = 10$ μm and $S_H = 105$ μm. For low-impedance sections, dielectric breakdown considerations are critical, as the CPS transmission line also serves as a DC biasing pathway for the transmitting PCS. To maintain effective DC biasing, the spacing S_L must exceed the transmitter gap $S_{Tx} = 10$ μm. Consequently, we selected $S_L = 15$ μm and $W_L = 100$ μm for this work.

Full-wave simulations performed using ANSYS HFSS determined the characteristic impedances as $Z_0 = 234\,\Omega$, $Z_L = 131\,\Omega$, and $Z_H = 362\,\Omega$. The next step is to compute the lengths of the individual impedance sections, following well-established synthesis techniques in [46].

In a stepped-impedance structure, alternating low- and high-impedance sections mimic a cascade of series inductors and shunt capacitors, forming a ladder network that exhibits low-pass filtering behavior. The lengths of these sections are given by:

$$l_{L,n} = \frac{g_n}{\beta_c}\frac{Z_L}{Z_0}, \qquad l_{H,n} = \frac{g_n}{\beta_c}\frac{Z_0}{Z_H}, \tag{4.10}$$

where $\beta_c = 2\pi f_c/c$, and g_n are filter element values. The filter element values, g_n, depend on the filter type (Bessel, Butterworth, Chebyshev, etc.) and order. For completeness, the element values are copied into Table 4.2 for the filters of interest [46]. The section lengths for the different filter orders are calculated using Eq. 4.10 and are summarized in Table 4.3.

Table 4.2: g_n for maximally flat time delay LPF prototype [46].

N	g_1	g_2	g_3	g_4	g_5	g_6
3	1.2550	0.5528	0.1922	1.0000	-	-
4	1.0598	0.5116	0.3181	0.1104	1.0000	-
5	0.9303	0.4577	0.3312	0.2090	0.0718	1.0000

Table 4.3: Section lengths for filters.

N	$l_1[\mu m]$	$l_2[\mu m]$	$l_3[\mu m]$	$l_4[\mu m]$	$l_5[\mu m]$
3	42	21	6	-	-
4	35	20	11	4	-
5	31	18	11	8	2

The same setup as shown in Fig. 3.2 was used to perform the THz-TDS measurements. Figure 4.14 presents the temporal and spectral responses measured experimentally for the filters depicted in Fig. 4.13. The temporal responses exhibit minimal pulse distortion, which aligns with the linear phase response of the designed filters. This characteristic is particularly beneficial for transient systems, where non-linear phase responses can introduce ringing effects that degrade the spectral resolution.

The spectral response is obtained by applying a DFT to the temporal data. Given that finite-duration transient pulses inherently lack a flat spectral profile, a natural roll-off is expected. This effect is illustrated by the dotted lines in Fig. 4.14, while the transition near the designed cutoff frequency of 0.8 THz is highlighted by the dashed lines. The exponential coefficients corresponding to these roll-off characteristics are provided in the figure legend. As anticipated, higher-order filters exhibit steeper attenuation, reflected in the increasing disparity between the exponential coefficients.

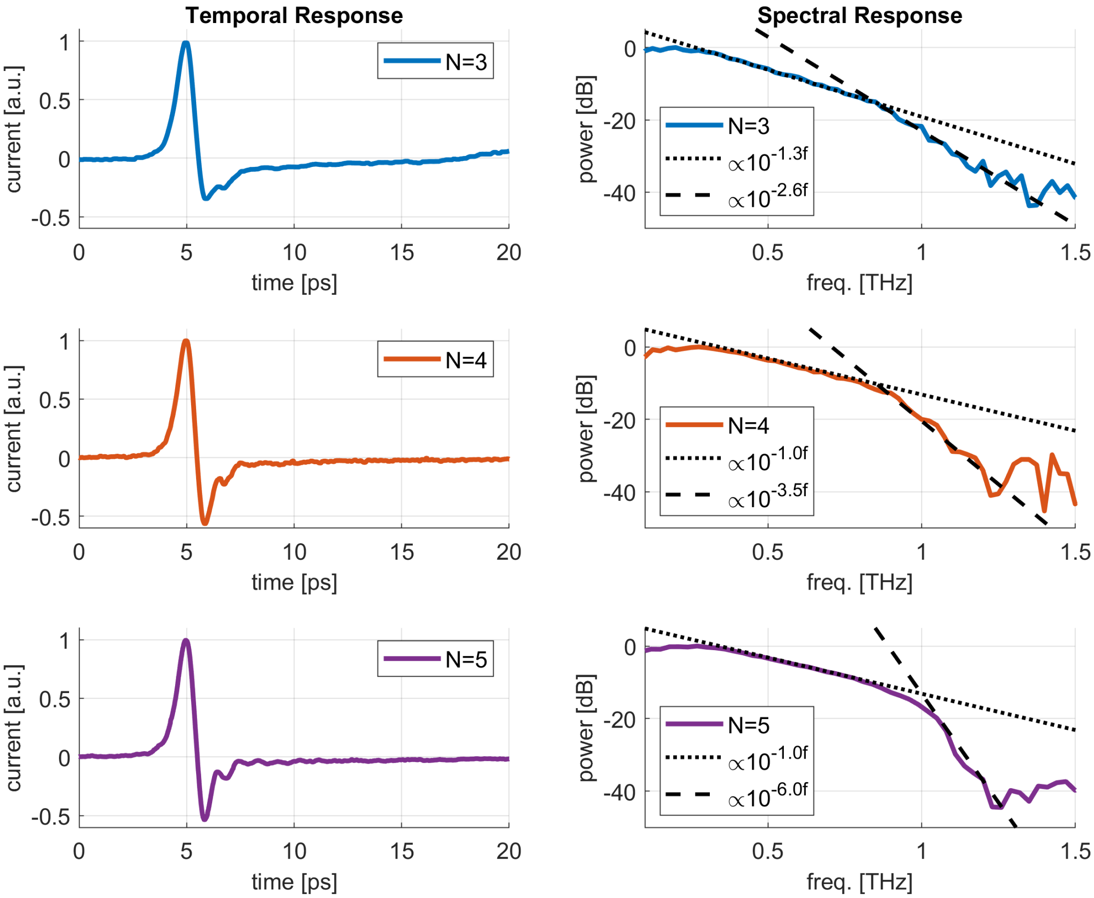

Figure 4.14: Experimental results for the N=3, 4, 5 Bessel filters.

In summary, this work presents the first experimental demonstration of a guided wave planar all-pole Bessel LPF at THz frequencies, designed using classical microwave network synthesis techniques. The filters were manufactured in a compact and integrated format and characterized using the TSoC platform. The excellent agreement between experimental results and theoretical predictions confirms the feasibility of extending network synthesis methodologies to planar structures in the THz regime. These LPFs were selected as a proof of concept, establishing a foundation for the development of more advanced planar synthesis-based filters in future THz systems.

4.4 Genetic Algorithm-Based Inverse Design of Guided Wave Planar Terahertz Filters

Our earlier investigations into THz filter design employed conventional methodologies, primarily based on analytical models and parameter sweeps. These approaches provided valuable insights into the behavior of filter geometries and served as a critical foundation for exploring compact and functional designs. Although they laid essential groundwork and advanced understanding of fundamental principles, they inherently lacked the adaptability required to address the increasingly complex and multi-objective optimization challenges posed by modern THz filter design. As performance demands for TSoC systems continued to increase, the need for a more flexible, automated, and powerful design framework became increasingly apparent.

An approach to overcome these limitations would be to exhaustively explore the entire design space to identify the globally optimal configuration. However, this strategy quickly becomes computationally intractable. For example, considering a binary pixel grid of size 50×100, the total number of possible configurations grows exponentially to $2^{50\times100}$ ($\approx 10^{1505}$), which far exceeds the capabilities of even the most advanced computing systems. This underscores the necessity of adopting intelligent optimization algorithms capable of efficiently navigating high-dimensional design spaces without exhaustive enumeration.

Motivated by the strengths and limitations observed in previous works, we developed a novel inverse design framework based on the genetic algorithm (GA) to address these challenges. This approach enables direct optimization of filter geometries with respect to specified electromagnetic performance metrics, thereby circumventing the rigid constraints imposed by traditional design methodologies. By formulating the synthesis process as an evolutionary search, the GA efficiently explores complex, high-dimensional design spaces to discover solutions that are both high-performing and structurally non-intuitive.

This framework has yielded significant improvements over conventional methods, producing GA-optimized designs with enhanced rejection depths, tunable bandwidths, and precise spectral control at flexible center frequencies. Integration with CPS transmission lines ensures fabrication compatibility and seamless monolithic integration within planar TSoC platforms.

Although inverse design methodologies have been successfully applied to various THz components—such as metasurfaces [81–83], absorbers [84], and antennas [85]—the efficient design of planar THz filters integrated with CPS transmission lines remains largely unexplored. Addressing this gap, we present a GA-based inverse design framework specifically tailored for planar TSoC filters.

To ensure computational feasibility, filter performance is evaluated using the ABCD matrix method, which offers substantial acceleration compared to full-wave simulations while maintaining sufficient modeling accuracy. The final validation of the optimized designs is performed through FEM simulations. As a proof-of-concept, we demonstrate the inverse design of band-stop filters with varying center frequencies and rejection depths, all within a fixed device footprint. To our knowledge, this is the first application of a GA-based inverse design approach based on GA that employs the ABCD matrix method for CPS-integrated THz filters, highlighting its potential for advancing compact, fabrication-ready devices in integrated THz systems.

The GA is well suited for the inverse design of complex electromagnetic structures due to its robustness in non-convex, high-dimensional design spaces and its independence from gradient computations [87]. In this work, we employ a GA to optimize the binary distribution of gold and air pixels in a planar THz filter, with each candidate encoded as a chromosome representing the spatial layout. These candidates evolve through selection, crossover, and mutation, with the GA parameters carefully tuned to address the discrete and high-dimensional nature of the problem.

Figure 5.6 presents the flow diagram of the GA optimization process that we used to design THz filters. The process begins with a randomly generated initial population of filters, each associated with its corresponding S-parameters, including both magnitude and phase. As the algorithm progresses, iteratively refines the population across successive generations based on performance feedback (fitness function). This evolutionary process enables the development of optimized THz filters that satisfy the specified design criteria.

To ensure compatibility with our THz test platform, a connectivity constraint is enforced in the design formulation to maintain structural continuity for the voltage biasing of the transmitter PCS. Each candidate solution is encoded as a binary matrix representing the spatial layout of gold and air pixels, with a pixel size of

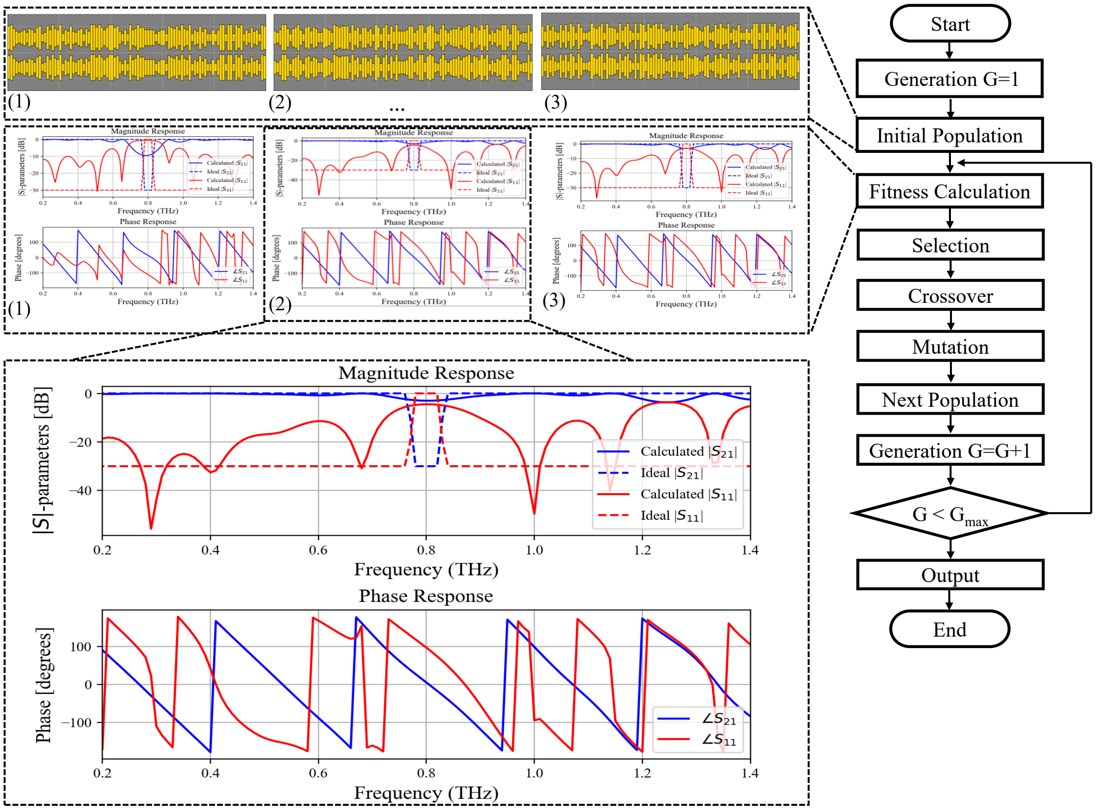

Figure 4.15: Flowchart of the GA optimization process. The randomly generated initial population of THz filters is depicted, along with their corresponding S-parameters (both magnitude and phase). The algorithm iterates through successive generations, refining the population until one of two stopping criteria is met: (1) the number of generations G reaches the predefined maximum G_{max}, or (2) the error function converges below a specified threshold.

4 μm × 10 μm to balance resolution, fabrication feasibility and computational cost. This binary structure is input to the GA, which evolves the population to maximize a fitness function that measures how well the simulated S parameters match the response of the target filter.

Figure 4.16 illustrates the design framework and key structural parameters of the planar THz filter investigated in this work. The filter region spans an area of 300 μm in width and 2000 μm in length, corresponding to 200 discrete columns along the propagation direction. This discretized domain serves as the optimization space for the GA-based inverse design process, wherein the binary configuration of each column defines the local characteristic impedance profile of the filter.

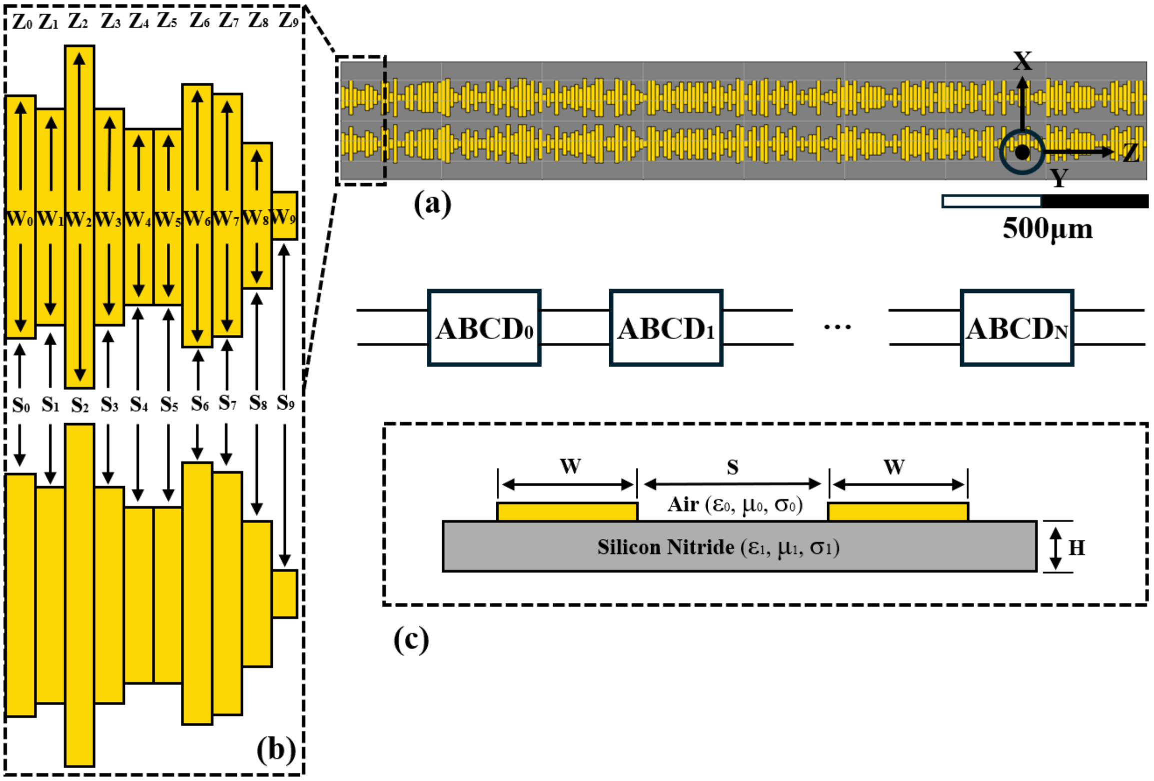

Figure 4.16: Illustration of the design framework and associated parameters. (a) Example of a planar THz filter structure synthesized using a GA-based inverse design approach. The overall framework dimensions are 300 μm × 2000 μm, corresponding to 200 discrete columns in the propagation direction. (b) Magnified view of a section of the filter. (c) Cross-sectional schematic of the filter structure.

A magnified view of a representative section is shown in Fig. 4.16(b). In the design space explored, the conductor width (W) varies between 10 μm and 90 μm, while the strip spacing (S) ranges from 5 μm to 90 μm, ensuring compatibility with the fabrication constraints and impedance requirements. Figure 4.16(c) presents a cross-sectional schematic of the filter and the metallic gold layer patterned on a silicon nitride membrane substrate. This material platform ensures compatibility with standard microfabrication processes while minimizing substrate losses at THz frequencies.

After initializing the population, each candidate design is evaluated using the fitness function. The fitness function quantifies performance by calculating the root-mean-square error (RMSE) between the simulated and target scattering parameters S-parameters), incorporating both magnitude and phase.

Formally, the fitness function $f(\mathbf{x}_i^t) : \mathbb{R}^n \to \mathbb{R}$ maps design parameters $\mathbf{x}_i^t$ at iteration t to a scalar score reflecting spectral deviation. The loss function $\mathcal{L} =$

−RMSE guiding optimization is expressed as:

$$\begin{aligned}\mathcal{L} =& w_1\sqrt{\frac{1}{N}\sum_{i=1}^{N}(S_{21}^{\text{dB}}(f_i) - S_{21,\text{target}}^{\text{dB}}(f_i))^2} + w_2\sqrt{\frac{1}{N}\sum_{i=1}^{N}(S_{11}^{\text{dB}}(f_i) - S_{11,\text{target}}^{\text{dB}}(f_i))^2} \\ &+ w_3\sqrt{\frac{1}{N}\sum_{i=1}^{N}(\angle S_{11}(f_i) - \angle S_{11,\text{target}}(f_i))^2} + w_4\sqrt{\frac{1}{N}\sum_{i=1}^{N}(\angle S_{21}(f_i) - \angle S_{21,\text{target}}(f_i))^2}\end{aligned} \tag{4.11}$$

where N is the number of frequency points, and w_1, w_2, w_3, w_4 are weighting factors for magnitude and phase components of transmission (S_{21}) and reflection (S_{11}) responses. This formulation enables precise, frequency-aware tuning of THz filter designs through genetic optimization.

This work targets a linear phase response, assigning w_3 and w_4 to 10% of the loss function weight. Consequently, early optimization focuses on minimizing magnitude-related terms (w_1 and w_2), while phase error becomes more influential in later stages as the algorithm refines differential phase variations.

A population size of 200 was chosen to balance the quality of the solution and the runtime, as larger sizes offered marginal gains with a higher computational cost. Each generation evolves through elitism, rank-based tournament selection, crossover, and mutation. The top 15% of the individuals (30 candidates) are preserved through elitism, an empirically tuned fraction that maintains diversity while avoiding premature convergence. Elite rates above 20% caused stagnation, while those below 10% hindered the speed of convergence.

The remaining 170 individuals are generated using genetic operators, with parent selection based on a probabilistic rank-based tournament method [113, 114]. This approach promotes diversity while favoring fitter solutions. A tournament size of $T = 4$, recommended in the literature for moderate selection pressure [87, 113], was adopted. Smaller T values slowed convergence, while larger ones reduced diversity.

Crossover is used as a recombination operator to generate new solutions by merging structural features from two parent individuals. For grid-based THz filter design, a two-point crossover strategy enables the creation of novel geometries while preserving connectivity and material constraints. Given parent grids P_1 and P_2, two crossover points c_1 and c_2 are randomly chosen such that $2 \leq c_1 < c_2 \leq C - 1$, where C is the total number of columns. Two offspring, O_1 and O_2, are produced by exchanging column segments between c_1 and c_2.

$$O_1 = [P_1(:, 1 : c_1), P_2(:, c_1 : c_2), P_1(:, c_2 : C)] \tag{4.12}$$

$$O_2 = [P_2(:, 1 : c_1), P_1(:, c_1 : c_2), P_2(:, c_2 : C)] \tag{4.13}$$

Here, $P(:, a : b)$ denotes the submatrix containing columns a to b.

To enhance diversity, the mutation is applied to 10% of the selected individuals. Each mutation flips a randomly chosen bit in the binary chromosome, toggling a pixel between gold and air, introducing stochastic variations into the population. This promotes exploration of the design space while all mutations respect the continuity constraint, ensuring uninterrupted conductive pathways for compatibility with the CPS platform.

To evaluate S-parameters and compute Root Mean Squared Error (RMSE), two methods are available: (1) the analytical ABCD transmission matrix method, and (2) full-wave numerical simulations using tools such as ANSYS HFSS. Due to the high computational cost of FEM-based simulations, the ABCD method was adopted as an efficient surrogate model. Offering a speed-up of over three orders of magnitude, it enables rapid candidate evaluation during optimization while maintaining sufficient accuracy. Its validity has been supported by strong agreement with experimental data in previous studies [52].

The designed filters consist of cascaded unit cells, each modeled as a transmission line segment with a defined characteristic impedance. These cells are arranged laterally, and each column in the design grid represents one unit. Each cell is represented by a two-port ABCD matrix. This approach assumes uniform transmission line behavior, which holds under the quasistatic regime, where unit cell dimensions are much smaller than the operating wavelength.

The ABCD matrix of a transmission line segment of length Λ, characteristic impedance Z, and phase constant β is given by:

$$\begin{bmatrix} A_{\text{cell}} & B_{\text{cell}} \\ C_{\text{cell}} & D_{\text{cell}} \end{bmatrix} = \begin{bmatrix} \cos(\beta\Lambda) & jZ\sin(\beta\Lambda) \\ j\frac{1}{Z}\sin(\beta\Lambda) & \cos(\beta\Lambda) \end{bmatrix} \tag{4.14}$$

The overall ABCD matrix for a filter composed of N cascaded unit cells is obtained by sequentially multiplying the individual ABCD matrices corresponding to each unit cell.

The quasistatic characteristic impedance of each section is computed analytically based on its lateral geometry, including the conductor width W and the inner strip spacing S, using the closed-form expression for CPS transmission lines in Eq. 4.6 [105]. Finally, the scattering parameters (S-parameters) are extracted from the total ABCD matrix using standard transformations in Eq. 4.9.

This modeling framework enables rapid and reasonably accurate prediction of the electromagnetic response of cascaded THz filters, making it well-suited for evaluating the fitness of a large number of candidate structures during the inverse design process, particularly in the early optimization stages, where full-wave simulations would be computationally prohibitive.

Figure 4.17 illustrates the spectral response and geometry of a planar band stop filter designed using the proposed GA-based inverse framework. The target specifications are a center frequency of 0.8 THz and a 3-dB bandwidth of 200 GHz. In Fig. 4.17(a), the calculated S_{21} and S_{11} magnitude responses from the ABCD matrix method closely match the target, meeting the desired rejection and bandwidth. Figure 4.17(b) shows the corresponding phase response, highlighting the linear phase progression of S_{21}, essential for dispersion-sensitive THz applications.

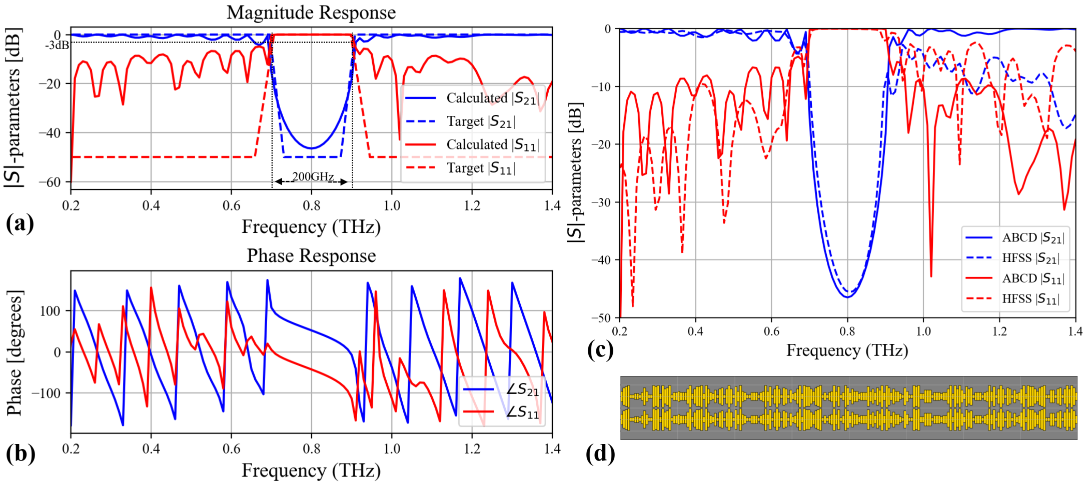

Figure 4.17: (a) Magnitude response of the optimized planar band-stop filter's S-parameters (S_{21} and S_{11}) via the ABCD method, compared to the target (3-dB bandwidth: 200 GHz, target rejection: -50 dB; achieved: -46 dB). (b) Phase response, highlighting the linear phase of S_{21} across the passband. (c) Comparison between ABCD predictions and HFSS simulations, showing strong agreement. (d) Final filter geometry generated.

A comparison between ABCD-based and full-wave HFSS results is shown in

Fig. 4.17(c), demonstrating strong agreement across most of the frequency range. However, minor discrepancies emerge at higher frequencies (above 0.9 THz), where the ABCD matrix method begins to diverge from the HFSS simulation. These deviations are primarily attributed to radiation losses and edge diffraction effects that are not captured by the quasi-static assumptions inherent in the ABCD matrix model. Finally, Fig. 4.17(d) displays the non-intuitive filter geometry generated by the GA, showcasing its ability to synthesize high-performance designs within fabrication constraints.

To further investigate the electromagnetic behavior of the optimized filter structure, we analyze the electric field distribution at multiple frequencies that span the passband and stopband. Figure 4.18(a) shows the simulated in-plane E-field profiles at 0.6 THz, 0.8 THz, and 1.0 THz. At 0.6 THz and 1.0 THz, the field propagates effectively through the structure, confirming the low insertion loss in the passbands. In contrast, at 0.8 THz—corresponding to the filter's stopband, strong field attenuation is observed, demonstrating effective suppression of transmission and validating the spectral selectivity of the inverse-designed filter.

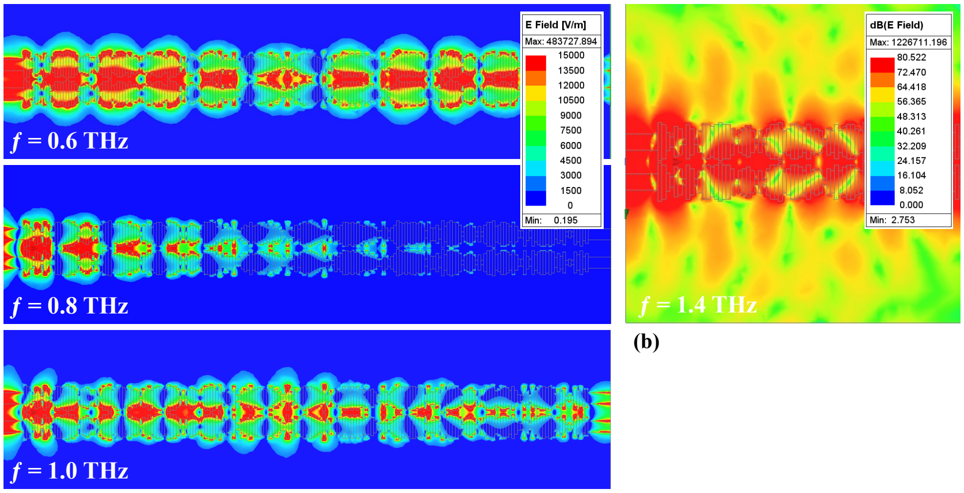

(a)

(b)

Figure 4.18: (a) Electric field distribution of the inverse-designed planar band-stop filter at 0.6 THz, 0.8 THz, and 1.0 THz. The filter exhibits strong suppression in the stopband (0.8 THz) and effective transmission in the passbands (0.6 THz and 1.0 THz), validating its spectral selectivity. (b) Logarithmic-scale field profile at 1.4 THz, illustrating radiation losses at higher frequencies due to edge diffraction and imperfect confinement, particularly from the conductor edges.

Figure 4.18(b) presents the field profile at 1.4 THz on a logarithmic scale to highlight radiation effects at higher frequencies. The simulation reveals radiation leakage originating from the edges of the metallic conductors, attributed to diffraction at frequencies beyond the designed stopband.

Figure 4.19 illustrates the evolutionary optimization process over multiple generations. The initial generation consists of randomly generated structures that are progressively refined as the algorithm minimizes the error function. After 120 generations, the optimization converges to a design that matches the desired band stop filter response, as evidenced by the corresponding S-parameters.

Generation	Filter Structure	RMSE
G = 0	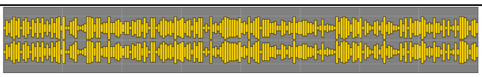	13.46
G = 1	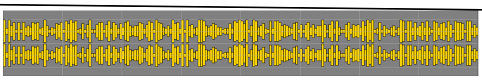	13.19
G = 2	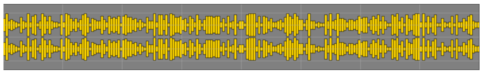	12.54
G = 10	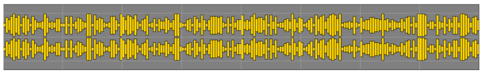	9.20
G = 120	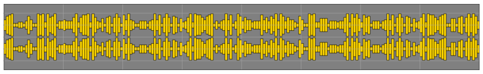	5.91

Figure 4.19: Evolutionary optimization of the planar THz band-stop filter. Starting from a random initial structure, the GA iteratively refines the design over 120 generations to converge to the target filter response.

To evaluate the capabilities of the proposed inverse design framework, two sets of design objectives were explored while maintaining a fixed device footprint of 2000 µm. The first set assessed the framework's ability to control rejection depth without changing physical dimensions. Specifically, band-stop filters centered at 0.8 THz with a fixed 3-dB bandwidth of 70 GHz were synthesized to achieve rejection depths of 10, 20, and 30 dB. This task benchmarks the algorithm's precision in tailoring stopband depth through internal geometry optimization.

Figure 4.20(a) shows the simulated S-parameters for the three designs, confirming the flexibility and effectiveness of the framework. Guided by the RMSE-based fitness function, the GA successfully generated nonintuitive structures that meet the target rejection levels. Compared to conventional Bragg grating filters with similar spectral performance [1,2], the GA-based designs achieve superior rejection (-30 dB vs. -18 dB) and reduce device length by $\approx$ 50%.

In the second set of designs, we evaluated the framework's ability to achieve center frequency tunability while maintaining the same physical footprint. Band-stop filters centered at 0.6 THz, 0.8 THz, and 1.0 THz, each with a 3-dB bandwidth of 150 GHz, were synthesized. This test highlights the adaptability of the framework to target different spectral responses without altering the dimensions of the device.

The simulated S-parameters, shown in Fig. 4.20(b), demonstrate successful tuning across a wide frequency range. The results confirm that the framework can generate distinct filter geometries for various center frequencies while preserving footprint constraints. This flexibility underscores the potential of the system for designing customized THz filters tailored to diverse applications on integrated platforms.

The comparison between the results obtained from the ABCD matrix method and full-wave electromagnetic simulations is presented in each figure. The two approaches exhibit strong agreement with minimal divergence across and below the operational bandwidth.

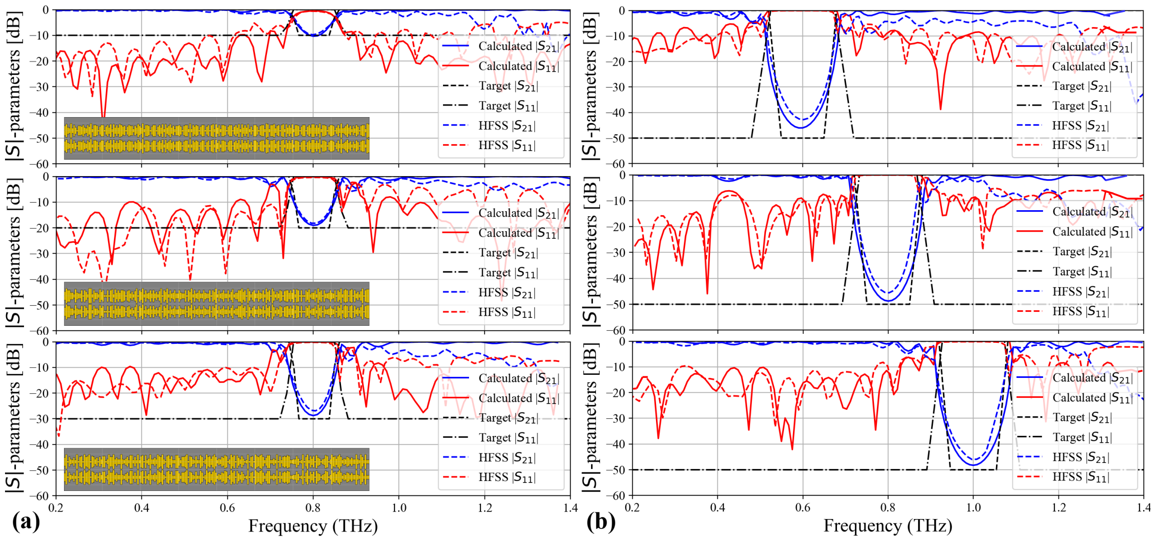

Figure 4.20: (a) Comparison of S-parameters of band-stop filters designed through the GA with different rejection depths centered at 0.8 THz, all within the same device footprint. (b) Comparison of S-parameters of band-stop filters designed through the GA targeting center frequencies of 0.6 THz, 0.8 THz, and 1.0 THz, respectively, all synthesized within the same structural framework and footprint.

Integrating the ABCD matrix method into the GA-based inverse design framework offered a significant computational advantage, enabling rapid evaluation of candidate filter structures. Each optimization run, 120 generations with a population of 200, completed in 40 minutes on an Intel i7-10700 CPU. In contrast, a single HFSS full-wave simulation (with $\Delta S = 0.02$ in 130 frequency points) took more than two hours, making large-scale optimization impractical without a surrogate model. The ABCD method thus enabled broad design space exploration and facilitated the discovery of non-intuitive high-performance filters compatible with CPS-integrated platforms.

Convergence analysis was performed to assess the stability of the framework. As shown in Fig. 4.21, the algorithm was executed ten times with different random seeds to examine sensitivity to initial population variation. Figure 4.21(a) plots the best fitness per generation for each run. The close overlap of fitness curves demonstrates consistent convergence behavior and low inter-run variability.

Figure 4.21(b) summarizes the statistical convergence behavior. The solid blue curve shows the best average fitness in ten runs, while the shaded region represents the ±1 standard deviation. The curve shows a rapid improvement in fitness within the first 40 to 50 generations, followed by gradual refinement, with the convergence typically achieved between generations 100 and 120. The consistently narrow standard deviation—below 3 dB in the final S_{21} response—indicates high repeatability and stable convergence.

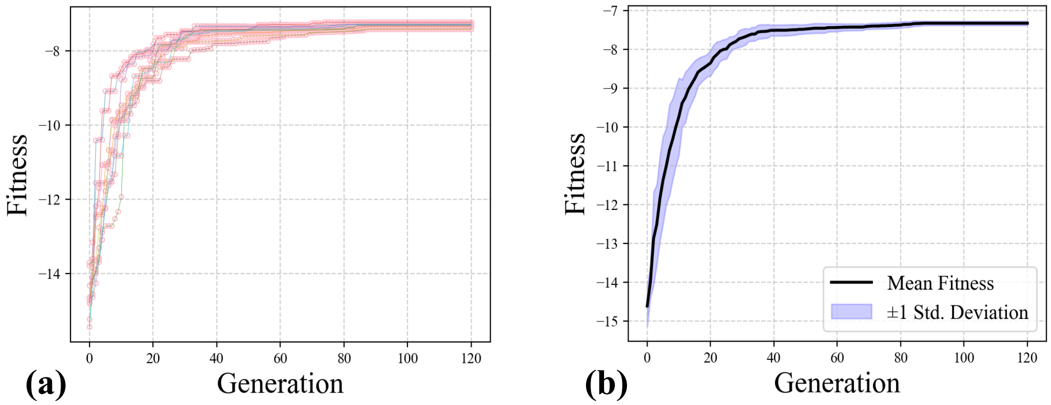

Figure 4.21: Convergence of the GA-based inverse design over 10 independent runs with different random seeds. (a) Ring markers show the best fitness per generation for each run. (b) Solid blue curve shows the average best fitness; the shaded area indicates ±1 standard deviation. Results confirm consistent convergence, low variance, and robustness to initial population variation.

Beyond conventional parameter sweep-based methods, the proposed approach enables automated, efficient, and flexible synthesis of THz filters by iteratively refining candidate solutions in non-convex high-dimensional design spaces. The adaptability of the framework allows it to accommodate diverse design objectives, including varying center frequencies, rejection depths, and impedance matching requirements, making it a promising tool for next-generation TSoC components. Future extensions will expand the framework's applicability to other planar devices such as couplers, reflectors, and absorbers.

Chapter 5

Conclusions and future works

5.1 Conclusions

This dissertation has successfully addressed the design, simulation, and experimental validation of planar terahertz (THz) filters, focusing on key challenges of signal propagation, high implementation costs, and integration complexity inherent to conventional free-space THz systems. The presented works demonstrate the viability of the Terahertz System-on-Chip (TSoC) platform for integrated THz filter design by leveraging impedance-engineered coplanar striplines (CPSs) to enable efficient and selective frequency control.

The study investigated and experimentally validated a range of THz filters, including band-stop apodized Bragg gratings (TABG), a planar multimodal tunable periodic filter, and low-pass planar all-pole network filters based on stepped-impedance Bessel designs of orders 3, 4, and 5. Experimental characterization using Terahertz Time-Domain Spectroscopy (THz-TDS) confirmed the effectiveness of these designs, with measured results closely matching simulation data.

Furthermore, a key contribution of this research is the development of an inverse design methodology based on a Genetic Algorithm (GA), allowing efficient exploration of the design space for optimal THz filter characteristics. The adaptability of the framework allows it to accommodate diverse design objectives, including varying center frequencies, rejection depths, and impedance matching requirements, making it a promising tool for next-generation TSoC components. This approach not only improves the filter design process, but also establishes a foundation for the automated synthesis of other THz components, such as couplers, multiplexers, and power

Table 5.1: Summary of principal contributions to planar THz filter design

Ref.	**Title / Methodology**	**Filter Type**	**Center/ Cutoff Frequency**	**Bandwidth**	**Key Contributions**
[1]	**THz Apodized Bragg Grating (TABG)**	Band-stop	0.8 THz	200 GHz	First on-chip demonstration of planar TABG integrated into a TSoC; achieved ≈20 dB rejection experimentally; strong agreement with simulation and theory.
[2]	**Multimodal Planar Periodic Filter**	Band-stop	0.8 THz	70 GHz	Planar multimodal periodic filter with alternating CPS and finite-ground CPW; proof-of-concept for tunable THz filtering; validated by theory, simulation, and measurement
[3]	**Planar All-Pole Network Synthesis Filters**	Low-pass (Bessel)	0.8 THz	0.8 THz	First planar THz all-pole filters via network synthesis; fabricated orders $N = 3$, 4, 5; tunable roll-off, minimal distortion; strong theoretical agreement; among most compact THz LPFs reported
[4]	**GA-Based Inverse Design Framework**	Band-stop (Tunable)	0.6 / 0.8 / 1.0 THz	150 GHz (Tunable)	Developed a GA-based framework for synthesizing THz filters; efficient optimization using ABCD method; validated by FEM; non-intuitive structure; demonstrated footprint-invariant tunability.

dividers.

In summary, this research advances the understanding and implementation of integrated THz filters within the TSoC framework. The proposed designs and optimization techniques, as summarized in Table 5.1, establish robust and scalable solutions for the realization of efficient and cost-effective THz systems. The findings of this dissertation offer a solid foundation for the continued exploration of compact planar filters using both classical and modern filter design techniques. Future work can build on these contributions by refining the proposed techniques, bridging them to industrial applications, and extending them to a broader class of components, with the aim of further enhancing the performance and versatility of integrated THz technologies.

5.2 Future Works

Future research may explore new filter configurations using both classical and advanced optimization techniques. On the classical side, one promising direction involves enhancing the Bessel filter response by integrating Butterworth synthesis, potentially combining the desirable group delay characteristics of Bessel filters with the sharper roll-off of Butterworth designs. From a modern perspective, the genetic algorithm-based inverse design framework presented in [4] can be further strengthened through integration with adjoint-based gradient optimization. This hybrid approach could offer improved design efficiency and robustness, leveraging the global search capabilities of evolutionary methods alongside the precision of gradient-based techniques.

Beyond filter design, the proposed methodologies may also support the translation of additional silicon photonic components—such as couplers, reflectors, and demultiplexers—into the THz domain. Such efforts would expand the functional scope of THz systems and enable the development of increasingly compact, versatile, and high-performance TSoC architectures.

5.2.1 Investigate Stepped-Impedance Low-Pass Terahertz Butterworth Filters

Building upon the demonstrated success of prior work on Bessel filters [3], this study advances the design and simulation of third-, fourth-, and fifth-order Butterworth filters using a stepped-impedance architecture. The selection of Butterworth filters is justified by their maximally flat passband response, which minimizes amplitude ripple and promotes spectral uniformity. In contrast to Bessel filters, which emphasize linear phase response to reduce signal distortion, Butterworth filters offer a favorable trade-off between spectral selectivity and amplitude flatness—making them advantageous for applications requiring precise magnitude control over the passband.

The design methodology parallels that of Bessel filters, with targeted modifications to achieve the desired Butterworth characteristics. Key design variables include the length and width of the stepped-impedance sections, which are systematically optimized. Figure 5.1 presents the geometry of the designed low-pass Butterworth filters.

The geometric parameters illustrated in Figure 5.1 are calculated using Eq. 4.10 and summarized in Table 5.2. The design of THz Butterworth filters involves selecting both the filter order and the desired cutoff frequency (e.g., $f_c = 0.6$ THz, guided by target application bandwidths). The filter order governs the steepness of the roll-off and the number of poles in the transfer function, directly influencing the filter's selectivity and transition characteristics.

Higher-order Butterworth filters offer enhanced frequency selectivity due to their steeper roll-off, a result of additional reactive elements that sharpen the transition band while preserving passband flatness. However, the increased number of

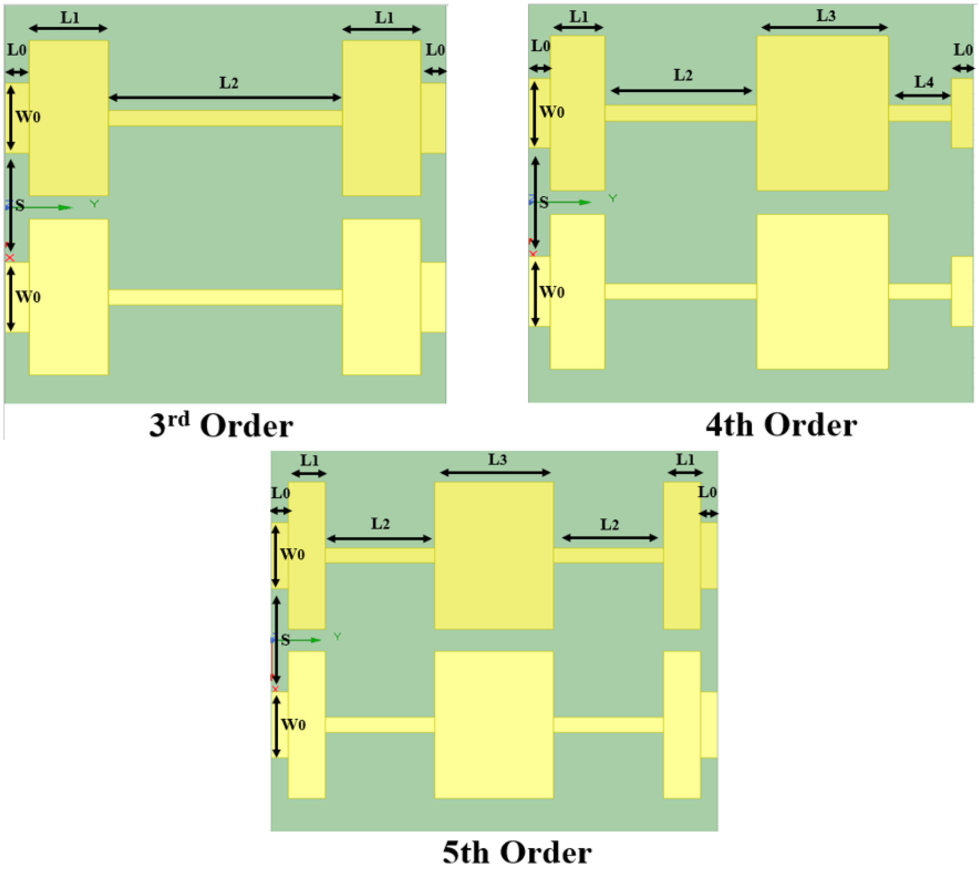

Figure 5.1: Geometrical layouts of third-, fourth-, and fifth-order THz Butterworth filters based on stepped-impedance transmission lines.

Table 5.2: Lengths of Sections for THz Butterworth Filters (all dimensions in μm).

Order	L_1	L_2	L_3	L_4	L_0	W_0	W_H	W_L	S
3	34.52	78.80	34.52	-	20	45	10	100	70
4	26.42	72.80	63.80	30.15	20	45	10	100	70
5	21.33	63.75	69.00	-	20	45	10	100	70

impedance transitions introduces higher insertion loss, highlighting a trade-off between spectral selectivity and practical realizability. Figure 5.2 illustrates how the characteristic impedance varies with section width in the stepped-impedance configuration, providing critical guidance for impedance matching and section dimensioning in the filter design process.

With the design parameters defined for each filter order, full-wave electromagnetic simulations were performed using ANSYS HFSS to extract the corresponding

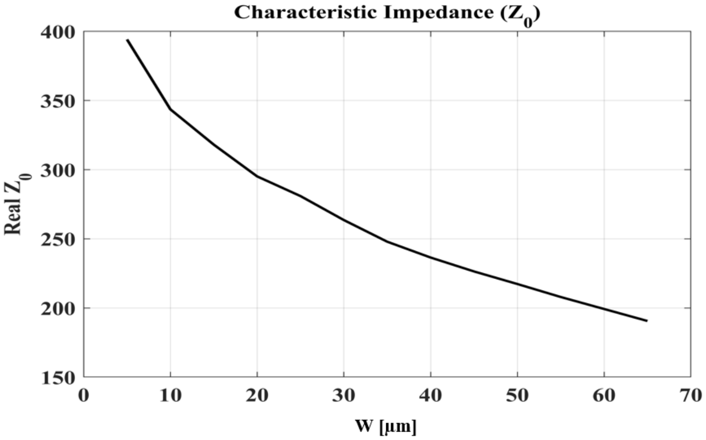

Figure 5.2: Characteristic impedance of the stepped-impedance Butterworth filter

S-parameters. The results, shown in Figure 5.3, enable a comparative evaluation of transmission characteristics across different filter orders.

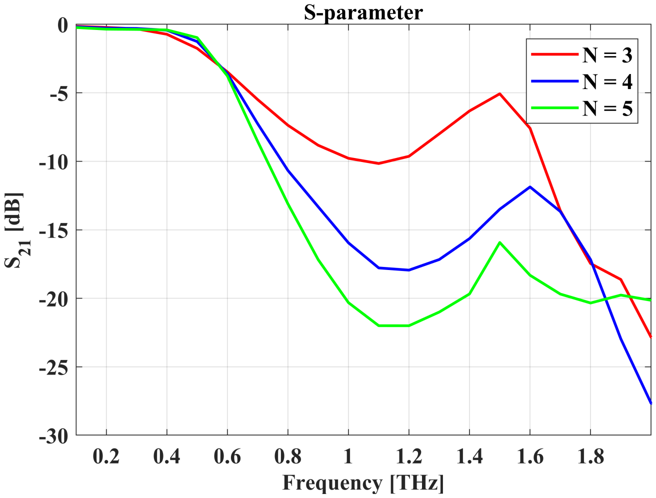

Figure 5.3: Simulated transmission coefficient (S_{21}) of the THz Butterworth filters for filter orders $N = 3, 4, 5$.

To gain a deeper understanding of wave propagation within the structures, E-field simulations were conducted, with the results for the 3rd order filter presented in Fig. 5.4 at various frequencies (100 GHz, 500 GHz, 1 THz, and 2 THz). The observations indicate that at higher frequencies beyond the passband, a significant portion of the waves is reflected or scattered by the structures.

A critical future step is the experimental validation of the simulated results. Their transmission responses—including insertion loss, roll-off rate, and stopband attenua-

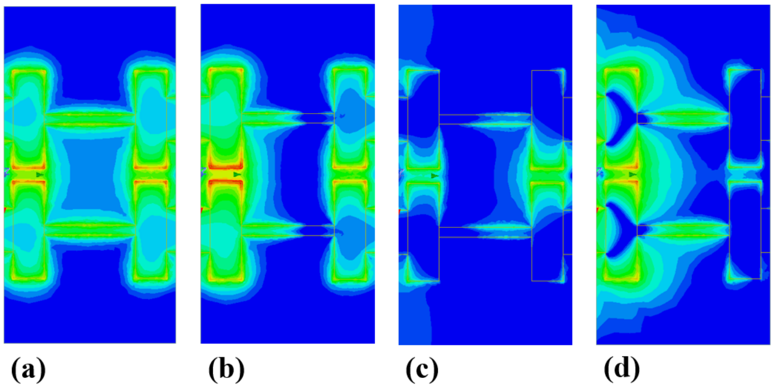

Figure 5.4: Electric field propagation of Butterworth filter (N = 3): (a) at 100 GHz (b) at 500 GHz (c) at 1 THz (d) at 2 THz

tion—will be compared with simulation results to evaluate the accuracy of the numerical model. This comparison will provide valuable insights into real-world performance, validate the robustness of the design methodology, and guide further refinement as part of future research.

5.2.2 Effects of Apodization in Terahertz Multimodal Band-Stop Filter

This section presents a complementary analysis that extends the original work in [2], outlining potential future directions. As demonstrated in the TABG design, similar apodization strategies can be applied to the periodic filter discussed in this work to suppress side lobes in the reflection spectrum. These side lobes arise from abrupt variations in grating strength, governed by changes in effective refractive index (or, equivalently, impedance). To mitigate this effect, a gradual tapering of impedance can be introduced through apodization, facilitating smoother mode transitions.

Figure 5.5 illustrates the designed structure. In our initial approach, a linear apodization function was used, where the width of the central conductor (W_m) was progressively increased symmetrically from both sides of the structure in increments of 2.5 μm. A detailed summary of the structure's key parameters and their corresponding values is presented in Table 5.3.

S	W	W_{m1}	W_{m2}	W_{m3}	W_{m4}	W_{m5}	W_{m6}	W_{m7}	W_{m8}	W_{m9}	W_{m10}
70	45	30	32.5	35	37.5	40	42.5	45	47.5	50	52.5

Table 5.3: Updated design parameters and dimensions corresponding to Fig. 5.5.

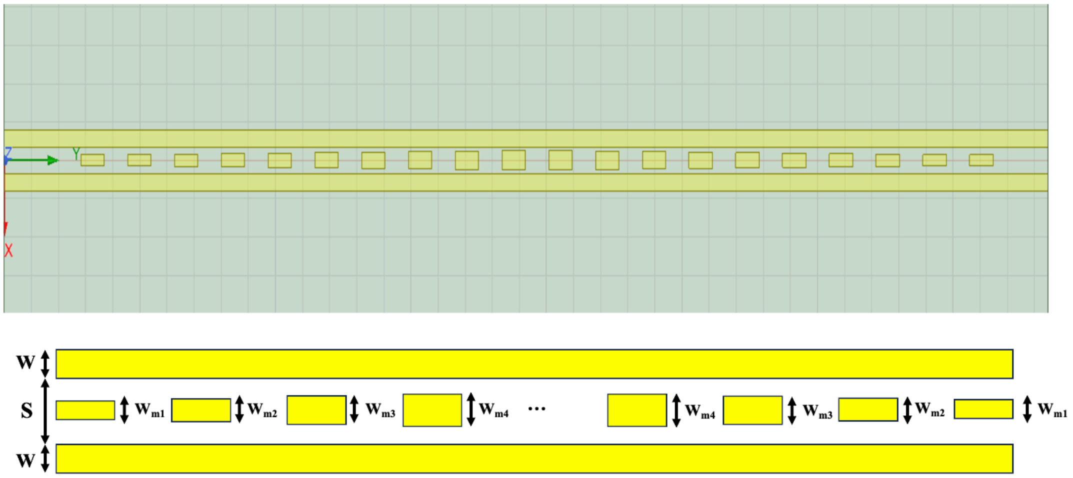

Figure 5.5: The updated band-stop multimodal design based on the linear apodization function and its parameters.

Figure 5.6 compares the simulated S-parameters of the original structure and its apodized counterpart. Although the apodized structure exhibits a slightly reduced rejection depth at the central frequency, it continues to provide effective attenuation within the stopband. Notably, the apodized configuration demonstrates improved radiation characteristics at higher frequencies, indicating its potential for enhanced broadband spectral performance. Future work will involve the fabrication and experimental characterization of apodized structures with varying apodization profiles, followed by experimental characterization and comparative evaluation.

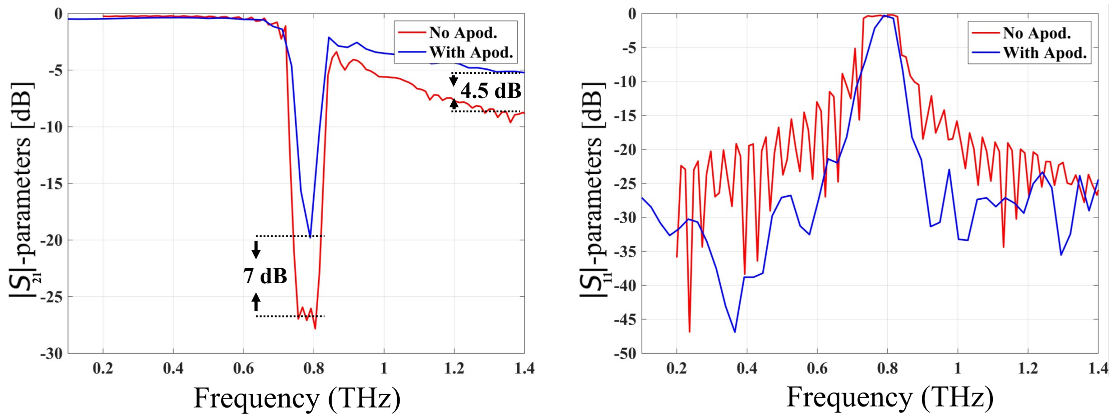

Figure 5.6: S_{21} and S_{11} at the load of the structure with and without apodization sections.

5.2.3 Hybrid Genetic and Adjoint Inverse Filter Design

The next step in the inverse design process involves incorporating a more advanced optimization technique—the adjoint method—as previously demonstrated in the context of nanophotonic device optimization [78, 115, 116]. This approach computes sensitivity gradients efficiently, enabling rapid convergence toward optimal designs with significantly reduced computational cost compared to traditional methods. Unlike brute-force techniques, which require multiple simulations per design variable, the adjoint method calculates all necessary objective function gradients using only two simulations, making it especially effective for high-dimensional design problems [117]. Such efficiency is particularly beneficial for refining complex THz filter architectures involving high-resolution grids or stringent performance constraints.

However, a key limitation of the adjoint method is its sensitivity to the initial design. As a local gradient-based technique, its optimization outcome strongly depends on the starting point and may lead to suboptimal solutions if poorly initialized. To overcome this limitation, we propose a hybrid strategy: first, employ a GA—extending previous work in [4]—to explore the global design space and identify a promising configuration. Once a satisfactory preliminary design is achieved, the adjoint method can be applied to tune the structure and reach the final optimized solution.

Beyond conventional filter synthesis, this approach may also support the inverse design of novel THz components, including waveguide bends, demultiplexers, and compact couplers. As an example, Figure 5.7 presents a possible initial demultiplexer design, which can first be optimized using the developed GA and subsequently refined through adjoint-based optimization. The structure can be excited via CPS feedlines operating over a 0.1–2 THz frequency range, enabling frequency separation tailored to application-specific requirements—analogous to similar inverse designs in nanophotonics [78, 116].

Future research will focus on implementing the adjoint method within the existing inverse design framework, systematically validating its effectiveness through numerical simulations, and ultimately fabricating and experimentally characterizing the optimized structures. The potential for integrating this method into the current TSoC platform should also be thoroughly explored.

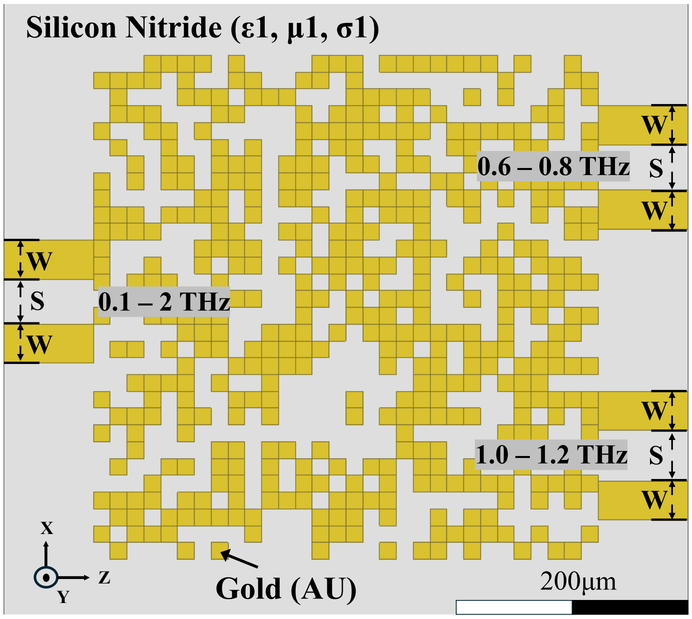

Figure 5.7: Initial presentation of a potential THz demultiplexer structure. This design can first undergo global optimization using a GA, followed by local refinement via the adjoint method. The structure is intended to operate within the 0.1–2 THz range and is excited using CPS feedlines, enabling frequency-selective functionality.

Appendix A

Demonstration of an Integrated Terahertz Band-Stop Filter Using an Apodized Bragg Grating, Copy of [1]

Research Article Vol. 31, No. 20 / 25 Sep 2023 / Optics Express 32582

Optics EXPRESS

Demonstration of an Integrated terahertz band-stop filter using an apodized Bragg grating

ALI DEHGHANIAN,[1,2] WALID GOMAA,[3] MOHSEN HAGHIGHAT,[1,2] THOMAS DARCIE,[1] AND LEVI SMITH[1,2,*]

[1] *Department of Electrical and Computer Engineering, University of Victoria, Victoria, BC, V8P 5C2, Canada*
[2] *Centre for Advanced Materials and Related Technology (CAMTEC), University of Victoria, 3800 Finnerty Rd., Victoria, BC, V8P 5C2, Canada*
[3] *Department of Engineering Physics, Military Technical College, Cairo, Egypt*
[*] *levismith@uvic.ca*

Abstract: This paper presents the demonstration of an on-chip integrated terahertz (THz) apodized Bragg grating (TABG) which functions as band-stop filter with a center frequency of 0.8 THz and a bandwidth of 200 GHz. For experimentation, we integrate the TABG into our THz system-on-chip to enable wideband (DC - 1.5 THz) device characterization. Using this methodology, we measure the signal transmission through the TABG and find the experimental results align with simulation and theory provides a rejection of approximately 20 dB across the stop-band.

© 2023 Optica Publishing Group under the terms of the Optica Open Access Publishing Agreement

1. Introduction

The terahertz (THz) gap spanning from 0.1 to 10 THz has garnered considerable attention because of its unique capabilities across various fields such as communication, sensing, imaging, and spectroscopy [1–6]. However, the progress in developing terahertz devices and systems has been challenging due to the absence of integrated system components such as transmitters, communication channels, receivers, and other passive devices such as filters. Band-stop filters play a crucial role in many applications because they enable the suppression of undesired frequencies within a specific spectral range. At frequencies above 500 GHz, there are limited experimental results for planar guided-wave band-stop filters [7], but there are a few key examples: in [7], the authors demonstrate a band-stop filter with a center frequency of 0.6 THz and a −3dB bandwidth of ≈160 GHz using a single conductor Goubau line loaded with capacitivly-coupled $\lambda/2$ resonators. This filter behaves well; however, Goubau-lines can be limiting when developing an integrated system because the single conductor is incompatible with two-terminal elements without necessitating a mode converter. Next, others have developed THz band-stop filters using a dielectric Bragg grating with a center frequency of 0.31 THz and a −3dB bandwidth of ≈20 GHz [8]. Again, their filter works well, but, as with most non-transverse electromagnetic (TEM) waveguides, the finite single-mode bandwidth can lead to dispersion in a wideband system. Next, in our prior work we loaded a transmission line (TL) with split-ring resonator (SRR) elements [9]. Using this method we created a band-stop filter which possessed a center frequency of 0.51 THz and a −3dB bandwidth of ≈100 GHz. These SRR filters are useful, but the design procedure is not systematic, the filter roll-off rates are sub-optimal, and higher-order resonator modes must be considered [9]. Lastly, we note that there are several non-planar guided-wave Bragg gratings which have been demonstrated. In [10], a corrugated circular waveguide was used as a Bragg grating which obtained a center frequency of 0.14 THz and a −3dB bandwidth of ≈9 GHz. In [11], a two-wire waveguide was periodically etched to fabricate the grating which achieved a center frequency of 0.53 THz and the −3dB bandwidth was ≈1 GHz.

#502363 https://doi.org/10.1364/OE.502363
Journal © 2023 Received 3 Aug 2023; revised 30 Aug 2023; accepted 6 Sep 2023; published 14 Sep 2023

This work expands upon the aforementioned list of THz band-stop filters by performing the experimental demonstration of an integrated terahertz apodized Bragg grating (TABG) proposed in [12]. Previously the TABG was analyzed via simulations, but no experimental results were presented. Also, we compliment the theory by adding periodic filter concepts from microwave engineering. The TABG was inspired by apodized fiber Bragg gratings (FBGs) found in optical communication systems which consist of alternating refractive indices (and wave impedance) along the propagation direction. FBGs experience detrimental side-lobes in the reflection spectrum which are proportional to the FBG strength (difference of refractive indices). The magnitude of the side-lobes can be reduced by gradually tapering the FBG strength with an apodization profile. The TABG analogously has a periodic modulation of the characteristic impedance and similarly benefits from gradual tapering of the grating strength.

To characterize the TABG we use our integrated THz system-on-chip (TSoC) platform which combines the THz transmitter, device-under-test (i.e., TABG), and THz receiver onto a single wafer. The TSoC platform consists of planar circuitry which is lithographically defined on an ultra-thin (1 μm) Si_3N_4 substrate to ensure signals exhibit low loss and low dispersion at THz frequencies. The ultra-thin substrate is a key requirement to perform wideband measurements otherwise radiation loss into the substrate becomes very problematic. We have used the TSoC platform in previous works to investigate several other THz components such as split-ring resonators [9], low-pass filters [13], tapers [14], and power dividers [15]. Overall, we have found the results from TSoC experiments to closely align with simulation and theory, thus we expect our experimental methodology to be suitable for investigating the TABG.

This work contains several novel aspects. First, we demonstrate a fully integrated (transmitter, feedlines, TABG, receiver) on-chip apodized Bragg filter in the THz gap. Second, we demonstrate the highest Bragg frequency achieved within the THz gap using a quasi-TEM feedlines on an ultra-thin Si_3N_4 membrane. Third, we verify that the theory for periodic filter is applicable to THz grating design. Lastly, we illustrate the radiative loss mechanism for frequencies above the Bragg bandgap for a CPS grating.

2. Design

In this paper, we perform the experimental verification of the TABG shown in Fig. 1 [12]. Specifically, we focus on a TABG where the stop-band is centered at f_c = 0.8 THz. The filter consists of N = 12 unit cell sections and 4 apodization sections which provide a gradual change in geometry and characteristic impedance between the feedlines and the grating unit cells. Fig. 2 illustrates an annotated portion of the TABG. The TABG response is defined by the reflections caused by characteristic impedance discontinuities along the grating. Thus knowledge of the characteristic impedance of each section is necessary to predict the filter response. In this work, the characteristic impedance of each section is obtained by performing full-wave simulations using ANSYS HFSS at 0.8 THz to ensure accurate values which include the impact of the thin Si_3N_4 substrate. Table 1 tabulates the dimensions and simulated characteristic impedances of each section. Next, the grating period, Λ, required to obtain a specified center frequency, f_c, is calculated using:

$$\Lambda = \frac{c}{2 f_c \sqrt{\varepsilon_{re}}}, \tag{1}$$

where c is the speed of light, ε_{re} is the effective relative permittivity of the propagating mode. Again, from simulation (ANSYS HFSS), we have found $\varepsilon_{re} \approx 1.3$ for the TABG CPS configuration, then using (1), we find $\Lambda = 165$ μm. Next, the fractional bandwidth, $\Delta f / f_c$, is dependent on the characteristic impedance of adjacent cells and is calculated by [16]:

$$\frac{\Delta f}{f_c} = \frac{4}{\pi} \sin^{-1}\left(\frac{Z_{n+1} - Z_n}{Z_{n+1} + Z_n}\right). \tag{2}$$

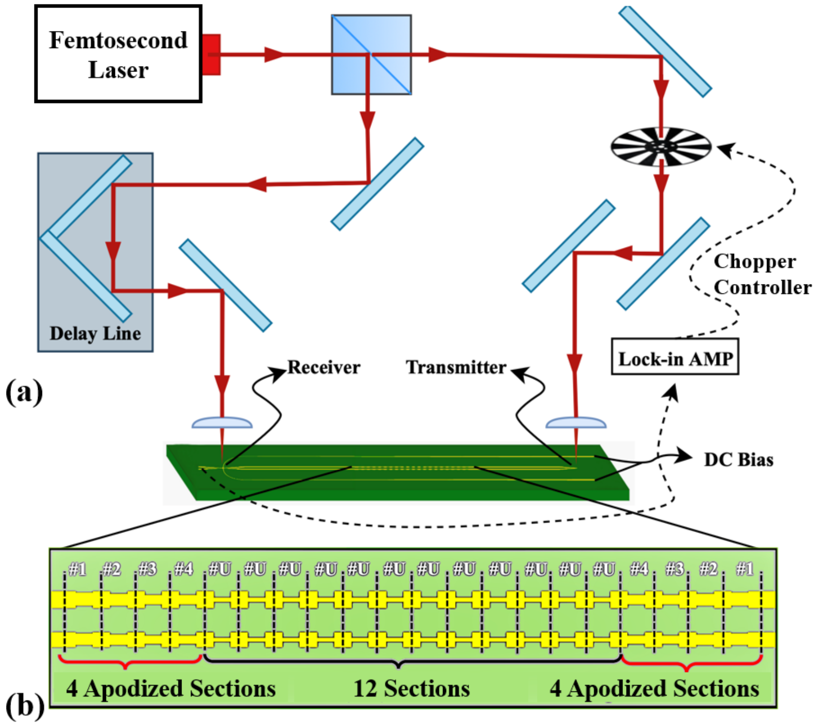

Fig. 1. The experimental setup and TABG. (a) The optical path of the transmitter is modulated by the optical chopper, while the receiver beam passes through an optical delay line. The transmitter has a DC bias applied (24V), and the receiver is connected to a lock-in amplifier. The bias lines for the transmitter and receiver are separated by a gap that blocks DC signals. (b) illustrates the TABG filter and its distinct sections.

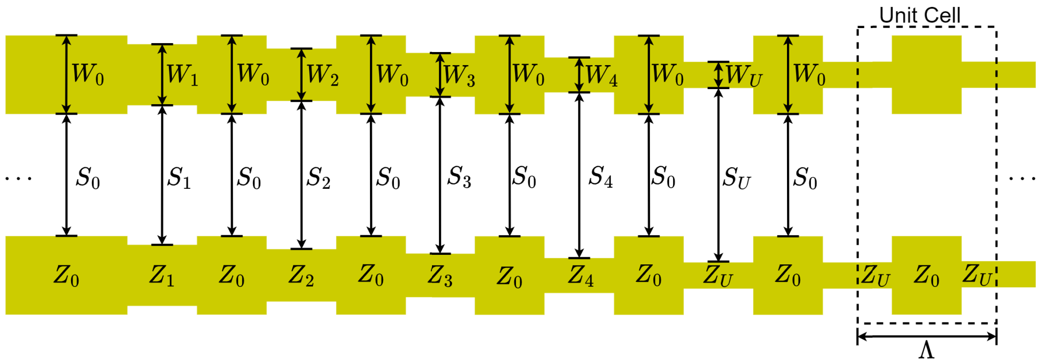

Fig. 2. Apodization sections and grating unit cell where $\Lambda = 165\mu m$. Dimensions and characteristic impedances are found in Table 1.

Using (2), with Z_0 and Z_U (Table 1), we find $\Delta f = 0.18$ THz.

Table 1. TABG dimensions and characteristic impedances for Fig. 2

n	0	1	2	3	4	U
W_n [μm]	45	35	30	25	20	15
S_n [μm]	70	80	85	90	95	100
Z_n [Ω]	234	260	274	290	311	332

3. Theory

In microwave engineering, the Bragg filter of [12] is commonly referred to as a periodic filter which can be described by a dispersion diagram and Bloch impedance [17]. To calculate these quantities we construct an ABCD matrix of the unit cell depicted in Fig. 2 as:

$$\begin{bmatrix} A & B \\ C & D \end{bmatrix} = \begin{bmatrix} \cos\beta\Lambda/4 & jZ_U\sin\beta\Lambda/4 \\ jY_U\sin\beta\Lambda/4 & \cos\beta\Lambda/4 \end{bmatrix} \cdot \begin{bmatrix} \cos\beta\Lambda/2 & jZ_0\sin\beta\Lambda/2 \\ jY_0\sin\beta\Lambda/2 & \cos\beta\Lambda/2 \end{bmatrix} \cdot \begin{bmatrix} \cos\beta\Lambda/4 & jZ_U\sin\beta\Lambda/4 \\ jY_U\sin\beta\Lambda/4 & \cos\beta\Lambda/4 \end{bmatrix}, \tag{3}$$

where $\beta = \omega\sqrt{\varepsilon_{re}}/c$ is the propagation constant.

After constructing the ABCD matrix we can obtain the dispersion diagram and Bloch impedance. The dispersion diagram is calculated using $\beta\Lambda = \mathrm{Imag}\{\cosh^{-1}[(A+D)/2]\}$ and the result is plotted in Fig. 3. This figure illustrates the stopband associated with the infinite periodic structure. We find that the filter has a center frequency at $f_c = 0.8$ THz and a bandwidth of $\Delta f \approx 0.18$ THz which is in agreement with (2). Next, we calculate the Bloch impedance using $Z_B = B/\sqrt{A^2 - 1}$ and then calculate the reflection coefficient between an infinite periodic filter and a load impedance from:

$$\Gamma = \frac{Z_L - Z_B}{Z_L + Z_B}. \tag{4}$$

We use (4) to illustrate the impact of apodization. If we negate the apodization sections, then $Z_L = Z_0$ which will result in a mismatch causing a less desirable reflection spectrum. Alternatively,

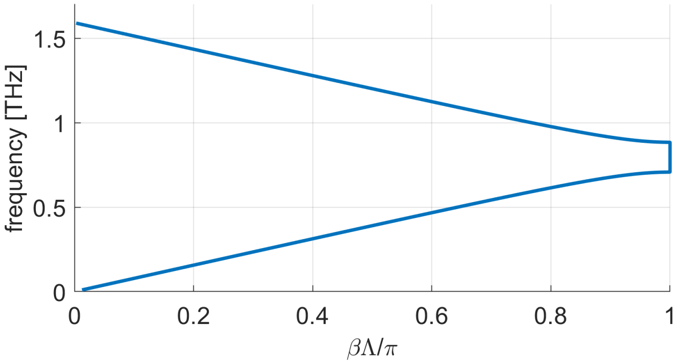

Fig. 3. Dispersion diagram for the TABG.

if we add an apodization section then we can significantly improve the matching and reduce the reflections. We model apodization section by cascading 4 ABCD matrices to represent each apodization cell in Fig. 2. The result of this procedure is plotted in Fig. 4 where we see the introduction of apodization sections improves the reflection response of the filter and we expect to see a sharp roll-off at the band-edge of the transmitted signal in our experimental results.

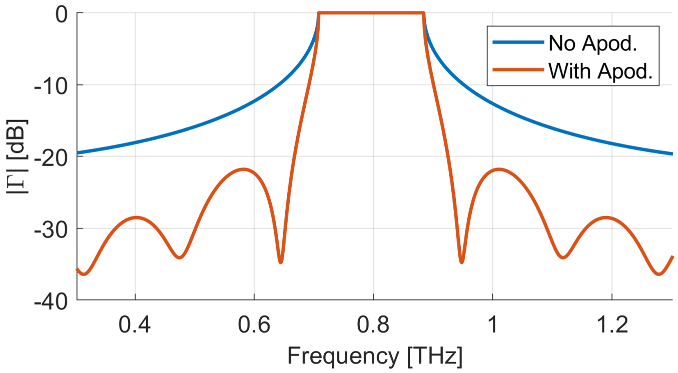

Fig. 4. Reflection coefficient at the load of the TABG with and without an apodization section.

4. Simulation

A full-wave frequency domain simulation was performed using ANSYS HFSS to characterize the scattering parameters of the TABG (Fig. 5). In the simulation, the material parameters are given by $\varepsilon_r = 7.6$, $\sigma_{Si_3N_4} = 0$, $\mu_r = 1$, $\tan\delta_e = 0.00526$ for the Si_3N_4 substrate [18] and $\sigma_{Au} = 4.1 \times 10^7$ S/m for the gold conductors. All geometric parameters are the same as the fabricated device (see Fig. 2 and Table 1). The simulated center frequency was found to be $f_c = 0.815$ THz and the -3 dB bandwidth was found to be 0.22 THz which illustrates reasonable agreement between theory and simulation. We do not expect perfect agreement between Fig. 4 ($|\Gamma|$) and Fig. 5 ($|S_{11}|$) because the reflection coefficient of (4) calculates the reflection between an infinite periodic structure and a constant load impedance, whereas the simulation accounts for the finite length grating and the frequency-dependent characteristic impedance. The insertion loss below the Bragg regime is less than 2 dB, whereas above the Bragg regime, the insertion loss increases

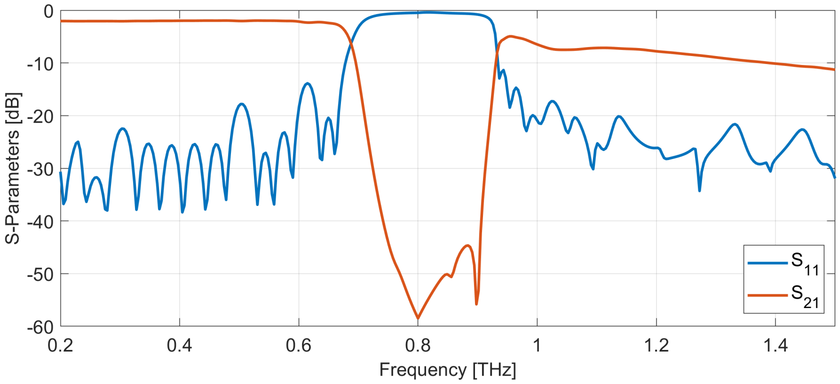

Fig. 5. Simulated S-Parameters. $f_c = 0.815$ THz and the -3 dB bandwidth is 0.22 THz.

from 5 dB at 0.95 THz up-to 11 dB at 1.5 THz. The increased insertion loss originates from diffractive grating radiation [19]. This effect is discussed and illustrated in Appendix A.

5. Methods

To perform the experimental characterization of the TABG we use a modified THz time-domain spectroscopy (THz-TDS) setup as shown in Fig. 1(a). An optical pulse train is generated by a 780 nm, 20 mW, 80 femtosecond laser and then is divided into two beams that are directed towards the transmitter and receiver photoconductive switches (PCSs) which are thin films of low-temperature grown gallium arsenide (LT-GaAs) measuring 70 µm×40 µm×1.8 µm. The procedure to fabricate a grid of PCS's is described in [13,20]. For the transmitter, the optical beam passes through a optical chopper before being focused onto the PCS. The receiver beam passes through a mechanical delay line before getting focused onto the PCS. The transmitter has a bias voltage applied (24V) and the receiver is connected to a lock-in amplifier. Translation of the mechanical delay line and measurement of the lock-in amplifier current reconstructs a signal proportional to the transmission characteristics of the TABG.

Figure 6(a) illustrates the transmitter which is placed on top of a lithographically-defined gold CPS TL situated on a thin Si_3N_4 layer. The TABG (Fig. 6) was fabricated from a Silicon wafer with a 1 μm Si_3N_4 layer deposited via low pressure chemical vapor deposition (LPCVD). The suspended Si_3N_4 regions were fabricated using photlithographic masking and wet-etching (potassium hydroxide). The conductors (10/200 nm Ti/Au) were patterned using photolithography and physical vapor deposition (e-beam). We use a thin Si_3N_4 membrane as the substrate to enable the transmission of sub-picosecond pulses over centimeter-scale distances. If a thicker substrate were used, radiation from the substrate would cause significant losses and dispersion [21]. We have successfully used this method in several other works [9,13–15]. After the transmitter PCS, we taper the CPS TL to achieve a wider cross-section (W = 45 µm and S = 70 µm) which has lower attenuation [14]. In Fig. 6(b), the TABG structure is displayed under a microscope. Figure 6(c) portrays the receiver section, which comprises of a DC block, DC bias lines for the Tx PCS, and bias lines to connect the Rx PCS to the lock-in amplifier.

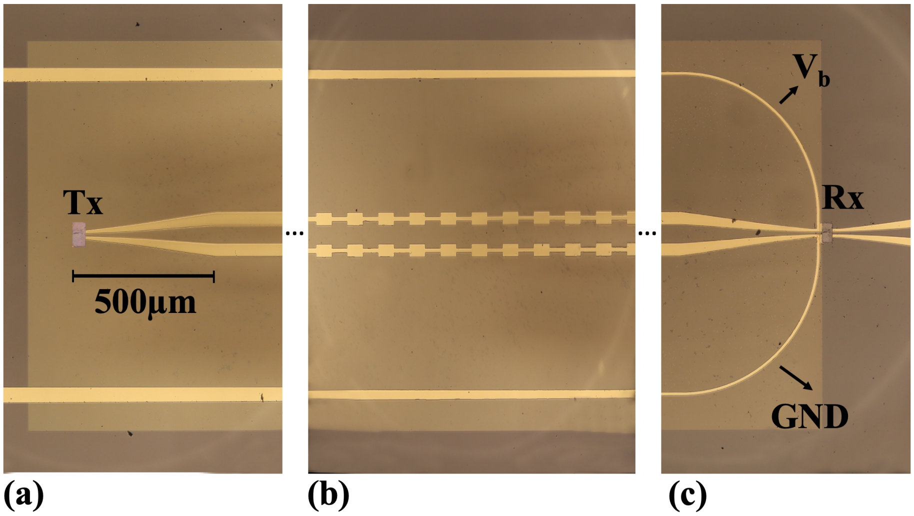

Fig. 6. TSoC with TABG. (a) illustrates a LT-GaAs PCS (Tx) on a gold TL on a 1µm-thin Si_3N_4 membrane. In (b), the TABG is displayed. (c) shows the LT-GaAs PCS receiver (Rx), coupling section, and the DC bias lines - V_b and ground (GND).

6. Results and discussion

Figure 7(a-b) plot the simulated and experimental temporal response of the received THz-bandwidth pulse after propagating through the TABG. Figure 7(c) plots the spectral response obtained by applying the discrete Fourier transform (DFT) to the temporal response. We also include a reference trace which corresponds to a simulation without a TABG. First, we note that the spectral roll-off associated with both the simulation and experiment is an expected consequence of a finite duration time-domain pulse. The maximum measurement frequency is defined to occur when the spectral dynamic range (SDR) becomes zero [22]. The maximum SDR for our measurement system is ≈60 dB and decreases towards zero as the frequency increases. Referring to Fig. 7(c), this implies that the maximum measurement frequency corresponds to the frequency associated with the normalized power reaching −60 dB which occurs near ≈1.5 THz. Next, we observe good agreement between experiment and simulation which is observed by comparing the stop-band center frequency and bandwidth. We do notice a discrepancy in the stop-band rejection. For the experiment the rejection is ≈30 dB, whereas for simulation it is ≈45 dB. The difference originates from a few different mechanisms. First, our photolithographic fabrication process is limited to a feature size of ≈2 μm, and thus there will not be perfect agreement between the simulated dimensions and the fabricated dimensions. Next, the material parameters will differ between simulation and experiment. While we expect the material parameters to be close, they will not match the fabricated device and will result in differences. Also, it is possible that another unexpected mode coupled across the filter experiencing less attenuation. Lastly, we explain a discrepancy temporal response. The simulation does not use a DC blocking capacitor, and thus it contains a DC component. The experiment requires a DC block, and therefore we observe the derivative behavior (high-pass filtering). Note that the cut-off frequency is below our frequencies of interest (0.2 THz) and it is not observed in the spectral response.

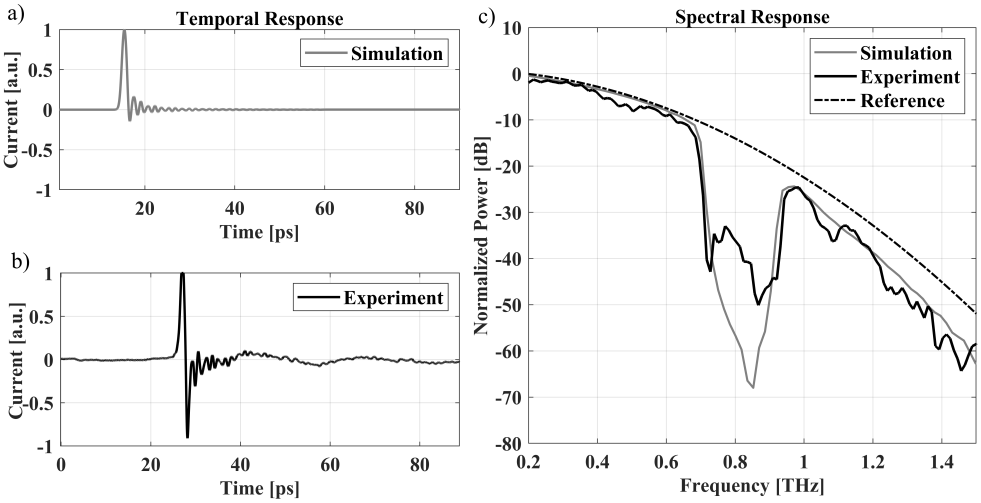

Fig. 7. The experimental result of the received THz-bandwidth pulse after propagation through the TABG. (a) The simulated temporal response (ANSYS HFSS) for TABG. (b) The experimental temporal response for TABG. (c) The DFT of the experimental and simulated temporal responses. The reference trace corresponds to a simulation without the TABG (the temporal response is not plotted).

7. Conclusion

This work presented the experimental validation of a THz apodized Bragg grating (TABG) [12]. The TABG was designed to have a center frequency of 0.8 THz and a bandwidth of 0.2 THz. These parameters were confirmed by experiment. Apodization serves to reduce the side-lobes and increase the roll-off rate of the filter which was observed in simulation and experiment. The results showed that the filter had a minimum rejection of approximately 20 dB over the stop-band.

Appendix A - Grating radiation above the stopband

When operating at frequencies above the Bragg bandgap there is an increased insertion loss which originates from diffractive grating radiation. Figure 8 illustrates this concept where the black arrows illustrate the direction of the Poynting vector. Note that the color scale is logarithmic and covers three orders of magnitude. Below the bandgap, Fig. 8(a), the Poynting vector illustrates a power flow from the left to right with no extra radiative loss. Within the bandgap, Fig. 8(b), the incident signal from is reflected such that minimal power is transmitted. Above the bandgap, Fig. 8(c), a portion of the reflected wave is back–scattered by grating in the tangential direction which contributes to the additional insertion loss.

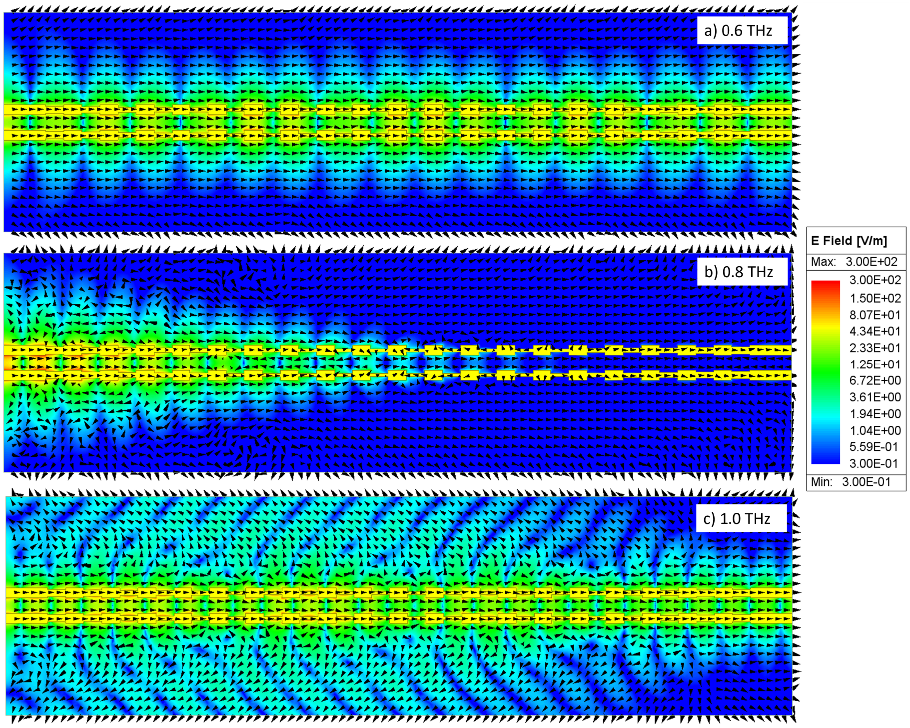

Fig. 8. Simulated electric field intensity profiles. Black arrows illustrate the Poynting vector direction. (a) Below the stopband, f = 0.6 THz. (b) In the stopband, f = 0.8 THz. (c) Above the stopband, f = 1.0 THz.

Funding. Natural Sciences and Engineering Research Council of Canada (RGPIN-2022-03277).

Acknowledgments. This work made use of the 4D LABS core facility at Simon Fraser University (SFU) supported by the Canada Foundation for Innovation (CFI), British Columbia Knowledge Development Fund (BCKDF), and Pacific Economic Development Canada (PacifiCan). We would like to acknowledge CMC Microsystems for the provision of products and services that facilitated this research.

Disclosures. The authors declare no conflicts of interest.

Data availability. Data underlying the results presented in this paper are not publicly available at this time but may be obtained from the authors upon reasonable request.

References

1. H.-J. Song and T. Nagatsuma, "Present and future of terahertz communications," IEEE Trans. Terahertz Sci. Technol. **1**(1), 256–263 (2011).
2. P. H. Siegel, "Terahertz technology in biology and medicine," IEEE Trans. Microwave Theory Tech. **52**(10), 2438–2447 (2004).
3. E. Pickwell and V. Wallace, "Biomedical applications of terahertz technology," J. Phys. D: Appl. Phys. **39**(17), R301–R310 (2006).
4. Z. Chen, X. Ma, B. Zhang, Y. Zhang, Z. Niu, N. Kuang, W. Chen, L. Li, and S. Li, "A survey on terahertz communications," China Commun. **16**(9), 1–14 (2019).
5. L. Zhu, S.-H. Shin, R. Payapulli, T. Machii, M. Motoyoshi, N. Suematsu, N. M. Ridler, and S. Lucyszyn, "3-D printed rectangular waveguide 123–129 GHz packaging for commercial CMOS RFICs," IEEE Microwave and Wireless Technology Letters (2023).
6. M. C. Beard, G. M. Turner, and C. A. Schmuttenmaer, "Terahertz spectroscopy," J. Phys. Chem. B **106**(29), 7146–7159 (2002).
7. J. Cabello-Sánchez, V. Drakinskiy, J. Stake, and H. Rodilla, "Capacitively-coupled resonators for terahertz planar-goubau-line filters," IEEE Trans. Terahertz Sci. Technol. **13**(1), 58–66 (2023).
8. W. Gao, W. S. L. Lee, C. Fumeaux, and W. Withayachumnankul, "Effective-medium-clad Bragg grating filters," APL Photonics **6**(7), 076105 (2021).
9. R. L. Smith, V. Shiran, W. Gomaa, and T. Darcie, "Characterization of a split-ring-resonator-loaded transmission line at terahertz frequencies," Opt. Express **29**(15), 23282–23289 (2021).
10. T. Ma, K. Nallapan, H. Guerboukha, and M. Skorobogatiy, "Analog signal processing in the terahertz communication links using waveguide Bragg gratings: example of dispersion compensation," Opt. Express **25**(10), 11009–11026 (2017).
11. J. Dong, A. Tomasino, G. Balistreri, P. You, A. Vorobiov, E. Charette, B. Le Drogoff, M. Chaker, A. Yurtsever, S. Stivala, M. A. Vincenti, C. De Angelis, D. Kip, J. Azana, and R. Morandotti, "Versatile metal-wire waveguides for broadband terahertz signal processing and multiplexing," Nat. Commun. **13**(1), 741 (2022).
12. W. Gomaa and T. Darcie, "Design and simulation of terahertz apodized Bragg grating using coplanar stripline transmission line a 1 μm-thin membrane," in *Journal of Physics: Conference Series*, vol. 2304 (2022), p. 012015.
13. W. Gomaa, R. L. Smith, V. Shiran, and T. Darcie, "Terahertz low-pass filter based on cascaded resonators formed by CPS bending on a thin membrane," Opt. Express **28**(21), 31967–31978 (2020).
14. R. L. Smith, W. Gomma, H. Esmaeilsabzali, and T. Darcie, "Tapered transmission lines for terahertz systems," Opt. Express **29**(11), 17295–17303 (2021).
15. W. Gomaa, R. L. Smith, H. Esmaeilsabzali, and T. E. Darcie, "Terahertz power divider using symmetric CPS transmission line on a thin membrane," IEEE Access **8**, 214425–214433 (2020).
16. S. Orfanidis, *Electromagnetic Waves and Antennas* (Online, 2016).
17. D. Pozar, *Microwave Engineering* (Wiley, 2011), 4th ed.
18. G. Cataldo, J. A. Beall, H.-M. Cho, B. McAndrew, M. D. Niemack, and E. J. Wollack, "Infrared dielectric properties of low-stress silicon nitride," Opt. Lett. **37**(20), 4200–4202 (2012).
19. P. Cheben, R. Halir, J. H. Schmid, H. A. Atwater, and D. R. Smith, "Subwavelength integrated photonics," Nature **560**(7720), 565–572 (2018).
20. R. D. V. Rios, S. Bikorimana, M. A. Ummy, R. Dorsinville, and S.-W. Seo, "A bow-tie photoconductive antenna using a low-temperature-grown GaAs thin-film on a silicon substrate for terahertz wave generation and detection," J. Opt. **17**(12), 125802 (2015).
21. R. L. Smith and T. Darcie, "Demonstration of a low-distortion terahertz system-on-chip using a CPS waveguide on a thin membrane substrate," Opt. Express **27**(10), 13653–13663 (2019).
22. M. Naftaly and R. Dudley, "Methodologies for determining the dynamic ranges and signal-to-noise ratios of terahertz time-domain spectrometers," Opt. Lett. **34**(8), 1213–1215 (2009).

66.51.131.199 {ts '2025-02-17 16:31:36'}

Appendix B

Demonstration of a Planar Multimodal Periodic Filter at THz Frequencies, Copy of [2]

Journal of Infrared, Millimeter, and Terahertz Waves (2025) 46:37
https://doi.org/10.1007/s10762-025-01056-6

RESEARCH

Demonstration of a Planar Multimodal Periodic Filter at THz Frequencies

Ali Dehghanian[1,2] · **Mohsen Haghighat**[1,2] · **Thomas Darcie**[1] · **Levi Smith**[1,2]

Received: 18 February 2025 / Accepted: 22 May 2025
© The Author(s), under exclusive licence to Springer Science+Business Media, LLC, part of Springer Nature 2025

Abstract

This paper presents a planar multimodal periodic filter that is constructed from alternating sections of coplanar stripline and the odd-mode of a finite-ground plane coplanar waveguide constructed on a 1 μm silicon nitride substrate to facilitate operation at THz frequencies. The multimodal configuration differs from standard single-mode periodic filters and enables flexible designs and the possibility for active control of the filter characteristics. For this proof-of-concept, we present the relevant theory and design procedures required to develop a band-stop filter that has a center frequency of $f_c = 0.8$ THz and a bandwidth of $\Delta f = 0.07$ THz. We find good agreement between theory, simulation, and experiment.

Keywords Terahertz · Filter · Multimode · Bandstop · Waveguide · Periodic

1 Introduction

Filters are commonly used to enhance signals in THz communication and sensing applications [1, 2]. In a communication system, the usage of a band-stop filter improves the dynamic range. For sensing applications, the filter characteristics such as center

---

Ali Dehghanian and Levi Smith contributed equally to this work.

Levi Smith
levismith@uvic.ca

Ali Dehghanian
adehghanian@uvic.ca

Mohsen Haghighat
mohsenh@uvic.ca

Thomas Darcie
tdarcie@uvic.ca

[1] Department of Electrical and Computer Engineering, University of Victoria, 3800 Finnerty Rd, Victoria V8P 5C2, BC, Canada

[2] Centre for Advanced Materials and Related Technology (CAMTEC), University of Victoria, 3800 Finnerty Rd, Victoria V8P 5C2, BC, Canada

Published online: 04 June 2025

frequency and bandwidth can be indicative of a nearby analyte. Bandstop filters are constructed using several different methods such as resonators [3–5] or distributed periodic structures [6–8]. This work presents the theory, simulation results, and experimental measurements for a new guided-wave multimode periodic band-stop filter topology that can be used at THz frequencies. The filter consists of alternating uniplanar waveguide configurations, specifically, a finite-ground plane coplanar waveguide (FGPCPW) and a coplanar stripline (CPS). For brevity, we will refer to FGPCPW as a CPW. This work primarily discusses the *odd*-mode of the CPW, which is sometimes called the “parasitic” mode [9]. We note that it is important to be diligent about the even/odd-mode distinction because literature commonly only discusses the “non-parasitic” *even*-mode of the CPW. The novel multimodal nature of the presented filter enables unique possibilities that are not viable with other periodic filters that use two conductors like in our previous work [8]. For example, the presented filter can be integrated with phase shifters [10], hybrids [11], and diodes for reconfigurability [12].

Characterizing devices at THz frequencies poses unique challenges because test instrumentation is not widely available and/or is cost-prohibitive. The vector network analyzers (VNAs) that are commonly used for microwave device characterization cannot be directly used at THz frequencies. Extension modules are commercially available (albeit costly) that allow for VNAs to characterize devices up to 1.5 THz [13]; however, they use rectangular waveguide feeds that are band-limited, which can further increase cost when attempting to perform wideband characterization since multiple extension modules are required. Also, interfacing a rectangular waveguide with a uniplanar requires mode conversion elements, which can pose a challenge due to the micrometer-scale non-planar dimensions. This work forgoes the use of VNAs and extension modules, and instead, uses thin-film photoconductive switches (PCSs) in conjunction with femtosecond optical pulses for the transmitting and receiving, which provides sufficient accuracy to characterize the filter performance considered in this work [14]. This method is similar to THz time-domain spectroscopy (THz-TDS) [15], and it allows for the CPS to be directly driven by a source with THz-bandwidth and resolves the signal that has traversed a device-under-test (i.e., a periodic filter in this work). Next, care must be taken when selecting the substrate thickness for uniplanar waveguides since substrate radiation can result in significant losses [16]. A straightforward method to overcome this issue is to use a very thin substrate [17]. In this work, the substrate is a 1 µm of silicon nitride (SiN) that is mechanically suspended by a 500 µm silicon (Si) frame.

Regarding filter specifications, this work is a proof-of-concept, and we select a center frequency of $f_c = 0.8$ THz and a bandwidth of $\Delta f = 0.07$ THz. We also select to use 20 unit cells, which resulted in a stopband rejection of 15–20 dB. These specifications were selected because we were confident that our experiments could clearly resolve device characteristics in this frequency window. The presented equations and theory can be scaled to higher frequencies.

Section 2 discusses the theory for the periodic filter in terms of modes and characteristic impedances using ABCD matrices. Section 3 presents the methods used for fabrication and performing the experiment. Section 4 presents the experimental results and discusses the measured spectrum. Section 5 is the conclusion. Appendix A illustrates an example that demonstrates that the multimode property can be exploited to convert the presented band-stop filter into a band-pass filter.

2 Design and Theory

2.1 Design

The filter is constructed from alternating transmission line configurations with different characteristic impedances. Specifically, we alternate between a CPS and a CPW (see Fig. 1a). Figure 1b illustrates the transverse cross-section of the CPW section. Figure 1c illustrates a section of the filter that clarifies the unit cell. The conductor width is $W = 45$ µm, and the separation is $S = 80$ µm. These parameters were selected because they exhibit reasonable loss characteristics at THz frequencies [18]. The width of the central conductor, W_m, is used to vary the characteristic impedance of the CPW mode, which is investigated in Section 2.3. For the experiment, we selected $W_m = 45$ µm, which corresponds to a stopband attenuation of approximately -20 dB with $N = 20$ filter periods. As mentioned, the filter is fabricated on a thin ($H_s = 1$ µm) SiN substrate to minimize radiation loss and dispersion at THz frequencies [17]. The conductor thickness was selected to be $H_a = 200$ nm to have reasonable conductor loss while remaining compatible with our transmitter and receivers' bonding method [19]. If other bonding methods are used, then thicker conductors can be used for lower conductor loss. The grating period is selected to be $\Lambda = 173$ µm, which corresponds to a filter center frequency of $f_c = 0.8$ THz (discussed later).

2.2 Simulation Details

Full-wave simulations (ANSYS HFSS 2024 R2) are used for obtaining mode impedances, S-parameters, and for producing field illustrations. The material constitutive parameters are as follows: the conductors are modeled as gold (Au) with

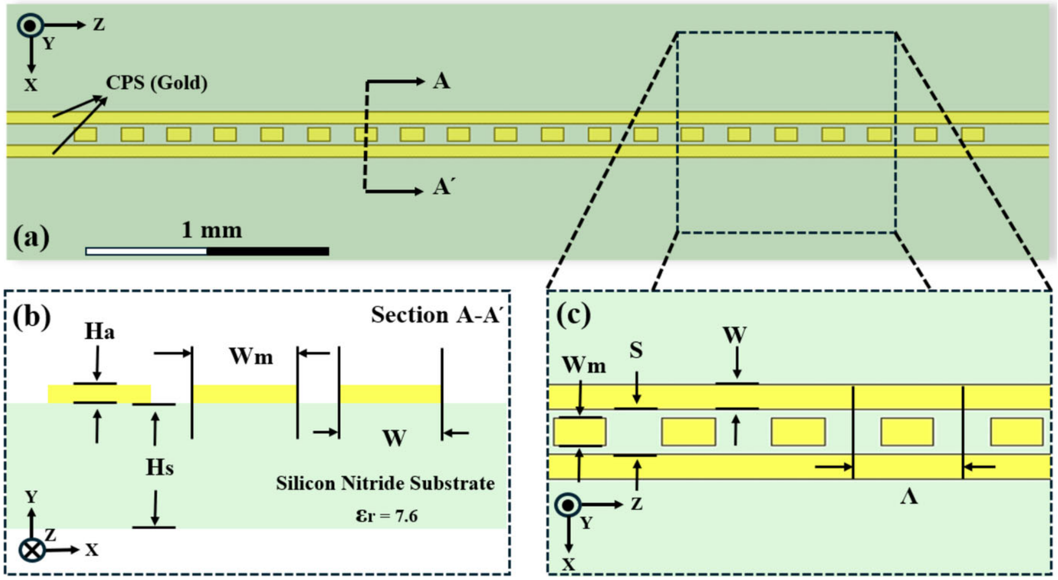

Fig. 1 **a** Overall structure. **b** Cross-section of the CPW sections. **c** Definition of the parameters associated with the unit cell

$\sigma_{\mathrm{Au}}(0.8\ \mathrm{THz}) = 2.16 \times 10^7$ S/m [20], and the substrate is silicon nitride (SiN) and modeled with $\varepsilon_{r,\mathrm{SiN}} = 7.6$, $\mu_{r,\mathrm{SiN}} = 1$, and $\tan \delta_{\varepsilon,\mathrm{SiN}} = 0.00526$ [21].

2.3 Modes and Coupling

The CPW consists of three conductors, and therefore, it supports an even and an odd mode. We use superscripts to differentiate the odd and even modes for the CPW, e.g., CPW^o and CPW^e. The two modes have different characteristic impedances: Z^o_{CPW} and Z^e_{CPW}. As previously mentioned, the CPW^e mode is typically the desired mode, whereas the CPW^o mode is generally considered parasitic and is suppressed by short-circuiting the outer conductors. However, in this work, the CPW^e mode is of secondary importance, and we focus on the CPW^o mode. As an aside, we note that it is possible to excite the CPW^e mode to create interesting devices. An example is given in Appendix A where the band-stop filter is converted to a band-pass filter by exploiting this property. Continuing on, the CPS has two conductors; thus, it only supports a single mode and characteristic impedance, Z_{CPS}. Figure 2 illustrates these three modes in the transverse plane. Investigation of Fig. 2a and b reveals that the CPS mode resembles CPW^o mode and significant modal coupling is expected. Figure 3 qualitatively and quantitatively illustrates the impact of a CPW^o-CPS interface. Figure 3a–c illustrates the electric field vector at 0.8 THz for several widths of the central conductor, W_m, where minimal disruption is observed at the CPW^o-CPS interface. To quantify the transmission at the interface, we plot $|S^o_{21}|^2$ (transmission between CPW^o and CPS) vs W_m in Fig. 3d. We do not plot $|S^e_{21}|^2$ (transmission between CPW^e and CPS) vs W_m, since it is less than -60 dB, which is expected when the CPW is symmetric

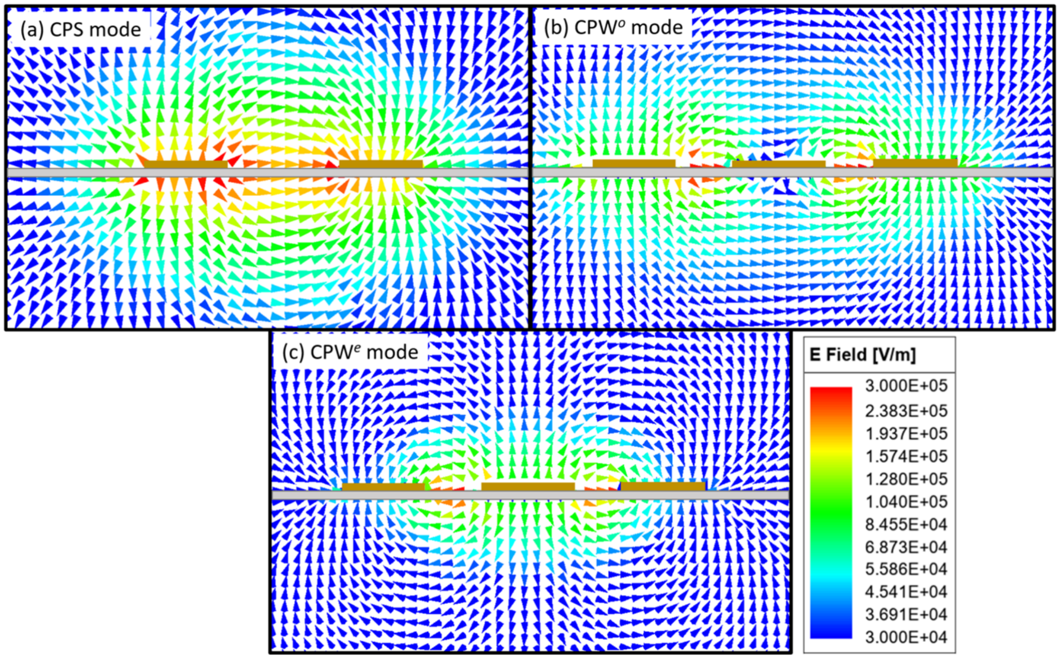

Fig. 2 Mode illustrations. **a** CPS mode. **b** CPW odd mode. **c** CPW even mode. The conductors and substrates are overlaid for visibility, and their thicknesses are not to scale (≈10× thinner than visualized)

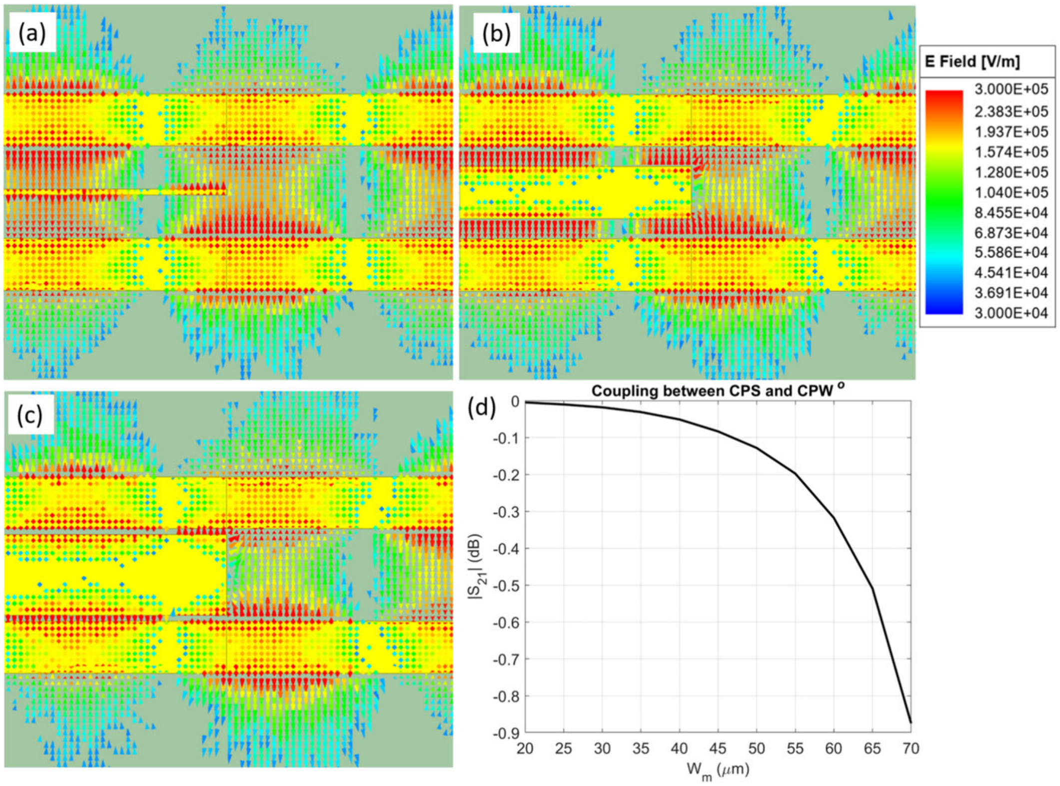

Fig. 3 CPS-to-CPW^o mode coupling at 0.8 THz. **a** W_m = 5 μm. **b** W_m = 45 μm. **c** W_m = 70 μm. **d** $|S^o_{21}|^2$ for CPS-to-CPW^o vs W_m

[22]. From Fig. 3d, it is apparent that there is good coupling between CPS and CPW^o modes and thus the configuration can form a building block for a periodic filter. We note that the central conductor does not need to be rectangular or symmetric, but the presented design and theory would become more complex, and these are not evaluated in this paper. Lastly, the transition between the CPS and CPW could include a shunt admittance to model parasitic effects, but we found that it had negligible impact on the periodic filter investigated in this work.

2.4 Filter Characteristics

The center frequency of the periodic filter is dependent on the period (Λ) by the following equation:

$$f_c = \frac{c}{2\Lambda\sqrt{\varepsilon_{re}}}, \tag{1}$$

where c is the speed of light and ε_{re} is the mean effective relative permittivity of the modes, which was obtained from full-wave simulation and is given by $\varepsilon_{re} \approx 1.2$, which results in f_c = 0.8 THz when Λ = 173 μm. Next, the fractional bandwidth is controlled by the characteristic impedance's (Z^o_{CPW} and Z_{CPS}) as follows:

$$\frac{\Delta f}{f_c} = \frac{4}{\pi}\sin^{-1}\left(\frac{Z_{\text{CPS}} - Z^o_{\text{CPW}}}{Z_{\text{CPS}} + Z^o_{\text{CPW}}}\right). \tag{2}$$

During the initial design, it is helpful to estimate the device parameters and characteristic impedances; this approximation can be performed assuming from the quasi-static (QS) expressions. For the CPW sections, the QS characteristic impedance of the odd-mode is given by [9]

$$Z^{o}_{\mathrm{CPW}} = \frac{120\pi}{\sqrt{\varepsilon_{re}}}\frac{K(k_{CPW})}{K(k'_{CPW})}, \quad k_{CPW} = \frac{S}{S+2W}\sqrt{\frac{1-\left(\frac{W_m}{S}\right)^2}{1-\left(\frac{W_m}{S+2W}\right)^2}}, \tag{3}$$

where $k'_{CPW} = \sqrt{1-k^2_{CPW}}$ and $K(\cdot)$ is the complete elliptic integral of the first kind. The QS characteristic impedance of the CPS sections is given by [23]

$$Z_{\mathrm{CPS}} = \frac{120\pi}{\sqrt{\varepsilon_{re}}}\frac{K(k_{CPS})}{K(k'_{CPS})}, \quad k_{CPS} = \frac{S}{S+2W}, \tag{4}$$

where $k'_{CPS} = \sqrt{1-k^2_{CPS}}$. Practical insight is obtained from Eqs. 3 and 4, specifically as $W_m \to 0$, then $k_{CPW} = k_{CPS}$, which leads to $Z^{o}_{\mathrm{CPW}} = Z_{\mathrm{CPS}}$. From Eq. 2, this implies that the fractional bandwidth reduces to zero, which is aligned with the expectation of connecting two identical sections of transmission line (i.e., the CPW with W_m = 0 and a CPS). Figure 4a plots the characteristic impedance of the modes using the QS expressions and at 0.8 THz, which was obtained from full-wave simulation. The QS and 0.8 THz traces exhibit similar characteristics but are shifted in value, which is expected as the characteristic impedance of CPW and CPS is frequency dependent [24, 25]. As noted, the QS expressions of Eqs. 3 and 4 can be used as a starting point

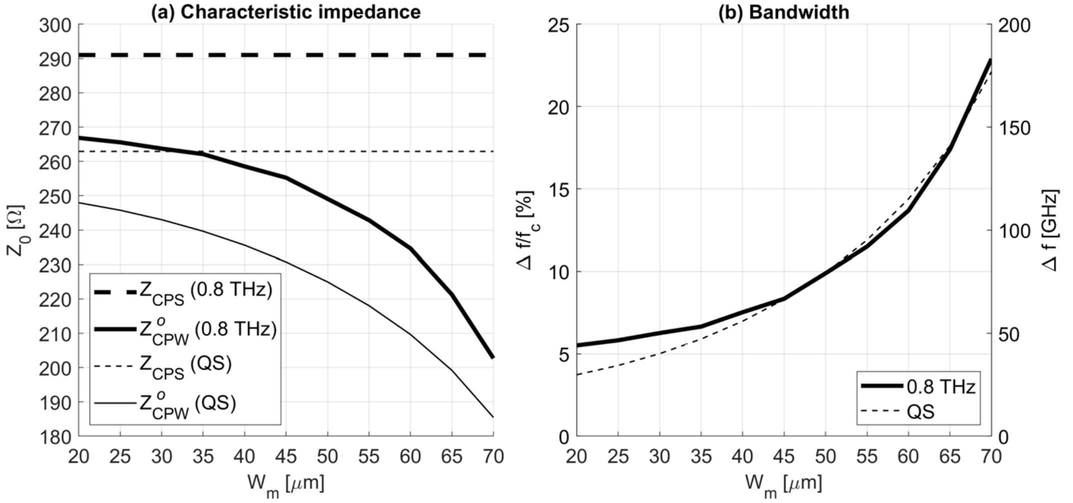

Fig. 4 **a** Characteristic impedance using QS expressions and full-wave simulation at 0.8 THz with S = 80 μm, W = 45 μm, H_s = 1 μm, H_a = 200 nm, and $\varepsilon_r = 7.6$. The impedance at 0.8 THz with W_m = 45 μm are $Z_{\mathrm{CPS}} = 291\Omega$ and $Z^{o}_{\mathrm{CPW}} = 254\Omega$. **b** The corresponding fractional bandwidth from Eq. 2 and bandwidth where $f_c = 0.8$ THz. At W_m = 45 μm, the bandwidth is 0.07 THz

for the initial design, but the final design should use full-wave simulation to obtain the characteristic impedance at the design frequency. The bandwidth is obtained using Eq. 2 and is plotted in Fig. 4b, where a bandwidth of 0.07 THz is predicted for the experimental structure with $W_m = 45$ μm.

To summarize, the design procedure begins by selecting a desired center frequency using Eq. 1. Next, the effective relative permittivity, ε_{re}, is obtained using full-wave simulation, but when using thin substrates (as in this work) then $\varepsilon_{re} \approx 1$. Next, the conductor width, W, should be selected to have desirable attenuation characteristics at THz frequencies such as $W = 30$ μm. The conductor separation, S, is then selected to obtain the desired characteristic impedance for the feedline, Z_{CPS}, using Eq. 4 (or full-wave simulation). The central conductor width, W_m, is selected to obtain Z^o_{CPW} using Eq. 3 (or full-wave simulation), which produces the specified fractional bandwidth given by Eq. 2.

2.5 Periodic Response

2.5.1 Theory

The periodic filter is constructed by cascading, N, unit cells that consist of two quarter wavelength ($\lambda/4$) sections of transmission lines with different characteristic impedances. The unit cells are modeled using ABCD matrices. To simplify the analysis, it is best to construct the unit cell's ABCD matrix using a CPS of length $\Lambda/4$, a CPW^o of length $\Lambda/2$, and a CPS of length $\Lambda/4$. This enables a straightforward method to calculate the total ABCD matrix by raising the unit cell's ABCD matrix to the power of N while retaining symmetry in the overall structure. The ABCD matrix for a unit cell (see Fig. 1) is given by the following:

$$\begin{aligned}\begin{bmatrix} A_{cell} & B_{cell} \\ C_{cell} & D_{cell} \end{bmatrix} = &\begin{bmatrix} \cos(\beta_{\mathrm{CPS}}\Lambda/4) & jZ_{\mathrm{CPS}}\sin(\beta_{\mathrm{CPS}}\Lambda/4) \\ j(1/Z_{\mathrm{CPS}})\sin(\beta_{\mathrm{CPS}}\Lambda/4) & \cos(\beta_{\mathrm{CPS}}\Lambda/4) \end{bmatrix} \\ &\cdot \begin{bmatrix} \cos(\beta^o_{\mathrm{CPW}}\Lambda/2) & jZ^o_{\mathrm{CPW}}\sin(\beta^o_{\mathrm{CPW}}\Lambda/2) \\ j(1/Z^o_{\mathrm{CPW}})\sin(\beta^o_{\mathrm{CPW}}\Lambda/2) & \cos(\beta^o_{\mathrm{CPW}}\Lambda/2) \end{bmatrix} \\ &\cdot \begin{bmatrix} \cos(\beta_{\mathrm{CPS}}\Lambda/4) & jZ_{\mathrm{CPS}}\sin(\beta_{\mathrm{CPS}}\Lambda/4) \\ j(1/Z_{\mathrm{CPS}})\sin(\beta_{\mathrm{CPS}}\Lambda/4) & \cos(\beta_{\mathrm{CPS}}\Lambda/4) \end{bmatrix}.\end{aligned} \tag{5}$$

The ABCD matrix for N sections is given by

$$\begin{bmatrix} A & B \\ C & D \end{bmatrix} = \begin{bmatrix} A_{cell} & B_{cell} \\ C_{cell} & D_{cell} \end{bmatrix}^N \tag{6}$$

The dispersion characteristics of the filter are obtained from Eq. 5 using the same methods presented in [8]. The result of this process is plotted in Fig. 5 where a 0.07 THz stopband is observed.

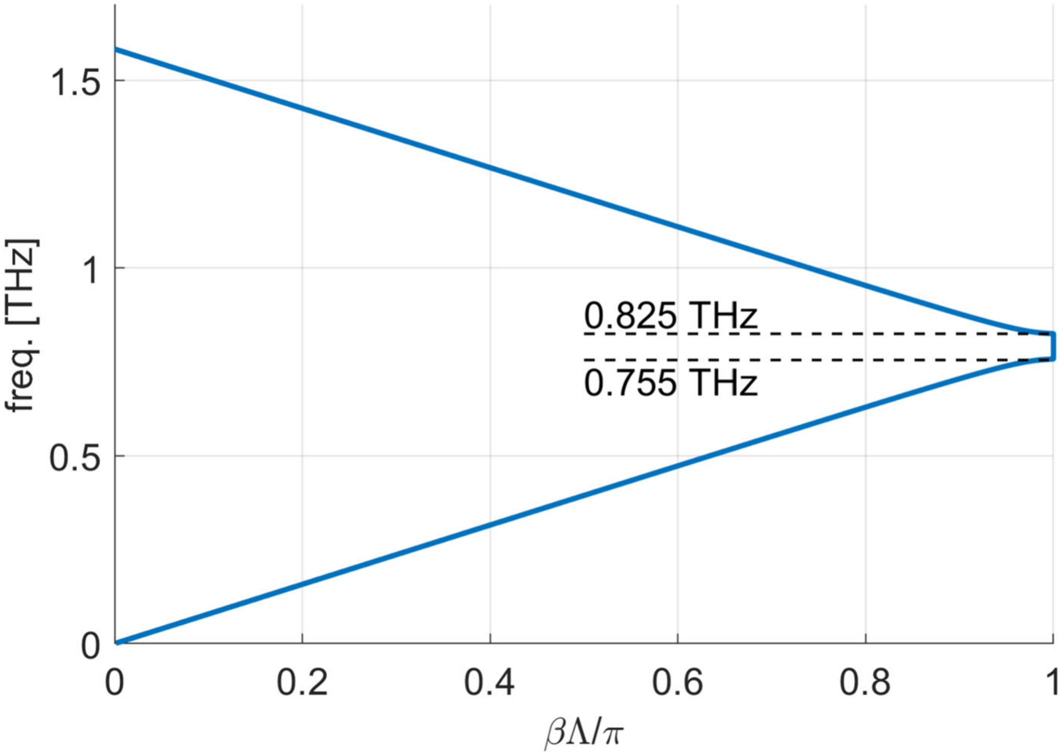

Fig. 5 Dispersion diagram for the unit cell

Lastly, the S-parameters are calculated from the ABCD matrix using standard methods [26]:

$$S_{11} = \frac{A + B/Z_{\mathrm{CPS}} - CZ_{\mathrm{CPS}} - D}{A + B/Z_{\mathrm{CPS}} + CZ_{\mathrm{CPS}} + D} \quad \text{and} \quad S_{21} = \frac{2}{A + B/Z_{\mathrm{CPS}} + CZ_{\mathrm{CPS}} + D} \tag{7}$$

2.5.2 Simulation

A full-wave simulation was also used to characterize the total response of the filter with $N = 20$ near the design frequency. These simulations account for the full-wave effects that are not modeled by the ABCD matrices. Figure 6a plots the S-parameters for $N = 20$ unit cells that were obtained using Eqs. 5, 6, and 7 where the characteristic impedances were obtained from Fig. 4 at 0.8 THz. Figure 6b plots the S-parameters for the periodic filter obtained from HFSS. Comparing Fig. 6a and b shows that the ABCD model provides a good first approximation. The main difference observed between theory and simulation is the introduction of passband insertion loss and a difference in the stopband rejection. At frequencies below the stopband, there is approximately 1 dB of insertion loss, which originates from conductor loss. This effect could be included in the ABCD matrix model if lossy transmission line models were used. Above the stopband, the insertion loss increases to 4–6 dB, which originates from grating radiation [27] and is not straightforward to model using ABCD matrices; thus, full-wave simulations should be used to obtain a comprehensive understanding

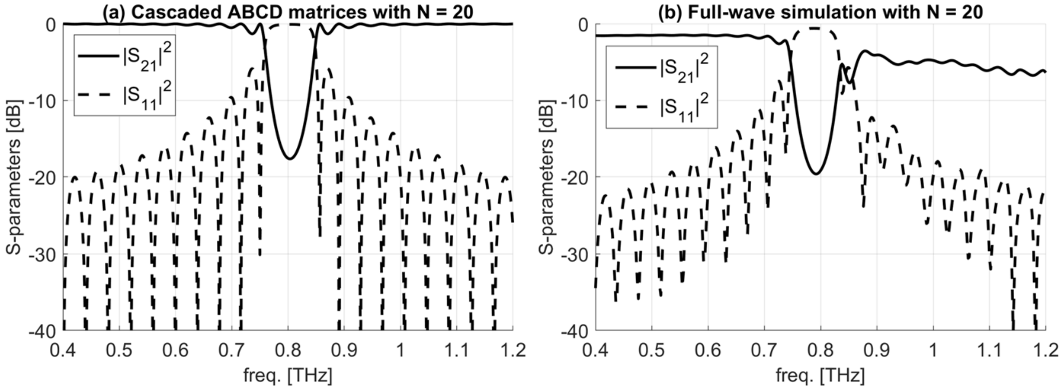

Fig. 6 **a** S-parameters obtained from cascading 20 unit cells ($N = 20$) using ABCD matrices. The unit cell is included as an inset. **b** S-parameters obtained from cascading 20 unit cells (N = 20) using ANSYS HFSS

of device performance. More details on grating radiation are found in Appendix B. Future work can explore methods to reduce its impact by reducing W_m.

Figure 7a and b use Eqs. 6 and 7 to plot the impact of the number of unit cells on the stopband rejection. From Fig. 7b, it is found that while $N > 10$, the minimum stopband transmission is given by $|S_{21}^{\min}|$ [dB] $= -1.18N + 5.90$. Figure 7c and d plots the same information, but uses full-wave simulation instead of ABCD matrices. The

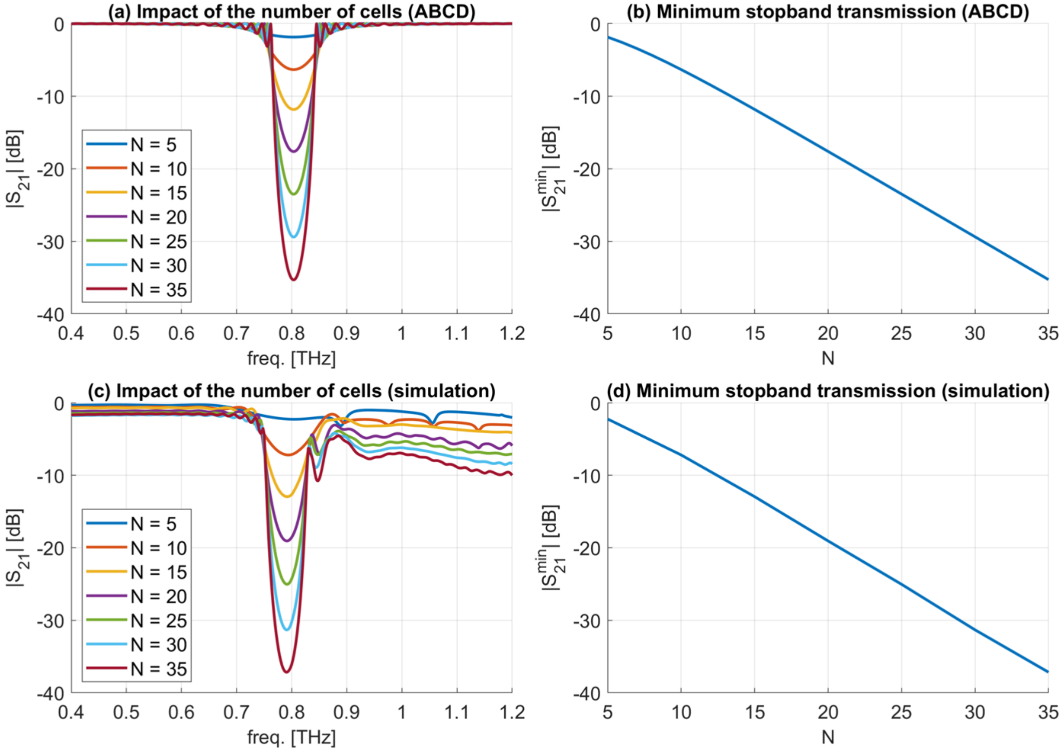

Fig. 7 **a** Transmission response of the filter using ABCD matrices for several different numbers of unit cells, N. **b** Minimum stopband transmission using ABCD matrices plotted against the number of unit cells, N. **c** Transmission response of the filter using ANSYS HFSS for several different numbers of unit cells, N. **d** Minimum stopband transmission using ANSYS HFSS plotted against the number of unit cells, N

minimum stopband transmission is given by $|S_{21}^{\min}|$ [dB] $= -1.21N + 5.00$, which is similar to the ABCD method; however, grating radiation is observed and reduces the transmission above the stopband by approximately $-0.2N$ in dB at 1.1 THz.

3 Methods

3.1 Fabrication

The fabricated filter (Fig. 8) consists of a patterned metallization on a thin SiN substrate that uses low-temperature grown gallium arsenide (LT-GaAs) photoconductive switches (PCSs) for signal generation and detection. The substrate is fabricated by depositing a 1 μm layer of SiN on a 500 μm silicon wafer. The metallization was subsequently deposited using a combination of ultraviolet (UV) lithography and electron-beam physical vapor deposition (EBPVD). The metallization used a 10 nm titanium (Ti) adhesion layer and a 200 nm gold (Au) layer. Lastly, the Si substrate is masked using UV lithography and selectively etched using potassium hydroxide (KOH), resulting in a suspended SiN window with the desired conductor pattern.

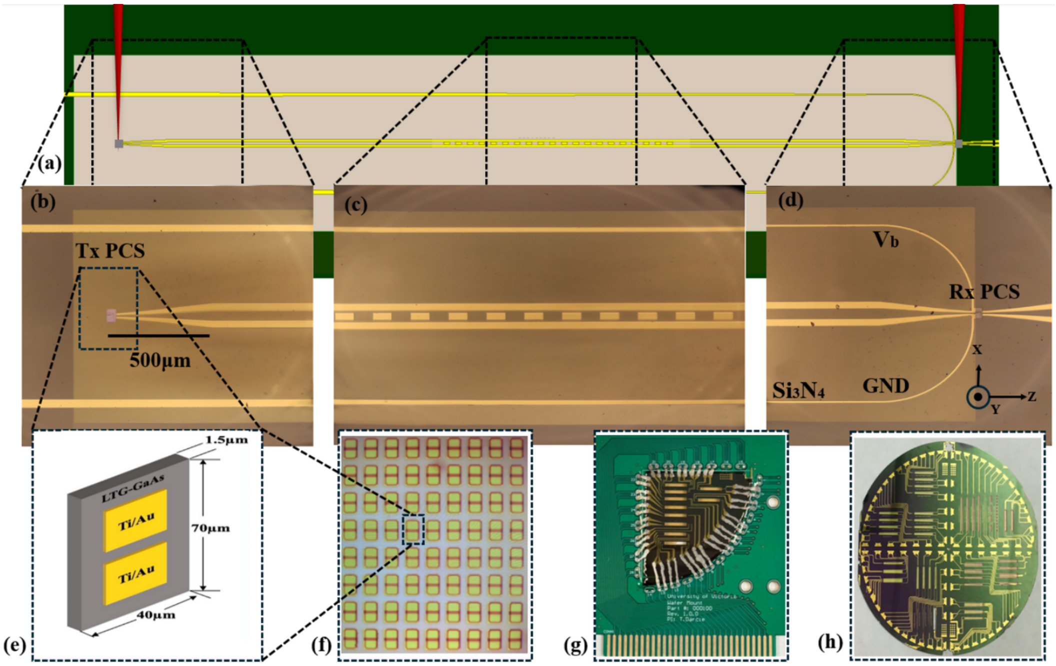

Fig. 8 **a** The complete integrated system fabricated on a thin SiN membrane. **b** The transmitter section, consisting of an LT-GaAs PCS, 200 nm thick gold CPS TL on a 1 μm SiN layer. **c** A microscopic view of the periodic filter. **d** The receiver section, including the DC block and bias lines for the PCS and lock-in amplifier connection. **e** Thin films of LT-GaAs with dimensions of 70 μm × 40 μm × 1.8 μm, used in the PCS arrays. **f** The PCS arrays after fabrication, used in both transmitter and receiver sections. **g** A quarter wafer mounted on a PCB for alignment and connection to the measurement setup, ensuring precise signal transmission. **h** Fabricated circuits on the wafer before being diced into four quarters

The LT-GaAs PCSs (Fig. 8e) were constructed using a method similar to the technique described in [19]. In short, an epitaxial lift-off method is used [28]. First, using molecular beam epitaxy (MBE), a 2 µm layer of LT-GaAs is deposited on a 50 nm aluminum arsenide (AlAs) layer on a 500 nm semi-insulating GaAs substrate. The AlAs layer is a sacrificial layer that is selectively etched using a 10% hydrofluoric (HF) acid etchant. Before etching the AlAs layer, a grid (Fig. 8f) of individual PCS devices is prepared by patterning the LT-GaAs surface with Ti/Au (10 nm/200 nm) via RF sputtering. Next, the LT-GaAs surface contact pairs are masked with a photoresist using UV lithography, and then the exposed regions of the LT-GaAs surface are etched using citric acid and hydrogen peroxide to produce discrete PCSs. Next, the surface is coated in an etch-resistant wax (Apiezon W) and then submerged in a HF acid bath until the AlAs is fully dissolved and the LT-GaAs layer is released. Next, a thin layer of LT-GaAs is dissolved from the backside using the citric acid and hydrogen peroxide etchant. Lastly, the individual PCS devices are obtained after dissolving the Apiezon W wax using trichloroethylene (TCE). The resultant discrete PCSs can then be placed on uniplanar circuits and connected using Van der Waals bonding [28].

3.2 Experiment

We characterize the response of the periodic filter at THz frequencies using a modified THz time-domain spectrometer (Fig. 9). The THz-bandwidth signal originates from a DC biased (V_B = 24 V) PCS that is illuminated by a femtosecond laser (CALMAR Carmel) with a pulse width of $\tau_p = 80$ fs, repetition rate of $f_{rep} = 80$ MHz, and an average optical power of P_{opt} = 10 mW. The biased PCS and transient photoconductivity

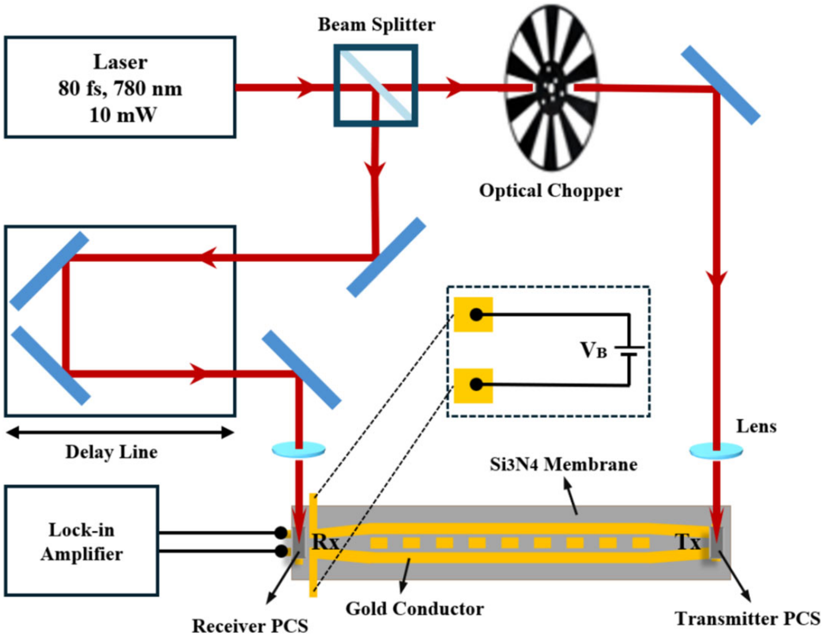

Fig. 9 Optical setup used for characterizing the filter response. The blue rectangles are mirrors

result in a subpicosecond current pulse that drives the feedlines and the periodic filter. The transient signal propagates through the periodic filter and is recovered by sampling the current via lock-in detection (Stanford Instruments SR830) generated by the combination of the incident voltage and receiver PCS at different times that are controlled by a mechanical delay line. The lock-in amplifier is referenced to the optically chopped (f_{chop} = 1 KHz) transmitter beam. The result of the experiment is a transient signal that contains frequency components up to THz frequencies that are obtained by applying the discrete Fourier transform (DFT). It is important to state that our experimental methodology is not akin to a standard vector network analyzer (VNA) measurement that directly exports the devices' S-parameters when properly calibrated. Our signal source is a finite duration transient pulse; thus, it exhibits an inherent roll-off with frequency. When interpreting the experimental results, the transmission is obtained by comparing the responses of a reference (W_m = 0 μm) and the filter (W_m = 45 μm).

4 Results and Discussion

Figure 10 plots the experimental results for a reference structure and the periodic filter illustrated in Fig. 8b–d. The temporal response is obtained using the experiment shown in Fig. 9, and the spectral response is obtained by applying the DFT to the temporal response. The temporal and spectral responses are normalized. The spectral response in Fig. 10c illustrates a stopband centered at 0.8 THz with a bandwidth of ≈0.1 THz, which aligns with the theory (Fig. 6a) and full-wave simulations (Fig. 6b).

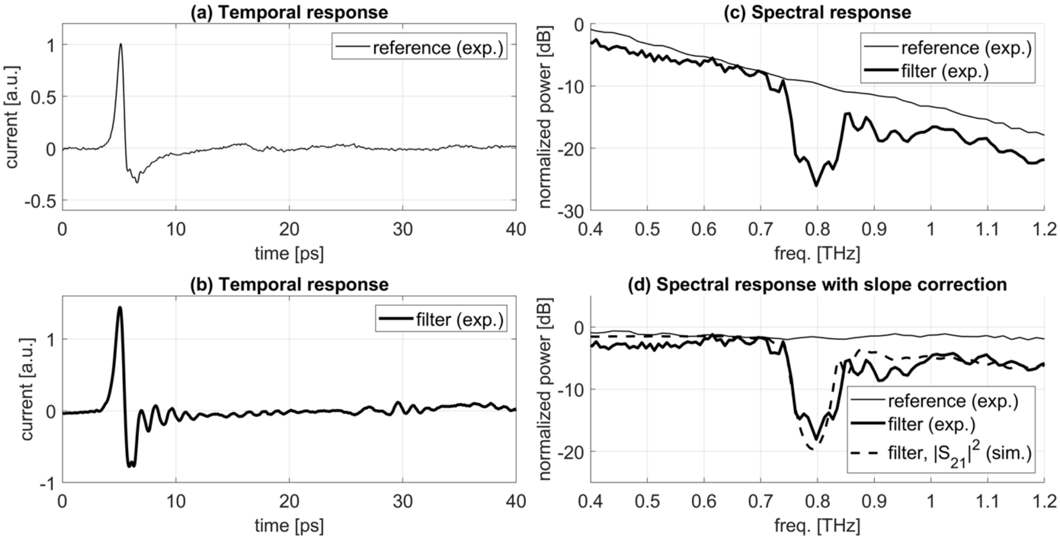

Fig. 10 Experimental results. **a** Temporal response for a reference (W_m = 0 μm). **b** Temporal response a for periodic filter (W_m = 45 μm) spectrally normalized to the reference. **c** Spectral response for a reference and periodic filter obtained via DFT. **d** Spectral response with 20 dB/THz slope correction alongside a full-wave $|S_{21}|^2$ simulation results from Fig. 6b

We reiterate that there is an expected frequency decay due to the transient excitation and detection methods. In Fig. 10c, this appears as an approximately linear slope (on a semi-log graph) of -20 dB/THz. The slope is not always linear and is dependent on many parameters but primarily the optical pulse duration and the PCS carrier lifetime [29–31]. To aid in interpreting the results, we add the 20 dB/THz slope to the experimental data and plot it alongside the full-wave simulation results in Fig. 10d. This slope is a characteristic of the transmitter and receiver; it does not mean that the filter exhibits a 20 dB/THz insertion loss. Applying the inverse slope correction to the spectral response flattens the spectrum to allow for better visual comparison against full-wave simulation ($|S_{21}|^2$). We find good relative agreement between the simulation and experimental results where the center frequency and bandwidth are in close agreement. We also observe the increased insertion loss above the stopband that is associated with grating radiation. The experimental bandwidth is also marginally wider than predicted, which likely originates from manufacturing differences.

5 Conclusion

We presented a multimode periodic band-stop filter based on alternating CPS and CPW sections. The filter had a center frequency of $f_c = 0.8$ THz and a bandwidth of $\Delta f \approx 0.1$ THz. The theory was based on cascading ABCD matrices that represented the CPS and the odd-mode of the CPW. The theory, simulation, and experiment are in agreement with each other. Lastly, to demonstrate a benefit of the multimode periodic filter, we provided a simulated example that used the even mode to convert the band-stop filter into a band-pass filter by introducing a short circuit between the conductors.

Appendix A: Multimode Band-Pass Filter Example

The filter presented in this work offers unique opportunities that are achieved by modifying the excitation of the even mode for the CPW sections. The bulk of this paper

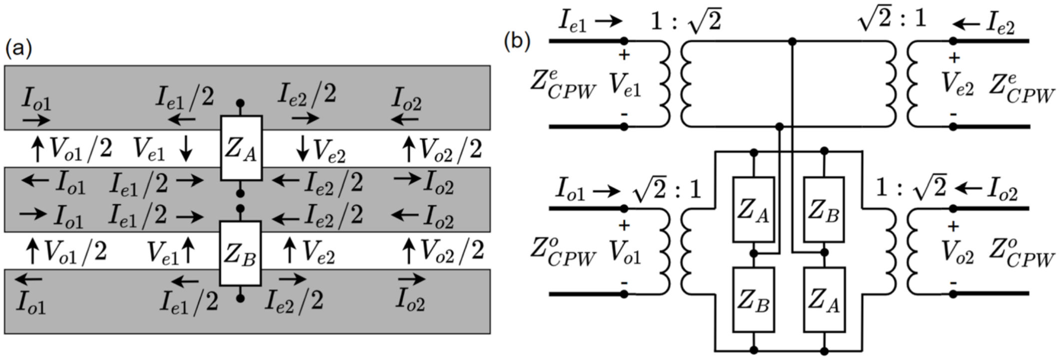

Fig. 11 Illustration of the even and odd modes for a CPW with an impedance placed between the conductors

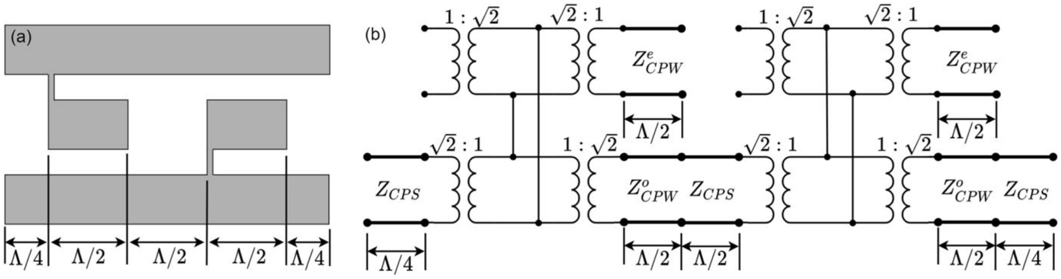

Fig. 12 **a** Illustration of the band-pass filter conversion which places short circuits between the conductors of the CPW sections. **b** Circuit representation of the band-pass filter

ignores the even mode because it is not excited; however, excitation can be achieved by considering the equivalent circuit of Fig. 11 [12, 22]. So far, $Z_A = Z_B = \infty$, which implies that the even mode cannot be excited. Alternatively, if a short circuit ($Z_A = 0$) was placed between the conductors and the other left open ($Z_B = \infty$), then the even mode would be excited. This additional short circuit can be used to convert the band-stop filter to a band-pass filter.

Figure 12a illustrates the unit cell modification that converts the band-stop filter to a band-pass filter by exciting the even mode. The short circuit alternates between Z_A and Z_B to ensure that the overall filter remains balanced. Figure 12b is the circuit representation of Fig. 12a.

The circuit of Fig. 12b can be simplified to the equivalent circuit of Fig. 13a. Using standard methods [26], Fig. 13a is represented with cascaded ABCD matrices and converted to S-parameters to predict the transmission response. From simulation, we found L_{eq} = 7 pH. We cascaded ten unit cells and compared full-wave simulation and theory in Fig. 13b where band-pass behavior is observed. This example demonstrates that exploitation of the multimode characteristics result in unique device possibilities that can be directly integrated into the filter. Lastly, it is possible to use active elements for Z_A and Z_B, which would enable active control of the filter performance.

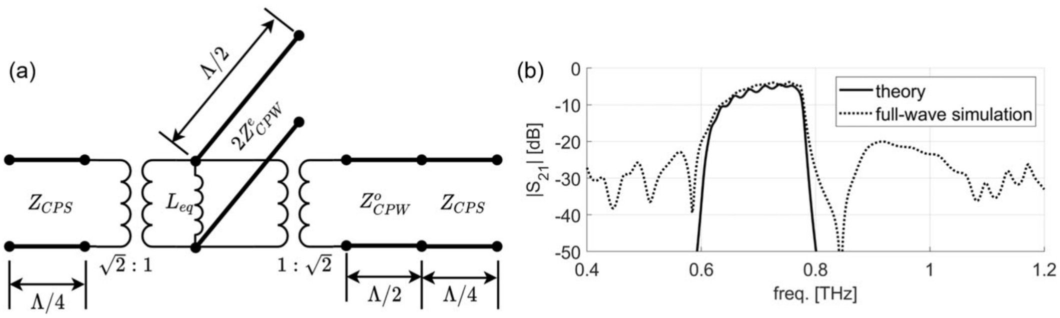

Fig. 13 **a** Equivalent circuit of Fig. 12b. **b** Theoretical and simulated $|S_{21}|^2$

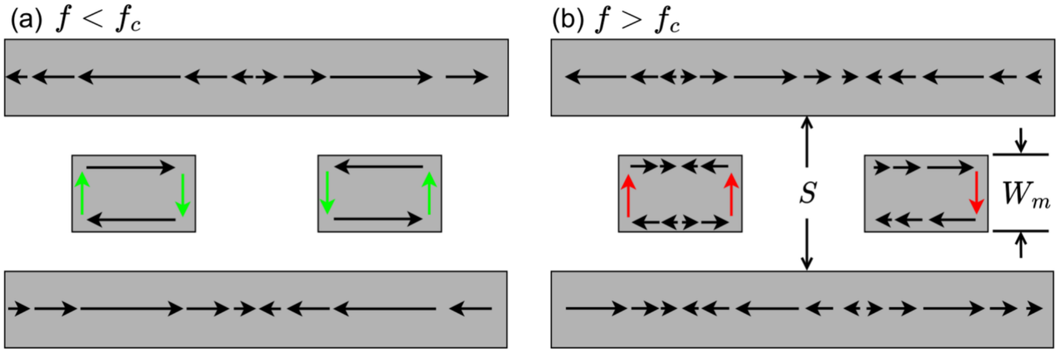

Fig. 14 Illustration of currents that contribute to grating radiation. Long arrows = large currents. Short arrows = small currents. **a** Below the stopband. **b** Above the stopband

Appendix B: Grating Radiation

In Figs. 6b, 7c, and 10c and d, we found additional loss above the stopband, which originates from grating radiation. The origin of this loss is described using Fig. 14, which illustrates the current distribution as arrows where the arrow length represents its relative magnitude. Below the stopband, the transverse currents (green arrows in Fig. 14a) cancel each other and do not radiate significantly. Above the stopband, the transverse currents (red arrows in Fig. 14b) do not cancel and can radiate. Thus, the central conductor of the CPW behaves as an antenna of length W_m. Therefore, a straightforward method to mitigate insertion loss above the stopband is to reduce the effectiveness of the "antennas" by reducing W_m. We opted to validate this concept using full-wave simulation while constraining the fraction bandwidth Eq. 2 to remain constant using the quasi-static expressions. The results are plotted in Fig. 15, which clearly shows that W_m impacts the insertion loss above the stopband, while the behavior in and below the stopband remain comparable. We note that the simulation in Fig. 15 does not include a thin SiN substrate for simulation expediency. This negation results in a center frequency shift and minor changes to the insertion loss, but does not affect the objective of illustrating the impact of W_m on S_{21} surrounding the stopband.

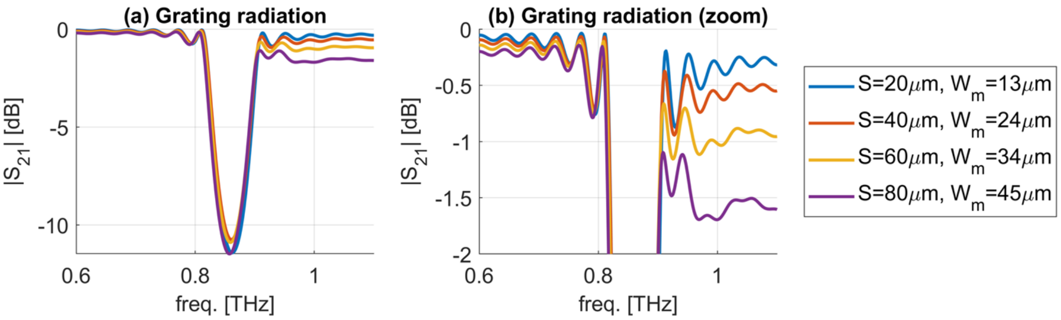

Fig. 15 Full-wave simulation investigating the impact of different values of W_m while maintaining the fractional bandwidth. **a** $|S_{21}|$ for four different values of S and W_m; W_m was numerically calculated to retain fractional bandwidth. **b** Same as **a**, but with a smaller y-axis for better visualization

Acknowledgements This work was supported by an NSERC Discovery Grant. The authors thank 4D LABS at Simon Fraser University for the fabrication of the CPS waveguides and the thin membrane, and also the Centre for Advanced Materials and Related Technology (CAMTEC) at the University of Victoria for providing Nanofab facilities for the fabrication of the PCS devices.

Author Contributions A. D. designed and simulated the device. M.H. assisted with device fabrication, assembly, and experiments. T.D. provided insight into device performance. L.S. developed the theory and wrote the manuscript text.

Funding Natural Sciences and Engineering Research Council of Canada (RGPIN-2022-03277).

Data Availability There are no supplementary materials, and the data is available upon reasonable request.

Declarations

Conflict of Interest The authors declare no competing interests.

Ethics Approval Not applicable.

References

1. Chen, Z., Ma, X., Zhang, B., Zhang, Y., Niu, Z., Kuang, N., Chen, W., Li, L., Li, S.: A survey on terahertz communications. China Communications 16(2), 1–35 (2019)
2. Singh, S.P., Tiwari, N.K., Akhtar, M.J.: Spoof surface plasmon-based coplanar waveguide sensor for dielectric sensing applications. IEEE Sensors Journal 20(1), 193–201 (2019)
3. Smith, L., Shiran, V., Gomaa, W., Darcie, T.: Characterization of a split-ring-resonator-loaded transmission line at terahertz frequencies. Optics Express 29(15), 23282–23289 (2021)
4. Cunningham, J., Wood, C., Davies, A.G., Hunter, I., Linfield, E.H., Beere, H.E.: Terahertz frequency range band-stop filters. Applied Physics Letters **86**(21) (2005)
5. Cabello-Sánchez, J., Drakinskiy, V., Stake, J., Rodilla, H.: Capacitively-coupled resonators for terahertz planar-goubau-line filters. IEEE Transactions on Terahertz Science and Technology 13(1), 58–66 (2022)
6. Ma, T., Nallapan, K., Guerboukha, H., Skorobogatiy, M.: Analog signal processing in the terahertz communication links using waveguide Bragg gratings: example of dispersion compensation. Opt. Express 25(10), 11009–11026 (2017)
7. Gao, W., Lee, W.S., Fumeaux, C., Withayachumnankul, W.: Effective-medium-clad Bragg grating filters. APL Photonics **6**(7) (2021)
8. Dehghanian, A., Gomaa, W., Haghighat, M., Darcie, T., Smith, L.: Demonstration of an integrated terahertz band-stop filter using an apodized bragg grating. Optics Express 31(20), 32582–32590 (2023)
9. Ghione, G., Naldi, C.: Coplanar waveguides for MMIC applications: Effect of upper shielding, conductor backing, finite-extent ground planes, and line-to-line coupling. IEEE transactions on Microwave Theory and Techniques 35(3), 260–267 (1987)
10. Llamas, M.A., Girbau, D., Ribo, M., Pradell, L., Lazaro, A., Giacomozzi, F., Margesin, B.: MEMS-based 180° phase switch for differential radiometers. IEEE Transactions on Microwave Theory and Techniques 58(5), 1264–1272 (2010)
11. Llamas, M.A., Ribo, M., Girbau, D., Pradell, L.: A rigorous multimodal analysis and design procedure of a uniplanar 180° hybrid. IEEE Transactions on Microwave Theory and Techniques 57(7), 1832–1839 (2009)
12. Contreras, A., Pradell, L., Ribó, M.: A novel tunable multimodal bandpass filter. In: 2011 41st European Microwave Conference, pp. 1059–1062 (2011). IEEE
13. Virginia Diodes: Vector Network Analyzer Extenders. https://vadiodes.com/en/products/vector-network-analyzer-extension-modules. Accessed: 2024-10-29

14. Grischkowsky, D.R., Ketchen, M.B., Chi, C.-C., Duling, I.N., Halas, N.J., Halbout, J.-M., May, P.G.: Capacitance free generation and detection of subpicosecond electrical pulses on coplanar transmission lines. IEEE journal of quantum electronics 24(2), 221–225 (1988)
15. Lee, Y.-S.: Principles of Terahertz Science and Technology vol. 170. Springer, New York (2009)
16. Rutledge, D.B.: Integrated circuit antennas. Infrared and millimeter waves 10, 1–90 (1983)
17. Cheng, H.-J., Whitaker, J.F., Weller, T.M., Katehi, L.P.: Terahertz-bandwidth characteristics of coplanar transmission lines on low permittivity substrates. IEEE Transactions on Microwave Theory and Techniques 42(12), 2399–2406 (1994)
18. Smith, R., Darcie, T.: Demonstration of a low-distortion terahertz system-on-chip using a cps waveguide on a thin membrane substrate. Optics Express 27(10), 13653–13663 (2019)
19. Rios, R.D.V., Bikorimana, S., Ummy, M.A., Dorsinville, R., Seo, S.-W.: A bow-tie photoconductive antenna using a low-temperature-grown GaAs thin-film on a silicon substrate for terahertz wave generation and detection. Journal of Optics 17(12), 125802 (2015)
20. Lucyszyn, S.: Investigation of anomalous room temperature conduction losses in normal metals at terahertz frequencies. IEE Proceedings-Microwaves, Antennas and Propagation 151(4), 321–329 (2004)
21. Cataldo, G., Beall, J.A., Cho, H.-M., McAndrew, B., Niemack, M.D., Wollack, E.J.: Infrared dielectric properties of low-stress silicon nitride. Optics Letters 37(20), 4200–4202 (2012)
22. Ribó, M., Pradell, L.: Circuit model for mode conversion in coplanar waveguide asymmetric shunt impedances. Electronics Letters 35(9), 713–715 (1999)
23. Ghione, G., Naldi, C.: Analytical formulas for coplanar lines in hybrid and monolithic MICs. Electronics Letters 20(4), 179–181 (1984)
24. Shih, Y., Itoh, T.: Analysis of conductor-backed coplanar waveguide. Electronics Letters 18(12), 538–440 (1982)
25. Phatak, D.S., Das, N.K., Defonzo, A.: Dispersion characteristics of optically excited coplanar striplines: comprehensive full-wave analysis. IEEE Transactions on Microwave Theory and Techniques 38(11), 1719–1730 (1990)
26. Pozar, D.M.: Microwave Engineering: Theory and Techniques. John Wiley & Sons, Hoboken (2021)
27. Cheben, P., Halir, R., Schmid, J.H., Atwater, H.A., Smith, D.R.: Subwavelength integrated photonics. Nature **560**(7720) (2018)
28. Yablonovitch, E., Hwang, D., Gmitter, T., Florez, L., Harbison, J.: Van der waals bonding of GaAs epitaxial liftoff films onto arbitrary substrates. Applied Physics Letters 56(24), 2419–2421 (1990)
29. Duvillaret, L., Garet, F., Roux, J.-F., Coutaz, J.-L.: Analytical modeling and optimization of terahertz time-domain spectroscopy experiments, using photoswitches as antennas. IEEE Journal of Selected Topics in Quantum Electronics 7(4), 615–623 (2001)
30. Garufo, A., Carluccio, G., Llombart, N., Neto, A.: Norton equivalent circuit for pulsed photoconductive antennas–part i: Theoretical model. IEEE Transactions on Antennas and Propagation 66(4), 1635–1645 (2018)
31. Zhang, H., Llombart, N., Bueno, J., Freni, A., Neto, A.: Time-domain equivalent circuits for the link modelling between pulsed photoconductive sources and receivers. IEEE Transactions on Terahertz Science and Technology (2024)

Publisher's Note Springer Nature remains neutral with regard to jurisdictional claims in published maps and institutional affiliations.

Springer Nature or its licensor (e.g. a society or other partner) holds exclusive rights to this article under a publishing agreement with the author(s) or other rightsholder(s); author self-archiving of the accepted manuscript version of this article is solely governed by the terms of such publishing agreement and applicable law.

Appendix C

Demonstration of a Terahertz Integrated Planar Network Synthesis Filter, Copy of [3]

Research Article Vol. 3, No. 1 / 15 Jan 2024 / *Optics Continuum* 71

OPTICS CONTINUUM

Demonstration of a terahertz integrated planar network synthesis filter

ALI DEHGHANIAN,[1] MOHSEN HAGHIGHAT,[1,2] THOMAS DARCIE,[1] AND LEVI SMITH[1,2,*]

[1] *Department of Electrical and Computer Engineering, University of Victoria, Victoria, BC V8P 5C2, Canada*
[2] *Centre for Advanced Materials and Related Technology (CAMTEC), University of Victoria, 3800 Finnerty Rd, Victoria, BC V8P 5C2, Canada*
[*] *levismith@uvic.ca*

Abstract: At terahertz (THz) frequencies, there are few experimental works that demonstrate the viability of all-pole network synthesis filters to obtain desired frequency characteristics (i.e., Chebyshev, Butterworth, Bessel, etc.) using planar waveguides. This capability has been proven with non-planar waveguides, but has yet to be demonstrated using planar waveguides, which are desirable due to their integration capabilities similar to printed circuit board or monolithic microwave integrated circuit structures. In this paper, we use network synthesis methods from microwave engineering to fabricate three integrated planar low-pass filters for THz applications that have the same cut-off frequency ($f_c = 0.8$ THz) but different orders (N = 3, 4, 5). We measure their response to a THz-bandwidth excitation pulse and find that the experimental results exhibit increasing roll-off rates with increasing filter order without incurring significant pulse distortion, which is aligned with theory.

© 2024 Optica Publishing Group under the terms of the Optica Open Access Publishing Agreement

1. Introduction

Filters are used throughout the electromagnetic (EM) spectrum for applications such as noise reduction, (de)multiplexing, and signal processing [1,2]. Filter design is a well established field for the electrical [3] and optical [4] frequencies. Within the terahertz (THz) gap (0.1-10 THz), filter design has primarily focused on THz-bulk optical components which are used with radiated waves commonly associated with THz-time domain spectroscopy (TDS) [5]. While these THz-bulk optical filters are useful, they do not integrate with miniaturized planar guided wave transmission lines (TLs) such as the coplanar striplines (CPS) and coplanar waveguides (CPW) [6–8].

Microwave filter synthesis is applicable at THz frequencies; however, current literature is lacking validating experiments. This gap in literature likely originates from the difficulty associated with performing experiments at THz frequencies. To the authors knowledge, there are three main methods for characterizing a device-under-test (DUT) at frequencies above 1 THz while remaining inside the THz gap. First, electronic vector network analyzers (VNAs) are typically limited to less than 100 GHz, but this range can be increased using extender modules up-to 1.5 THz [9–12]. This method is attractive because it uses techniques that are commonplace in microwave engineering and does not require the use of photonics. However, the rectangular feedlines are dispersive and band-limited, thus many extension modules (costly) are required to perform broadband measurements. Next, THz optics (free-space radiation) can be used to to perform investigation of a DUT [13–15]. The source of THz radiation could be a photoconductive antenna or mixer, quantum cascade laser, free-electron laser, etc. [16]. The detector could be another photoconductive antenna, electro-optic crystal (ZnTe), Golay cell, bolometer, etc. [17]. THz optics provides valuable information about the DUT, but experiments are adversely impacted by field coupling errors which can be difficult to manage depending on the feedline geometry.

#505492 https://doi.org/10.1364/OPTCON.505492
Journal © 2024 Received 11 Sep 2023; accepted 20 Dec 2023; published 3 Jan 2024

Lastly, planar transmission lines (TLs) can be integrated with an transmitter and receiver used to investigate a DUT [18–22]. Typically these structures are integrated into a CPS or CPW TL with an shunt or series photoconductive switch. There are some key benefits using this method; namely, the structure is inherently compatible with planar structures, the propagating mode is quasi-TEM which does not exhibit significant dispersion, and the overall system cost is relatively inexpensive. In this work we investigate filters using photoconductive switches integrated with CPS TLs. Currently, this combination allows for characterization of DUTs up-to 3 THz [22].

In previous works, planar filter demonstrations at THz frequencies do not perform network filter synthesis, that is, selecting the filter geometry to obtain a specific transfer function [23]. Instead, authors perform filter analysis which generally involves designing a periodic device [21] or metastructure [22,24–27], then confirming the transmission and reflection characteristics. While filter analysis is acceptable, it is generally advantageous to begin the design process by specifying targets such as cut-off frequency, minimal pass-band ripple, phase response, or roll-off rates. Here, we aim to demonstrate that microwave network synthesis filter design methods are valid at THz frequencies for *planar* structures. We note that many others have performed filter synthesis at THz frequencies using *non-planar* rectangular waveguides [28–30]. These non-planar filters are more common because they can be directly interfaced with a VNA equipped with extension modules. These filters are typically limited to operation as a band-pass filter due to the nature of wave propagation in a rectangular waveguide. We emphasize that the presented *planar* network synthesis filter utilizes the quasi-TEM mode and can be designed as a low-pass, high-pass, band-pass, or band-stop filter. A Bessel configuration has been selected for this proof-of-concept because it has desirable characteristics for pulsed THz systems. The linear phase response results in minimal pulse distortion which ensures the transmitted pulse is not significantly broadened. Reduction of pulse broadening improves the systems performance by reducing the impact of reflections and interference of the signal at the receiver which ultimately affects the spectral resolution.

We note that it is not straightforward to characterize devices at THz frequencies due to limitations such as source and detector availability and signal loss from potential substrate radiation. We have had success using our THz system-on-chip (TSoC) platform that uses planar CPS TLs on a thin Si_3N_4 substrate to overcome these challenges [31]. This methodology enables device characterization from DC to frequencies beyond 3 THz and is compatible with several planar TL configurations. In this work, we integrate a synthesized Bessel stepped-impedance low-pass filters (LPF) into a CPS TL. Other TL configurations (i.e. CPW, slotline, etc.) are equally viable; however, the CPS configuration is best suited to work with photoconductive switches as a sliding contact source and detector [6].

The novelty of this work can be summarized as the first demonstration of an THz integrated planar guided-wave all-pole filter (Bessel) using network filter synthesis using methods adopted from microwave engineering. We note that we have selected a common filter topology (stepped-impedance LPF) for this proof-of-concept verification at THz frequencies.

2. Design

In this work we implement and test several linear-phase stepped-impedance low-pass filters on the TSoC. This filter consists of alternating sections of low and high characteristic impedance of varying lengths which depending on the specific filter configuration (Butterworth, Bessel, Chebyshev, etc.). Figure 1 illustrates this concept. Here, we focus on the Bessel filter because of the short physical length and minimal pulse distortion characteristics.

Figure 2 illustrates cross section of a CPS TL on a thin substrate. The conductor width, separation, thickness, and conductivity are given by W, S, T = 200 nm, and $\sigma_c = 4.1 \times 10^7$ S/m, respectively. The selection of W and S is discussed below. The substrate thickness, relative

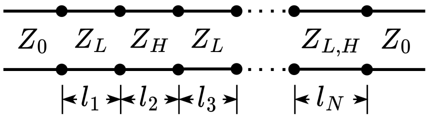

Fig. 1. Stepped Impedance Filter

permittivity, and loss tangent are given by $H = 1\mu m$, $\varepsilon_r = 7.6$, and $\tan\delta_e = 0.0056$, respectively [32].

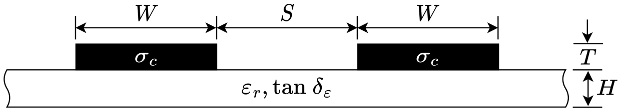

Fig. 2. Coplanar strip transmission cross section

We are interested in the systematic design and experimental results of a planar low-pass Bessel filter which has a uniquely high cut-off frequency (f_c>500 GHz) . This can be demonstrated by fabrication on a thin substrate. The design procedure consists of specifying the desired cut-off frequency (f_c) and filter order (N), then selecting the appropriate feedline impedance (Z_0), low impedance (Z_L), and high impedance (Z_H), then calculating the section lengths (l_n).

In this work, we select $f_c = 0.8$ THz and fabricate 3rd, 4th, and 5th order filters (N = 3, 4, 5). Figure 3 illustrates the overall structure and the three different filters. The manufacturing procedure consisted of depositing a 1 μm layer of Si_3N_4 onto a 500 μm thick Silicon wafer then etching regions where THz bandwidth signals propagates. This process results in a 1 μm thick Si_3N_4 substrate suspended in air which is supported on the edges by the Silicon frame. Next, the conductors were placed using mask alignment physical vapour deposition (Ti/Au, 10/200 nm). Lastly, the photoconductive switches (PCSs) were aligned with the conductors using a micromanipulator and bonded to the surface using Van der Waals bonding [33,34].

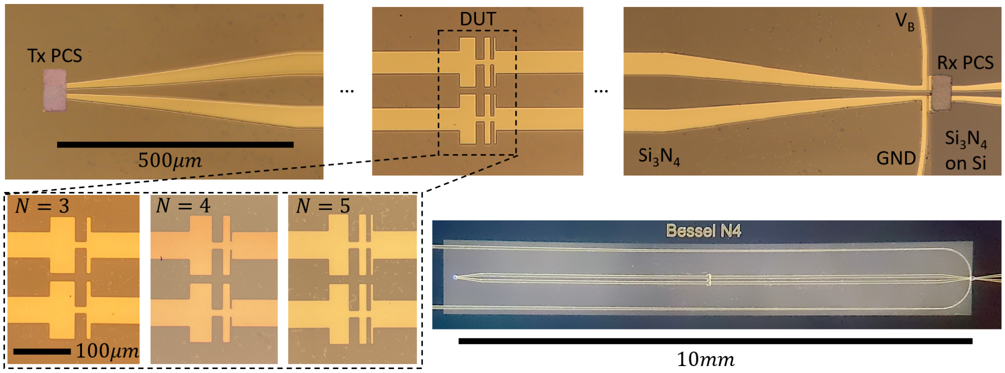

Fig. 3. Microscope images of the TSoC structure with integrated filters. V_B is the bias voltage with respect to ground (GND).

The feedline impedance, Z_0, was selected to correspond to a low loss ($\alpha \approx 0.8$ dB/mm at ≈800 GHz [21]) configuration which occurs when $S_0 = 70\mu m$ and $W_0 = 45\mu m$. For a stepped impedance LPF, it is desired to maximize the Z_H/Z_L ratio. Note that selection of Z_L and Z_H are subject to limitations. Also, we opted to keep the conductor center spacing constant (S+W=const.) throughout the filter length. Structures must have dimensions larger than 2 μm because of our photolithography resolution. At the upper end, given that we selected $S_0 = 70\mu m$ and $W_0 = 45\mu m$, this implies $S + W = 115\mu m$ and that $2\mu m < S_{L,H} < 113\mu m$ and $2\mu m < W_{L,H} < 113\mu m$.

In the past work [31], we found that structures with $W = 10\mu m$ behave well with acceptable resistive loss. Thus, for this work, we selected our high impedance sections to have $W_H = 10\mu m$ and $S_H = 105\mu m$. For the low impedance sections, dielectric breakdown must be considered because the CPS TL also functions to DC bias the transmitting photoconductive switch. To ensure proper DC biasing, S_L should be larger than S at the transmitter ($S_{Tx} = 10\mu m$). For this work, we have selected $S_L = 15\mu m$ and $W_L = 100\mu m$.

Next we must obtain Z_0, Z_H, and Z_L which requires the use of full-wave simulations to obtain the impedance at the cut-off frequency ($f_c = 0.8$ THz). Using ANSYS HFSS, we find $Z_0 = 234\Omega$, $Z_L = 131\Omega$, and $Z_H = 362\Omega$. We note that it is possible to use a quasi-static analytic models [35] to approximate these the characteristic impedances, but the frequency-dependence degrades the accuracy, for example, we find the quasi-static characteristic impedances to be $Z_0^{qs} = 264\Omega$, $Z_L^{qs} = 128\Omega$, and $Z_H^{qs} = 470\Omega$ which are not representative of the characteristic impedances at 0.8 THz.

Next we calculate the lengths of the individual sections. This is accomplished using well known methods [1]; we will quickly review the procedure here. Alternating low-impedance and high-impedance sections behave like alternating series inductors and shunt capacitors in a ladder circuit which exhibits low-pass behavior. The length of the individual sections are calculated using:

$$l_{L,n} = \frac{g_n}{\beta_c}\frac{Z_L}{Z_0}, \qquad l_{H,n} = \frac{g_n}{\beta_c}\frac{Z_0}{Z_H}. \tag{1}$$

where $\beta_c \approx 2\pi f_c/c$. The filter element values, g_n, depend on the filter type (Bessel, Butterworth, Chebyshev, etc.) and order. For completeness, the element values are copied into Table 1 for the filters of interest [1]. The sections lengths for the different filter orders are calculated using (1) and tabulated into Table 2.

Table 1. g_n for maximally flat Time Delay LPF prototype [1]

N	g_1	g_2	g_3	g_4	g_5	g_6
3	1.2550	0.5528	0.1922	1.0000	-	-
4	1.0598	0.5116	0.3181	0.1104	1.0000	-
5	0.9303	0.4577	0.3312	0.2090	0.0718	1.0000

Table 2. Section lengths for filters

N	$l_1[\mu m]$	$l_2[\mu m]$	$l_3[\mu m]$	$l_4[\mu m]$	$l_5[\mu m]$
3	42	21	6	-	-
4	35	20	11	4	-
5	31	18	11	8	2

3. Experiment

To characterize the filters we use a method similar to our previous work [22]. The experiment (Fig. 4) consists of a modified THz-time domain spectroscopy (TDS) system which requires the use of electrical and optical components.

The transmitter is a thin (1.5 μm) DC-biased (24V) PCS made of low-temperature grown gallium arsenide (LT-GaAs) that is Van der Waals (VDW) bonded to CPS TLs. A sub-picosecond (THz-bandwidth) electrical pulse is generated by illuminating the transmitter PCS with an 80 femtosecond (10 mW average) optical pulse from a mode-locked fiber laser. The electrical pulse

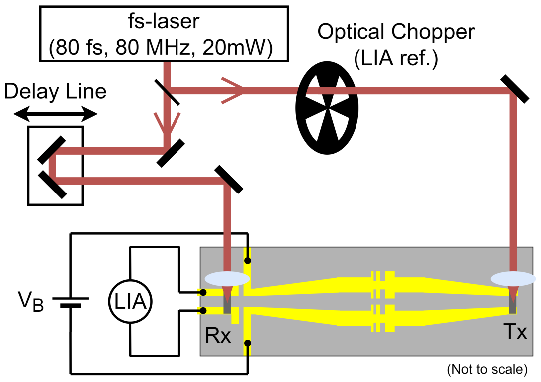

Fig. 4. Simplified experimental setup.

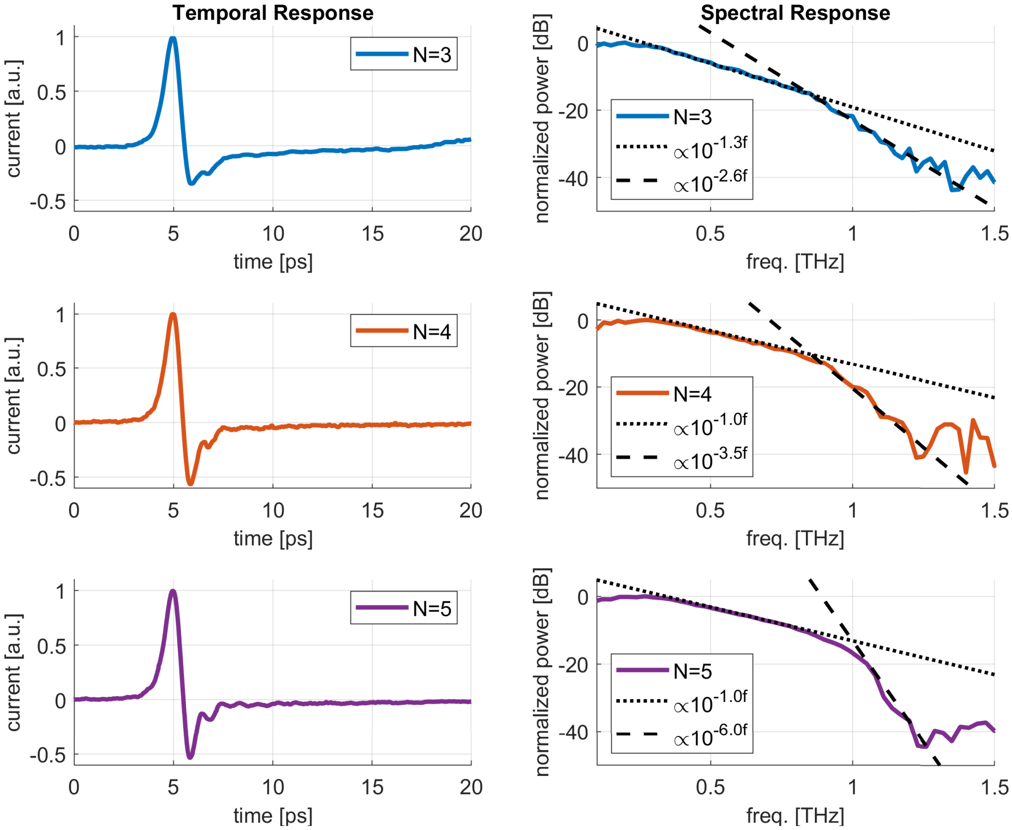

Fig. 5. Normalized experimental results for the N=3,4,5 Bessel filters.

propagates along the CPS TL and through the filters, or device-under-test (DUT), prior to arriving at the receiver. The receiver is another thin LT-GaAs PCS which is partially isolated from the transmitter circuit using a DC block. The receiver PCS is illuminated by the same optical pulse from the same mode-locked fiber laser, however, the pulse arrival time is made variable by the use of a mechanical delay line. Translation of the mechanical delay line reconstructs

OPTICS CONTINUUM

the transmitted signal which is given by the convolution of the incident electrical signal and receiver photoconductance which is measured by a lock-in amplifier (LIA) referenced to an optical chopper which modulates the optical beam in the transmitter path.

4. Results and discussion

Figure 5 plots the normalized experimental temporal and spectral responses for the filters illustrated in Fig. 3. The temporal response illustrates minimal pulse distortion which is consistent with the linear phase response of the designed filters. This property is desired in a transient system because the ringing associated with a non-linear phase response can adversely impact the spectral resolution. The spectral response is obtained by applying the discrete Fourier transform to the temporal response. Recognizing that finite duration transient pulses do not have a flat spectral response, we expect an inherent roll-off. This concept is illustrated by the dotted lines in Fig. 5. It is seen that the spectral response experiences a change of slope near the designed cut-off frequency at 0.8 THz. This effect is illustrated by the dashed lines. The exponential coefficients for the dotted and dashed lines are noted in the legend of Fig. 5. The increasing difference between the exponential coefficients for increasing filter order is expected since the higher order filters have a larger roll-off rate. Lastly, we note that any minor reflections which may occur between the receiver and other discontinuities are removed by windowing of the temporal response.

5. Conclusion

In this work we have designed, fabricated, and tested several integrated planar stepped-impedance low-pass Bessel filters for THz applications. Characterization at THz frequencies was enabled by the use of the TSoC platform. We found that the experimental results align well with theory which illustrates the great potential for further experiment and developing other network synthesis filters at THz frequencies. To the authors knowledge, this work demonstrates the first time a guided-wave planar filter designed using network synthesis has been demonstrated in the THz gap.

Funding. Natural Sciences and Engineering Research Council of Canada (RGPIN-2022-03277).

Acknowledgments. This work made use of the 4D LABS core facility at Simon Fraser University (SFU) supported by the Canada Foundation for Innovation (CFI), British Columbia Knowledge Development Fund (BCKDF), and Pacific Economic Development Canada (PacifiCan). We would like to acknowledge CMC Microsystems for the provision of products and services that facilitated this research.

Disclosures. The authors declare no conflicts of interest.

Data availability. Data underlying the results presented in this paper are not publicly available at this time but may be obtained from the authors upon reasonable request.

References

1. D. Pozar, *Microwave Engineering* (Wiley, 2011), 4th ed.
2. A. Oppenheim, A. Willsky, and S. Nawab, *Signals and Systems* (Prentice Hall, 1997), 2nd ed.
3. M. George, L. Young, and E. Jones, *Microwave Filters, Impedance-Matching Networks, and Coupling Structures* (Artech House, New York, 1980).
4. A. Yariv and P. Yeh, *Photonics: Optical Electronics in Modern Communications* (Oxford University Press, 2006), 6th ed.
5. G. Valušis, A. Lisauskas, H. Yuan, *et al.*, "Roadmap of terahertz imaging 2021," Sensors **21**(12), 4092 (2021).
6. D. Grischkowsky, M. Ketchen, C.-C. Chi, *et al.*, "Capacitance free generation and detection of subpicosecond electrical pulses on coplanar transmission lines," IEEE J. Quantum Electron. **24**(2), 221–225 (1988).
7. H. Cheng, J. Whitaker, T. Weller, *et al.*, "Terahertz-bandwidth pulse propagation on a coplanar stripline fabricated on a thin membrane," IEEE Microw. Guid. Wave Lett. **4**(3), 89–91 (1994).
8. L. Smith, W. Gomaa, H. Esmaeilsabzali, *et al.*, "Tapered transmission lines for terahertz systems," Opt. Express **29**(11), 17295–17303 (2021).
9. D. Koller, S. Durant, C. Rowland, *et al.*, "Initial measurements with wm164 (1.1–1.5 THz) VNA extenders," in *2016 41st International Conference on Infrared, Millimeter, and Terahertz waves (IRMMW-THz)*, (IEEE, 2016), pp. 1–2.

10. W. Gao, W. S. L. Lee, C. Fumeaux, *et al.*, "Effective-medium-clad Bragg grating filters," APL Photonics **6**(7), 076105 (2021).
11. J. Cabello-Sánchez, V. Drakinskiy, J. Stake, *et al.*, "A corrugated planar-Goubau-line termination for terahertz waves," IEEE Microw. Wireless Tech. Lett. **33**(6), 643–646 (2023).
12. M. F. Bauwens, N. Alijabbari, A. W. Lichtenberger, *et al.*, "A 1.1 THz micromachined on-wafer probe," in *2014 IEEE MTT-S International Microwave Symposium (IMS2014)*, (IEEE, 2014), pp. 1–4.
13. S.-H. Kim, E. S. Lee, Y. B. Ji, *et al.*, "Improvement of THz coupling using a tapered parallel-plate waveguide," Opt. Express **18**(2), 1289–1295 (2010).
14. M. Mbonye, R. Mendis, and D. M. Mittleman, "A terahertz two-wire waveguide with low bending loss," Appl. Phys. Lett. **95**(23), 233506 (2009).
15. S. Atakaramians, S. Afshar, T. M. Monro, *et al.*, "Terahertz dielectric waveguides," Adv. Opt. Photonics **5**(2), 169–215 (2013).
16. R. A. Lewis, "A review of terahertz sources," J. Phys. D: Appl. Phys. **47**(37), 374001 (2014).
17. R. A. Lewis, "A review of terahertz detectors," J. Phys. D: Appl. Phys. **52**(43), 433001 (2019).
18. L. Desplanque, J.-F. Lampin, and F. Mollot, "Generation and detection of terahertz pulses using post-process bonding of low-temperature-grown gaas and algaas," Appl. Phys. Lett. **84**(12), 2049–2051 (2004).
19. S. Kasai, A. Tanabashi, K. Kajiki, *et al.*, "Micro strip line-based on-chip terahertz integrated devices for high sensitivity biosensors," Appl. Phys. Express **2**, 062401 (2009).
20. A. M. Potts, A. K. Nayak, M. Nagel, *et al.*, "On-chip time-domain terahertz spectroscopy of superconducting films below the diffraction limit," Nano Lett. **23**(9), 3835–3841 (2023).
21. W. Gomaa, L. Smith, V. Shiran, *et al.*, "Terahertz low-pass filter based on cascaded resonators formed by cps bending on a thin membrane," Opt. Express **28**(21), 31967–31978 (2020).
22. L. Smith, V. Shiran, W. Gomaa, *et al.*, "Characterization of a split-ring-resonator-loaded transmission line at terahertz frequencies," Opt. Express **29**(15), 23282–23289 (2021).
23. D. Swanson and G. Macchiarella, "Microwave filter design by synthesis and optimization," IEEE Microwave Mag. **8**(2), 55–69 (2007).
24. M. Gil, J. Bonache, and F. Martín, "Metamaterial filters: a review," Metamaterials **2**(4), 186–197 (2008).
25. J. Cabello-Sánchez, V. Drakinskiy, J. Stake, *et al.*, "Capacitively-coupled resonators for terahertz planar-Goubau-line filters," IEEE Trans. THz Sci. Technol. **13**(1), 58–66 (2023).
26. Y. J. Guo, K. D. Xu, and X. Tang, "Spoof plasmonic waveguide developed from coplanar stripline for strongly confined terahertz propagation and its application in microwave filters," Opt. Express **26**(8), 10589–10598 (2018).
27. K.-D. Xu, F. Zhang, Y. Guo, *et al.*, "Spoof surface plasmon polaritons based on balanced coplanar stripline waveguides," IEEE Photon. Technol. Lett. **32**(1), 55–58 (2020).
28. S. Liu, J. Hu, Y. Zhang, *et al.*, "1 THz micromachined waveguide band-pass filter," J. Infrared, Millimeter, and Terahertz Waves **37**(5), 435–447 (2016).
29. X. Shang, H. Yang, D. Glynn, *et al.*, "Submillimeter-wave waveguide filters fabricated by SU-8 process and laser micromachining," IET Microwaves, Antennas & Propag. **11**, 2027–2034 (2017).
30. Z.-W. Miao, X. Liu, Z.-C. Hao, *et al.*, "A 0.9-THz integrally manufactured high-precision waveguide cavity filter using electrochemical micromachining technology," IEEE Trans. on Microw. Theory Tech. **71**(10), 4494–4504 (2023).
31. L. Smith and T. Darcie, "Demonstration of a low-distortion terahertz system-on-chip using a CPS waveguide on a thin membrane substrate," Opt. Express **27**(10), 13653–13663 (2019).
32. G. Cataldo, J. A. Beall, H.-M. Cho, *et al.*, "Infrared dielectric properties of low-stress silicon nitride," Opt. Lett. **37**(20), 4200–4202 (2012).
33. E. Yablonovitch, D. Hwang, T. Gmitter, *et al.*, "Van der Waals bonding of GaAs epitaxial liftoff films onto arbitrary substrates," Appl. Phys. Lett. **56**(24), 2419–2421 (1990).
34. R. D. V. Ríos, S. Bikorimana, M. A. Ummy, *et al.*, "A bow-tie photoconductive antenna using a low-temperature-grown GaAs thin-film on a silicon substrate for terahertz wave generation and detection," J. Opt. **17**(12), 125802 (2015).
35. R. Garg, I. Bahl, and M. Bozzi, *Microstrip Lines and Slotlines* (Artech House, 2013), 3rd ed.

66.51.131.199 {ts '2025-02-17 14:59:19'}

Appendix D

Genetic Algorithm-Based Inverse Design of Guided Wave Planar Terahertz Filters, Copy of [4]

arXiv:2506.03372v1 [physics.app-ph] 3 Jun 2025

Genetic Algorithm-Based Inverse Design of Guided Wave Planar Terahertz Filters

Ali Dehghanian[1,2], *Student, IEEE,* Thomas Darcie[1], *Fellow, IEEE* and Levi Smith[1,2,*], *Member, IEEE,*

***Abstract*—We present a genetic algorithm (GA)-based inverse design framework for synthesizing high-performance planar terahertz (THz) filters integrated with coplanar striplines (CPSs). The method efficiently explores high-dimensional design spaces to generate filter geometries matching user-defined S-parameter magnitude and phase responses, while enforcing structural connectivity for compatibility with terahertz system-on-chip (TSoC) platforms. To accelerate optimization, filter performance is evaluated using the ABCD matrix method, providing a significant computational advantage over full-wave simulations. Final validation is performed through finite element method (FEM) simulations. As a proof of concept, we design band-stop filters with center frequencies of 0.6, 0.8, and 1.0 THz, each with a 150 GHz target bandwidth, and demonstrate tunable rejection depths within a constant physical footprint. Optimization is guided by minimizing the root-mean-square error (RMSE) between simulated and target S-parameters.**

***Index Terms*—Terahertz filters, Genetic algorithm (GA), Inverse design, Coplanar stripline (CPS), Terahertz System-on-chip (TSoC), ABCD matrix method**

I. INTRODUCTION

TERAHERTZ (THz) filters are required for next-generation THz systems, allowing spectral control by selectively transmitting desired frequency bands while suppressing out-of-band signals. These functionalities are vital for a range of applications, including high-speed wireless communications, non-invasive medical imaging, and spectroscopic sensing [1]–[6]. The ability to engineer and tailor spectral responses with high accuracy directly impacts the efficiency, resolution, and functionality of THz devices across scientific, medical, and industrial domains.

Structurally, THz filters can be classified into planar and non-planar topologies, each offering specific advantages in terms of performance metrics such as insertion loss, bandwidth, and frequency selectivity, as well as fabrication compatibility and system-level integrability. Waveguide-based filters, such as rectangular metallic and parallel plate waveguides, are popular for their low insertion loss and effective mode confinement in conventional setups [7], [8]. Planar configurations, including coplanar waveguides (CPW) and coplanar striplines (CPS), are particularly attractive for on-chip applications due to their compatibility with standard photolithography and compact on-chip footprint [9]–[11].

Alternative filter designs, such as photonic crystal filters, exploit periodic dielectric structures to induce photonic bandgaps, offering precise spectral shaping capabilities [12]. Metamaterial and metasurface filters, composed of engineered sub-wavelength resonant elements, provide enhanced design flexibility and enable tailored responses such as narrowband, broadband, and multi-band filtering [13], [14]. Resonator-based filters, including ring and cavity resonators, are also widely used in integrated planar formats due to their high quality (Q) factors and small footprint [15], [16].

Traditionally, the design of THz filters has relied heavily on the designer's expertise and theoretical models rooted in microwave and optical engineering. These conventional methods typically involve iterative tuning of structural parameters based on analytical frameworks such as transmission line theory and coupled-mode theory. While these models offer valuable physical insight, they are often limited in their applicability to geometrically complex or multi-objective structures. Consequently, the design process remains labor-intensive and constrained in its ability to efficiently explore the vast and high-dimensional design space, increasing the risk of overlooking high-performing or unconventional solutions. These limitations are particularly evident in the development of THz components such as filters, resonators, polarizers, and power splitters, where optimal performance often depends on intricate geometries and tightly coupled physical effects.

Here we adopt inverse design that was originally developed to optimize nanophotonic and electromagnetic structures beyond the capabilities of traditional analytical approaches. Early applications in photonic systems demonstrated its ability to generate compact, high-performance devices with non-intuitive geometries that satisfy specific optical transmission or field distribution requirements. In particular, its application to photonic integrated circuits (PICs) has facilitated the design of densely integrated components that offer enhanced functionality, compact footprints, and improved performance [17]. The maturity and success of inverse design in silicon photonics not only validate its effectiveness but also highlight its potential for addressing analogous challenges in emerging THz integrated systems.

Several recent studies have explored inverse design strategies for optimizing THz components. Zhang et al. [18] proposed a genetic algorithm (GA)-based inverse design framework to optimize dispersion profiles for broadband impedance matching. Their dual-metasurface absorber achieved 88% absorption from 0.21 to 5 THz, demonstrating both high performance and computational efficiency. In a follow-up study, the same group used GA-assisted optimization to enhance THz metasurface design, using multiple objective functions

---

[1]Department of Electrical and Computer Engineering, University of Victoria, Victoria, BC, V8P 5C2 Canada

[2]Centre for Advanced Materials and Related Technology (CAMTEC), University of Victoria, 3800 Finnerty Rd, Victoria, BC, V8P 5C2, Canada.

[*]Corresponding author: levismith@uvic.ca

This work was supported by a NSERC Discovery Grant.

Manuscript received May xx, xxxx; revised May xx, xxxx.

to improve design reliability and automation [19].

Beyond GAs, machine learning-based approaches have been applied to accelerate and enhance the inverse design process. Li et al. [20] used artificial neural networks (ANNs) to accurately predict reflection spectra and optimize micro/nano THz metasurface structures with custom optical responses. Similarly, Mashayekhi et al. [21] developed an ANN-assisted inverse-designed graphene-based absorber, achieving 96.33% absorption across 0.5–10 THz and enabling rapid parameter selection for THz detection. Deep learning has also been extended to THz antenna design. Karahan et al. [22] introduced a deep neural network (DNN)-based inverse design approach for multi-band graphene patch antennas operating between 2–5 THz. Their model achieved 13 frequency bands, up to 8.8 dB gain, full 360° beam steering, and 93% prediction accuracy, significantly accelerating the design cycle. Furthermore, Ding et al. [23] proposed a Finite-Difference Time-Domain (FDTD)-based inverse design framework for a 3D-printable diffractive optical element (DOE) capable of THz spectral splitting between 0.5–0.7 THz. Their simulation and experimental results demonstrated a compact, low-cost solution for portable THz spectroscopy and communication.

Although inverse design methodologies have been successfully applied to various THz components, such as metasurfaces, absorbers, antennas, and filters, the efficient design of planar THz filters integrated with guided-wave transmission lines remains largely unexplored. Addressing this gap, we present a GA-based inverse design framework specifically tailored for planar guided-wave THz on-chip filters. Using evolutionary optimization strategies, the proposed method enables the systematic exploration of complex, high-dimensional design spaces and facilitates the realization of high-performance THz filters compatible with standard lithographic fabrication processes.

To ensure computational feasibility, filter performance is evaluated using the ABCD matrix method, which offers substantial acceleration compared to full-wave simulations while maintaining sufficient modeling accuracy. The final validation of the optimized designs is performed through finite element method (FEM) simulations. As a proof-of-concept, we demonstrate the inverse design of band-stop filters with varying center frequencies and rejection depths, all within a fixed device footprint. To the best of our knowledge, this is the first application of a GA-based inverse design approach that employs the ABCD matrix method for CPS-integrated THz filters, highlighting its potential to advance compact, fabrication-ready devices in integrated THz systems.

II. METHODS

Traditional forward design methodologies for THz filters are largely rooted in analytical theories derived from microwave engineering. Typically, the design of periodic band-stop THz filters in planar waveguide structures begins by specifying a center frequency and target bandwidth, followed by estimating the filter period based on the effective relative permittivity of supported modes, usually obtained through full-wave simulations. The geometric parameters are then derived from this model and iteratively fine-tuned through additional simulations. Although this approach can yield functional designs, it inherently depends on simplifying assumptions and limited parameter sweeps, which constrain the design space and limit opportunities for performance optimization.

In contrast, inverse design frameworks allow users to define a desired spectral response, including both magnitude and phase characteristics, and automatically search for optimal geometries that meet those specifications. This enables the discovery of non-intuitive, high-performance structures that would be difficult to realize through conventional methods. Moreover, by formulating the design task as an optimization problem, inverse design reduces the reliance on trial-and-error tuning and provides a direct route to meeting stringent spectral requirements, particularly in compact and fabrication-constrained THz platforms.

In this work, we focus on the inverse design of optimized planar THz filters using a GA-based framework. Several synthesized band-stop filters are presented as proof-of-concept demonstrations to validate the proposed optimization approach. These filters feature varying center frequencies, bandwidths, and rejection depths, showcasing the flexibility and capability of the inverse design method. Band-stop filters were chosen as the initial test case to allow direct comparison with previous forward-designed filters, providing a meaningful benchmark for evaluating the performance improvements achieved through the GA-based inverse design process.

A. *Inverse design with genetic algorithm*

The GA offers several advantages that make it particularly suitable for the inverse design of complex electromagnetic structures. Unlike gradient-based optimization methods, GA does not require computation of gradients of the fitness (objective) function. This characteristic makes it more robust against local minima, which are common in non-convex high-dimensional design spaces [24].

In this work, we employ a GA to optimize the binary distribution of gold (Au) and air pixels within a planar THz filter structure. Each candidate solution is encoded as a chromosome representing the spatial arrangement of pixels that evolve over successive generations through selection, crossover, and mutation. The GA parameters are carefully tuned to address the discrete, high-dimensional nature of the problem.

The mutation operator introduces diversity by toggling individual bits, corresponding to changing the material assignment of specific pixels. This allows for the exploration of novel topologies that can enhance the S-parameter response. Crossover combines favorable traits from two parent designs, while elitism ensures that top-performing individuals are preserved. The population size balances exploration breadth with computational feasibility, considering the cost of simulations [24].

Several strategies are employed to mitigate the risk of convergence to local minima that are common in nonconvex optimization landscapes defined by electromagnetic performance metrics. Increasing the mutation rate enhances diversity and allows broader sampling of the solution space. When

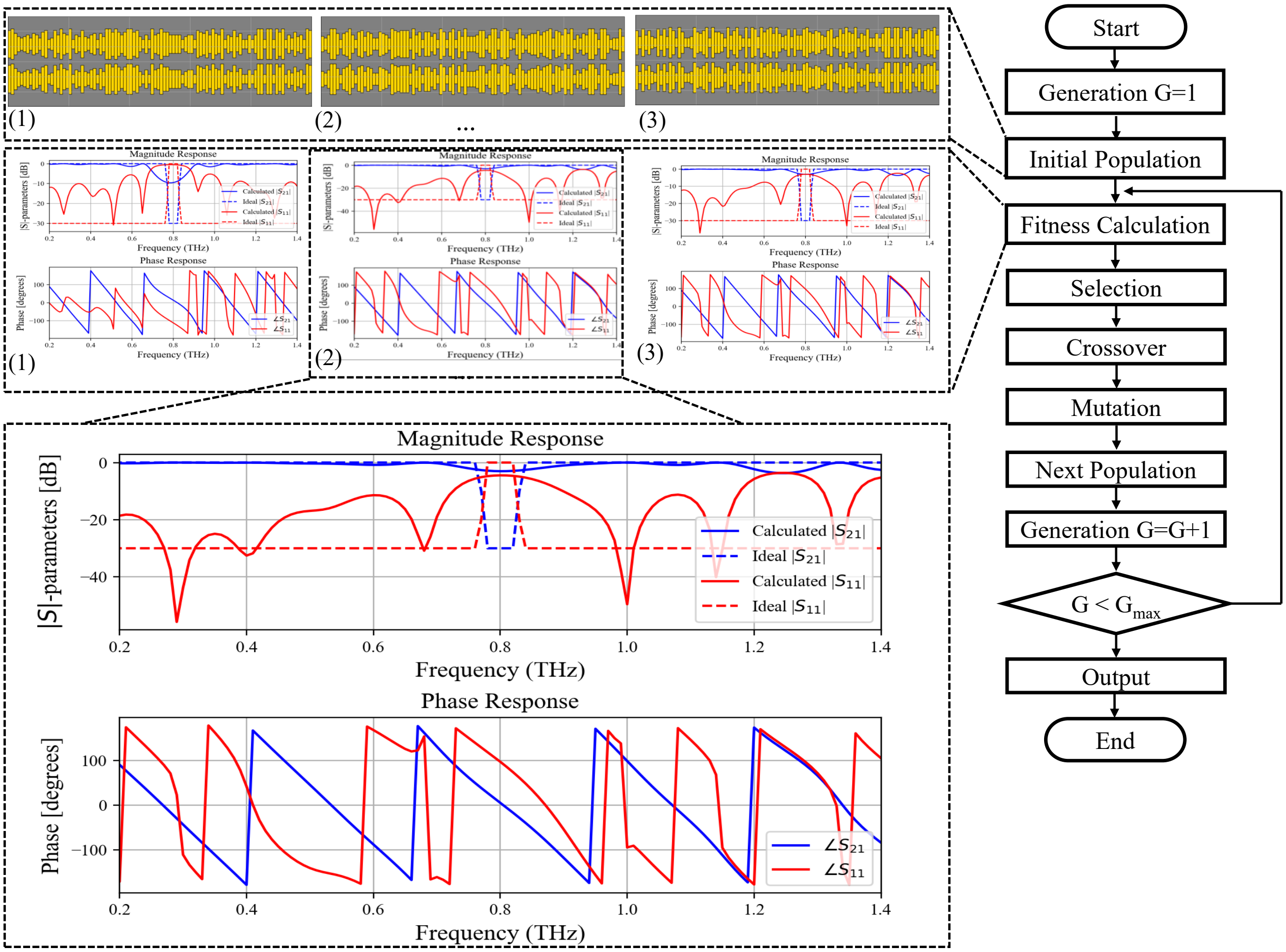

Fig. 1. Flowchart of the GA optimization process. The randomly generated initial population of THz filters is depicted, along with their corresponding S-parameters (both magnitude and phase). The algorithm iterates through successive generations, refining the population until one of two stopping criteria is met: (1) the number of generations G reaches the predefined maximum $G_{\max}$, or (2) the error function converges below a specified threshold.

a locally optimal design is suspected, its genome can be reintroduced in subsequent runs to allow refined exploration around its neighborhood. Extending the number of generations provides additional opportunities for the evolution of high-performance filter geometries. Additionally, running the GA multiple times with randomized initial populations allows for statistical comparison across runs, providing information on the robustness of the solutions and the sensitivity of the design problem to initial conditions.

Figure 1 presents the flow diagram of the GA optimization process that we used to design THz filters. The process begins with a randomly generated initial population of filters, each associated with its corresponding S-parameters, including both magnitude and phase. As the algorithm progresses, iteratively refines the population across successive generations based on performance feedback (fitness function). This evolutionary process enables the development of optimized THz filters that satisfy the specified design criteria.

We enforce structural continuity for compatibility with our THz test platform using a connectivity constraint that is incorporated into the design formulation. Specifically, the filter must maintain a continuous conductive pathway to facilitate voltage biasing of the transmitter photoconductive switch (PCS). Without such a constraint, generated structures may introduce discontinuities (i.e., a DC block), and the device would fail to operate correctly during experimentation. While this work does not include experimental validation, the design framework is developed with all necessary constraints in place to facilitate future experimental implementation.

With the structural constraints integrated into the initialization process, the inverse design problem is formally defined and formulated for optimization. Each candidate solution is represented as a binary matrix encoding the spatial distribution of gold and air pixels within the designated design region. The pixel size was set to 4 µm×10 µm to balance resolution requirements, fabrication feasibility, and computational cost. This binary representation serves as input to the GA, which iteratively evolves the population to maximize the fitness function, defined as the figure of merit (FOM), that quantifies how closely the simulated electromagnetic response matches the S-parameters of the target filter.

Figure 2 illustrates the design framework and key structural

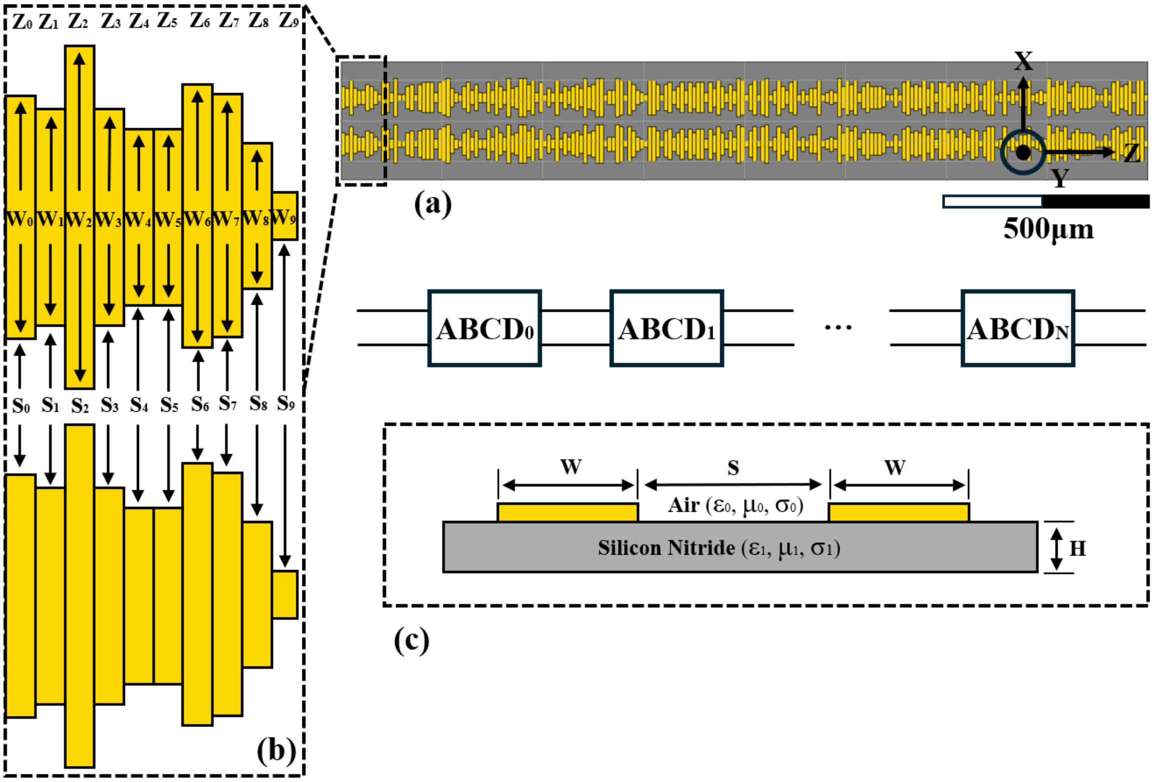

Fig. 2. Illustration of the design framework and associated parameters. (a) Example of a planar THz filter structure synthesized using a GA-based inverse design approach. The overall framework dimensions are 300 μm $\times$ 2000 μm, corresponding to 200 discrete columns in the propagation direction. (b) Magnified view of a section of the filter, highlighting key design parameters: impedance (Z), conductor width (W), and strip spacing (S). (c) Cross-sectional schematic of the filter structure, depicting gold metallic layers patterned on a silicon nitride ($\mathrm{Si_3N_4}$) membrane substrate.

parameters of the planar THz filter investigated in this work. The filter region spans an area of 300 μm in width and 2000 μm in length, corresponding to 200 discrete columns along the propagation direction. This discretized domain serves as the optimization space for the GA-based inverse design process, wherein the binary configuration of each column defines the local characteristic impedance profile of the filter.

A magnified view of a representative section is shown in Fig. 2(b), highlighting essential design parameters, including the local characteristic impedance (Z), conductor width (W), and strip spacing (S). These geometrical features collectively govern the electromagnetic response of the structure, enabling fine-tuning of the filter's spectral characteristics. In the design space explored, W varies between 10 μm and 90 μm, while S ranges from 5 μm to 90 μm, ensuring compatibility with fabrication constraints and impedance requirements.

Figure 2(c) presents a cross-sectional schematic of the filter, depicting gold metallic layers patterned on a silicon nitride ($\mathrm{Si_3N_4}$) membrane substrate. This material platform ensures compatibility with standard microfabrication processes while minimizing substrate losses at THz frequencies. The combination of geometrical flexibility and material selection facilitates the realization of high-performance THz filters within a compact planar footprint.

After initializing the population, each candidate design is evaluated using the fitness function. The fitness function quantifies performance by calculating the root-mean-square error (RMSE) between the simulated and target scattering parameters S-parameters), incorporating both magnitude and phase.

Formally, the fitness function $f(\mathbf{x}_i^t) : \mathbb{R}^n \to \mathbb{R}$ maps design parameters $\mathbf{x}_i^t$ at iteration t to a scalar score reflecting spectral deviation. The loss function $\mathcal{L} = -\mathrm{RMSE}$ guiding optimization is expressed as:

$$\begin{aligned}\mathcal{L} = {} & w_1\sqrt{\frac{1}{N}\sum_{i=1}^{N}(S_{21}^{\mathrm{dB}}(f_i) - S_{21,\mathrm{target}}^{\mathrm{dB}}(f_i))^2} \\ & + w_2\sqrt{\frac{1}{N}\sum_{i=1}^{N}(S_{11}^{\mathrm{dB}}(f_i) - S_{11,\mathrm{target}}^{\mathrm{dB}}(f_i))^2} \\ & + w_3\sqrt{\frac{1}{N}\sum_{i=1}^{N}(\angle S_{11}(f_i) - \angle S_{11,\mathrm{target}}(f_i))^2} \\ & + w_4\sqrt{\frac{1}{N}\sum_{i=1}^{N}(\angle S_{21}(f_i) - \angle S_{21,\mathrm{target}}(f_i))^2}\end{aligned} \tag{1}$$

where N is the number of frequency points, and w_1, w_2, w_3, w_4 are weighting factors for magnitude and phase components of transmission (S_{21}) and reflection (S_{11}) responses. This formulation enables precise, frequency-aware tuning of THz filter designs through genetic optimization.

In this work, the target phase response was specified as linear; therefore, w_3 and w_4 were assigned to 10% of the total loss function weight. As a result, the optimization process initially prioritizes minimizing the magnitude-related components (w_1 and w_2) of the loss function, with phase error contributing less strongly during early optimization. In the later stages, the algorithm fine-tunes the design by evaluating the differential phase between adjacent frequency points and reducing phase variations through the influence of w_3 and w_4.

A population size of 200 was selected to balance exploration breadth with computational feasibility. Preliminary experiments conducted with population sizes of 50, 100, 200, and 400 showed diminishing fitness improvements beyond 200, while computational time scaled proportionally. Each generation evolves through a combination of elitism, selection, crossover, and mutation, with the objective of maximizing the fitness function.

To guide the evolutionary process toward optimal solutions, an elite group comprising the top 30 individuals (15% of the population) with the highest fitness values is directly carried over to the next generation. This elite fraction was empirically chosen to balance convergence stability and exploration diversity: higher elite rates ($> 20\%$) accelerated convergence but increased the risk of premature convergence to local optima, while lower rates ($< 10\%$) slowed convergence without yielding notable diversity gains. The elite individuals are identified by simulating all 200 candidates, ranking them by fitness, and preserving the top 30.

The remaining 170 candidates are generated through the application of genetic operators: selection, crossover, and mutation. To maintain population diversity and promote exploration of the design space, a probabilistic rank-based tournament selection strategy is employed. In this method, a subset of T individuals is randomly sampled from the population, and an individual is selected from the tournament with a probability that favors higher-ranked individuals. The probability of selecting an individual i with rank r_i (where $r = 1$ corresponds to the highest fitness) is given by:

$$P(i) = \frac{(1-s)s^{r_i - 1}}{1 - s^T} \tag{2}$$

where $s \in (0, 1)$ is the selection pressure and T is the tournament size [25], [26]. This probabilistic approach allows lower-ranked individuals to be selected with nonzero probability, promoting genetic diversity while still biasing selection toward fitter individuals.

A tournament size of $T = 4$ was selected based on literature recommendations for moderate selection pressure in combinatorial GAs [24], [25]. Preliminary tests showed that smaller T slowed convergence, while larger T reduced diversity. This value was empirically validated to achieve consistent fitness improvements across runs, balancing exploitation and exploration and reducing the risk of premature convergence.

Crossover is employed as a recombination operator to generate new candidate solutions by combining structural characteristics from two parent individuals. In the context of grid-based THz filter design, a two-point crossover strategy is implemented to facilitate the creation of novel geometries while preserving connectivity and material constraints (Fig. 3). Given two parent grids P_1 and P_2, two crossover points c_1 and c_2 are randomly selected at uniformly distributed positions within the grid such that $2 \leq c_1 < c_2 \leq C - 1$, where C represents the total number of columns in the grid. Two offspring, O_1 and O_2, are then generated by exchanging the column segments between c_1 and c_2:

$$O_1 = [P_1(:, 1 : c_1),\ P_2(:, c_1 : c_2),\ P_1(:, c_2 : C)] \tag{3}$$

$$O_2 = [P_2(:, 1 : c_1),\ P_1(:, c_1 : c_2),\ P_2(:, c_2 : C)] \tag{4}$$

Here, $P(:, a : b)$ denotes the submatrix containing columns a to b. The use of two crossover points allows for greater structural variation compared to single-point schemes, while maintaining design continuity and compatibility with the CPS platform.

To further enhance diversity, mutation is applied to 10% of the selected individuals. During mutation, a randomly chosen bit in the binary chromosome is flipped (i.e., "0" to "1" or "1" to "0"), corresponding to a material change at a specific pixel—effectively toggling it between a gold and air region. This stochastic perturbation introduces novel traits into the population and supports broader exploration of the design space. Importantly, all mutation operations are performed while enforcing the continuity constraint, ensuring that conductive pathways remain uninterrupted to maintain compatibility with the CPS platform in future experiments.

III. SIMULATION RESULTS AND DISCUSSION

To compute the S-parameters and subsequently evaluate the RMSE, two computational methodologies are available: (1) an analytical approach based on the ABCD transmission matrix method, and (2) a full-wave numerical analysis performed using commercial software such as ANSYS HFSS. Given the substantial computational cost associated with FEM-based simulations, the ABCD transmission matrix method was employed as an efficient surrogate modeling approach. This method provides a computational speed-up exceeding three orders of magnitude compared to full-wave simulations, thereby enabling rapid evaluation of design candidates during the optimization process while maintaining sufficient accuracy for guiding the inverse design. Prior studies have demonstrated a strong correlation between the results obtained from this analytical approach and experimental measurements, thereby validating its accuracy [27].

The designed filters are composed of cascaded unit cells, each modeled as a section of transmission line with a specific characteristic impedance. These unit cells are arranged laterally along the column axis of the design grid, with each column corresponding to one such unit cell. To accurately model the behavior of these structures, each unit cell is represented by a two-port ABCD matrix, which characterizes the voltage and current relationship at its input and output ports. This modeling approach assumes that each section behaves as a uniform transmission line, which is a valid approximation under the

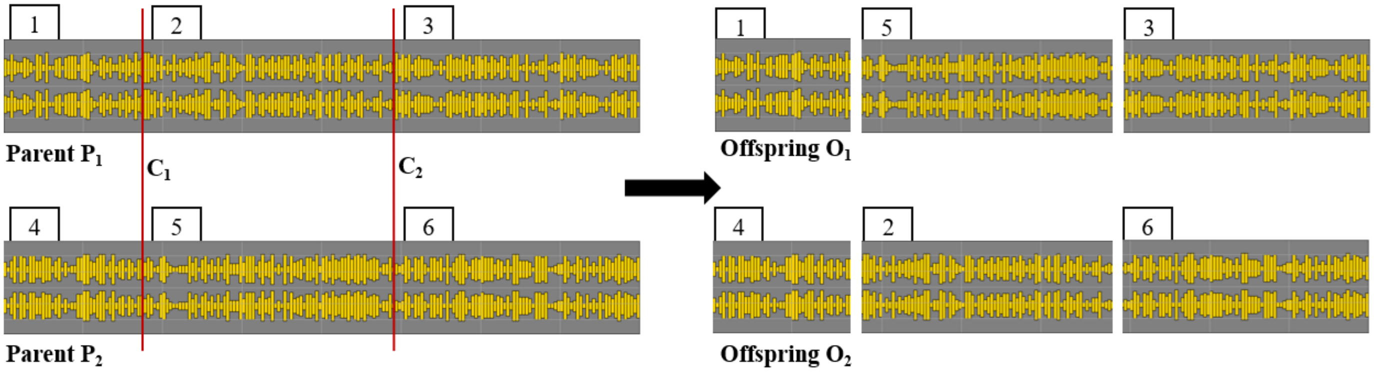

Fig. 3. Illustration of the two-point crossover mechanism employed in the GA-based inverse design of THz filters. This crossover process facilitates the recombination of structural features from two-parent designs, generating offspring with inherited characteristics that contribute to the optimization of the filter's electromagnetic response.

quasi-static (QS) regime—where the physical dimensions of the unit cells are much smaller than the operating wavelength.

The ABCD matrix of a transmission line segment of length Λ, characteristic impedance Z, and phase constant β is given by:

$$\begin{bmatrix} A_{\text{cell}} & B_{\text{cell}} \\ C_{\text{cell}} & D_{\text{cell}} \end{bmatrix} = \begin{bmatrix} \cos(\beta\Lambda) & jZ\sin(\beta\Lambda) \\ j\frac{1}{Z}\sin(\beta\Lambda) & \cos(\beta\Lambda) \end{bmatrix} \tag{5}$$

The overall ABCD matrix for a filter composed of N cascaded unit cells is obtained by sequentially multiplying the individual ABCD matrices corresponding to each unit cell:

$$\begin{bmatrix} A & B \\ C & D \end{bmatrix}_{\text{total}} = \begin{bmatrix} A_{C1} & B_{C1} \\ C_{C1} & D_{C1} \end{bmatrix} \cdot \begin{bmatrix} A_{C2} & B_{C2} \\ C_{C2} & D_{C2} \end{bmatrix} \cdots \begin{bmatrix} A_{CN} & B_{CN} \\ C_{CN} & D_{CN} \end{bmatrix} \tag{6}$$

Each section's QS characteristic impedance is computed analytically based on its lateral geometry, including the conductor width W and the inner strip spacing S, using the closed-form expression for CPS transmission lines [28]:

$$Z_{\text{CPS}} = \frac{120\pi}{\sqrt{\varepsilon_{re}}}\frac{K(k_{\text{CPS}})}{K(k'_{\text{CPS}})}, \quad k_{\text{CPS}} = \frac{S}{S+2W} \tag{7}$$

where $K(k)$ and $K(k')$ are the complete elliptic integrals of the first kind, and ε_{re} is the effective relative permittivity of the substrate.

Finally, the scattering parameters (S-parameters) are extracted from the total ABCD matrix using standard transformations [29]:

$$S_{11} = \frac{A + \frac{B}{Z_{\text{CPS}}} - CZ_{\text{CPS}} - D}{A + \frac{B}{Z_{\text{CPS}}} + CZ_{\text{CPS}} + D}, S_{21} = \frac{2}{A + \frac{B}{Z_{\text{CPS}}} + CZ_{\text{CPS}} + D} \tag{8}$$

This modeling framework enables rapid and reasonably accurate prediction of the electromagnetic response of cascaded THz filters, making it well-suited for evaluating the fitness of a large number of candidate structures during the inverse design process, particularly in early optimization stages where full-wave simulations would be computationally prohibitive.

Figure 4 summarizes the spectral response and structural realization of a planar band-stop filter synthesized using the proposed GA-based inverse design framework. The target specifications include a center frequency of 0.8 THz and a 3-dB bandwidth of 200 GHz. In Fig. 4(a), the calculated magnitude response of S_{21} and S_{11}, obtained via the ABCD matrix method, is compared against the target response. The design meets the specified rejection depth and bandwidth with high accuracy. Figure 4(b) presents the corresponding phase response, with particular emphasis on the linear phase progression of S_{21} across the passband, which is critical for dispersion-sensitive THz applications. A direct comparison between the ABCD matrix-based results and full-wave electromagnetic simulations from ANSYS HFSS is provided in Fig. 4(c). Strong agreement is observed across most of the frequency range, validating the modeling framework. However, minor discrepancies emerge at higher frequencies (above 0.9 THz), where the ABCD matrix method begins to diverge from HFSS simulation. These deviations are primarily attributed to radiation losses and edge diffraction effects that are not captured by the quasi-static assumptions inherent in the ABCD matrix model. Lastly, Fig. 4(d) depicts the unconventional filter geometry synthesized through the GA optimization process, illustrating the method's ability to generate non-intuitive yet high-performance designs within the imposed fabrication constraints.

To further investigate the electromagnetic behavior of the optimized filter structure, the electric field distribution was analyzed at multiple frequencies spanning the passband and stopband. Figure 5(a) shows the simulated in-plane E-field profiles at 0.6 THz, 0.8 THz, and 1.0 THz. At 0.6 THz and 1.0 THz, the field propagates effectively through the structure, confirming low insertion loss in the passbands. In contrast, at 0.8 THz—corresponding to the filter's stopband—strong field attenuation is observed, demonstrating effective suppression of transmission and validating the spectral selectivity of the inverse-designed filter.

Figure 5(b) presents the field profile at 1.4 THz on a logarithmic scale to highlight radiation effects at higher frequencies. The simulation reveals radiation leakage originating from

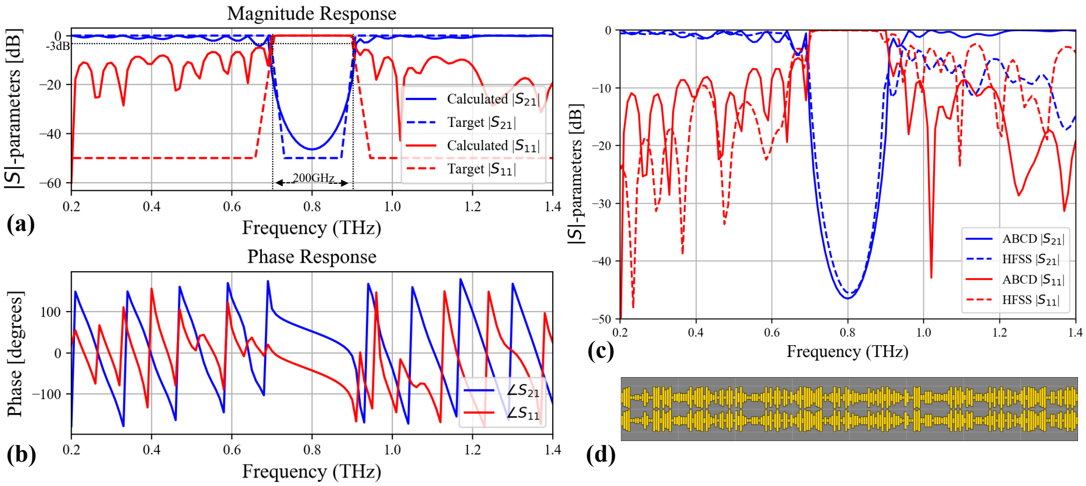

Fig. 4. (a) Calculated magnitude response of the planar band-stop filter's S-parameters (S_{21} and S_{11}) using the ABCD matrix method, compared against the target response. The design specifies a 3-dB bandwidth of 200 GHz and a rejection level of -50 dB, with the computed response achieving a rejection depth of approximately -46 dB. (b) Phase response of the calculated S-parameters, emphasizing the linear phase progression of S_{21} across the passband. (c) Comparison between the results predicted by the ABCD matrix method and full-wave electromagnetic simulations using ANSYS HFSS, showing strong agreement. (d) Final optimized filter geometry synthesized using the proposed GA-based inverse design framework.

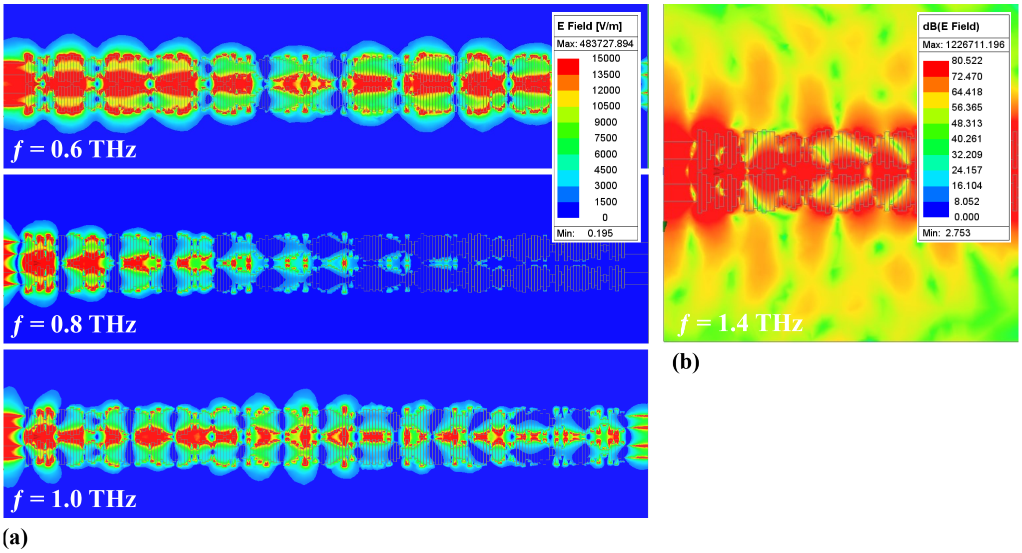

Fig. 5. (a) Electric field distribution of the inverse-designed planar band-stop filter at 0.6 THz, 0.8 THz, and 1.0 THz. The filter exhibits strong suppression in the stopband (0.8 THz) and effective transmission in the passbands (0.6 THz and 1.0 THz), validating its spectral selectivity. (b) Logarithmic-scale field profile at 1.4 THz, illustrating radiation losses at higher frequencies due to edge diffraction and imperfect confinement, particularly from the conductor edges.

the edges of the metallic conductors, attributed to diffraction at frequencies beyond the designed stopband.

Figure 6 illustrates the evolutionary optimization process over multiple generations. The initial generation consists of randomly generated structures, which are progressively refined as the algorithm minimizes the error function. After 120 generations, the optimization converges to a design that matches the desired band stop filter response, as evidenced by the corresponding S-parameters (S_{21} and S_{11} in both magnitude and phase).

To demonstrate the capabilities of the proposed inverse design framework, two sets of design objectives were considered to systematically evaluate the ability of the framework to achieve distinct spectral responses while maintaining a fixed physical footprint of 2000 µm in length. In the first set, we investigated the system's ability to control the rejection depth without altering the device geometry. Specifically, the GA-based inverse design framework was tasked to synthesize band-stop filters centered at 0.8 THz with a fixed 3-dB bandwidth of 70 GHz, while achieving three distinct rejection depths of 10 dB, 20 dB, and 30 dB, respectively. This evaluation serves as a critical benchmark of the algorithm's capability to precisely tailor the depth of the stopband response by optimizing the internal geometry, despite the fixed device dimensions and fabrication constraints. Figure 7(a) presents the simulated S-parameters of the designed filters, demonstrating the system's flexibility in producing filters with different rejection depths. The results confirm that, through appropriate geometry optimization guided by the RMSE-based fitness function, the framework successfully generates non-intuitive filter structures capable of meeting the specified rejection levels. Compared to conventional Bragg grating filters of similar spectral specifications [11], the GA-based inverse-designed filters achieve superior performance (-30 dB rejection compare to -18 dB) with approximately 50% reduction in device length, underscoring the effectiveness of the proposed method for compact THz filter synthesis.

Generation	Filter Structure	RMSE
G = 0	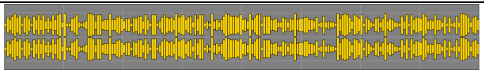	13.46
G = 1	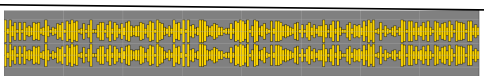	13.19
G = 2	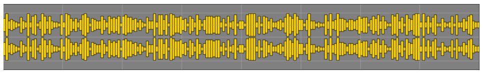	12.54
G = 10	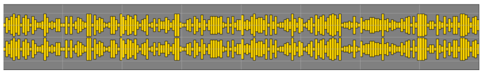	9.20
G = 120	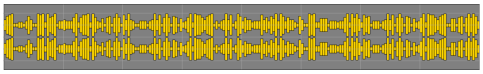	5.91

Fig. 6. (e) Evolutionary optimization process for the inverse-designed planar THz band-stop filter. The initial generation begins with a randomly selected structure, which is iteratively refined across successive generations. The algorithm progressively minimizes the error function until, after 120 generations, the design converges to the desired target filter configuration, demonstrating the efficacy of the proposed inverse design framework.

In the second set, we explored the framework's capability to achieve center frequency tunability within the same physical platform and device length. Band-stop filters with center frequencies of 0.6 THz, 0.8 THz, and 1.0 THz, each targeting a 3-dB bandwidth of 150 GHz, were synthesized. This evaluation demonstrates the adaptability of the inverse design framework to achieve wide frequency tunability by modifying the target spectral response in the optimization process, without requiring changes to the overall device footprint. The simulated S-parameters of these filters are shown in Fig. 7(b). These findings highlight the ability of the proposed framework to design frequency-selective filters with distinct geometries, adapted to various operational frequencies, while preserving a consistent physical footprint and ensuring compatibility with existing fabrication constraints. This underlines the versatility of the developed system for creating customized THz filters capable of meeting diverse application requirements in integrated platforms.

The comparison between the results obtained from the ABCD matrix method and full-wave electromagnetic simulations is presented in each figure. The two approaches exhibit strong agreement with minimal divergence across and below the operational bandwidth. Minor discrepancies at higher frequencies can be attributed to radiation losses and edge diffraction effects, which are not captured by the quasi-static assumptions of the ABCD matrix model, as discussed previously.

The integration of the ABCD matrix method into the GA-based inverse design framework provided a critical computational advantage, enabling rapid and efficient evaluation of candidate filter structures. Each optimization run—consisting of 120 generations and a population size of 200—was completed in approximately 40 minutes on an Intel i7-10700 CPU. In contrast, a single full-wave simulation in ANSYS HFSS (with a maximum $\Delta S = 0.02$ and 130 frequency points) required over two hours, making large-scale optimization infeasible without a surrogate model. The use of the ABCD method thus enabled extensive design space exploration and facilitated the discovery of non-intuitive, high-performance filter geometries compatible with planar CPS-integrated platforms.

Convergence analysis was performed to assess the stability and consistency of the GA-based inverse design framework. As illustrated in Fig. 8, the algorithm was independently executed ten times, each with a different random seed to evaluate the sensitivity of the optimization process to initial population variation. Figure 8(a) visualizes the best fitness value at each generation for all ten runs using circular ring markers. The overlapping distribution of fitness values across runs highlights the consistent convergence trajectory and low inter-run variability.

Figure 8(b) presents a statistical summary of the convergence behavior. The solid blue curve represents the average best fitness value across the ten runs at each generation, while the shaded region indicates the ± 1 standard deviation range. The convergence curve exhibits a rapid increase in fitness during the first 40–50 generations, followed by a slower refinement phase, with convergence typically reached between generations 100 and 120. The narrow standard deviation—remaining below 3-dB in the final S_{21} magnitude response—demonstrates high repeatability and convergence stability.

Although a no-improvement stopping condition was implemented, defined as halting the run if no progress was observed for 30 consecutive generations, it was not triggered in any of the cases. This behavior confirms that the optimization process continued to explore the design space effectively until the predefined maximum generation limit, ensuring thorough solution refinement without early stagnation.

Beyond conventional parameter sweep-based methods, the proposed approach enables automated, efficient, and flexible synthesis of THz filters by iteratively refining candidate solutions in high-dimensional, nonconvex design spaces. The adaptability of the framework allows it to accommodate diverse design objectives, including varying center frequencies, rejection depths, and impedance matching requirements, making it a promising tool for next-generation TSoC components. Future extensions will expand the framework's applicability to other planar devices such as couplers, reflectors, and absorbers.

IV. CONCLUSION

We presented a GA-based inverse design framework for synthesizing planar THz band-stop filters integrated with

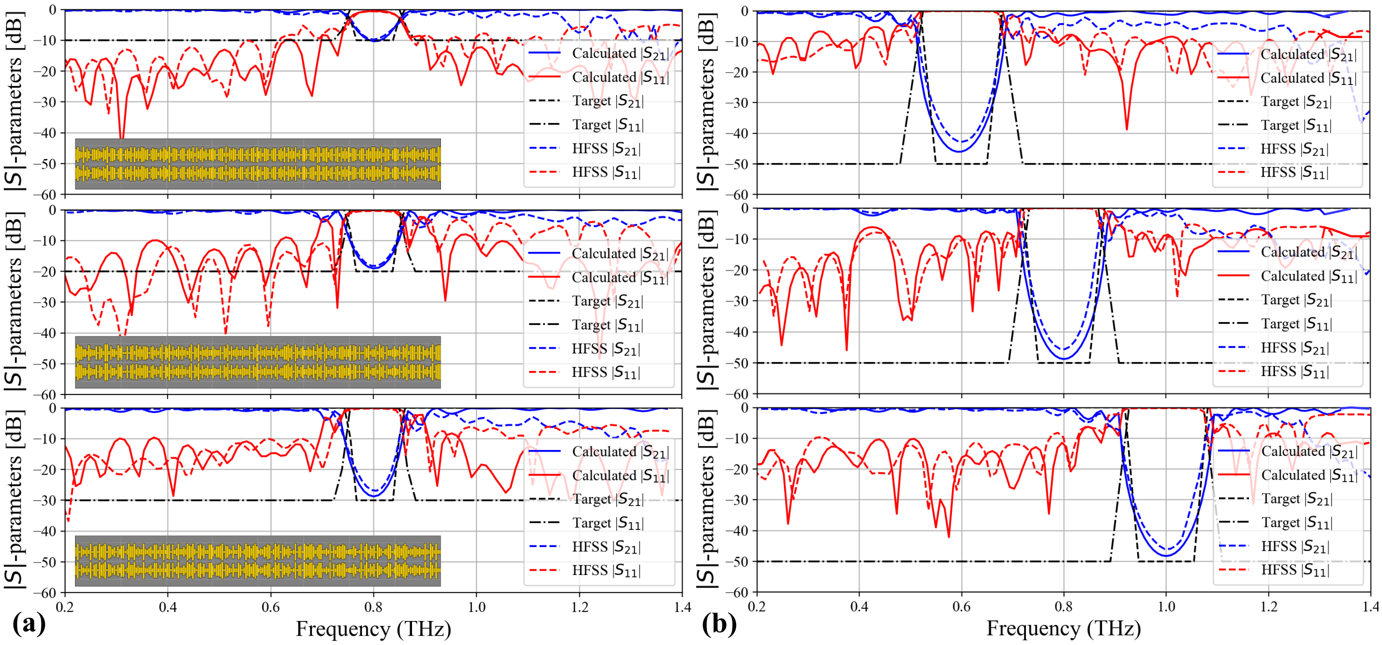

Fig. 7. Comparison of S-parameters of band-stop filters designed using the GA-based inverse design framework. (a) Filters with varying rejection depths centered at 0.8 THz, all within the same device footprint. (b) Filters targeting different center frequencies of 0.6 THz, 0.8 THz, and 1.0 THz, respectively, synthesized within the same device footprint. In both cases, S-parameters obtained using the ABCD matrix method are compared with full-wave simulations performed in ANSYS HFSS, demonstrating strong agreement.

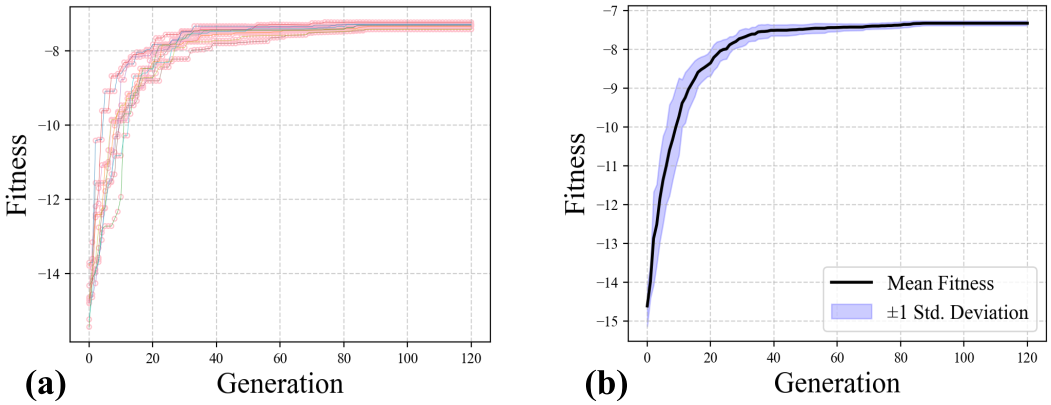

Fig. 8. Convergence behavior of the GA-based inverse design framework over 10 independent runs initialized with different random seeds. (a) Each ring marker represents the best fitness value achieved in that generation for a single run. (b) The solid blue curve indicates the average best fitness across generations, while the shaded region denotes the ±1 standard deviation range. The results demonstrate consistent convergence behavior, low variance across runs, and robustness with respect to initial population randomness.

coplanar stripline (CPS) transmission lines. The framework enabled efficient exploration of complex design spaces, generating non-intuitive, high-performance filter geometries. To accelerate the optimization process, the ABCD matrix method was employed, offering a substantial speed-up over full-wave simulations, with final validation performed using FEM-based electromagnetic analysis. The framework successfully demonstrated the design of filters with tunable rejection depths and center frequencies within fixed device footprints. This work represents the first application of GA-based inverse design using the ABCD matrix method for CPS-integrated THz filters and highlights its potential to advance compact, fabrication-ready components in terahertz system-on-chip (TSoC) platforms.

ACKNOWLEDGMENTS

This work was supported by a NSERC Discovery Grant. This article used Writeful in Overleaf for editing purposes.

REFERENCES

[1] J. Federici and L. Moeller, “Review of terahertz and subterahertz wireless communications,” *Journal of Applied Physics*, vol. 107, no. 11, 2010.

[2] K.-C. Huang and Z. Wang, “Terahertz terabit wireless communication,” *IEEE microwave magazine*, vol. 12, no. 4, pp. 108–116, 2011.

[3] W. Jiang, Q. Zhou, J. He, M. A. Habibi, S. Melnyk, M. El-Absi, B. Han, M. Di Renzo, H. D. Schotten, F.-L. Luo *et al.*, "Terahertz communications and sensing for 6g and beyond: A comprehensive review," *IEEE Communications Surveys & Tutorials*, 2024.

[4] M. Gezimati and G. Singh, "Terahertz imaging and sensing for healthcare: Current status and future perspectives," *IEEE Access*, vol. 11, pp. 18 590–18 619, 2023.

[5] Z. Yan, L.-G. Zhu, K. Meng, W. Huang, and Q. Shi, "Thz medical imaging: from in vitro to in vivo," *Trends in Biotechnology*, vol. 40, no. 7, pp. 816–830, 2022.

[6] X. Fu, Y. Liu, Q. Chen, Y. Fu, and T. J. Cui, "Applications of terahertz spectroscopy in the detection and recognition of substances," *Frontiers in Physics*, vol. 10, p. 869537, 2022.

[7] M. Gerhard, R. Beigang, and M. Rahm, "Comparative terahertz study of rectangular metal waveguides with and without a ridge," *Journal of Infrared, Millimeter, and Terahertz Waves*, vol. 36, pp. 327–334, 2015.

[8] E. S. Lee, S.-G. Lee, C.-S. Kee, and T.-I. Jeon, "Terahertz notch and low-pass filters based on band gaps properties by using metal slits in tapered parallel-plate waveguides," *Optics express*, vol. 19, no. 16, pp. 14 852–14 859, 2011.

[9] J. Cabello-Sánchez, V. Drakinskiy, J. Stake, and H. Rodilla, "Capacitively-coupled resonators for terahertz planar-goubau-line filters," *IEEE Transactions on Terahertz Science and Technology*, vol. 13, no. 1, pp. 58–66, 2022.

[10] W. Gomaa, L. Smith, V. Shiran, and T. Darcie, "Terahertz low-pass filter based on cascaded resonators formed by cps bending on a thin membrane," *Optics Express*, vol. 28, no. 21, pp. 31 967–31 978, 2020.

[11] A. Dehghanian, M. Haghighat, T. Darcie, and L. Smith, "Demonstration of a planar multimodal periodic filter at thz frequencies," *arXiv preprint arXiv:2502.10611*, 2025.

[12] S. Li, H. Liu, Q. Sun, and N. Huang, "A tunable terahertz photonic crystal narrow-band filter," *IEEE Photonics Technology Letters*, vol. 27, no. 7, pp. 752–754, 2015.

[13] A. B. Asl, A. Rostami, and I. Amiri, "Terahertz band pass filter design using multilayer metamaterials," *Optical and Quantum Electronics*, vol. 52, pp. 1–13, 2020.

[14] A. K. Horestani, W. Withayachumnankul, A. Chahadih, A. Ghaddar, M. Zehar, D. Abbott, C. Fumeaux, and T. Akalin, "Metamaterial-inspired bandpass filters for terahertz surface waves on goubau lines," *IEEE Transactions on Terahertz Science and Technology*, vol. 3, no. 6, pp. 851–858, 2013.

[15] Y.-S. Lin, S. Liao, X. Liu, Y. Tong, Z. Xu, R. Xu, D. Yao, and Y. Yu, "Tunable terahertz metamaterial by using three-dimensional double split-ring resonators," *Optics & Laser Technology*, vol. 112, pp. 215–221, 2019.

[16] R. S. Parker-Jervis, S. J. Park, and J. E. Cunningham, "Tunable terahertz band-stop filter using strongly coupled split ring resonators integrated with on-chip waveguide," *Journal of Applied Physics*, vol. 129, no. 5, 2021.

[17] S. Molesky, Z. Lin, A. Y. Piggott, W. Jin, J. Vucković, and A. W. Rodriguez, "Inverse design in nanophotonics," *Nature Photonics*, vol. 12, no. 11, pp. 659–670, 2018.

[18] M. Zhang, N. Zhang, J. Zhang, X. Zhang, P. Dong, B. Wang, L. Yang, R. Wu, and W. Hou, "Automatic and inverse design of broadband terahertz absorber based on optimization of genetic algorithm for dual metasurfaces," *Optics Express*, vol. 30, no. 13, pp. 22 974–22 985, 2022.

[19] M. Zhang, J. Zhang, C. Cui, P. Dong, B. Wang, L. Yang, and X. Zhang, "Accurate inverse design for high-efficiency and broadband terahertz devices by co-simulation with genetic algorithms," *Journal of the Optical Society of America B*, vol. 40, no. 10, pp. 2674–2683, 2023.

[20] J. Li, Y. Li, Y. Cen, C. Zhang, T. Luo, and D. Yang, "Applications of neural networks for spectrum prediction and inverse design in the terahertz band," *IEEE Photonics Journal*, vol. 12, no. 5, pp. 1–9, 2020.

[21] M. Mashayekhi, P. Kabiri, A. S. Nooramin, and M. Soleimani, "A reconfigurable graphene patch antenna inverse design at terahertz frequencies," *Scientific Reports*, vol. 13, no. 1, p. 8369, 2023.

[22] E. A. Karahan, Z. Liu, A. Gupta, Z. Shao, J. Zhou, U. Khankhoje, and K. Sengupta, "Deep-learning enabled generalized inverse design of multi-port radio-frequency and sub-terahertz passives and integrated circuits," *Nature Communications*, vol. 15, no. 1, p. 10734, 2024.

[23] Z. Ding, W. Su, Y. Luo, L. Ye, W. Li, Y. Zhou, J. Zou, B. Tang, and H. Yao, "Metasurface inverse designed by deep learning for quasi-entire terahertz wave absorption," *Nanoscale*, vol. 16, no. 3, pp. 1384–1393, 2024.

[24] R. L. Haupt and D. H. Werner, *Genetic algorithms in electromagnetics*. John Wiley & Sons, 2007.

[25] B. L. Miller, D. E. Goldberg *et al.*, "Genetic algorithms, tournament selection, and the effects of noise," *Complex systems*, vol. 9, no. 3, pp. 193–212, 1995.

[26] G. J. Rawlins, *Foundations of Genetic Algorithms 1991 (FOGA 1)*. Elsevier, 2014, vol. 1.

[27] M. Y. Frankel, S. Gupta, J. A. Valdmanis, and G. A. Mourou, "Terahertz attenuation and dispersion characteristics of coplanar transmission lines," *IEEE Transactions on microwave theory and techniques*, vol. 39, no. 6, pp. 910–916, 1991.

[28] G. Ghione and C. Naldi, "Analytical formulas for coplanar lines in hybrid and monolithic MICs," *Electronics letters*, vol. 20, no. 4, pp. 179–181, 1984.

[29] D. M. Pozar, *Microwave engineering: theory and techniques*. John wiley & sons, 2021.

Bibliography

[1] A. Dehghanian, W. Gomaa, M. Haghighat, T. Darcie, and L. Smith, “Demonstration of an integrated terahertz band-stop filter using an apodized bragg grating,” *Optics Express*, vol. 31, no. 20, pp. 32582–32590, 2023.

[2] A. Dehghanian, M. Haghighat, T. Darcie, and L. Smith, “Demonstration of a planar multimodal periodic filter at thz frequencies,” *Journal of Infrared, Millimeter, and Terahertz Waves*, vol. 46, no. 6, pp. 1–17, 2025.

[3] A. Dehghanian, M. Haghighat, T. Darcie, and L. Smith, “Demonstration of a terahertz integrated planar network synthesis filter,” *Optics Continuum*, vol. 3, no. 1, pp. 71–77, 2024.

[4] A. Dehghanian, T. Darcie, and L. Smith, “Genetic algorithm-based inverse design of guided wave planar terahertz filters,” 2025.

[5] M. Haghighat, A. Dehghanian, T. Darcie, and L. Smith, “Demonstration of terahertz spoof surface plasmon polariton waveguides using coplanar striplines with internal corrugations,” *Optics Express*, vol. 32, no. 27, pp. 48803–48814, 2024.

[6] S. Asadi, M. Haghighat, A. Dehghanian, T. Darcie, and L. Smith, “Terahertz bandstop filter using varying radii split-ring resonators,” *Optics Express*, vol. 33, no. 3, pp. 6421–6430, 2025.

[7] R. Smith and T. Darcie, “Demonstration of a low-distortion terahertz system-on-chip using a cps waveguide on a thin membrane substrate,” *Optics express*, vol. 27, no. 10, pp. 13653–13663, 2019.

[8] A. Y. Pawar, D. D. Sonawane, K. B. Erande, and D. V. Derle, “Terahertz technology and its applications,” *Drug invention today*, vol. 5, no. 2, pp. 157–163, 2013.

[9] Y.-S. Lee, *Principles of terahertz science and technology*, vol. 170. Springer Science & Business Media, 2009.

[10] T. Kleine-Ostmann and T. Nagatsuma, “A review on terahertz communications research,” *Journal of Infrared, Millimeter, and Terahertz Waves*, vol. 32, pp. 143–171, 2011.

[11] Z. Chen, X. Ma, B. Zhang, Y. Zhang, Z. Niu, N. Kuang, W. Chen, L. Li, and S. Li, “A survey on terahertz communications,” *China Communications*, vol. 16, no. 2, pp. 1–35, 2019.

[12] K. Tekbıyık, A. R. Ekti, G. K. Kurt, and A. Görçin, “Terahertz band communication systems: Challenges, novelties and standardization efforts,” *Physical Communication*, vol. 35, p. 100700, 2019.

[13] P. U. Jepsen, D. G. Cooke, and M. Koch, “Terahertz spectroscopy and imaging–modern techniques and applications,” *Laser & Photonics Reviews*, vol. 5, no. 1, pp. 124–166, 2011.

[14] K.-E. Peiponen, A. Zeitler, and M. Kuwata-Gonokami, *Terahertz spectroscopy and imaging*, vol. 171. Springer, 2012.

[15] X. Yang, X. Zhao, K. Yang, Y. Liu, Y. Liu, W. Fu, and Y. Luo, “Biomedical applications of terahertz spectroscopy and imaging,” *Trends in biotechnology*, vol. 34, no. 10, pp. 810–824, 2016.

[16] L. Afsah-Hejri, P. Hajeb, P. Ara, and R. J. Ehsani, “A comprehensive review on food applications of terahertz spectroscopy and imaging,” *Comprehensive Reviews in Food Science and Food Safety*, vol. 18, no. 5, pp. 1563–1621, 2019.

[17] J. Grzyb, B. Heinemann, and U. R. Pfeiffer, “Solid-state terahertz superresolution imaging device in 130-nm sige bicmos technology,” *IEEE Transactions on Microwave Theory and Techniques*, vol. 65, no. 11, pp. 4357–4372, 2017.

[18] M. Danciu, T. Alexa-Stratulat, C. Stefanescu, G. Dodi, B. I. Tamba, C. T. Mihai, G. D. Stanciu, A. Luca, I. A. Spiridon, L. B. Ungureanu, *et al.*, “Terahertz spectroscopy and imaging: a cutting-edge method for diagnosing digestive cancers,” *Materials*, vol. 12, no. 9, p. 1519, 2019.

[19] P. Tewari, Z. D. Taylor, D. Bennett, R. S. Singh, M. O. Culjat, C. P. Kealey, J. P. Hubschman, S. White, A. Cochran, E. R. Brown, *et al.*, “Terahertz imaging of biological tissues,” in *Medicine Meets Virtual Reality 18*, pp. 653–657, IOS Press, 2011.

[20] L. Guo, X. Wang, and Y. Zhang, “Terahertz digital holographic imaging of biological tissues,” in *International Symposium on Ultrafast Phenomena and Terahertz Waves*, pp. IW4B–3, Optica Publishing Group, 2016.

[21] S. Smye, J. Chamberlain, A. Fitzgerald, and E. Berry, “The interaction between terahertz radiation and biological tissue,” *Physics in Medicine & Biology*, vol. 46, no. 9, p. R101, 2001.

[22] E. S. Lee, K. Moon, I.-M. Lee, H.-S. Kim, D. W. Park, J.-W. Park, D. H. Lee, S.-P. Han, N. Kim, and K. H. Park, “Semiconductor-based terahertz photonics for industrial applications,” *Journal of Lightwave Technology*, vol. 36, no. 2, pp. 274–283, 2017.

[23] E. S. Lee, M. Kim, K. Moon, I.-M. Lee, D. W. Park, J.-H. Shin, H.-S. Kim, D.-H. Choi, K. S. Choi, D. H. Lee, *et al.*, “High-speed and cost-effective reflective terahertz imaging system using a novel 2d beam scanner,” *Journal of Lightwave Technology*, vol. 38, no. 16, pp. 4237–4243, 2020.

[24] G. Ducournau, “Silicon photonics targets terahertz region,” *Nature Photonics*, vol. 12, no. 10, pp. 574–575, 2018.

[25] M. Tonouchi, “Cutting-edge terahertz technology,” *Nature photonics*, vol. 1, no. 2, pp. 97–105, 2007.

[26] S. K. Mathanker, P. R. Weckler, and N. Wang, “Terahertz (thz) applications in food and agriculture: A review,” *Transactions of the ASABE*, vol. 56, no. 3, pp. 1213–1226, 2013.

[27] M. C. Hoffmann, K.-L. Yeh, J. Hebling, and K. A. Nelson, “Efficient terahertz generation by optical rectification at 1035 nm,” *Optics Express*, vol. 15, no. 18, pp. 11706–11713, 2007.

[28] Y. J. Ding, “Progress in terahertz sources based on difference-frequency generation,” *JOSA B*, vol. 31, no. 11, pp. 2696–2711, 2014.

[29] E. Castro-Camus and M. Alfaro, “Photoconductive devices for terahertz pulsed spectroscopy: a review,” *Photonics Research*, vol. 4, no. 3, pp. A36–A42, 2016.

[30] N. T. Yardimci, S. Cakmakyapan, S. Hemmati, and M. Jarrahi, “A high-power broadband terahertz source enabled by three-dimensional light confinement in a plasmonic nanocavity,” *Scientific reports*, vol. 7, no. 1, p. 4166, 2017.

[31] Q. Lu, D. Wu, S. Sengupta, S. Slivken, and M. Razeghi, “Room temperature continuous wave, monolithic tunable thz sources based on highly efficient mid-infrared quantum cascade lasers,” *Scientific reports*, vol. 6, no. 1, p. 23595, 2016.

[32] B. S. Williams, “Terahertz quantum-cascade lasers,” *Nature photonics*, vol. 1, no. 9, pp. 517–525, 2007.

[33] N. T. Yardimci and M. Jarrahi, “Nanostructure-enhanced photoconductive terahertz emission and detection,” *Small*, vol. 14, no. 44, p. 1802437, 2018.

[34] Y. Jiang, B. Jin, W. Xu, L. Kang, J. Chen, and P. Wu, “Terahertz detectors based on superconducting hot electron bolometers,” *Science China Information Sciences*, vol. 55, pp. 64–71, 2012.

[35] D. Glaab, S. Boppel, A. Lisauskas, U. Pfeiffer, E. Öjefors, and H. G. Roskos, “Terahertz heterodyne detection with silicon field-effect transistors,” *Applied physics letters*, vol. 96, no. 4, p. 042106, 2010.

[36] W. Knap, M. Dyakonov, D. Coquillat, F. Teppe, N. Dyakonova, J. Łusakowski, K. Karpierz, M. Sakowicz, G. Valusis, D. Seliuta, *et al.*, “Field effect transistors for terahertz detection: Physics and first imaging applications,” *Journal of Infrared, Millimeter, and Terahertz Waves*, vol. 30, pp. 1319–1337, 2009.

[37] D. Auston, “Impulse response of photoconductors in transmission lines,” *IEEE Journal of Quantum Electronics*, vol. 19, no. 4, pp. 639–648, 1983.

[38] D. H. Auston, K. P. Cheung, and P. R. Smith, “Picosecond photoconducting hertzian dipoles,” *Applied physics letters*, vol. 45, no. 3, pp. 284–286, 1984.

[39] W. Kaiser and D. H. Auston, *Ultrashort laser pulses: generation and applications.* Springer, 1993.

[40] K. McIntosh, K. Nichols, S. Verghese, and E. Brown, "Investigation of ultrashort photocarrier relaxation times in low-temperature-grown gaas," *Applied physics letters*, vol. 70, no. 3, pp. 354–356, 1997.

[41] D. C. Look, D. Walters, G. Robinson, J. Sizelove, M. Mier, and C. Stutz, "Annealing dynamics of molecular-beam epitaxial gaas grown at 200° c," *Journal of applied physics*, vol. 74, no. 1, pp. 306–310, 1993.

[42] F. Doany, D. Grischkowsky, and C. Chi, "Carrier lifetime vs. ion-implantation dose in silicon on sapphire," in *Picosecond Electronics and Optoelectronics*, p. WE11, Optica Publishing Group, 1987.

[43] M. Tani, S. Matsuura, K. Sakai, and S.-i. Nakashima, "Emission characteristics of photoconductive antennas based on low-temperature-grown gaas and semi-insulating gaas," *Applied optics*, vol. 36, no. 30, pp. 7853–7859, 1997.

[44] L. Smith, W. Gomma, H. Esmaeilsabzali, and T. Darcie, "Tapered transmission lines for terahertz systems," *Optics Express*, vol. 29, no. 11, pp. 17295–17303, 2021.

[45] G. Gallot, S. Jamison, R. McGowan, and D. Grischkowsky, "Terahertz waveguides," *JOSA B*, vol. 17, no. 5, pp. 851–863, 2000.

[46] D. M. Pozar, *Microwave engineering.* John wiley & sons, 2011.

[47] D. Melati, A. Melloni, and F. Morichetti, "Real photonic waveguides: guiding light through imperfections," *Advances in Optics and Photonics*, vol. 6, no. 2, pp. 156–224, 2014.

[48] D. R. Grischkowsky, M. B. Ketchen, C.-C. Chi, I. N. Duling, N. J. Halas, J.-M. Halbout, and P. G. May, "Capacitance free generation and detection of subpicosecond electrical pulses on coplanar transmission lines," *IEEE journal of quantum electronics*, vol. 24, no. 2, pp. 221–225, 1988.

[49] R. L. Smith, *Experimental evaluation of low-loss/non-dispersive terahertz waveguides.* PhD dissertation, University of Victoria, 2019.

[50] S. Gevorgian and H. Berg, "Line capacitance and impedance of coplanar-strip waveguides on substrates with multiple dielectric layers," 2001.

[51] S. Gevorgian, H. Berg, H. Jacobsson, and T. Lewin, "Application notes-basic parameters of coplanar-strip waveguides on multilayer dielectric/semiconductor substrates, part 1: high permittivity superstrates," *IEEE microwave magazine*, vol. 4, no. 2, pp. 60–70, 2003.

[52] M. Y. Frankel, S. Gupta, J. A. Valdmanis, and G. A. Mourou, "Terahertz attenuation and dispersion characteristics of coplanar transmission lines," *IEEE Transactions on microwave theory and techniques*, vol. 39, no. 6, pp. 910–916, 1991.

[53] D. P. Kasilingam and D. B. Rutledge, "Surface-wave losses of coplanar transmission lines," in *1983 IEEE MTT-S International Microwave Symposium Digest*, pp. 113–116, IEEE, 1983.

[54] H.-J. Cheng, J. F. Whitaker, T. M. Weller, and L. P. Katehi, "Terahertz-bandwidth characteristics of coplanar transmission lines on low permittivity substrates," *IEEE Transactions on Microwave Theory and Techniques*, vol. 42, no. 12, pp. 2399–2406, 1994.

[55] G. Hasnain, A. Dienes, and J. Whinnery, "Dispersion of picosecond pulses in coplanar transmission lines," *IEEE Transactions on Microwave Theory and Techniques*, vol. 34, no. 6, pp. 738–741, 1986.

[56] W. Gomaa, L. Smith, V. Shiran, and T. Darcie, "Terahertz low-pass filter based on cascaded resonators formed by cps bending on a thin membrane," *Optics Express*, vol. 28, no. 21, pp. 31967–31978, 2020.

[57] Z. Zhu, X. Zhang, J. Gu, R. Singh, Z. Tian, J. Han, and W. Zhang, "A metamaterial-based terahertz low-pass filter with low insertion loss and sharp rejection," *IEEE Transactions on Terahertz Science and Technology*, vol. 3, no. 6, pp. 832–837, 2013.

[58] I. Hunter, *Theory and design of microwave filters.* No. 48, Iet, 2001.

[59] N. Zhang, R. Song, M. Hu, G. Shan, C. Wang, and J. Yang, "A low-loss design of bandpass filter at the terahertz band," *IEEE Microwave and Wireless Components Letters*, vol. 28, no. 7, pp. 573–575, 2018.

[60] H. S. Bark, G. J. Kim, and T.-I. Jeon, "Transmission characteristics of all-dielectric guided-mode resonance filter in the thz region," *Scientific reports*, vol. 8, no. 1, p. 13570, 2018.

[61] L. Tan, D. Wang, and K.-D. Xu, "Terahertz metamaterials for spectrum modulation: structural design, materials and applications," *Materials & Design*, p. 113217, 2024.

[62] L. Smith, V. Shiran, W. Gomaa, and T. Darcie, "Characterization of a split-ring-resonator-loaded transmission line at terahertz frequencies," *Optics Express*, vol. 29, no. 15, pp. 23282–23289, 2021.

[63] H. Zhu, Y. Zhang, L. Ye, Y. Li, Y. Chen, R. Xu, and B. Yan, "Compact terahertz on-chip filter with broadband rejection based on spoof surface plasmon polaritons," *IEEE Electron Device Letters*, vol. 43, no. 6, pp. 970–973, 2022.

[64] X. Shang, M. Ke, Y. Wang, and M. J. Lancaster, "Wr-3 band waveguides and filters fabricated using su8 photoresist micromachining technology," *IEEE Transactions on Terahertz Science and Technology*, vol. 2, no. 6, pp. 629–637, 2012.

[65] M. Vahidpour and K. Sarabandi, "Micromachined j-band rectangular waveguide filter," in *2011 XXXth URSI General Assembly and Scientific Symposium*, pp. 1–4, IEEE, 2011.

[66] E. S. Lee, S.-G. Lee, C.-S. Kee, and T.-I. Jeon, "Terahertz notch and low-pass filters based on band gaps properties by using metal slits in tapered parallel-plate waveguides," *Optics express*, vol. 19, no. 16, pp. 14852–14859, 2011.

[67] C. Wang, B. Lu, C. Lin, Q. Chen, L. Miao, X. Deng, and J. Zhang, "0.34-thz wireless link based on high-order modulation for future wireless local area network applications," *IEEE Transactions on Terahertz Science and Technology*, vol. 4, no. 1, pp. 75–85, 2014.

[68] F. Lan, Z. Yang, L. Qi, X. Gao, and Z. Shi, "Terahertz dual-resonance bandpass filter using bilayer reformative complementary metamaterial structures," *Optics letters*, vol. 39, no. 7, pp. 1709–1712, 2014.

[69] Y.-J. Chiang, C.-S. Yang, Y.-H. Yang, C.-L. Pan, and T.-J. Yen, “An ultrabroad terahertz bandpass filter based on multiple-resonance excitation of a composite metamaterial,” *Applied Physics Letters*, vol. 99, no. 19, 2011.

[70] Y. Huang, K. Nakamura, Y. Takida, H. Minamide, K. Hane, and Y. Kanamori, “Actively tunable thz filter based on an electromagnetically induced transparency analog hybridized with a mems metamaterial,” *Scientific Reports*, vol. 10, no. 1, p. 20807, 2020.

[71] J.-F. Ruan, F. Lan, Z. Tao, Z.-F. Meng, and S.-W. Ji, “Tunable terahertz metamaterial filter based on applying distributed load,” *Physics Letters A*, vol. 421, p. 127705, 2022.

[72] Z. Wang, G. Dong, S. Yuan, L. Chen, X. Wu, and X. Zhang, “Voltage-actuated thermally tunable on-chip terahertz filters based on a whispering gallery mode resonator,” *Optics letters*, vol. 44, no. 19, pp. 4670–4673, 2019.

[73] D. Wu, N. Fang, C. Sun, X. Zhang, W. J. Padilla, D. N. Basov, D. R. Smith, and S. Schultz, “Terahertz plasmonic high pass filter,” *Applied Physics Letters*, vol. 83, no. 1, pp. 201–203, 2003.

[74] S. Liu, J. Hu, Y. Zhang, Z. Zheng, Y. Liu, R. Xu, and Q. Xue, “1 thz micromachined waveguide band-pass filter,” *Journal of Infrared, Millimeter, and Terahertz Waves*, vol. 37, pp. 435–447, 2016.

[75] S. Molesky, Z. Lin, A. Y. Piggott, W. Jin, J. Vucković, and A. W. Rodriguez, “Inverse design in nanophotonics,” *Nature Photonics*, vol. 12, no. 11, pp. 659–670, 2018.

[76] P. R. Wiecha, A. Arbouet, C. Girard, and O. L. Muskens, “Deep learning in nano-photonics: inverse design and beyond,” *Photonics Research*, vol. 9, no. 5, pp. B182–B200, 2021.

[77] R. E. Christiansen and O. Sigmund, “Inverse design in photonics by topology optimization: tutorial,” *Journal of the Optical Society of America B*, vol. 38, no. 2, pp. 496–509, 2021.

[78] T. W. Hughes, M. Minkov, I. A. Williamson, and S. Fan, “Adjoint method and inverse design for nonlinear nanophotonic devices,” *ACS Photonics*, vol. 5, no. 12, pp. 4781–4787, 2018.

[79] Z. Yu, H. Cui, and X. Sun, “Genetically optimized on-chip wideband ultracompact reflectors and fabry–perot cavities,” *Photonics Research*, vol. 5, no. 6, pp. B15–B19, 2017.

[80] J. C. Mak, C. Sideris, J. Jeong, A. Hajimiri, and J. K. Poon, “Binary particle swarm optimized 2× 2 power splitters in a standard foundry silicon photonic platform,” *Optics letters*, vol. 41, no. 16, pp. 3868–3871, 2016.

[81] M. Zhang, N. Zhang, J. Zhang, X. Zhang, P. Dong, B. Wang, L. Yang, R. Wu, and W. Hou, “Automatic and inverse design of broadband terahertz absorber based on optimization of genetic algorithm for dual metasurfaces,” *Optics Express*, vol. 30, no. 13, pp. 22974–22985, 2022.

[82] M. Zhang, J. Zhang, C. Cui, P. Dong, B. Wang, L. Yang, and X. Zhang, “Accurate inverse design for high-efficiency and broadband terahertz devices by co-simulation with genetic algorithms,” *Journal of the Optical Society of America B*, vol. 40, no. 10, pp. 2674–2683, 2023.

[83] J. Li, Y. Li, Y. Cen, C. Zhang, T. Luo, and D. Yang, “Applications of neural networks for spectrum prediction and inverse design in the terahertz band,” *IEEE Photonics Journal*, vol. 12, no. 5, pp. 1–9, 2020.

[84] M. Mashayekhi, P. Kabiri, A. S. Nooramin, and M. Soleimani, “A reconfigurable graphene patch antenna inverse design at terahertz frequencies,” *Scientific Reports*, vol. 13, no. 1, p. 8369, 2023.

[85] E. A. Karahan, Z. Liu, A. Gupta, Z. Shao, J. Zhou, U. Khankhoje, and K. Sengupta, “Deep-learning enabled generalized inverse design of multi-port radiofrequency and sub-terahertz passives and integrated circuits,” *Nature Communications*, vol. 15, no. 1, p. 10734, 2024.

[86] Z. Ding, W. Su, Y. Luo, L. Ye, W. Li, Y. Zhou, J. Zou, B. Tang, and H. Yao, “Metasurface inverse designed by deep learning for quasi-entire terahertz wave absorption,” *Nanoscale*, vol. 16, no. 3, pp. 1384–1393, 2024.

[87] R. L. Haupt and D. H. Werner, *Genetic algorithms in electromagnetics.* John Wiley & Sons, 2007.

[88] M. C. Nuss and J. Orenstein, “Terahertz time-domain spectroscopy,” *Millimeter and submillimeter wave spectroscopy of solids*, pp. 7–50, 2007.

[89] R. D. V. Ríos, S. Bikorimana, M. A. Ummy, R. Dorsinville, and S.-W. Seo, "A bow-tie photoconductive antenna using a low-temperature-grown gaas thin-film on a silicon substrate for terahertz wave generation and detection," *Journal of Optics*, vol. 17, no. 12, p. 125802, 2015.

[90] J. Blakemore, "Semiconducting and other major properties of gallium arsenide," *Journal of Applied Physics*, vol. 53, no. 10, pp. R123–R181, 1982.

[91] M. Stellmacher, R. Bisaro, P. Galtier, J. Nagle, K. Khirouni, and J. Bourgoin, "Defects and defect behaviour in gaas grown at low temperature," *Semiconductor science and technology*, vol. 16, no. 6, p. 440, 2001.

[92] M. Ettenberg, A. Sigai, A. Dreeben, and S. Gilbert, "Vapor growth and properties of alas," *Journal of The Electrochemical Society*, vol. 118, no. 8, p. 1355, 1971.

[93] P. Petroff, A. Gossard, and W. Wiegmann, "Structure of alas-gaas interfaces grown on (100) vicinal surfaces by molecular beam epitaxy," *Applied physics letters*, vol. 45, no. 6, pp. 620–622, 1984.

[94] W. Gomaa and T. Darcie, "Design and simulation of terahertz apodized Bragg grating using coplanar stripline transmission line a 1 μm-thin membrane," in *Journal of Physics: Conference Series*, vol. 2304, p. 012015, IOP Publishing, 2022.

[95] S. Orfanidis, *Electromagnetic Waves and Antennas*. Online, 2016.

[96] W. Gomaa, L. Smith, V. Shiran, and T. Darcie, "Terahertz low-pass filter based on cascaded resonators formed by CPS bending on a thin membrane," *Optics Express*, vol. 28, no. 21, pp. 31967–31978, 2020.

[97] M. Naftaly and R. Dudley, "Methodologies for determining the dynamic ranges and signal-to-noise ratios of terahertz time-domain spectrometers," *Optics letters*, vol. 34, no. 8, pp. 1213–1215, 2009.

[98] M. A. Llamas, D. Girbau, M. Ribo, L. Pradell, A. Lazaro, F. Giacomozzi, and B. Margesin, "MEMS-based 180° phase switch for differential radiometers," *IEEE Transactions on Microwave Theory and Techniques*, vol. 58, no. 5, pp. 1264–1272, 2010.

[99] M. A. Llamas, M. Ribo, D. Girbau, and L. Pradell, “A rigorous multimodal analysis and design procedure of a uniplanar 180° hybrid,” *IEEE Transactions on Microwave Theory and Techniques*, vol. 57, no. 7, pp. 1832–1839, 2009.

[100] A. Contreras, L. Pradell, and M. Ribó, “A novel tunable multimodal bandpass filter,” in *2011 41st European Microwave Conference*, pp. 1059–1062, IEEE, 2011.

[101] R. D. V. Rios, S. Bikorimana, M. A. Ummy, R. Dorsinville, and S.-W. Seo, “A bow-tie photoconductive antenna using a low-temperature-grown GaAs thin-film on a silicon substrate for terahertz wave generation and detection,” *Journal of Optics*, vol. 17, no. 12, p. 125802, 2015.

[102] G. Cataldo, J. A. Beall, H.-M. Cho, B. McAndrew, M. D. Niemack, and E. J. Wollack, “Infrared dielectric properties of low-stress silicon nitride,” *Optics Letters*, vol. 37, no. 20, pp. 4200–4202, 2012.

[103] M. Ribó and L. Pradell, “Circuit model for mode conversion in coplanar waveguide asymmetric shunt impedances,” *Electronics Letters*, vol. 35, no. 9, pp. 713–715, 1999.

[104] G. Ghione and C. Naldi, “Coplanar waveguides for MMIC applications: Effect of upper shielding, conductor backing, finite-extent ground planes, and line-to-line coupling,” *IEEE transactions on Microwave Theory and Techniques*, vol. 35, no. 3, pp. 260–267, 1987.

[105] G. Ghione and C. Naldi, “Analytical formulas for coplanar lines in hybrid and monolithic MICs,” *Electronics letters*, vol. 20, no. 4, pp. 179–181, 1984.

[106] Y. Shih and T. Itoh, “Analysis of conductor-backed coplanar waveguide,” *Electronics Letters*, vol. 18, no. 12, pp. 538–440, 1982.

[107] D. S. Phatak, N. K. Das, and A. Defonzo, “Dispersion characteristics of optically excited coplanar striplines: comprehensive full-wave analysis,” *IEEE Transactions on Microwave Theory and Techniques*, vol. 38, no. 11, pp. 1719–1730, 1990.

[108] L. Duvillaret, F. Garet, J.-F. Roux, and J.-L. Coutaz, “Analytical modeling and optimization of terahertz time-domain spectroscopy experiments, using photo-

switches as antennas," *IEEE Journal of Selected Topics in Quantum Electronics*, vol. 7, no. 4, pp. 615–623, 2001.

[109] A. Garufo, G. Carluccio, N. Llombart, and A. Neto, "Norton equivalent circuit for pulsed photoconductive antennas–part i: Theoretical model," *IEEE Transactions on Antennas and Propagation*, vol. 66, no. 4, pp. 1635–1645, 2018.

[110] H. Zhang, N. Llombart, J. Bueno, A. Freni, and A. Neto, "Time-domain equivalent circuits for the link modelling between pulsed photoconductive sources and receivers," *IEEE Transactions on Terahertz Science and Technology*, 2024.

[111] X. Shang, H. Yang, D. Glynn, and M. J. Lancaster, "Submillimeter-wave waveguide filters fabricated by su-8 process and laser micromachining," *IET Microwaves, Antennas & Propagation*, vol. 11, no. 14, pp. 2027–2034, 2017.

[112] Z.-W. Miao, X. Liu, Z.-C. Hao, Y. Zeng, C.-Y. Ding, and W. Hong, "A 0.9-thz integrally manufactured high-precision waveguide cavity filter using electrochemical micromachining technology," *IEEE Transactions on Microwave Theory and Techniques*, vol. 71, no. 10, pp. 4494–4504, 2023.

[113] B. L. Miller, D. E. Goldberg, *et al.*, "Genetic algorithms, tournament selection, and the effects of noise," *Complex systems*, vol. 9, no. 3, pp. 193–212, 1995.

[114] G. J. Rawlins, *Foundations of Genetic Algorithms 1991 (FOGA 1)*, vol. 1. Elsevier, 2014.

[115] C. M. Lalau-Keraly, S. Bhargava, O. D. Miller, and E. Yablonovitch, "Adjoint shape optimization applied to electromagnetic design," *Optics express*, vol. 21, no. 18, pp. 21693–21701, 2013.

[116] A. Y. Piggott, J. Lu, K. G. Lagoudakis, J. Petykiewicz, T. M. Babinec, and J. Vučković, "Inverse design and demonstration of a compact and broadband on-chip wavelength demultiplexer," *Nature photonics*, vol. 9, no. 6, pp. 374–377, 2015.

[117] J. Kim, J.-Y. Kim, J. Kim, Y. Hyeong, B. Neseli, J.-B. You, J. Shim, J. Shin, H.-H. Park, and H. Kurt, "Inverse design of nanophotonic devices enabled by optimization algorithms and deep learning: recent achievements and future prospects," *Nanophotonics*, no. 0, 2025.